

## CANADIAN THESES ON MICROFICHE

I.S.B.N.

## THESES CANADIENNES SUR MICROFICHE



National Library of Canada  
Collections Development Branch

Bibliothèque nationale du Canada  
Direction du développement des collections

Canadian Theses on  
Microfiche Service

Service des thèses canadiennes  
sur microfiche

Ottawa, Canada  
K1A 0N4

### NOTICE

The quality of this microfiche is heavily dependent upon the quality of the original thesis submitted for microfilming. Every effort has been made to ensure the highest quality of reproduction possible.

If pages are missing, contact the university which granted the degree.

Some pages may have indistinct print especially if the original pages were typed with a poor typewriter ribbon or if the university sent us a poor photocopy.

Previously copyrighted materials (journal articles, published tests, etc.) are not filmed.

Reproduction in full or in part of this film is governed by the Canadian Copyright Act, R.S.C. 1970, c. C-30. Please read the authorization forms which accompany this thesis.

THIS DISSERTATION  
HAS BEEN MICROFILMED  
EXACTLY AS RECEIVED

### AVIS

La qualité de cette microfiche dépend grandement de la qualité de la thèse soumise au microfilmage. Nous avons tout fait pour assurer une qualité supérieure de reproduction.

S'il manque des pages, veuillez communiquer avec l'université qui a conféré le grade.

La qualité d'impression de certaines pages peut laisser à désirer, surtout si les pages originales ont été dactylographiées à l'aide d'un ruban usé ou si l'université nous a fait parvenir une photocopie de mauvaise qualité.

Les documents qui font déjà l'objet d'un droit d'auteur (articles de revue, examens publiés, etc.) ne sont pas microfilmés.

La reproduction, même partielle, de ce microfilm est soumise à la Loi canadienne sur le droit d'auteur, SRC 1970, c. C-30. Veuillez prendre connaissance des formules d'autorisation qui accompagnent cette thèse.

LA THÈSE A ÉTÉ  
MICROFILMÉE TELLÉ QUE  
NOUS L'AVONS REÇUE



National Library  
of Canada

Bibliothèque nationale  
du Canada

Canadian Theses Division

Division des thèses canadiennes

Ottawa, Canada  
K1A 0N4

67310

## PERMISSION TO MICROFILM — AUTORISATION DE MICROFILMER

• Please print or type — Écrire en lettres moulées ou dactylographier

Full Name of Author — Nom complet de l'auteur

Joanne C.M. Zwinkels

~~Canada~~

Date of Birth — Date de naissance

24 / 07 / 55

Country of Birth — Lieu de naissance

Canada

Permanent Address — Résidence fixe

#1204-11147 82nd Ave.  
Edmonton, Alberta  
T6G 0T5

Title of Thesis — Titre de la thèse

Infrared Optical Properties of Barium Chlorate  
Monohydrate by Specular Reflectance Spectroscopy

University — Université

of Alberta

Degree for which thesis was presented — Grade pour lequel cette thèse fut présentée

Ph.D.

Year this degree conferred — Année d'obtention de ce grade

1984

Name of Supervisor — Nom du directeur de thèse

Dr. J. E. Bertie

Permission is hereby granted to the NATIONAL LIBRARY OF CANADA to microfilm this thesis and to lend or sell copies of the film.

The author reserves other publication rights, and neither the thesis nor extensive extracts from it may be printed or otherwise reproduced without the author's written permission.

L'autorisation est, par la présente, accordée à la BIBLIOTHÈQUE NATIONALE DU CANADA de microfilmer cette thèse et de prêter ou de vendre des exemplaires du film.

L'auteur se réserve les autres droits de publication; ni la thèse ni de longs extraits de celle-ci ne doivent être imprimés ou autrement reproduits sans l'autorisation écrite de l'auteur.

Date

December 23 / 83

Signature

Joanne Zwinkels

THE UNIVERSITY OF ALBERTA

INFRARED OPTICAL PROPERTIES OF BARIUM  
CHLORATE MONOHYDRATE BY SPECULAR REFLECTANCE SPECTROSCOPY

BY

JOANNE CORNELIA MARY ZWINKELS

A THESIS

SUBMITTED TO THE FACULTY OF GRADUATE STUDIES AND RESEARCH  
IN PARTIAL FULFILMENT OF THE REQUIREMENTS FOR THE DEGREE  
OF

DOCTOR OF PHILOSOPHY

DEPARTMENT OF CHEMISTRY

EDMONTON, ALBERTA

SPRING, 1984

THE UNIVERSITY OF ALBERTA

RELEASE FORM

NAME OF AUTHOR Joanne Cornelia Mary Zwinkels

TITLE OF THESIS Infrared Optical Properties of Barium  
Chlorate Monohydrate by Specular  
Reflectance Spectroscopy

DEGREE FOR WHICH THESIS WAS PRESENTED Ph.D.

YEAR THIS DEGREE GRANTED 1984

Permission is hereby granted to THE UNIVERSITY OF ALBERTA LIBRARY to reproduce single copies of this thesis and to lend or sell such copies for private, scholarly or scientific research purposes only.

The author reserves other publication rights, and neither the thesis nor extensive extracts from it may be printed or otherwise reproduced without the author's written permission.

(Signed) *Joanne Zwinkels*

Permanent Address

#1204 - 11147-82nd Ave.

Edmonton, Alberta T6G 0T5

Dated *December 10* 1983.

THE UNIVERSITY OF ALBERTA  
FACULTY OF GRADUATE STUDIES AND RESEARCH

The undersigned certify that they have read, and  
recommend to the Faculty of Graduate Studies and Research  
for acceptance, a thesis entitled

'INFRARED OPTICAL PROPERTIES OF BARIUM CHLORATE  
MONOHYDRATE BY SPECULAR REFLECTANCE SPECTROSCOPY'

submitted by JOANNE CORNELIA MARY ZWINKELS in partial  
fulfilment of the requirements for the degree of Doctor of  
Philosophy.

.....  
Supervisor

.....  
Benny Hendrick

.....  
J. Della Lona

.....  
W.R. Thorne

.....  
J. H. P. Brown

.....  
Roger French

External Examiner

Date 16 December 1983

To Terry .

## ABSTRACT

The room-temperature infrared reflectance spectra of polycrystalline and single crystal barium chlorate monohydrate,  $\text{Ba}(\text{ClO}_3)_2 \cdot \text{H}_2\text{O}$ , were measured at  $9.5^\circ$  incidence, over the range  $100\text{--}7200\text{ cm}^{-1}$ . The (001) crystal face was studied under polarized radiation, with the electric vector parallel and perpendicular to the b-axis. Major sources of error affecting the measured reflectance were thoroughly investigated and, where necessary, a suitable correction was applied. Excellent experimental reproducibility was achieved in this manner.

The optical constants,  $n$  and  $k$ , were obtained from a Kramers-Kronig analysis, assuming normal incidence and constant reflectivity in the unmeasured spectral regions. Model calculations showed that these assumptions gave accurate results, provided that the measurements were performed over a sufficiently broad spectral range.

The resonance frequency, damping constant, and transition strength, for each of the fundamental vibrations, were determined from a classically damped harmonic oscillator model for the infrared band shapes. These values, known as the dispersion parameters, were then refined by a trial-and-adjustment procedure, requiring them to simultaneously reproduce both the observed reflectance and Kramers-Kronig-derived dielectric loss,  $\epsilon''$ , spectra. The overall agreement between the observed and the final theoretical spectra

was good, indicating that the damped harmonic oscillator model is a reasonable description of the absorption process in  $\text{Ba}(\text{ClO}_3)_2 \cdot \text{H}_2\text{O}$ . The measured deviations can be attributed to anharmonic coupling.

Our polarization results largely confirm earlier vibrational assignments of  $\text{Ba}(\text{ClO}_3)_2 \cdot \text{H}_2\text{O}$ . Important contributions of this work include resolving the ambiguity in the assignment of the water librational modes, and determining the symmetry species of the crystal modes involving chlorate stretching and in-plane water translation. This symmetry information could not be obtained from more conventional single crystal transmission spectra, because reflection effects caused severe band distortion.

From the measured transition strengths, the dipole moment derivatives with respect to the crystal normal coordinates were calculated, under the assumption of a Lorentz local field. In the case of the internal water modes, the results of a previous normal coordinate analysis were used to convert the crystal dipole moment derivatives to molecular and even individual bond moment derivatives, under the Bond Moment approximation. These values were then compared with those reported for water in the vapor, liquid and solid phases.

## ACKNOWLEDGEMENTS

I would like to express my deepest appreciation to Dr. John E. Bertie for suggesting this project, and for his guidance during the course of the work and the preparation of the thesis.

Special thanks also go to my husband, Dr. Terry Cyr, for proofreading this thesis, and his constant encouragement. Helpful discussions with various members of the Chemistry, Geology, and Engineering departments, and the prompt and excellent service provided by the electronic, machine, and glass shops of the Chemistry Department, are all gratefully acknowledged. Shirley Stawnychy deserves special mention for her excellent typing of this thesis.

I would also like to thank the University of Alberta and the Natural Sciences and Engineering Research Council of Canada for their financial support.

## TABLE OF CONTENTS

	Page
Abstract .....	v
Acknowledgements .....	vii
List of Tables .....	xii
List of Figures .....	xvii
 <u>Chapter I. Introduction</u> .....	 1
1.1 Theory of Optical Properties .....	2
1.1a Wave Propagation and the Optical Constants .....	3
1.1b Reflection and Transmission of Plane Waves .....	10
1.1c Optical Anisotropy .....	15
1.1d Dispersion of the Optical Constants .....	22
1.2 Methods of Obtaining Optical Constants .....	31
1.2a Direct Methods .....	32
1.2b Indirect Methods .....	43
1.3 Properties of $\text{Ba}(\text{ClO}_3)_2 \cdot \text{H}_2\text{O}$ .....	58
1.4 Infrared Optical Constant Studies of Solids ...	76
1.5 Objectives of this Work .....	95
 <u>Chapter II. Experimental</u> .....	 98
2.1 Introduction .....	98
2.2 Sample Preparations .....	98
2.2a Preparation of Polycrystalline $\text{Ba}(\text{ClO}_3)_2 \cdot \text{H}_2\text{O}$ .....	98
2.2b Preparation of Single Crystal $\text{Ba}(\text{ClO}_3)_2 \cdot \text{H}_2\text{O}$ ..	103

	Page
2.3 Crystal Cutting and Polishing .....	109
2.4 Precession X-Ray Study of the Single Crystals .....	110
2.5 Instrumentation .....	111
2.6 Reflectance Measurements .....	119
2.6a Determination of Angle of Incidence .....	122
2.6b Design of Sample Holders .....	124
2.6c Design of R.I.I.C. Sample Compartment .....	127
2.6d Reference Mirror and Calibration Standard .....	129
2.7 Operating Procedures and Parameters .....	133
2.7a Near-Infrared ( $1800-7000\text{ cm}^{-1}$ ) .....	136
2.7b Mid-Infrared ( $400-4000\text{ cm}^{-1}$ ) .....	137
2.7c Far-Infrared on Nicolet ( $100-400\text{ cm}^{-1}$ ) .....	137
2.7d Far-Infrared on R.I.I.C. ( $20-250\text{ cm}^{-1}$ ) .....	138

### Chapter III. Sample Characterization, Data Handling Pro-

#### cedures and Reflection Results for $\text{Ba}(\text{ClO}_3)_2 \cdot \text{H}_2\text{O}$ ...

3.1 Sample Characterization .....	140
3.1a Characterization of Single Crystal $\text{Ba}(\text{ClO}_3)_2 \cdot \text{H}_2\text{O}$ .....	140
3.1b Characterization of Polycrystalline $\text{Ba}(\text{ClO}_3)_2 \cdot \text{H}_2\text{O}$ .....	148
3.2 Data Handling .....	157
3.2a Subtraction of Water Vapour and Carbon Dioxide Features .....	157
3.2b Calibration of the Reference Mirror .....	162
3.2c Merging of Data from Various Spectral Regions .....	173

	Page
3.3 Reflection Results for $\text{Ba}(\text{ClO}_3)_2 \cdot \text{H}_2\text{O}$ .....	179
3.3a Near-Infrared Results .....	183
3.3b Polycrystalline $\text{Ba}(\text{ClO}_3)_2 \cdot \text{H}_2\text{O}$ --- Mid- and Far-Infrared .....	186
3.3c Single Crystal $\text{Ba}(\text{ClO}_3)_2 \cdot \text{H}_2\text{O}$ --- Mid- and Far-Infrared .....	189
 <u>Chapter IV. The Optical and Dielectric Properties of Poly-</u>	
<u>crystalline and Single Crystal <math>\text{Ba}(\text{ClO}_3)_2 \cdot \text{H}_2\text{O}</math> .....</u>	<u>193</u>
4.1 Kramers-Kronig Method for Optical Constants .....	193
4.1a Description of Method .....	194
4.1b Analysis of Method .....	197
4.2 Kramers-Kronig Derived Optical Constants for $\text{Ba}(\text{ClO}_3)_2 \cdot \text{H}_2\text{O}$ .....	205
4.2a Polycrystalline $\text{Ba}(\text{ClO}_3)_2 \cdot \text{H}_2\text{O}$ .....	206
4.2b Single Crystal $\text{Ba}(\text{ClO}_3)_2 \cdot \text{H}_2\text{O}$ .....	213
4.3 Combined Kramers-Kronig/Classical Dispersion Method for Obtaining Optical Constants .....	223
<u>Chapter V. Error Analysis .....</u>	<u>250</u>
5.1 Experimental Errors .....	250
5.1a Effect of Non-Normal Incidence .....	251
5.1b Apparatus Polarization .....	252
5.1c Polarizer Efficiency .....	252
5.1d Optical and Electronic Errors .....	254
5.1e Reference Mirror Reflectance .....	263
5.1f Extraneous Reflection .....	265
5.1g Sample Deterioration .....	266
5.1h Sample Holder Positioning .....	269

	Page
5.1i Sample Uniformity .....	269
5.1j Residual Systematic and Random Errors .....	270
5.2 Computational Errors .....	273
<u>Chapter VI. Interpretation of Optical Spectra for Ba(ClO<sub>3</sub>)<sub>2</sub>·H<sub>2</sub>O - Vibrational Assignment and Dipole Moment Derivative Calculations .....</u>	
6.1 Factor Group Analysis .....	279
6.2 Vibrational Assignment .....	290
6.2a Vibrations of Water Molecules .....	302
6.2b Internal Vibrations of the ClO <sub>3</sub> <sup>-</sup> Ion Modes.....	314
6.2c Lattice Vibrations Involving Ba <sup>2+</sup> and ClO <sub>3</sub> <sup>-</sup> Ions..	331
6.3 Dipole Moment Derivative Calculations .....	339
<u>Chapter VII. Conclusion .....</u>	363
<u>References .....</u>	367
<u>Appendix A. Derivation of Kramers-Kronig Dispersion Relation Between the Real and Imaginary Dielectric Constant .....</u>	380
<u>Appendix B. Reflectance of Polycrystalline Ba(ClO<sub>3</sub>)<sub>2</sub>·H<sub>2</sub>O at 298°K .....</u>	383
<u>Appendix C. Reflectance of (001) Face of Single Crystal Ba(ClO<sub>3</sub>)<sub>2</sub>·H<sub>2</sub>O at 298 K; E  b and E⊥b .....</u>	386
<u>Appendix D. Kramers-Kronig Derived Values of the Dielectric Function for Polycrystalline Ba(ClO<sub>3</sub>)<sub>2</sub>·H<sub>2</sub>O .....</u>	391
<u>Appendix E. Kramers-Kronig Derived Values of the Dielectric Function for the (001) Crystal Face of Ba(ClO<sub>3</sub>)<sub>2</sub>·H<sub>2</sub>O ...</u>	395

## LIST OF TABLES

<u>Table</u>	<u>Page</u>
1.1 Relation of Principal Axes of the Optical Indicatrix to Crystal Axes .....	21
1.2 Solubility and Density Data for $\text{Ba}(\text{ClO}_3)_2 \cdot \text{H}_2\text{O}$ in $\text{H}_2\text{O}$ at Atmospheric Pressure .....	60
1.3 Crystal Structure Data for $\text{Ba}(\text{ClO}_3)_2 \cdot \text{H}_2\text{O}$ .....	62
1.4 Average Dimensions of the $\text{ClO}_3^-$ Ion in Different Chlorates .....	62
1.5 Optical Data for $\text{Ba}(\text{ClO}_3)_2 \cdot \text{H}_2\text{O}$ .....	66
1.6 Frequencies Assigned to the Librational Modes of the Water Molecule in $\text{Ba}(\text{ClO}_3)_2 \cdot \text{H}_2\text{O}$ .....	73
2.1 Applied Pressure Timetable for the Preparation of $\text{Ba}(\text{ClO}_3)_2 \cdot \text{H}_2\text{O}$ Pellets .....	101
2.2 Source, Beamsplitters, and Detectors Used on the Nicolet 7199 FTIR Instrument .....	117
2.3 Differences in Operation and Data Processing for R.I.I.C. and Nicolet 7199 Instruments .....	118
2.4 Frequency Range Covered by the Mylar Beamsplitters on the R.I.I.C. ....	138
3.1 Comparison of Literature and Measured Axial Lengths for a b Crystal Face of $\text{Ba}(\text{ClO}_3)_2 \cdot \text{H}_2\text{O}$ ...	143
3.2 Infrared Reflectance of Silicon for $10^\circ$ Incidence, and Corrected for Apparatus Polarization..	165
3.3 Calibration of Mid-Infrared Reflectance of Gold Mirror #3 for 13/01/82 .....	168
3.4 Comparison of Calibrated and Averaged b-Polarized Mid-Infrared Reflectance of Single Crystal $\text{Ba}(\text{ClO}_3)_2 \cdot \text{H}_2\text{O}$ .....	169
3.5 Merging Data for the Composite Reflectance Spectra of Polycrystalline $\text{Ba}(\text{ClO}_3)_2 \cdot \text{H}_2\text{O}$ .....	180

## List of Tables, Continued

<u>Table</u>	<u>Page</u>
3.6 Merging Data for the Composite Reflectance Spectra of Single Crystal $\text{Ba}(\text{ClO}_3)_2 \cdot \text{H}_2\text{O}$ .....	181
3.7 Maximum Discrepancies Between Merged $\text{Ba}(\text{ClO}_3)_2 \cdot \text{H}_2\text{O}$ Sub-Spectra, After Scaling .....	182
3.8 Peak and Trough Reflectance Values for Fundamental Bands of Polycrystalline $\text{Ba}(\text{ClO}_3)_2 \cdot \text{H}_2\text{O}$ at 298°K .....	188
3.9 Peak and Trough Reflectance Values for (001) Face of Single Crystal $\text{Ba}(\text{ClO}_3)_2 \cdot \text{H}_2\text{O}$ at 298°K .....	192
4.1 Definition of Terms in Kramers-Kronig Program .....	198
4.2 Parameters for a 7-Band Simulated Spectrum Generated from a Set of Damped Harmonic Oscillator Functions .....	202
4.3 Comparison of Theoretical and Calculated Dielectric Constants for Various Integration Ranges .....	204
4.4 Integration Range Data for Kramers-Kronig Transformation of $\text{Ba}(\text{ClO}_3)_2 \cdot \text{H}_2\text{O}$ Reflectance Spectra .....	208
4.5 Effect of Integration Range on Calculated Dielectric Constants for Polycrystalline $\text{Ba}(\text{ClO}_3)_2 \cdot \text{H}_2\text{O}$ .....	212
4.6 Integration Range-Dependence of Calculated Dielectric Constant Values for a'-Polarized (001) Face of $\text{Ba}(\text{ClO}_3)_2 \cdot \text{H}_2\text{O}$ .....	222
4.7 Peak Characteristics of Conductivity Spectra for (001) Crystal Face of $\text{Ba}(\text{ClO}_3)_2 \cdot \text{H}_2\text{O}$ .....	225
4.8 Initial Set of Classical Oscillator Parameters for Polarized Single Crystal $\text{Ba}(\text{ClO}_3)_2 \cdot \text{H}_2\text{O}$ Data .....	229

## List of Tables, Continued

<u>Table</u>	<u>Page</u>
4.9 Final Set of Classical Oscillator Parameters for b-Polarized Single Crystal $\text{Ba}(\text{ClO}_3)_2 \cdot \text{H}_2\text{O}$ Data .....	243
4.10 Final Set of Classical Oscillator Parameters for a'-Polarized Single Crystal $\text{Ba}(\text{ClO}_3)_2 \cdot \text{H}_2\text{O}$ Data .....	244
5.1 Determination of Electronic Amplification Errors for Nicolet 7199 FTIR Instrument .....	261
5.2 Effect of Small Differences in Measured Reflectance Upon KK-Derived Dielectric Constants; Illustrated for b-Polarized Reflectance Data for $\text{Ba}(\text{ClO}_3)_2 \cdot \text{H}_2\text{O}$ .....	276
6.1 Equivalent Sites in $\text{Ba}(\text{ClO}_3)_2 \cdot \text{H}_2\text{O}$ , Space Group $\text{C}_{2h}^6$ .....	284
6.2 Character Table for Group $\text{C}_{2h}$ .....	284
6.3 Correlation Table for Group $\text{C}_{2h}$ and its Subgroups .....	284
6.4 Correlation Table for the Water Molecule and Barium Ion Vibrational Modes of $\text{Ba}(\text{ClO}_3)_2 \cdot \text{H}_2\text{O}$ ..	287
6.5 Correlation Table for Internal and External Vibrational Modes of $\text{ClO}_3^-$ Ion in $\text{Ba}(\text{ClO}_3)_2 \cdot \text{H}_2\text{O}$ .....	287
6.6 Irreducible Representation and Spectral Activity for $\text{Ba}(\text{ClO}_3)_2 \cdot \text{H}_2\text{O}$ .....	291
6.7 Comparison of Conductivity Features Observed for Polycrystalline $\text{Ba}(\text{ClO}_3)_2 \cdot \text{H}_2\text{O}$ and the (001) Crystal Face .....	292
6.7a Continuation of Table 6.7 .....	293
6.8 Comparison of Peak Reflectance Values for c- and ab- Polarized Spectra of the (110) Face of $\text{Ba}(\text{ClO}_3)_2 \cdot \text{H}_2\text{O}$ and $\text{Ba}(\text{ClO}_3)_2 \cdot \text{D}_2\text{O}$ .....	298

## List of Tables, Continued

<u>Table</u>	<u>Page</u>
6.9 Comparison of Observed Frequencies for $\text{Ba}(\text{ClO}_3)_2 \cdot \text{H}_2\text{O}$ and $\text{Ba}(\text{ClO}_3)_2 \cdot \text{D}_2\text{O}$ Reflectance Maxima .....	300
6.10 Comparison of Observed Frequencies and Polarization of Water Vibrational Modes in $\text{Ba}(\text{ClO}_3)_2 \cdot \text{H}_2\text{O}$ with those Predicted for a water Molecule in a Trigonal Environment .....	307
6.11 Intensity Ratios for a'- and c-Polarized Components of Water Rocking and Wagging Vibrations, Calculated Under Oriented Gas Model .....	308
6.12 Site and Davydov Splitting of the Water Modes in $\text{Ba}(\text{ClO}_3)_2 \cdot \text{H}_2\text{O}$ .....	313
6.13 Previous Assignments of $\text{ClO}_3^-$ Internal Modes in $\text{Ba}(\text{ClO}_3)_2 \cdot \text{H}_2\text{O}$ .....	316
6.14 Relative Intensity of Features in Conductivity and Raman Spectra of Single Crystal $\text{Ba}(\text{ClO}_3)_2 \cdot \text{H}_2\text{O}$ in the $\text{ClO}_3^-$ Ion Internal Mode Region .....	318
6.15 Comparison of Calculated $^{37}\text{Cl}/^{35}\text{Cl}$ Splittings of $\text{ClO}_3^-$ Ion Internal Modes in $\text{KClO}_3$ and Observed Frequency Range for these Vibrations in $\text{Ba}(\text{ClO}_3)_2 \cdot \text{H}_2\text{O}$ .....	322
6.16 Assignment of $\text{ClO}_3^-$ Ion Stretching Modes in $\text{Ba}(\text{ClO}_3)_2 \cdot \text{H}_2\text{O}$ and Suggested Correspondence with Previous Results .....	326
6.17 Site and Correlation Splitting of the Internal Chlorate Ion Modes in $\text{Ba}(\text{ClO}_3)_2 \cdot \text{H}_2\text{O}$ .....	329
6.18 Comparison of Chlorate Ion Vibrational Frequencies in Aqueous Solution and in Solid $\text{NaClO}_3$ , $\text{KClO}_3$ , and $\text{Ba}(\text{ClO}_3)_2 \cdot \text{H}_2\text{O}$ .....	330
6.19 Previous Lattice Mode Assignments for $\text{NaClO}_3$ , $\text{KClO}_3$ , and $\text{Ba}(\text{ClO}_3)_2 \cdot \text{H}_2\text{O}$ .....	333
6.20 Comparison of Infrared Lattice Mode Frequencies Previously Reported for $\text{Ba}(\text{ClO}_3)_2 \cdot \text{H}_2\text{O}$ .....	334
6.21 Assignment of Lattice Modes in $\text{Ba}(\text{ClO}_3)_2 \cdot \text{H}_2\text{O}$ and Suggested Correspondence with Raman Results..	336

## List of Tables, Continued

<u>Table</u>	<u>Page</u>
6.22 Crystal Data Used in Dipole Moment Derivative Calculations for $\text{Ba}(\text{ClO}_3)_2 \cdot \text{H}_2\text{O}$ .....	342
6.23 Crystal Dipole Moment Derivatives of the Internal Water Modes in $\text{Ba}(\text{ClO}_3)_2 \cdot \text{H}_2\text{O}$ .....	342
6.24 Transformation of Dipole Moment Derivatives from Crystal Normal Coordinates to Internal Symmetry Coordinates and Application to the Water Modes of $\text{Ba}(\text{ClO}_3)_2 \cdot \text{H}_2\text{O}$ .....	347
6.25 Dipole Moment Derivatives with Respect to Symmetry Coordinates for the Internal Water Modes of $\text{Ba}(\text{ClO}_3)_2 \cdot \text{H}_2\text{O}$ .....	348
6.26 Calculated Values of $\partial \mu / \partial r$ and $\partial \mu / \partial \theta$ for Internal Water Modes in $\text{Ba}(\text{ClO}_3)_2 \cdot \text{H}_2\text{O}$ .....	348
6.27 Literature Values of Integrated Absorption Intensities for $\text{H}_2\text{O}$ Vibrations in the Gas, Liquid and Solid Phases .....	351
6.28 Calculated Molecular Dipole Derivatives for $\text{H}_2\text{O}$ Vapor and Comparison with Stark Measured Values .....	351
6.29 Comparison of Molecular Dipole and Bond Moment Derivatives of $\text{H}_2\text{O}$ Internal Modes in Different Substances .....	355
6.30 Crystal Dipole Moment Derivatives of the External Water Modes in $\text{Ba}(\text{ClO}_3)_2 \cdot \text{H}_2\text{O}$ .....	355
6.31 Crystal Dipole Moment Derivatives of the Internal Chlorate Ion Modes in $\text{Ba}(\text{ClO}_3)_2 \cdot \text{H}_2\text{O}$ .....	357
6.32 Comparison of Chlorate Ion Dipole Derivatives Calculated for $\text{NaClO}_3$ , $\text{RbClO}_3$ and $\text{ClO}_3^-$ in KBr .....	360

## LIST OF FIGURES

<u>Figure</u>		<u>Page</u>
1.1	Coordinate system for analyzing reflection and refraction at a plane boundary between a transparent and an absorbing medium .....	11
1.2	Dependence of reflectance of plane-polarized light upon angle of incidence .....	16
1.3	The optical indicatrix .....	18
1.4	Section through the $\gamma$ - $\alpha$ vibration plane, optic axial plane of a biaxial indicatrix .....	18
1.5	Frequency behavior of $\epsilon'$ and $\epsilon''$ .....	28
1.6	Corresponding frequency behavior of $n$ and $k$ .....	28
1.7	Projection of the structure of $\text{Ba}(\text{ClO}_3)_2 \cdot \text{H}_2\text{O}$ on the (010) plane .....	63
1.8	Illustration of the librational modes of a water molecule .....	73
1.9	A typical reststrahlen spectrum .....	79
1.10	Shape of reststrahlen band for different values of the damping constant, $\gamma$ .....	79
2.1	The pressure vessel used to prepare polycrystalline samples of $\text{Ba}(\text{ClO}_3)_2 \cdot \text{H}_2\text{O}$ .....	99
2.2	Growth of $\text{Ba}(\text{ClO}_3)_2 \cdot \text{H}_2\text{O}$ single crystals by circulation method .....	106
2.2a	Glass crucible used as polycrystalline material holder .....	106
2.3	Schematic diagram of an FTIR instrument .....	112
2.4	The relationship between an interferogram and a single-beam energy spectrum .....	112
2.5	Harrick Variable Angle Reflectance Accessory, modified to operate at a fixed angle of incidence ( $I = 9.5^\circ$ ) .....	120

## List of Figures, Continued

<u>Figure</u>		<u>Page</u>
2.6	Typical mid-infrared throughput curve for Harrick reflectance accessory with gold reference mirror and $9.5^\circ$ incidence .....	123
2.7	Design of polycrystalline sample holder .....	125
2.8	Design of single crystal sample holder .....	128
2.9	Design of R.I.I.C. sample compartment .....	130
2.10	Dimensions of silicon calibration standard .....	132
3.1	A typical single crystal of $\text{Ba}(\text{ClO}_3)_2 \cdot \text{H}_2\text{O}$ .....	141
3.2	Crystal habit of $\text{Ba}(\text{ClO}_3)_2 \cdot \text{H}_2\text{O}$ .....	141
3.3	Crystal face of $\text{Ba}(\text{ClO}_3)_2 \cdot \text{H}_2\text{O}$ obtained on cutting single crystal perpendicular to prismatic c-axis .....	143
3.4	Comparison of a'-polarized reflectance from (001) face of two different samples of single crystal $\text{Ba}(\text{ClO}_3)_2 \cdot \text{H}_2\text{O}$ .....	146
3.5	Comparison of b-polarized reflectance from (001) face of two different samples of single crystal $\text{Ba}(\text{ClO}_3)_2 \cdot \text{H}_2\text{O}$ .....	147
3.6	Reflectance spectra of polycrystalline $\text{Ba}(\text{ClO}_3)_2 \cdot \text{H}_2\text{O}$ before and after polishing treatments .....	150
3.7	Comparison of unpolarized reflectance of two different samples of polycrystalline $\text{Ba}(\text{ClO}_3)_2 \cdot \text{H}_2\text{O}$ .....	151
3.8	Polarized reflectance spectra of polycrystalline $\text{Ba}(\text{ClO}_3)_2 \cdot \text{H}_2\text{O}$ with electric vector parallel (TM) and perpendicular (TE) to the plane of incidence, at $\phi = 9.5^\circ$ .....	152
3.9	Day-dependence of near-infrared reflectance of polycrystalline $\text{Ba}(\text{ClO}_3)_2 \cdot \text{H}_2\text{O}$ .....	154

## List of Figures, Continued

<u>Figure</u>		<u>Page</u>
3.10	Effect of sample evacuation on mid-infrared reflectance of polycrystalline $\text{Ba}(\text{ClO}_3)_2 \cdot \text{H}_2\text{O}$ ..	156
3.11	Effect of sample purging with dry nitrogen gas on mid-infrared reflectance of polycrystalline $\text{Ba}(\text{ClO}_3)_2 \cdot \text{H}_2\text{O}$ .....	158
3.11a	Continuation of Figure 3.11 .....	159
3.12	Subtraction of Water Vapour and Carbon Dioxide features from observed reflectance spectra ....	163
3.13	Percent transmission curves for s-(TE) and p-(TM) polarized light through Harrick reflectance accessory ( $\phi = 9.5^\circ$ ) in Nicolet 7199 instrument .....	165
3.14	Average mid-infrared reflectance spectrum of silicon calibration standard on 13/01/82 .....	168
3.15	Mid-infrared region calibration curve for gold mirror #3 on 13/01/82 .....	169
3.16	Near-infrared region calibration curve for gold mirror #3 on 03/02/82 .....	172
3.17	Comparison of overlap region for calibrated near-infrared and averaged mid-infrared results for a'-polarized reflectance from (001) face of single crystal $\text{Ba}(\text{ClO}_3)_2 \cdot \text{H}_2\text{O}$ .....	172
3.18	Procedure for merging data from various spectral regions - on Nicolet 7199 instrument .....	175
3.19	Overlap of mid- and far-infrared reflectance data for a'-polarized (001) face of single crystal $\text{Ba}(\text{ClO}_3)_2 \cdot \text{H}_2\text{O}$ .....	177
3.20	Overlap of far-infrared Nicolet and R.I.I.C. data for polycrystalline $\text{Ba}(\text{ClO}_3)_2 \cdot \text{H}_2\text{O}$ .....	178
3.21	Near-infrared reflectance spectra of polycrystalline and polarized (001) face single crystal $\text{Ba}(\text{ClO}_3)_2 \cdot \text{H}_2\text{O}$ at $-298^\circ\text{K}$ and $8\text{ cm}^{-1}$ resolution .....	184

## List of Figures, Continued

<u>Figure</u>		<u>Page</u>
3.22	Comparison of overlap region for "best" near-infrared and averaged mid-infrared results for polycrystalline $\text{Ba}(\text{ClO}_3)_2 \cdot \text{H}_2\text{O}$ .....	185
3.23	Composite reflectance spectrum of polycrystalline $\text{Ba}(\text{ClO}_3)_2 \cdot \text{H}_2\text{O}$ at $-298^\circ\text{K}$ and $2\text{ cm}^{-1}$ resolution .....	187
3.24	Composite a'-polarized reflectance spectrum of (001) face of single crystal $\text{Ba}(\text{ClO}_3)_2 \cdot \text{H}_2\text{O}$ at $-298^\circ\text{K}$ and $2\text{ cm}^{-1}$ resolution .....	190
3.25	Composite b-polarized reflectance spectrum of (001) face of single crystal $\text{Ba}(\text{ClO}_3)_2 \cdot \text{H}_2\text{O}$ at $-298^\circ\text{K}$ and $2\text{ cm}^{-1}$ resolution .....	191
4.1	Schematic of Kramers-Kronig computer program, with Simpson's rule integration procedure .....	196
4.2	Schematic for checking Kramers-Kronig program with theoretical reflection data .....	200
4.3	Theoretical reflection spectrum derived from dispersion parameters of Table 4.3 .....	202
4.4	Comparison of theoretical $\epsilon'$ spectrum and Kramers-Kronig derived $\epsilon'$ spectra for various integration ranges .....	203
4.5	Definition of integration sub-intervals for Kramers-Kronig integration procedure .....	207
4.6	Optical constants n and k for polycrystalline $\text{Ba}(\text{ClO}_3)_2 \cdot \text{H}_2\text{O}$ at $298^\circ\text{K}$ ; resolution = $2\text{ cm}^{-1}$ ....	209
4.7	Dielectric constants $\epsilon'$ and $\epsilon''$ polycrystalline $\text{Ba}(\text{ClO}_3)_2 \cdot \text{H}_2\text{O}$ at $298^\circ\text{K}$ ; resolution = $2\text{ cm}^{-1}$ .....	210
4.8	Optical constants n and k for (001) face of $\text{Ba}(\text{ClO}_3)_2 \cdot \text{H}_2\text{O}$ measured with the electric vector parallel to the b-axis at $298^\circ\text{K}$ ; resolution = $2\text{ cm}^{-1}$ .....	214

## List of Figures, Continued

<u>Figure</u>		<u>Page</u>
4.9	Dielectric constants $\epsilon'$ and $\epsilon''$ for (001) face of $\text{Ba}(\text{ClO}_3)_2 \cdot \text{H}_2\text{O}$ measured with the electric vector parallel to the b-axis at 298°K; resolution = 2 $\text{cm}^{-1}$ .....	215
4.10	Calculated b-polarized transmittance spectra of the (001) face of $\text{Ba}(\text{ClO}_3)_2 \cdot \text{H}_2\text{O}$ for sample thicknesses of 0.20, 2.0, and 20 $\mu\text{m}$ .....	217
4.11	Optical constants n and k for (001) face of $\text{Ba}(\text{ClO}_3)_2 \cdot \text{H}_2\text{O}$ measured with the electric vector parallel to the a'-axis at 298°K; resolution = 2 $\text{cm}^{-1}$ .....	219
4.12	Dielectric constants $\epsilon'$ and $\epsilon''$ for (001) face of $\text{Ba}(\text{ClO}_3)_2 \cdot \text{H}_2\text{O}$ measured with the electric vector parallel to the a'-axis at 298°K; resolution = 2 $\text{cm}^{-1}$ .....	220
4.13	Conductivity spectra, $\omega\epsilon''/2$ , for (001) face of $\text{Ba}(\text{ClO}_3)_2 \cdot \text{H}_2\text{O}$ measured with the electric vector parallel and perpendicular to the b-axis at 298°K .....	224
4.14	Combined Kramers-Kronig/classical dispersion procedure for obtaining a classical oscillator fit to reflection data .....	228
4.15	Comparison of observed a'-polarized reflectance from (001) face of $\text{Ba}(\text{ClO}_3)_2 \cdot \text{H}_2\text{O}$ and theoretical reflectance, based on initial set of dispersion parameters .....	230
4.16	Comparison of KK-derived $\epsilon''(\nu)$ spectrum for a'-polarized reflectance from (001) face of $\text{Ba}(\text{ClO}_3)_2 \cdot \text{H}_2\text{O}$ and theoretical $\epsilon''(\nu)$ spectrum, based on initial set of dispersion parameters..	231
4.17	Comparison of observed b-polarized reflectance from (001) face of $\text{Ba}(\text{ClO}_3)_2 \cdot \text{H}_2\text{O}$ and theoretical reflectance, based on initial set of dispersion parameters .....	232
4.18	Comparison of KK-derived $\epsilon''(\nu)$ spectrum for b-polarized reflectance from (001) face of $\text{Ba}(\text{ClO}_3)_2 \cdot \text{H}_2\text{O}$ and theoretical $\epsilon''(\nu)$ spectrum, based on initial set of dispersion parameters..	233

## List of Figures, Continued

<u>Figure</u>		<u>Page</u>
4.19	Comparison of experimental b-polarized reflectance from (001) crystal face of $\text{Ba}(\text{ClO}_3)_2 \cdot \text{H}_2\text{O}$ and KK-derived $\epsilon''(\nu)$ spectrum with corresponding theoretical spectra from combined Kramers-Kronig/classical dispersion fit .....	236
4.19a	Continuation of Figure 4.19 .....	237
4.19b	Continuation of Figure 4.19 .....	238
4.20	Comparison of experimental a'-polarized reflectance from (001) crystal face of $\text{Ba}(\text{ClO}_3)_2 \cdot \text{H}_2\text{O}$ and KK-derived $\epsilon''(\nu)$ spectrum with corresponding theoretical spectra from combined Kramers-Kronig/classical dispersion fit .....	239
4.20a	Continuation of Figure 4.20 .....	240
4.20b	Continuation of Figure 4.20 .....	241
5.1	Degree of apparatus polarization for the Nicolet 7199 FTIR instrument with the $\text{CaF}_2$ and 3 $\mu\text{m}$ mylar beamsplitters .....	253
5.2	Comparison of 100% lines obtained with and without the room lights on; 3 $\mu\text{m}$ mylar beam-splitter and DTGS/polyethylene detector .....	257
5.3	Typical 100% lines obtained for the various spectral regions on the Nicolet instrument for 2 $\text{cm}^{-1}$ resolution .....	258
5.4	Background reflectance contributed by single crystal sample holder for different tapers of the sample aperture .....	267
5.5	Error in KK-derived $\epsilon''(\nu)$ values associated with a localized error in the measured reflectance .....	275
5.6	Error in KK-derived $\epsilon''(\nu)$ values associated with an ~2% error in the measured reflectance over a wide frequency range .....	277

## List of Figures, Continued

<u>Figure</u>		<u>Page</u>
6.1	Approximate forms of the $\text{ClO}_3^-$ ion $\nu_1$ unit-cell modes in $\text{Ba}(\text{ClO}_3)_2 \cdot \text{H}_2\text{O}$ .....	288
6.2	Trigonal environment of $\text{H}_2\text{O}$ molecules in $\text{Ba}(\text{ClO}_3)_2 \cdot \text{H}_2\text{O}$ .....	308
6.3	Spectral behavior of amalgamation- and persistence-type mixed crystals .....	321
6.4	Boundary of the amalgamation and persistence type systems .....	322
6.5	Expected behavior for a crystal of intermediate amalgamation-persistence character ....	323
6.6	Equilibrium $\text{ClO}_3^-$ ion geometry in $\text{Ba}(\text{ClO}_3)_2 \cdot \text{H}_2\text{O}$ .....	334

## CHAPTER I.

### INTRODUCTION

Chapter I of this thesis provides the theoretical and experimental background material necessary to an understanding of the optical properties of a solid. The experimental methods used for the preparation of polycrystalline and single crystal samples of barium chlorate monohydrate,  $\text{Ba}(\text{ClO}_3)_2 \cdot \text{H}_2\text{O}$ , and for the measurement of specular reflectance are described in Chapter II. Sample characterization, data handling procedures, and the reflection results appear in Chapter III. The optical and dielectric functions derived from both a Kramers-Kronig and Classical Dispersion analysis are presented in Chapter IV. Random and systematic experimental errors are discussed in Chapter V. The vibrational assignment of  $\text{Ba}(\text{ClO}_3)_2 \cdot \text{H}_2\text{O}$  and the calculated dipole moment derivatives with respect to the crystal normal coordinates are given in Chapter VI. For the internal water modes, the bond moment derivatives are also estimated. The significant aspects of this investigation are summarized in the Conclusion.

The introductory chapter is sub-divided into five sections. The first section (1.1) is largely devoted to a description of the basic physics involved in the study of optical properties. The experimental methods for obtaining optical constants, with particular emphasis on the Kramers-Kronig procedure for specular reflection results (Section

1.2) are presented; and the properties of  $\text{Ba}(\text{ClO}_3)_2 \cdot \text{H}_2\text{O}$ , including a review of previous spectroscopic investigations, are described (Section 1.3). In order to bring this work into perspective with our current understanding of optical properties of solids in the infrared region, a short synopsis of major developments in this field of study, is presented in Section 1.4. This is followed by a brief outline of the objectives of this work in Section 1.5.

### 1.1 Theory of Optical Properties

The optical behavior of an optically isotropic solid is determined by the frequency dependence of two parameters: the real and imaginary parts of the refractive index, or the real and imaginary parts of the dielectric function. Either pair of constants uniquely defines the other set. The real and imaginary parts of the refractive index are commonly referred to as the optical constants of the solid, and describe the speed and attenuation, respectively, of a plane electromagnetic wave progressing through the material.<sup>1</sup> Since it is the electrically charged particles of the material that interact strongly with the electric field of the electromagnetic radiation, the optical constants describe the fundamental constitution of the solid. In the case of infrared radiation, the optical constants give the frequencies, lifetimes, and intensities of the vibrational modes.

However, the optical property usually available directly from experiment is the frequency-dependent reflectance

or transmittance. In order to interpret experimental measurements in terms of the optical constants of the solid one requires a knowledge of Maxwell's equations, the nature of the interaction between electromagnetic fields and matter, and an understanding of the dependence of the optical constants on the frequency and, in the case of anisotropic materials, the vibration direction of the propagating wave.

This section will provide this necessary background information.

#### 1.1a Wave Propagation and the Optical Constants

The propagation of light in a medium is described by Maxwell's equations.<sup>2</sup> For a nonmagnetic, electrically neutral material, the appropriate relations are:

$$\nabla \cdot \underline{D} = 0 \quad [1.1]$$

$$\nabla \cdot \underline{B} = 0 \quad [1.2]$$

$$\nabla \times \underline{H} = \frac{1}{c} \frac{\partial \underline{D}}{\partial t} + \frac{4\pi}{c} \underline{J} \quad [1.3]$$

$$\nabla \times \underline{E} = -\frac{1}{c} \frac{\partial \underline{B}}{\partial t} \quad [1.4]$$

where an underlined character denotes a vector quantity.

These equations are given in Gaussian units, i.e. electrostatic and electromagnetic cgs units, since this is the convention adopted by most standard texts on electromagnetic theory. The material presented in this section is largely derived from Chapter II of Wooten's book, "Optical Proper-

ties of Solids",<sup>2</sup> and the definition of terms is according to Von Hippel, in "Dielectrics and Waves",<sup>3</sup> unless otherwise stated. For a description of wave propagation in rationalized mks units, consult either Stern<sup>4</sup> or Fowles.<sup>5</sup>

The terms in Maxwell's equations have the following definitions:

$\underline{D}$  = dielectric displacement or electric flux density

$\underline{E}$  = electric field strength

$\underline{H}$  = magnetic field strength

$\underline{B}$  = magnetic flux density

$\underline{J}$  = current density

$c$  = velocity of light in vacuum.

The connection between the wave properties and the optical properties of solids is given by the constitutive relations:

$$\underline{J} = \sigma \underline{E} \quad [1.5]$$

$$\underline{D} = \epsilon \underline{E} \quad [1.6]$$

$$\underline{B} = \mu \underline{H} \quad [1.7]$$

where

$\epsilon$  = the dielectric constant or permittivity

$\sigma$  = conductivity

$\mu$  = magnetic permeability.

Equation [1.5] is just a formulation of Ohm's law and describes the response of the conduction electrons to the electric field. Equation [1.6] describes the response of

the bound charges to the electric field, and equation [1.7] is the corresponding magnetic relation.

An alternative way of describing the response of the bound charges is:

$$\underline{D} = \underline{E} + 4\pi \underline{P} \quad [1.8]$$

where

$\underline{P}$  = polarization = electric dipole moment induced per unit volume.

From equations [1.6] and [1.8], we have that:

$$\underline{P} = \frac{(\epsilon-1)}{4\pi} \underline{E} = \chi_E \underline{E} \quad [1.9]$$

The proportionality constant,  $\chi_E$ , between the electric field strength and the polarization, is known as the electric susceptibility.<sup>6</sup>

The constitutive constants are  $\mu$ ,  $\sigma$ , and  $\epsilon$ . However, for a non-magnetic material,  $\mu$  equals unity. The values of  $\epsilon$  and  $\sigma$  are constant only insofar as the frequency of the wave is constant. In the case of isotropic media,  $\epsilon$  and  $\sigma$  are scalar quantities having the same value for any direction of the applied electric field. But for anisotropic media, the magnitude of the induced conduction and polarization varies with the direction of the applied electric field and, consequently,  $\epsilon$  and  $\sigma$  must be expressed as tensor quantities.<sup>7</sup>

To simplify the discussion in Sections 1.1a and 1.1b, an isotropic medium is assumed.

The general wave equation for the electric field is obtained by taking the curl of [1.4] and the time derivative of [1.3] and eliminating  $\underline{H}$  with the help of [1.7]. The result is:

$$\nabla \times (\nabla \times \underline{E}) = \frac{-\epsilon\mu}{c^2} \frac{\partial^2 \underline{E}}{\partial t^2} - \frac{4\pi\sigma\mu}{c^2} \frac{\partial \underline{E}}{\partial t} \quad [1.10]$$

This may be simplified by the vector identity:

$$\nabla \times (\nabla \times \underline{U}) = \nabla \times (\nabla \cdot \underline{U}) - \nabla^2 \underline{U}$$

where  $\underline{U}$  is a vector field. Maxwell's equation [1.1] states that  $\nabla \cdot \underline{D} = 0$ . Since  $\underline{D} = \epsilon \underline{E}$  from [1.6], this implies that  $\nabla \cdot \underline{E} = 0$  or  $\epsilon = 0$ . In the former case, the wave vector is perpendicular to  $\underline{E}$  and called transverse; in the latter case, the wave vector has a longitudinal component, i.e. parallel to  $\underline{E}$ . In general,  $\epsilon \neq 0$  which gives the condition that the wave must be transverse,<sup>8</sup> and equation [1.10] reduces to:

$$\nabla^2 \underline{E} = \frac{\epsilon\mu}{c^2} \frac{\partial^2 \underline{E}}{\partial t^2} + \frac{4\pi\sigma\mu}{c^2} \frac{\partial \underline{E}}{\partial t} \quad [1.11]$$

The solution for monochromatic plane waves is:

$$\underline{\hat{E}} = \underline{\hat{E}}_0 \exp i (\underline{\hat{K}} \cdot \underline{r} - \omega t) \quad [1.12]$$

where the circumflex denotes a complex quantity

$\underline{\hat{K}}$  = complex propagation constant or wave vector

$\omega$  = angular frequency in radians/sec

$t$  = time in seconds

$\underline{r}$  = position vector in space

$i = \sqrt{-1}$ .

The frequency,  $\omega$ , is also called the transverse optic frequency,  $\omega_{TO}$ . Although only the real part of  $\hat{\underline{E}}$  represents the wave, the use of complex notation is helpful in describing the phase relationships between various real quantities. By writing equation [1.12] in the form:

$$\underline{E} = \underline{E}_0 \exp(-\underline{K}'' \cdot \underline{r}) \exp i (\underline{K}' \cdot \underline{r} - \omega t) \quad [1.13]$$

where

$$\hat{\underline{K}} = \underline{K}' + i \underline{K}'',$$

it can be seen that the vector  $\underline{K}'$  is normal to the surfaces of constant phase and the vector  $\underline{K}''$  is normal to the surfaces of constant amplitude. If  $\underline{K}'$  and  $\underline{K}''$  have the same direction in space, the wave is called homogeneous; otherwise, the wave is called inhomogeneous.<sup>8</sup>

Substitution of [1.12] into [1.11] gives:

$$\hat{\underline{K}} \cdot \hat{\underline{K}} = \frac{\mu \omega^2}{c^2} \left( \epsilon + i \frac{4\pi\sigma}{\omega} \right) \quad [1.14]$$

We can now define a complex refractive index,  $\hat{n}$ , such that:

$$\hat{\underline{K}} \cdot \hat{\underline{K}} = \left( \frac{\omega}{c} \right)^2 \hat{n}^2 = \left( \frac{\omega}{c} \right)^2 (n + ik)^2 \quad [1.15]$$

where

$n$  = refractive index

and

$k$  = extinction coefficient.

The quantities  $n$  and  $k$  are known as the optical constants of the material, although this term is really a misnomer since  $n$  and  $k$  depend upon the frequency of the wave.

In the case of homogeneous transverse waves, we obtain the simple result that  $|\underline{K}'| = n\omega/c$  and  $|\underline{K}''| = k\omega/c$ , which gives us a ready interpretation of the optical constants.

This can be seen by rewriting equation [1.13] as:

$$\underline{\hat{E}} = \underline{\hat{E}}_0 \left[ \exp\left(-\frac{\omega}{c} kr\right) \right] \left[ \exp i\left(\frac{\omega}{c} nr - \omega t\right) \right] \quad [1.16]$$

The first exponential term describes the attenuation of wave amplitude with path length through the material. The absorption coefficient,  $\alpha$ , which describes the fractional decrease in intensity with distance, is defined by:

$$I = I_0 \exp(-\alpha r), \quad \text{i.e.}$$

$$\alpha = -\frac{1}{I} \frac{dI}{dr} \quad \text{where} \quad \begin{array}{l} I = \text{transmitted intensity} \\ I_0 = \text{incident intensity.} \end{array} \quad [1.17]$$

Since the intensity is proportional to the square of the wave amplitude,<sup>9</sup> equations [1.16] and [1.17] give:

$$\alpha = \frac{2\omega k}{c} = \frac{4\pi k}{\lambda} = 4\pi \nu k \quad [1.18]$$

where

$\lambda$  = vacuum wavelength

$\nu$  = vacuum wavenumber.

The second exponential term describes a wave traveling with velocity,  $v = c/n$ , which confirms our earlier identification of  $n$  as the refractive index.

Equations [1.14] and [1.15] can be used to express  $\epsilon$  and  $\sigma$  as functions of  $n$  and  $k$ .

$$\epsilon = n^2 - k^2 \quad [1.19]$$

$$\frac{4\pi\sigma}{\omega} = 2nk \quad [1.20]$$

where  $\mu$  has been set equal to unity. If we now define a complex dielectric function  $\hat{\epsilon}$  as

$$\hat{\epsilon} = \epsilon' + i\epsilon'' = \hat{n}^2 \quad [1.21]$$

where  $\epsilon'$  is the old  $\epsilon$  of equation [1.19], then

$$\epsilon' = n^2 - k^2 \quad [1.22]$$

$$\epsilon'' = 2nk = \frac{4\pi\sigma}{\omega} \quad [1.23]$$

The real part of the complex dielectric function, measured at radio-frequencies, is what we commonly refer to as the dielectric constant, and is the ratio of the capacitance in the dielectric medium to that in vacuum,<sup>10</sup> i.e.

$$\epsilon' = \frac{C_{\text{diel.}}}{C_{\text{vac.}}} \quad [1.24]$$

The imaginary part of the complex dielectric function is commonly called the dielectric loss.<sup>10</sup> Since the electrical conductivity is a maximum value at the transverse optic frequency,<sup>11</sup> equation [1.23] shows that  $\omega_{\text{TO}}$  corres-

ponds to a maximum value of  $\epsilon''\omega$ .

When the conductivity is zero, the crystal is transparent ( $k=0$ ), and the optical properties are given by

$$\epsilon'(\omega) = n^2(\omega).$$

Equations [1.22] and [1.23] also show that  $\epsilon'$  and  $\epsilon''$  are interdependent quantities. We shall see later in Section 1.2b that  $\epsilon'$  and  $\epsilon''$ , as well as  $n$  and  $k$ , are related in a quite fundamental way by means of the Kramers-Kronig relations.<sup>2</sup>

### 1.1b Reflection and Transmission of Plane Waves

The relationships between the experimentally measured reflectance and transmittance and the optical constants of a material can be derived from an analysis of the character and direction of the waves reflected and transmitted at a plane boundary.

Consider a plane wave of amplitude  $E_i$  travelling in a transparent medium of refractive index  $n_1$  incident at an angle  $\phi$  on the interface of an absorbing medium, whose complex refractive index is  $\hat{n}_2$ . Take the permeabilities  $\mu_1$  and  $\mu_2$  as unity. Let the boundary of the two media be at  $z=0$ , and with the incident wave in the  $xz$  plane. Figure 1.1 defines this coordinate system. Let  $E_r$  and  $E_t$  denote the amplitudes of the reflected and transmitted waves, respectively. The incident electric vector  $\underline{E}_i$  can be resolved into components perpendicular and parallel to the plane of incidence,  $xz$ . These two cases are considered separately.

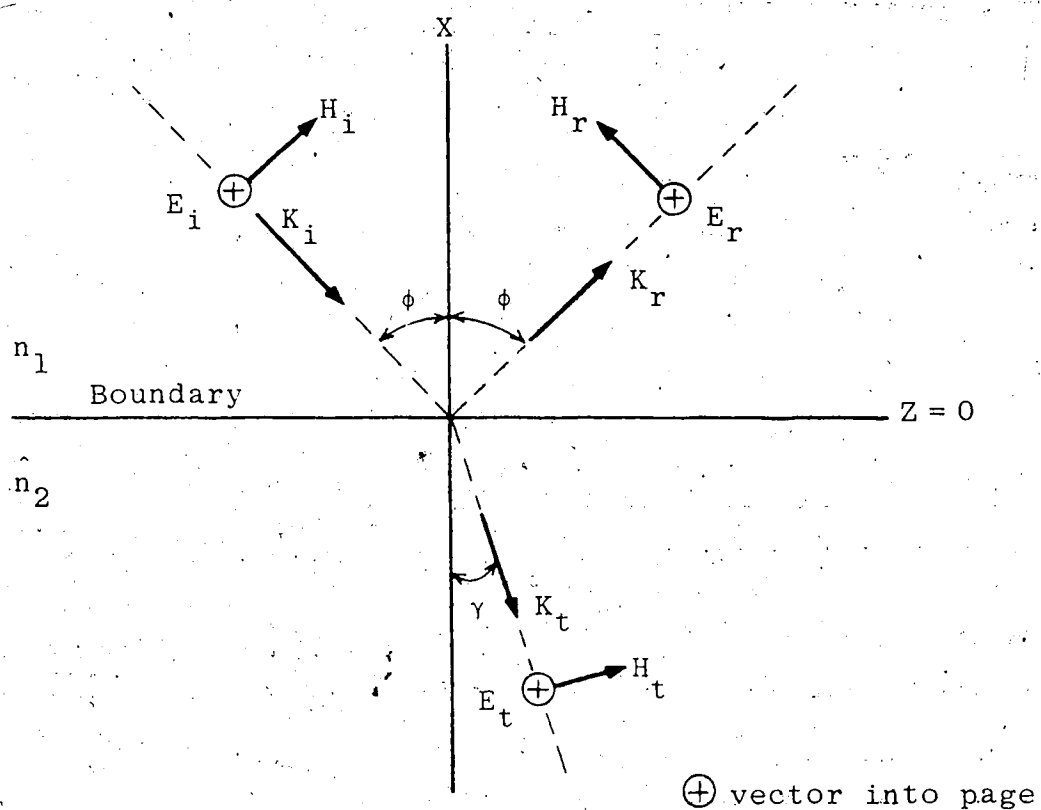


Figure 1.1. Coordinate system for analyzing reflection and refraction at a plane boundary between a transparent and an absorbing medium.

The wave vectors and associated electric and magnetic field components are shown for the case of s-polarized waves (TE polarization).

If the electric vector is polarized perpendicular to the plane of incidence, it is called s-polarized or transverse electric (TE) polarization. If the electric vector is polarized parallel to the plane of incidence, it is called p-polarized and, because the associated magnetic field vector is perpendicular to the plane of incidence, it is also called transverse magnetic (TM) polarization. The magnitude of the corresponding s- and p-polarized reflected and transmitted waves are determined by the boundary conditions. These require that the tangential components of the electric and magnetic fields be continuous as the boundary is crossed.<sup>12</sup>

The solutions to these electromagnetic boundary conditions are called Fresnel's relations. For the situation described, the formulae for the complex amplitude reflection coefficients,  $\hat{r}_s$  and  $\hat{r}_p$ , and for the complex amplitude transmission coefficients,  $\hat{t}_s$  and  $\hat{t}_p$ , are given by:<sup>13</sup>

$$\hat{r}_s = \left( \frac{E_r}{E_i} \right)_{TE} = \frac{n_1 \cos \phi - \hat{n}_2 \cos \hat{\gamma}}{n_1 \cos \phi + \hat{n}_2 \cos \hat{\gamma}} = \frac{\sin(\hat{\gamma} - \phi)}{\sin(\hat{\gamma} + \phi)} \quad [1.25]$$

$$\hat{r}_p = \left( \frac{E_r}{E_i} \right)_{TM} = \frac{n_1 \cos \hat{\gamma} - \hat{n}_2 \cos \phi}{n_1 \cos \hat{\gamma} + \hat{n}_2 \cos \phi} = \frac{\tan(\hat{\gamma} - \phi)}{\tan(\hat{\gamma} + \phi)} \quad [1.26]$$

$$\hat{t}_s = \left( \frac{E_t}{E_i} \right)_{TE} = \frac{2n_1 \cos \phi}{n_1 \cos \phi + \hat{n}_2 \cos \hat{\gamma}} \quad [1.27]$$

$$\hat{t}_p = \left( \frac{E_t}{E_i} \right)_{TM} = \frac{2n_1 \cos \phi}{n_1 \cos \hat{\gamma} + \hat{n}_2 \cos \phi} \quad [1.28]$$

where  $\hat{\gamma}$  is the complex angle of refraction.  $\hat{\gamma}$  is complex as a consequence of the complex refractive index  $\hat{n}_2$ , indicating the change in phase in the reflected and transmitted waves.

The power reflectance, which is the ratio of the reflected to the incident power, or intensity, is given by:

$$R_s = \hat{r}_s \hat{r}_s^* = \frac{\sin^2(\hat{\gamma} - \phi)}{\sin^2(\hat{\gamma} + \phi)} \quad [1.29]$$

$$R_p = \hat{r}_p \hat{r}_p^* = \frac{\tan^2(\hat{\gamma} - \phi)}{\tan^2(\hat{\gamma} + \phi)} \quad [1.30]$$

where the superscript \* denotes the complex conjugate.

For a nonabsorbing dielectric,  $\gamma$  is real. From equation [1.30], it can be seen that for the special case when  $\gamma + \phi = \pi/2$ ,  $R_p$  goes to zero. The angle of incidence is then called the Brewster angle,  $\phi_B$ , and Snell's law<sup>14</sup> gives  $\tan \phi_B = n_2/n_1$ .  $R_s$  is different from zero at the Brewster angle, hence the reflected light is totally s-polarized.

For an absorbing dielectric, the angle of incidence corresponding to the minimum in the  $R_p$  curve is called the pseudo-Brewster angle.

In the case of normal incidence, both  $\phi$  and  $\hat{\gamma}$  are zero, and the expressions for  $\hat{r}_s$  and  $\hat{r}_p$  both reduce to:

$$\hat{r}_s = \hat{r}_p = \hat{r} = \frac{n_1 - \hat{n}_2}{n_1 + \hat{n}_2} \quad [1.31]$$

If the first medium is air, this equation further simplifies to:

$$\hat{r} = \frac{1 - \hat{n}_2}{1 + \hat{n}_2} = \frac{1 - (n + ik)}{1 + (n + ik)} \quad [1.32]$$

where the subscript is no longer required. This gives the power reflectance at normal incidence as:

$$R = \frac{(n-1)^2 + k^2}{(n+1)^2 + k^2} \quad [1.33]$$

Fresnel's equations for  $R_s$  and  $R_p$  may be written in a simpler form by recognizing that Snell's law:  $\hat{n}_2 \sin \hat{\gamma} = n_1 \sin \phi$ , gives that  $\hat{n}_2 \cos \hat{\gamma} = (\hat{n}_2^2 - n_1^2 \sin^2 \phi)^{\frac{1}{2}}$ , and by defining:

$$(\hat{n}_2^2 - n_1^2 \sin^2 \phi)^{\frac{1}{2}} = a + ib. \quad [1.34]$$

If the first medium is air, equation [1.25] then reduces to:

$$\hat{r}_s = \frac{\cos \phi - (a + ib)}{\cos \phi + (a + ib)} \quad [1.35]$$

$$\text{and } R_s = \frac{(a - \cos \phi)^2 + b^2}{(a + \cos \phi)^2 + b^2} \quad [1.36]$$

The square of equation [1.34], with  $n_1 = 1$  and  $\hat{n}_2 = \hat{n}$ , gives:

$$\begin{aligned} (\hat{n}^2 - \sin^2 \phi) &= a^2 + 2iab - b^2 \\ &= (n^2 - k^2 + 2ink - \sin^2 \phi) = a^2 + 2iab - b^2. \end{aligned} \quad [1.37]$$

The real and imaginary parts of [1.37] are:

$$a^2 - b^2 = n^2 - k^2 - \sin^2 \phi \quad [1.38]$$

$$ab = nk. \quad [1.39]$$

A similar analysis for  $R_p$  shows that:

$$R_p = R_s \left[ \frac{(a - \sin \phi \tan \phi)^2 + b^2}{(a + \sin \phi \tan \phi)^2 + b^2} \right] \quad [1.40]$$

Thus, the optical constants  $n$  and  $k$  can be simply derived from a measure of  $R_s$  or  $R_p$  at two or more angles of incidence. The dependence of reflectance of plane-polarized light upon angle of incidence is shown in Figure 1.2. It should be noted that for near-normal incidence, i.e.  $\phi \leq 15^\circ$ , to a very good approximation,  $R_s = R_p = R$ .

### 1.1c Optical Anisotropy

The discussion in Section 1.1b was confined to isotropic materials such as glass or cubic crystals. However, most crystals are optically anisotropic, their optical properties depending on the direction of propagation and the polarization of the light. This phenomenon is also referred to as birefringence or double refraction.<sup>15</sup> In a birefringent crystal, plane waves travelling along a given direction may vibrate in two mutually perpendicular directions which are associated with different wave velocities, and therefore, different refractive indices. The variation in the crystal's refractive index with the vibration direction

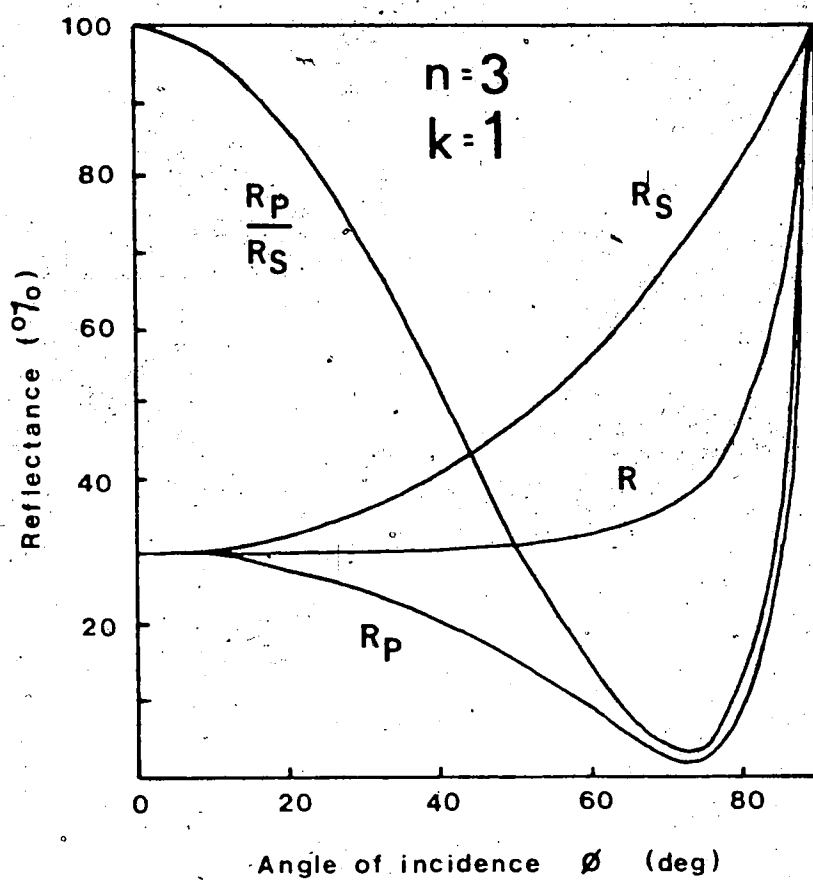


Figure 1.2 Dependence of reflectance of plane-polarized light upon angle of incidence.

The subscripts s and p refer to the components polarized perpendicular and parallel, respectively, to the plane of incidence. The reflectance  $R$  corresponds to unpolarized light.

of the light is pictorially represented by an optical indicatrix, which is an ellipsoid surface whose principal axes are equal to the three principal refractive indices. This representation surface is illustrated in Figure 1.3.

For light propagating along the ON direction, the crystal's optical properties are determined by an elliptical section of the indicatrix normal to this direction. The semi-axes of the elliptical section, OL and OM, define the two mutually perpendicular vibration directions permitted for this wave, and the lengths of the semi-axes are proportional to the appropriate refractive index. For a transparent crystal, the relationship between the magnitude of the wave vector sustained by the crystal and the refractive index is given by equation [1.15], i.e.  $K = n\omega/c$ . For an anisotropic, absorbing crystal, this simple relationship is only valid when the vibration direction of the wave is parallel to a principal axis of the optical indicatrix which is fixed by symmetry.<sup>16</sup>

This dependence of the crystal's optical properties on the crystal symmetry is due to the fact that light is symmetrical about its direction of propagation. Thus, the symmetry of the optical indicatrix is necessarily determined by the maximum symmetry that can be displayed by the unit-cell shape, i.e. the Bravais lattice.<sup>17</sup> The optical properties of crystals belonging to the tetragonal, trigonal, or hexagonal classes are described by an ellipsoid of revolution, in which two of the axes of the indicatrix are

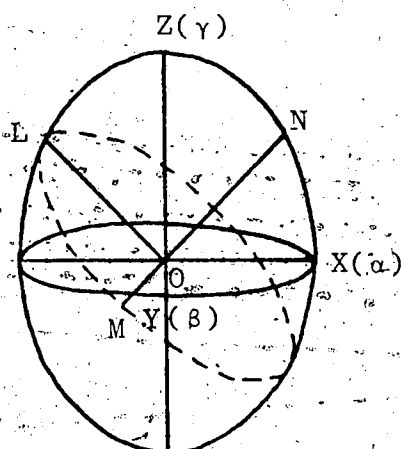


Figure 1.3 The optical indicatrix.

Waves travelling along the direction ON vibrate along OL or OM, the magnitudes of which give the two corresponding refractive indices.

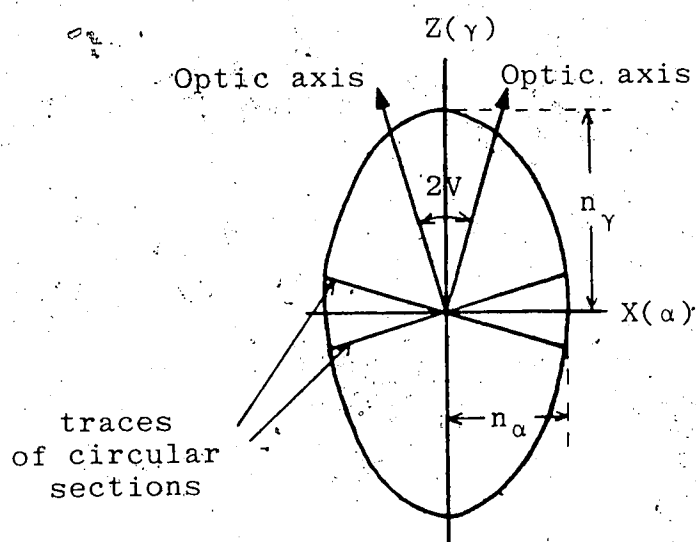


Figure 1.4 Section through the  $\gamma$ - $\alpha$  vibration plane, optic axial plane of a biaxial indicatrix.

Crystal is of positive optic sign.

equal in magnitude. These crystals are referred to as uniaxial; and the three axes of the indicatrix are determined by the three crystallographic axes, for all frequencies.

In particular, the c-crystallographic axis is normal to the circular cross-section of the indicatrix. For light propagating along this direction, the phase velocities of the two orthogonally polarized waves have the same value. This direction of propagation, for which the phenomenon of double refraction does not occur, is called the optic axis. Rays vibrating in the plane perpendicular to the optic axis are referred to as ordinary rays, since they obey the ordinary laws of refraction; whereas, rays vibrating in the plane parallel to the optic axis are referred to as extraordinary, since they do not obey these laws.

The optical properties of crystals belonging to the orthorhombic, monoclinic, and triclinic classes are described by a triaxial ellipsoid, in which all three principal refractive indices are different. By convention, the refractive indices are designated  $n_\alpha$ ,  $n_\beta$  and  $n_\gamma$ , where  $n_\gamma > n_\beta > n_\alpha$  and  $\alpha$ ,  $\beta$ , and  $\gamma$  define the principal vibration directions.<sup>18</sup> A complete description of the indicatrix requires a correlation of  $\alpha$ ,  $\beta$  and  $\gamma$  to the crystallographic directions. Because these crystals possess two optic axes, they are termed biaxial. The two optic axes are perpendicular to the two circular cross-sections of the ellipsoid and lie in the  $\alpha\gamma$  section of the indicatrix, which is often called the optic axial plane. This elliptical section is

shown in Figure 1.4. The angles between the optic axes are bisected by the indicatrix axes,  $OX(\alpha)$  and  $OZ(\gamma)$ ; the one which bisects the acute angle (commonly called the optic axial angle and denoted  $2V$ ) is termed the acute bisectrix, and the other is the obtuse bisectrix. If  $\gamma$  is the acute bisectrix, the crystal is said to be optically positive; if  $\alpha$  is the acute bisectrix, the crystal is optically negative.

For an orthorhombic crystal, the indicatrix is oriented so that the principal vibration directions are parallel to the three crystallographic axes, for all frequencies. However, there is no criterion associating a particular vibration direction to a particular crystal axis.

For monoclinic crystals, one axis of the indicatrix, but any one, is aligned parallel to the b-crystallographic axis, for all frequencies. The other two indicatrix axes lie in the ac plane, but anywhere in that plane, their positions depending upon the frequency.

For triclinic crystals, there is no relationship between the indicatrix and crystallographic axes.

These general characteristics of the optical indicatrix for the various crystal classes<sup>19</sup> are summarized in Table 1.1.

In the case of absorbing crystals, the preceding discussion is complicated by the required addition of another ellipsoid surface, defining the extinction coefficient in different vibration directions. Also the principal axes of

Table 1.1. Relation of Principal Axes of the Optical Indicatrix to Crystal Axes

Optical System	Crystal System	Orientation	Remarks
Isotropic	Cubic	Any	$n_x = n_y = n_z$
Uniaxial	Hexagonal	Z parallel to $C_6$ or $C_3$ ; X or Y any directions in plane perpendicular to Z	$n_x = n_y$
	Rhombohedral (Trigonal)	Z parallel to $C_3$ ; X, Y any directions in plane perpendicular to Z	$n_x = n_y$
Biaxial	Orthorhombic	X, Y, Z parallel to the three $C_2$ axes in $D_2$ or $D_{2h}$ ; Z parallel to $C_2$ and X and Y perpendicular to $\sigma_v$ planes in $C_{2v}$	$n_x \neq n_y \neq n_z$
	Monoclinic	Z parallel to $C_2$ or perpendicular to $\sigma$ ; X and Y not fixed by symmetry, and frequency dependent	X and Y different for real and imaginary parts of $\hat{n}$
	Triclinic	No axes fixed by symmetry and all three axes may be frequency dependent	Real and imaginary parts of $\hat{n}$ have different principal axes

X, Y, and Z are the principal axes of the optical indicatrix.

the  $k$  ellipsoid do not necessarily coincide with the principal axes of the  $n$  ellipsoid, unless the symmetry of the crystal requires it (see Table 1.1). However, the relationship between optical and morphological symmetry is the same as for transparent crystals.<sup>12</sup>

### 1.1d Dispersion of the Optical Constants

In Section 1.1c, it was shown that the dependence of the optical constants on the vibration direction of the wave in the crystal was related to the crystal's macroscopic symmetry. In order to probe the microscopic nature of the crystal, it is necessary to study the frequency dependence, or dispersion, of the optical constants. Strictly speaking, the optical constants are also dependent upon the magnitude of the wave vector of the electromagnetic wave, an effect known as spatial dispersion.<sup>20,21</sup> However, the usual practice is to neglect spatial dispersion effects when discussing infrared optical properties. This simplification is justified on the following grounds. The complete, independent set of allowed wave vectors of crystal vibrations is given by the first Brillouin zone, which is the primitive unit cell in wave vector space.<sup>22</sup> On the scale of this first Brillouin zone ( $\approx 10^7 \text{ cm}^{-1}$ ), the wave vectors for infrared radiation are very small ( $\approx 10^3 \text{ cm}^{-1}$ ). Conservation of momentum requires that for a fundamental transition, the wave vector of radiation in the crystal,  $\underline{K}$ , be equal to the wave vector of vibration  $\underline{k}$ , that is,  $\underline{K} = \underline{k}$ .

It can be seen that this selection rule is only satisfied when  $\underline{k} \approx 0$ , which means that all of the unit cells in the crystal vibrate in-phase. Thus, the  $\underline{k} \approx 0$  approximation greatly simplifies the description of the crystal's infrared-active modes, since one primitive unit cell gives all the required information.

In the limit of  $\underline{k} \rightarrow 0$ , a discussion of the dispersion of the complex dielectric constant can be restricted to its frequency dependence. Many different mechanisms contribute to this frequency dependence; in broad terms, these are: reorientational polarization, distortion polarization, and electronic polarization.<sup>23</sup> In the infrared region, the mechanism of importance is distortion polarization, which arises from induced vibrations in the crystal.

The general frequency behavior of the optical constants is most readily explained by a classical model which considers a solid as an assembly of damped harmonic oscillators set into motion by a driving electric field. This model was originally formulated by Lorentz to explain the contribution of electronic polarization to the dielectric constant.<sup>24</sup> An adaptation of this treatment is given here to explain the contribution of distortion polarization to the dielectric constant:

For this model, the damped harmonic oscillator describes a unit cell mode in the  $\underline{k} \approx 0$  approximation. This unit cell mode is a symmetrized linear combination of the molecular normal coordinates, and may describe either an intermolecu-

lar or intramolecular vibration of the crystal.<sup>25</sup> The mass-weighted normal coordinate which defines this mode is denoted  $Q$ . If the lattice is subjected to an electric field  $\underline{E}$ ,  $Q$  satisfies the equation of motion:

$$\frac{d^2 Q}{dt^2} + \gamma_0 \frac{dQ}{dt} + \omega_0^2 Q = -\frac{d\mu}{dQ} \cdot \underline{E} \quad [1.41]$$

where

$\frac{d\mu}{dQ}$  = change in dipole moment of the unit cell during the unit cell vibration

$\omega_0$  = the resonance frequency

$\gamma_0$  = damping constant.

The allowed orientations of the dipole moment derivatives in the crystal are given by the principal axis directions of the optical indicatrix, when the latter are determined by symmetry (see Table 1.1). To simplify the following discussion, it is assumed that the electric field is parallel to  $d\mu/dQ$  and therefore the dot product and vector notation may be discarded. The wave vector of radiation is then perpendicular to  $d\mu/dQ$ , and  $\omega_0$  is called the transverse optic mode frequency  $\omega_{TO}$ .

For a time-varying field of the form  $\hat{\underline{E}} = \underline{E}_0 \exp(-i\omega t)$ , the steady-state solution of [1.41] is:

$$\hat{Q} = -\hat{\underline{E}} \left( \frac{d\mu}{dQ} \right) \cdot \frac{1}{(\omega^2 - \omega_0^2 + i\omega\gamma_0)} \quad [1.42]$$

The polarization of the material associated with this unit cell mode is:

$$\hat{P} = NQ \left( \frac{d\mu}{dQ} \right)$$

where  $N$  represents the number of unit cells per unit volume. The total polarization is given by:

$$\hat{P} = NQ \left( \frac{d\mu}{dQ} \right) + \frac{(\epsilon_{\infty} - 1)}{4\pi} \hat{E} \quad [1.43]$$

where the high frequency dielectric constant,  $\epsilon_{\infty}$ , encompasses the effect of all other mechanisms contributing to the polarization at frequency  $\omega$ . A complex polarization means that the induced polarization differs in phase from the applied electric field at all frequencies.

From equation [1.8], the corresponding displacement vector is:

$$\hat{D} = \hat{E} + 4\pi\hat{P} = \left[ -N \left( \frac{d\mu}{dQ} \right)^2 \frac{4\pi}{(\omega^2 - \omega_0^2 + i\omega\gamma_0)} + \epsilon_{\infty} \right] \hat{E} = \hat{\epsilon} \hat{E} \quad [1.44]$$

This gives the complex dielectric function  $\hat{\epsilon}$  as:

$$\hat{\epsilon}(\omega) = \epsilon_{\infty} + 4\pi N \left( \frac{d\mu}{dQ} \right)^2 \frac{1}{(\omega_0^2 - \omega^2 - i\omega\gamma_0)} \quad [1.45]$$

At zero frequency, equation [1.45] becomes:

$$\epsilon_0 = \hat{\epsilon}(0) = \epsilon_{\infty} + \frac{4\pi N}{\omega_0^2} \left( \frac{d\mu}{dQ} \right)^2 \quad [1.46]$$

the static dielectric constant of the material.

With this result, equation [1.45] can be rewritten as:

$$\hat{\epsilon}(\omega) = \epsilon_{\infty} + \frac{(\epsilon_0 - \epsilon_{\infty}) \omega_0^2}{(\omega_0^2 - \omega^2 - i\omega\gamma_0)} \quad [1.47]$$

$$\text{The difference } \epsilon_0 - \epsilon_{\infty} = \frac{4\pi N}{\omega_0^2} \left( \frac{d\mu}{dQ} \right)^2 \quad [1.48]$$

gives a direct measure of the strength of the absorption.

If the primitive unit cell contains more than one infrared-active unit cell mode, equation [1.45] can be generalized by simply summing over all such frequencies:

$$\hat{\epsilon}(\nu) = \epsilon_{\infty} + \sum_j \frac{N}{\pi c} \left( \frac{\partial \mu}{\partial Q_j} \right)^2 \frac{1}{(\nu_j^2 - \nu^2 - i\nu\gamma_j)} \quad [1.49]$$

where  $\nu_j$  = resonance frequency in wavenumber units.

By equating the real and imaginary parts of equation [1.49] with  $\hat{\epsilon}(\nu) = \epsilon'(\nu) + i\epsilon''(\nu) = \hat{n}^2(\nu)$ , the following results are obtained:

$$\epsilon'(\nu) = n^2(\nu) - k^2(\nu) = \epsilon_{\infty} + \sum_j \frac{N}{\pi c} \left( \frac{\partial \mu}{\partial Q_j} \right)^2 \frac{(\nu_j^2 - \nu^2)}{[(\nu_j^2 - \nu^2)^2 + \gamma_j^2 \nu^2]} \quad [1.50]$$

$$\epsilon''(\nu) = 2n(\nu)k(\nu) = \sum_j \frac{N}{\pi c} \left( \frac{\partial \mu}{\partial Q_j} \right)^2 \frac{\gamma_j \nu}{[(\nu_j^2 - \nu^2)^2 + \gamma_j^2 \nu^2]} \quad [1.51]$$

A time dependent quantum mechanical analysis of absorption and dispersion gives equations formally similar to [1.50] and [1.51], although the oscillator parameters have different definitions. <sup>24</sup>

These equations indicate that in the neighborhood of  $\nu = \nu_j$ , there is an absorption maximum, and that to low frequency of  $\nu_j$ ,  $\epsilon'$  increases with increasing frequency. This is called normal dispersion. However, at, or near the resonance frequency, the dispersion becomes "anomalous" in the sense that  $\epsilon'$  decreases with increasing frequency. Beyond this region, normal dispersion is resumed. Figure 1.5 illustrates the frequency dependence of  $\epsilon'$  and  $\epsilon''$ .

The corresponding frequency behavior of the optical constants  $n$  and  $k$  is depicted in Figure 1.6. Comparison of Figures 1.5 and 1.6 shows that  $n(\nu)$  and  $\epsilon'(\nu)$  exhibit a similar frequency dependence. In the case of more than one absorption band, both  $\epsilon'$  and  $n$  decrease as we pass from low to high frequency through each absorption, asymptotically approaching unity at infinite frequency. It should also be noted that the  $k(\nu)$  curve is quite asymmetric and that its maximum does not coincide with that of the  $\epsilon''(\nu)$  curve.

However, the optical property considered of the most fundamental significance in the study of solids<sup>26</sup> is  $\nu\epsilon''$ . This can be understood from the characteristics of this function under the damped harmonic oscillator model:

$$\nu\epsilon''(\nu) = \sum_j \frac{N}{\pi c} \frac{1}{2} \left( \frac{\partial \mu}{\partial Q_j} \right)^2 \frac{\gamma_j \nu^2}{[(\nu_j^2 - \nu^2)^2 + \gamma_j^2 \nu^2]} \quad [1.52]$$

The shape of the  $\nu\epsilon''$  curve is determined by the term:

$$\frac{\gamma_j \nu^2}{[(\nu_j^2 - \nu^2)^2 + \gamma_j^2 \nu^2]}$$

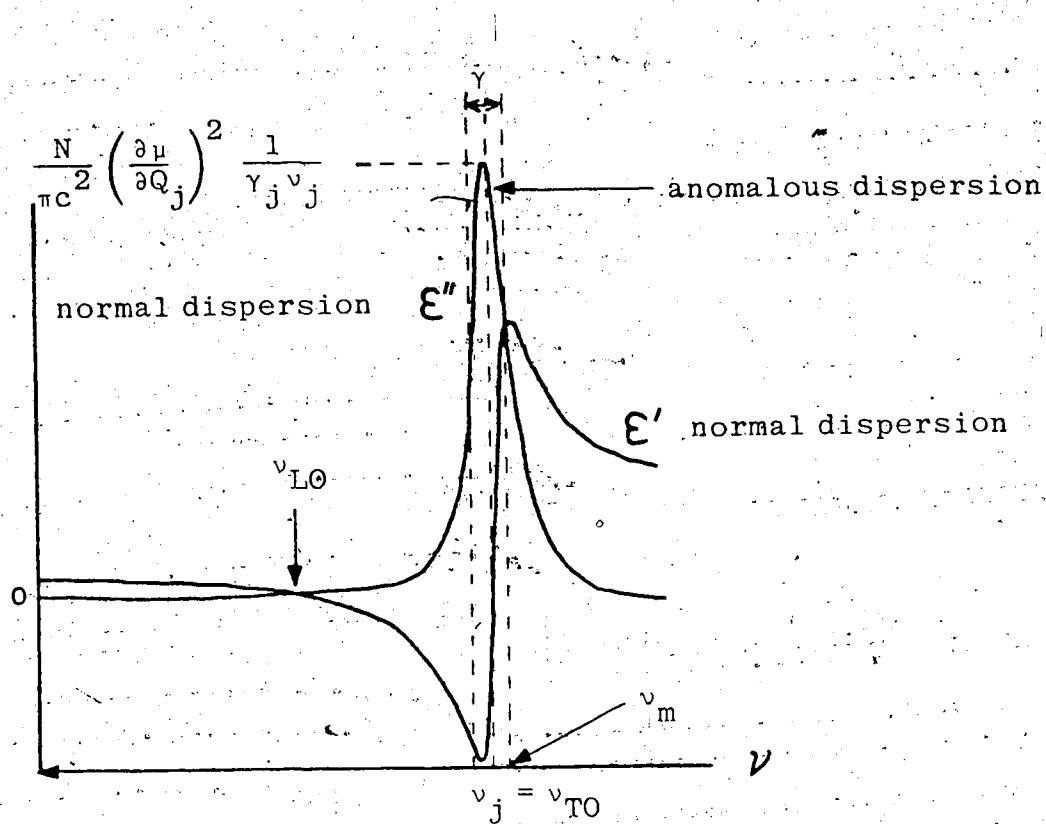


Figure 1.5 Frequency behavior of  $\epsilon'$  and  $\epsilon''$ .

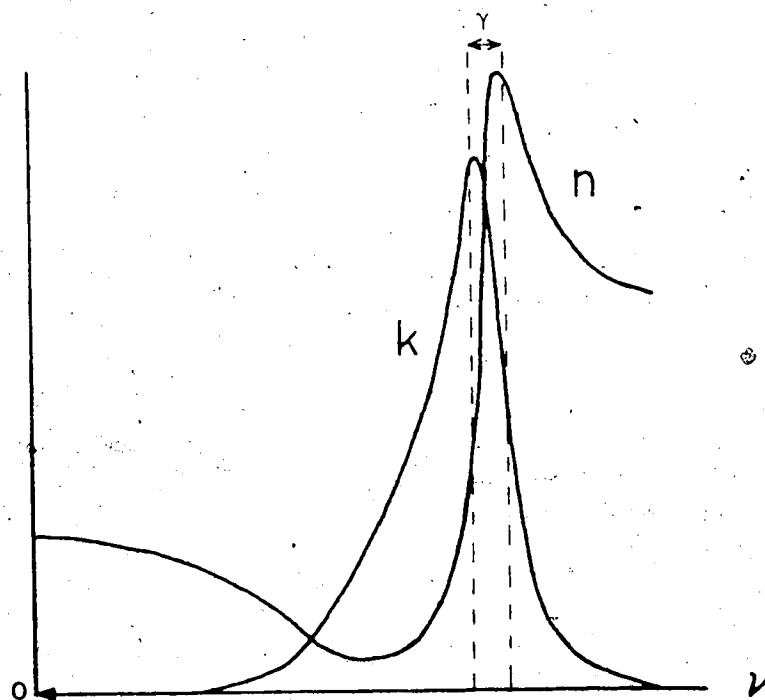


Figure 1.6 Corresponding frequency behavior of  $n$  and  $k$ .  
Figures redrawn from Reference 24.

For small values of  $\gamma_j$ , this expression can be written as:

$$\frac{\gamma_j v^2}{[(v_j^2 - v^2)^2 + \gamma_j^2 v^2]} \approx \frac{\gamma_j v^2}{4v^2(v_j - v)^2 + \gamma_j^2 v^2} = \frac{\gamma_j/4}{(v_j - v)^2 + (\gamma_j/2)^2} \quad [1.53]$$

This is the equation of a Lorentzian-shaped band, symmetric about  $v_j$ , with peak height of  $\gamma_j^{-1}$ , and full width at half-maximum height (FWHM) equal to  $\gamma_j$ . This latter property is satisfied even for values of  $\gamma_j$  close to  $v_j$ . The derivative of equation [1.52] shows that the resonance frequency,  $v_j$ , or transverse optic frequency,  $v_{TO}$ , occurs at the maximum value of  $v\epsilon''$ , i.e.

$$(v\epsilon'')_{\max} = \frac{N}{\pi c} \frac{2}{2} \left( \frac{\partial \underline{\mu}}{\partial Q_j} \right)^2 \frac{1}{\gamma_j} \quad [1.54]$$

This result is valid for any value of  $\gamma_j$  and is the same result that was obtained in Section 1.1a from the identification of  $v\epsilon''$  with the sample's conductivity. For small values of  $\gamma_j$  relative to  $v_j$ , the peak position and half-width of the  $\epsilon''(v)$  spectrum give reasonably good values of  $v_j$  and  $\gamma_j$ . The percentage error in the value of  $v_j$  obtained from the maximum of the  $\epsilon''$  curve<sup>27</sup> is proportional to  $(\gamma_j^2/v_j^2)$ .

Associated with each transverse optic (TO) mode is a longitudinal optic (LO) mode, for which the wave vector is parallel to  $\partial \underline{\mu} / \partial Q$ . Recall from Section 1.1a, that two solutions to the wave equation exist, since  $\nabla \cdot \underline{D} = 0$ , either when  $\nabla \cdot \underline{E} = 0$  or when  $\epsilon' = 0$ . This latter solution defines the con-

dition for the LO mode. A more correct definition of the LO mode is the frequency for which the sample's resistivity is a maximum.<sup>11</sup> Since resistivity is the inverse of conductivity, this suggests that  $\nu_{LO}$  is given by the frequency for which  $(1/\nu\epsilon'')$  is a maximum value. It should be noted, that the  $k=0$  approximation requires that the TO and LO modes be degenerate. Since, in general,  $\nu_{LO}$  does not coincide with  $\nu_{TO}$ ,  $k$  must be finite.<sup>28</sup>

In the preceding discussion, it has been assumed that the effective electric field acting on the molecules of the crystal is equal to the applied macroscopic electric field. However, each molecule experiences an additional field due to the polarization of all other molecules in the crystal by the applied field. Thus, it is necessary to include a local field correction factor,  $F_j^2$  in equations [1.50], [1.51], and [1.52]. For the case of molecules situated on sites of tetrahedral or higher symmetry, this correction factor is given simply by the Lorentz local field:<sup>29,30</sup>

$$F_j = \frac{|\underline{E}_{eff}|}{|\underline{E}|} = \frac{\epsilon_\infty + 2}{3} \quad [1.55]$$

The method of determining the field corrections for molecules on crystal sites of lower symmetry is described in detail by Decius and Hexter.<sup>30</sup> Because of the effect of the local field, the damped harmonic oscillator resonance frequency,  $\nu_0$ , no longer coincides with the transverse optic frequency,  $\nu_{TO}$ .<sup>29,31</sup>

The expressions for the dielectric functions may be simplified by defining an effective oscillator strength,<sup>31</sup>

$S_j$  as:

$$S_j = F_j^2 \frac{N}{\pi c^2} \left( \frac{\partial \mu}{\partial Q_j} \right)^2 \quad [1.56]$$

Comparison with equation [1.54] shows that:

$$S_j = (\nu \epsilon'')_{\max} \gamma_j \quad [1.57]$$

Thus, it has been demonstrated that the dielectric function,  $\hat{\epsilon}(\nu)$  provides all of the desired information on the transverse optic (TO) and longitudinal optic (LO) frequencies, damping constants, and absolute intensities for the various allowed absorption processes. In summary, these quantities may be determined for well-separated unit cell modes, under the classical damped harmonic oscillator approximation, as follows:

- i) the number of peaks in the  $\epsilon''(\nu)$  spectrum gives the number of infrared-active vibrations.
- ii)  $\nu_{TO}$  is  $\nu$  at maximum  $\nu \epsilon''$ .
- iii)  $\nu_{LO}$  is  $\nu$  at  $\epsilon' = 0$ , or maximum  $(1/\nu \epsilon'')$ .
- iv)  $\gamma$  is the FWHM of the  $\nu \epsilon''$  band.
- v)  $S_j = (\nu \epsilon'')_{\max} \gamma_j$ .

## 1.2 Methods of Obtaining Optical Constants

A variety of methods is available for the measurement of optical constants. The choice of method is determined by the nature of the compound under investigation and the

particular demands of the experimenter. In the following discussion, the various methods are characterized by their relative precision, experimental convenience and limitations, and whether they are useful at only a few, or a wide range of, frequencies. To facilitate this discussion, the methods are broadly classified as either direct (Section 1.2a) or indirect (Section 1.2b) procedures. In order to obtain the optical constants of an absorbing medium at a particular frequency, two pieces of information are required. The direct methods involve direct measurement of two independent quantities which both depend upon the optical constants; while the indirect methods involve the measurement of one quantity, usually the reflectance, over a wide range of frequencies followed by either a Kramers-Kronig integration to find the complementary quantity, or a classical oscillator fit to the data.

### 1.2a Direct Methods

If the sample is weakly absorbing and its thickness can be accurately determined, the transmittance spectrum, after correction for reflection effects, gives the absorption coefficient,  $\alpha(\nu)$ . In the usual case of stochastic multiple internal reflections within the sample, the relationship between the measured transmittance,  $T^*(\nu)$  and the true transmittance,  $T(\nu)$ , where  $T(\nu) = \exp[-\alpha(\nu)r]$ ;  $r$  = sample thickness, is given by:

$$T^*(\nu) = \frac{T(\nu) \{1-R(\nu)\}^2}{\{1-R^2(\nu)T^2(\nu)\}}$$

$R$  = usual primary reflectance from the entrance face.

It can be seen that a measurement of the transmittance of two films of different thicknesses determines  $\alpha(\nu)$ . Alternatively, the optical constants can be obtained from measurements of the reflectance and transmittance of the same film,<sup>33</sup> or the transmittance and phase shift on transmission for the same film.<sup>34</sup> This latter experiment has also been performed for various film thicknesses in order to determine, and hence eliminate, the effect of any surface films.<sup>35</sup>

If the sample also possesses plane parallel surfaces, its transmittance spectrum will exhibit an interference fringe pattern due to phase-related multiple internal reflections from the entrance and exit faces.<sup>36</sup> The maxima in the channeled spectrum occur when the optical path length (i.e. the product of the sample's refractive index and thickness,  $n(\nu)r$ ), corresponds to an integral number of half-wavelengths in vacuum. For this condition, the reflected partial waves differ in phase by an integral number of cycles. The measured reflectance or transmittance is the sum total of their respective partial wave components. Thus, provided the sample absorption is not too large, the real refractive index can be measured from the fringe spacing. Once  $n$  is known, the extinction coefficient,  $k$ , can be derived from the averaged transmittance spectrum.<sup>36</sup> This channeled spectrum procedure for obtaining optical constants is primarily used in

the far-infrared region where the restrictions on the sample's thickness and parallelism are least severe.

In the visible region, the refractive index of transparent materials is most commonly determined by a refractometer, which measures the angle of total reflection at the boundary of the sample with a medium of known refractive index,  $n_1$ . Assuming  $n_2$  is real, Snell's law gives  $\theta = \arcsin(n_2/n_1)$ . Another method which is frequently used for non-absorbing solids is to prepare the sample in the form of a prism and measure the angle of minimum deviation,  $\delta$ . If the prism has a refracting angle of  $A$ , the refractive index is given by<sup>37</sup>  $n = \sin(A+\delta)/\sin A$ . This technique has also been successfully used to obtain the infrared refractive indices of germanium, silicon, and selenium glass.<sup>38</sup>

Although the simplicity of transmission measurements makes them a desirable experimental procedure for obtaining optical constants, there are many occasions when they are not feasible or provide erroneous results, particularly when the sample absorption is so strong that it is accompanied by strong reflection. It then becomes necessary to separate frequency-dependent reflection losses from pure absorption losses. Thus, Decius and Hexter<sup>26</sup> note that thick samples may exhibit a complicated transmission spectrum, from which it is difficult to identify the transverse optic frequencies. For such samples,<sup>26</sup> the region of low transmission spreads out unsymmetrically from  $\nu_{TO}$ . Problems are also encountered with very thin samples. There are experimental difficulties

associated with sample preparation and accurate film-thickness measurements and there often remains some uncertainty about whether the thin film is optically<sup>39</sup> and structurally<sup>40</sup> characteristic of the bulk sample. In addition, some transmission studies are further complicated by a dependence of the spectra upon the sampling technique.<sup>41</sup>

These problems with transmission measurements are most frequently met in the solid state with various glasses, oxides, silicates and semiconductors.<sup>42</sup> Ionic crystals, such as the alkali halides also present difficulties; they exhibit strong, broad absorption in the infrared region due to the large dipole moment change associated with the oscillation of the atoms or ions,<sup>27</sup> and in the far-ultraviolet region their absorption coefficients<sup>43</sup> are of the order of  $10^5 - 10^6 \text{ cm}^{-1}$ . This makes it necessary to use extremely thin ( $\sim 1 \text{ }\mu\text{m}$ ) samples in order to obtain reliable transmission data. For these situations, where intense sample absorption complicates transmission measurements, reflection methods are more commonly employed.

The sample reflectance is usually measured relative to a reflection standard of known, constant, and high reflectivity throughout the spectral region of interest. Various pairs of reflection measurements will uniquely define the sample's optical constants at a given frequency. The formulae, [1.36]-[1.40] show that the reflected intensities at oblique incidence,  $R_s$  and  $R_p$ , are functions of  $n$ ,  $k$  and  $\phi$ . As the angle of incidence,  $\phi$  is known from the experiment,

$n$  and  $k$  may be determined from any of the following measurements:  $R_p$  and  $R_s$  at one angle of incidence, the ratio  $R_p/R_s$  at two angles of incidence (thus avoiding the measurement of absolute intensities), or the reflectance at two angles for incident light having a known state of polarization. From Figure 1.2, it can be seen that the relative sensitivity of these methods for a particular angle of incidence is:  $R_p/R_s > R_p > R > R_s$ .  $R_p/R_s$  measurements have a further advantage in that the sample assumes the role of a limiting aperture in the optical system, thereby enabling very small samples to be studied.<sup>44</sup> In these experiments, it is most desirable to make the measurements at angles near the principal angle of incidence, for which  $\hat{r}_p$  and  $\hat{r}_s$  are  $90^\circ$  out-of-phase. Unfortunately, this angle practically coincides with the angle of incidence at which minimum  $R_p$  reflection occurs and therefore the increase in accuracy due to the optimum sensitivity is partially cancelled by the errors in measuring very small reflectance values.<sup>45</sup> Working at large angles of incidence has further disadvantages. The effect of apparatus polarization, that is, the discrimination of the instrument for a particular component of polarization, is more pronounced at large angles of incidence, and the demands on the sample become more stringent: larger sample surfaces are required<sup>46</sup> and nonflatness and contamination of the surface have a greater influence on the measured reflectance.<sup>33</sup>

For typical metals, the pseudo-Brewster angle is near  $90^\circ$  in the infrared region.<sup>47</sup> The optical constants of these samples cannot be usefully measured by the aforementioned direct reflection procedures. More accurate results are obtained by the method of ellipsometry. This technique is based on the fact that, for plane-polarized incident radiation, the s- and p-polarized reflectance components,  $\hat{r}_s$  and  $\hat{r}_p$ , are generally phase shifted and, therefore, the reflected light is elliptically polarized. Equations [1.25] and [1.26] give that:

$$\frac{\hat{r}_p}{\hat{r}_s} = \frac{\cos(\hat{\gamma} + \phi)}{\cos(\hat{\gamma} - \phi)} = \frac{|\hat{r}_p|}{|\hat{r}_s|} \exp i(\theta_p - \theta_s) = \tan \rho \exp i\Delta \quad [1.58]$$

$$\text{where } \tan \rho = |\hat{r}_p| / |\hat{r}_s|$$

$$\text{and } \Delta = \theta_p - \theta_s.$$

Thus,  $n$  and  $k$  can be obtained from measurement of  $\rho$  and  $\Delta$ . A serious disadvantage of ellipsometry is the requirement of two polarizers (one in the incident beam and one in the reflected beam) which significantly reduces the energy throughput.<sup>48</sup> The method is also very slow since it requires several manual adjustments at each frequency. This greatly increases the risk of surface contamination. In the visible region, an improvement in the measurement time has been achieved by the application of modulation techniques.<sup>49,50</sup>

The determination of the optical constants from these direct experimental methods is not a straightforward problem. This is because the Fresnel's reflection relations cannot be

written in a form which explicitly defines  $n$  and  $k$  in terms of the directly measured quantities. This computational problem has been tackled in a number of different ways. However, these all employ some type of graphical procedure for the simultaneous solution of Fresnel's equations. The method of Simon<sup>42</sup> illustrates the basic strategy: A number of curves of the reflectance ( $R$ ,  $R_s$  or  $R_p$ ) are plotted as a function of  $n$ , for constant values of  $k$  and for a particular angle of incidence. Suppose the measured value of  $R$  for angle  $\phi_1$  and frequency  $\nu_1$  is equal to  $R_1$ . This value of  $R$  corresponds to many pairs of  $n$  and  $k$ , which, when plotted in the  $n$ - $k$  plane, define an isorefectance curve for  $(\nu_1, R_1, \phi_1)$ . Similarly, a reflectance measurement  $R_2$ , at another angle of incidence  $\phi_2$ , provides a second isorefectance curve  $(\nu_1, R_2, \phi_2)$ , and the intersection with the first curve gives the solution for  $n$  and  $k$ . The sensitivity of this method is determined by the angle of intersection of the two isorefectance curves, i.e. the steeper the angle of intersection, the greater is the accuracy of the derived optical constants.<sup>45</sup> The angle of incidence at which the maximum intersection angle occurs is the principal angle of incidence. It is for this reason, that it is desirable to perform the reflectance-versus-angle-of-incidence measurements near the principal angle. Simon<sup>42</sup> did not seem to appreciate this fact since he prepared families of curves for  $R_s$ ,  $R_p$  and  $R$  at  $\phi = 20^\circ$  and  $70^\circ$ . Various improvements of this graphical reduction procedure have since appeared in the

literature. Avery<sup>51</sup> plotted a set of curves of  $R_p/R_s$  as a function of  $n$  with  $k/n$  as a parameter, for several specific angles of incidence. Lindquist and Ewald<sup>44</sup> also measured  $R_p/R_s$ , but by a simple geometric construction evaluated  $\epsilon'$  and  $\epsilon''$ . They defined the quantities:

$$\rho^2 = \frac{R_p}{R_s} \quad S = \frac{(1+\rho^2)}{(1-\rho^2)} \quad \text{and } m = \sin \phi \tan \phi$$

where  $\phi$  = angle of incidence

$$\text{and } \hat{\epsilon} = \epsilon' + i\epsilon'' = A + Be^{i\tau} + Ce^{i2\tau}$$

The coefficients  $A$ ,  $B$ , and  $C$  are functions of  $\rho^2$ ,  $S$ , and  $m$ . For a given  $\rho^2$  and  $\phi$ , the last equation determines an epicycloid in the  $\epsilon'$  and  $i\epsilon''$  plane, as the parameter  $\tau$  is varied from 0 to  $2\pi$ . A second epicycloid is drawn for a second value of  $\rho^2$  measured at another angle of incidence, and the intersection of the two curves gives the values of  $\epsilon'$  and  $\epsilon''$ .

Field and Murphy<sup>52</sup> measured the reflectance at three angles of incidence and used isorefectance ratio curves to obtain  $n$  and  $k$ . The graphical routine was circumvented by Juekner<sup>53</sup> who produced the points of the isorefectance curves directly by digital computation. The optical constants were then determined via a centroid search program. However, it can be readily appreciated that all of these procedures are long and tedious, particularly if the optical constants are desired over an extended frequency range. A detailed discussion of the comparative sensitivity of the various reflectance-versus-angle-of-incidence methods for obtaining optical constants is given by Hunter.<sup>45</sup>

A variation of the reflection method, called attenuated total reflectance (ATR), has been extensively used for compounds with absorption coefficients too small to give good reflection spectra and yet too large to give good transmission spectra. This technique was first introduced by Fahrenfort<sup>54</sup> in 1961 and differs from the conventional reflection method in that the reflecting surface is the interface between the sample and a dielectric of higher refractive index, instead of that between the sample and air. If the angle of incidence,  $\phi$ , and the dielectric material are selected so that  $\sin \phi \geq n_{\text{diel}}$ , then total reflection occurs for those frequencies where the sample is nonabsorbing. If, for the sample,  $k \neq 0$ , part of the incident radiation is absorbed, thereby reducing the reflected energy. The ATR spectrum then resembles a transmission spectrum, the attenuation of the reflectance increasing with increasing values of  $k$ . However, for an angle of incidence less than this critical angle, the reflectance spectrum resembles a real refractive index spectrum, exhibiting the effects of anomalous dispersion.<sup>55</sup> The optical constants are derived either by measuring  $R_p$  and  $R_s$  at one angle of incidence or  $R_p$  at two angles of incidence, followed by a graphical analysis similar to Simon's, or by measuring  $R_s$ ,  $R_p$ , or  $R_p/R_s$  as a function of frequency, at one angle of incidence, followed by a Kramers-Kronig integration procedure. Although ATR is most useful for liquid samples, it has also been successfully applied to such solids as naphthalene<sup>55,56</sup> and alkali-metal

nitrate crystals.<sup>57</sup> The main disadvantages of this method are problems with incomplete optical contact between the sample and the dielectric material and the necessity for accurate control of the angle of incidence.

The development of Fourier transform infrared spectroscopy has introduced a new method for measuring optical constants. In this technique,<sup>58</sup> a reference interferogram is recorded without the sample in the infrared beam. The sample is then placed in one arm of the Michelson interferometer and a sample interferogram is collected. Comparison of the Fourier transforms of the reference and sample interferograms shows how the sample attenuates and phase-shifts each spectral component of the radiation. These measured differences determine the sample's optical constants. This method is restricted to samples which can be prepared in the form of a plane parallel-faced slab, and whose thickness can be accurately measured. It has been used, for example, to obtain the far-infrared optical constants of quartz.<sup>59</sup>

Fourier spectroscopy has also been applied to the measurement of optical constants from channeled spectra. This method involves subtracting the Fourier transform of the sample interferogram from the Fourier transform of the reference interferogram and normalizing the resultant difference spectrum.<sup>60</sup> The analysis differs from the previously discussed channeled spectrum procedure in that the refractive index is obtained from the zero crossings, rather than the maxima and minima, in the fringe intensity pattern. The

extinction coefficient is obtained in the usual manner. In addition to the strict requirements of a thin, weakly absorbing sample with plane parallel surfaces, it is necessary that all windows and filters be wedged so that their signatures are removed entirely from the measured interferograms.

Another direct procedure has been recently developed. It involves measuring the reflectance maxima and minima at a given frequency, as a function of the thickness of a wedged nonabsorbing thin film layer deposited on the sample of interest.<sup>61</sup> Again, a complicated graphical analysis is required to obtain the optical constants. This method is limited to materials with moderate to large values of  $n$  and  $k$ , capable of being both formed into a substrate of the required shape, and coated with a wedged nonabsorbing film. It has been used to determine the far-infrared optical constants of fused silica and sapphire.<sup>61</sup>

Although this survey of direct procedures for obtaining optical constants of solids is not comprehensive, it serves to illustrate the wide variety of methods available. The main disadvantage besetting all these methods is that they do not readily give the detailed shape of optical structure over a wide frequency range. Also, the method of obtaining  $n$  and  $k$  from reflectance measurements at two angles of incidence can only be applied to isotropic materials.<sup>62</sup> As was seen in Section 1.1c, the optical constants of anisotropic materials are dependent upon both the direction of propagation and polarization of the incident wave. The procedure

for analyzing these systems is discussed in Section 1.4.

### 1.2b Indirect Methods

There are two main categories of indirect procedures for obtaining optical constants. The first involves the measurement of one optical property over the whole spectral range from  $0 \rightarrow \infty$  frequency. The complementary optical property can then be determined because of the existence of integral relationships between them, the so-called Kramers-Kronig (KK) or dispersion relations.<sup>63</sup> These relations connect the real and imaginary parts of a complex quantity which describes a linear relationship between two amplitudes. The only other requirements are boundedness and causality,<sup>64</sup> i.e. the response of the system to the driving force cannot precede the application of the driving force. Because only these very general conditions have to be fulfilled, dispersion relations are valid in many fields of physics and engineering. They are termed KK relations because of the work of H.A. Kramers and R. de L. Kronig<sup>65</sup> who developed these equations for the dielectric constant and the refractive index.

The appropriate relations for the complex dielectric constant are:<sup>63</sup>

$$\epsilon'(\nu) = 1 + \frac{2}{\pi} P \int_0^{\infty} \frac{\nu' \epsilon''(\nu') d\nu'}{\nu'^2 - \nu^2} \quad [1.59]$$

$$\epsilon''(\nu) = -\frac{2\nu}{\pi} P \int_0^{\infty} \frac{\epsilon'(\nu') d\nu'}{\nu'^2 - \nu^2} \quad [1.60]$$

where  $P$  means the Cauchy principal value of the integral.

In the case of metals,<sup>66</sup> which have a nonvanishing static conductivity,  $\sigma_0$ , it is necessary to include the term,

$2\sigma_0/cv$ , on the right-hand side of equation [1.60]. The der-

ivation of these KK relations is given in Appendix A. It

can be readily seen that the function,  $\hat{\epsilon}(v) = \epsilon'(v) + i\epsilon''(v)$

satisfies the necessary criteria of the KK relations: it

expresses a linear relationship between the electric field

$\underline{E}$  and the electric displacement  $\underline{D}$ , i.e.  $\underline{D} = \hat{\epsilon}(v) \underline{E}$ ; the dis-

placement, or induced polarization of the medium, cannot

occur before the application of the electric field; and  $\hat{\epsilon}(v)$

approaches unity, as the frequency approaches infinity.

In the radio-frequency region, the quantity  $v\epsilon''$  can be measured as the conductivity<sup>67</sup> and, therefore,  $\epsilon'$  can be obtained from equation [1.59]. However, this particular KK relation is rarely used.

An analogous KK relation exists between the real and imaginary parts of the complex refractive index,<sup>63</sup> since  $n(v) = \sqrt{\hat{\epsilon}(v)}$  :

$$n(v) = 1 + \frac{2}{\pi} P \int_0^{\infty} \frac{v' k(v') dv'}{v'^2 - v^2} \quad [1.61]$$

$$k(v) = \frac{-2v}{\pi} P \int_0^{\infty} \frac{n(v') dv'}{v'^2 - v^2} \quad [1.62]$$

An absorption experiment after correction for reflection

losses, measures the quantity  $\alpha(v) = 4\pi v k(v)$ . Equation [1.61]

expressed in terms of  $\alpha(\nu)$  is:

$$n(\nu) = 1 + \frac{1}{2\pi^2} P \int_0^{\infty} \frac{\alpha(\nu') d\nu'}{\nu'^2 - \nu^2} \quad [1.63]$$

Jones *et al.*<sup>68</sup> have used this particular integral relation to determine the optical constants of a series of thirteen organic liquids over the range 250-4200  $\text{cm}^{-1}$ , via ATR measurements. Williams *et al.*<sup>69</sup> have also employed this equation to obtain  $n(\nu)$  from the absorbance spectrum of solid ammonia in the range 950-5300  $\text{cm}^{-1}$ .

At zero frequency, the static refractive index  $n_0$ , is given by:

$$n_0 = 1 + \frac{1}{2\pi^2} \int_0^{\infty} \frac{\alpha(\nu') d\nu'}{\nu'^2} \quad [1.64]$$

Thus the contribution  $\Delta n$  of an absorption band to  $n_0$  is:

$$\Delta n = \frac{1}{2\pi^2} \int_{\text{band}} \frac{\alpha(\nu') d\nu'}{\nu'^2} \quad [1.65]$$

From equation [1.17], it can be seen that:

$$\log_{10} \frac{I_0(\nu)}{I(\nu)} = \frac{\alpha(\nu)r}{2.303} \quad [1.66]$$

Whalley *et al.*<sup>70</sup> have determined the film thickness,  $r$ , of samples of Ice 1h at 100°K by equating the KK integral [1.65] to the known infrared contribution to the static refractive index, via equation [1.66]; they then calculated the optical

and dielectric constants over the spectral range 30-4000  $\text{cm}^{-1}$ .

However, the dispersion relations between  $n$  and  $k$ , and  $\epsilon'$  and  $\epsilon''$  have limited usefulness because of the difficulty of obtaining any one of these quantities over a sufficiently wide frequency range to accurately evaluate the integral.

On the other hand, a corresponding relation between the phase and the amplitude of reflectance has been frequently used because reflectance data are more readily available over a wide spectral range. Recall from Section 1.1b that the complex amplitude reflection coefficient,  $\hat{r}$ , expresses a linear relationship between the amplitudes of the incident and reflected light. It may be written as:

$$\hat{r} = |\hat{r}| \exp(i\theta) \quad [1.67]$$

where  $|\hat{r}|$  = modulus of reflection.  
 $\theta$  = phase of reflection.

For a lossless medium, that is one with zero damping,  $\theta = 180^\circ$ . The experimentally measured quantity is the power reflectance,  $R = \hat{r}\hat{r}^*$ , which from equation [1.67] is simply  $|\hat{r}|^2$ . Thus,

$$\begin{aligned} \hat{r} &= \sqrt{R} \exp(i\theta) \\ \text{or } \ln \hat{r} &= \frac{1}{2} \ln R + i\theta. \end{aligned} \quad [1.68]$$

The appropriate KK relation<sup>63</sup> is:

$$\theta(\nu) = \frac{-\nu}{\pi} P \int_0^\infty \frac{\ln R(\nu') d\nu'}{\nu'^2 - \nu^2} \quad [1.69]$$

This particular  $R$ - $\theta$  form of the KK relations was first used by Robinson and Price<sup>71</sup> in 1953 to obtain the optical constants of polytetrafluorethylene and a crystal of urea.

The relationship between  $R$  and  $\theta$  and  $n$  and  $k$  for normal incidence reflectance can be determined from equations [1.32] and [1.68] and Euler's equality  $[\exp(i\theta) = \cos \theta + i \sin \theta]$ , i.e. at any frequency,

$$r = \frac{1-n+ik}{1+n+ik} = \sqrt{R} (\cos \theta + i \sin \theta). \quad [1.70]$$

Separation of real and imaginary parts, gives:

$$n(\nu) = \frac{1-R(\nu)}{1+R(\nu)-2\sqrt{R(\nu)}\cos \theta(\nu)} \quad [1.71]$$

$$\text{and } k(\nu) = \frac{2\sqrt{R(\nu)} \sin \theta(\nu)}{1+R(\nu)-2\sqrt{R(\nu)} \cos \theta(\nu)} \quad [1.72]$$

The singularity in equation [1.69] can be removed by writing:

$$\theta(\nu) = \frac{\nu}{\pi} \int_0^{\infty} \frac{\ln R(\nu) - \ln R(\nu')}{\nu^2 - \nu'^2} d\nu' \quad [1.73]$$

$$\text{since } \int_0^{\infty} \frac{1}{\nu^2 - \nu'^2} d\nu' = 0.$$

An equivalent formulation of [1.69] is:

$$\theta(\nu) = \frac{-1}{2\pi} \int_0^{\infty} \ln R(\nu') \frac{d}{d\nu'} \ln \left| \frac{\nu' - \nu}{\nu' + \nu} \right| d\nu' \quad [1.74]$$

Integration by parts gives:

$$\theta(\nu) = \frac{-1}{2\pi} \left[ \ln R(\nu') \ln \left| \frac{\nu' - \nu}{\nu' + \nu} \right| \right]_0^{\infty} + \frac{1}{2\pi} \int_0^{\infty} \ln \left| \frac{\nu' - \nu}{\nu' + \nu} \right| \frac{d \ln R(\nu') d\nu'}{d\nu'}$$

where the first term is zero, i.e.:

$$\theta(\nu) = \frac{1}{2\pi} \int_0^{\infty} \ln \left| \frac{\nu' - \nu}{\nu' + \nu} \right| \frac{d \ln R(\nu') d\nu'}{d\nu'} \quad [1.75]$$

This equation is an exact relationship and does not depend upon any physical model for the absorption process.<sup>72</sup> In strict terms, it states that the phase angle  $\theta$  at a given frequency  $\nu$  depends upon the power reflectance  $R(\nu)$  at all frequencies from zero to infinity. However, in practice, it is only possible to obtain reflectance data over a limited spectral range. The fact that this experimental limitation does not pose a serious problem for many applications, may be understood from the nature of the integrand. It can be seen that a constant reflectivity term with zero derivative at all frequencies contributes nothing to  $\theta(\nu)$ , and thus corresponds to no absorption. A constant percentage error in the reflectance for all frequencies does not affect the phase, since such errors still yield the correct reflectance ratio. However, the magnitudes of the optical constants are affected since they depend upon the absolute reflectance. The logarithmic term  $\ln\{|\nu' - \nu|/|\nu' + \nu|\}$  in the integrand acts as a weighting function. It peaks sharply for frequen-

cies in the neighborhood of  $\nu$  and decreases rapidly for more remote frequencies.

This local character of the KK integral enables accurate results to be obtained if the whole of the dominant structure associated with an absorption system is scanned, and the reflectivity is approximately constant over a moderate frequency range at the extremities of this region.<sup>43</sup> These conditions are frequently met in infrared reflection studies. It is still not possible to exclude the contribution of the low and high frequency regions to the phase angle. This unmeasured reflectance data can often be reasonably approximated by replacing the low frequency end,  $0 \leq \nu \leq \nu_{\min}$ , with a constant reflectance  $R_{\min}$ , and the high frequency end,  $\nu_{\max} \leq \nu \leq \infty$ , with a constant reflectance  $R_{\max}$ .<sup>73</sup> The expression for the phase angle can then be expressed as the sum of three integrals:

$$\begin{aligned} \theta(\nu) &= \frac{\nu}{\pi} \int_0^{\nu_{\min}} \frac{\ln R(\nu) - \ln R(\nu') d\nu'}{\nu'^2 - \nu^2} \\ &+ \frac{\nu}{\pi} \int_{\nu_{\min}}^{\nu_{\max}} \frac{\ln R(\nu) - \ln R(\nu') d\nu'}{\nu'^2 - \nu^2} \\ &+ \frac{\nu}{\pi} \int_{\nu_{\max}}^{\infty} \frac{\ln R(\nu) - \ln R(\nu') d\nu'}{\nu'^2 - \nu^2} \\ &= \theta_1(\nu) + \theta_2(\nu) + \theta_3(\nu). \end{aligned} \quad [1.76]$$

The integrals,  $\theta_1(\nu)$  and  $\theta_3(\nu)$  may be solved analytically, to give:

$$\begin{aligned} \theta(\nu) = & \frac{1}{2\pi} \ln \left[ \frac{R_{\min}}{R(\nu)} \right] \ln \left[ \frac{\nu + \nu_{\min}}{\nu - \nu_{\min}} \right] \\ & + \frac{\nu}{\pi} \int_{\nu_{\min}}^{\nu_{\max}} \frac{\ln R(\nu) - \ln R(\nu') d\nu'}{\nu'^2 - \nu^2} \\ & + \frac{1}{2\pi} \ln \left[ \frac{R_{\max}}{R(\nu)} \right] \ln \left[ \frac{\nu_{\max} - \nu}{\nu_{\max} + \nu} \right]. \end{aligned} \quad [1.77]$$

For the case of absorption in the far-ultraviolet or far-infrared regions, this simplifying assumption cannot be made, since experimental difficulties often prevent measurements being extended to sufficiently high or low frequencies to cover the whole of the absorption band system.<sup>43</sup>

In these cases where the reflectivity is still varying at the limits of the measured reflection data, various extrapolation procedures have been used.<sup>72, 74-80</sup> It is generally found that the region  $(0, \nu_{\min})$  influences the computed phase very little, except in the immediate vicinity of  $\nu_{\min}$ , so that a constant reflectance can be assumed.<sup>81</sup> Alternatively, an improved set of low frequency optical constants may be obtained by generating a non-linear reflectance wing, based on an undamped harmonic oscillator model.<sup>72</sup> However, the magnitude of the derived optical constants is much more sensitive to the region  $(\nu_{\max}, \infty)$ , since most materials are

characterized by intense, continuous absorption from the far-ultraviolet to the X-ray region. Because of the local nature of the KK-integral, it can be seen that this effect is most important for optical studies in the ultraviolet and of minor significance for infrared measurements on transparent materials.

Two main types of approximations are found in the literature. One common type of approach is to assume some simple behavior of the reflectance in the unobserved frequency regions,<sup>72,74</sup> e.g. in the high frequency region,  $R(\nu) = R_{\max} (\nu/\nu_{\max})^{-s}$ , where  $s$  is an empirical parameter chosen to agree with known values of the reflectance.<sup>74</sup> Extrapolations based on physical intuition have also been used,<sup>80</sup> e.g. for infrared measurements on a transparent solid, it is necessary that the values of  $n$  and  $k$  when extrapolated to the visible region be equal to the visible refractive index and zero, respectively. Another approach has been to compute the error in the KK-derived phase angle by directly measuring the optical constants at various frequencies, and then assuming the error term is a smoothly varying function of frequency.<sup>76-79</sup> Leveque<sup>75</sup> found that when the experimental range was  $(\nu_{\min}, \nu_{\max})$ , all of these extrapolation procedures provided good optical constants only over the range  $(2\nu_{\min}, \nu_{\max}/2)$ . It should also be noted that none of these extrapolation methods are theoretically justified and they completely neglect all specific optical structure in the wing regions.

Another important characteristic of the KK integral [1.75], is the fact that small reflectance values make a large contribution to the computed phase. Thus, the accuracy of the derived optical constants is very dependent upon the reliability of the reflectance measurements in the low reflectance region. A detailed evaluation of the sensitivity of the KK method to various experimental errors is given in Chapter V.

Although the KK procedure has been applied extensively to the analysis of reflectance data at near-normal incidence, it is not restricted to this particular type of reflectance measurement. In 1965, Roessler<sup>43</sup> showed that the optical constants could be obtained from s-polarized reflectance spectra measured at an oblique angle. From equation [1.35],

$$\hat{r}_s = \frac{\cos \phi - (a+ib)}{\cos \phi + (a+ib)}$$

If  $\hat{r}_s$  is expressed in terms of its argument,  $\gamma$ , and power reflectance,  $R_s$ , then:

$$\frac{\cos \phi - (a+ib)}{\cos \phi + (a+ib)} = \sqrt{R_s} (\cos \gamma + i \sin \gamma).$$

Separation of real and imaginary parts gives:

$$a = \frac{(1-R_s)\cos \phi}{1+R_s-2\sqrt{R_s}\cos \gamma} \quad b = \frac{2\sqrt{R_s}\cos \phi \sin \gamma}{1+R_s-2\sqrt{R_s}\cos \gamma} \quad [1.78]$$

where  $a$  and  $b$  are related to the optical constants  $n$  and  $k$  by equations [1.38] and [1.39]. The angle of incidence  $\phi$  is

known and the phase angle is determined by the KK relation:

$$\theta(\nu) = \frac{\nu}{\pi} \int_0^{\infty} \frac{\ln R_S(\nu') - \ln R_S(\nu)}{\nu'^2 - \nu^2} d\nu' \quad [1.79]$$

In 1967, Berreman<sup>82</sup> extended this analysis to p-polarized radiation.

The KK dispersion method has also been applied to ratio reflectance spectra, measured at an oblique angle,<sup>83</sup> where the ratio reflectance  $R_{ps}$  is defined as  $R_{ps} = R_p/R_s$ . In this case, the phase difference,  $\Delta\theta_{ps} = \theta_p - \theta_s$ , is given by:

$$\Delta\theta_{ps}(\nu) = \frac{-\nu}{\pi} \int_0^{\infty} \frac{\ln R_{ps}(\nu') d\nu'}{\nu'^2 - \nu^2} \quad [1.80]$$

The expressions for  $n$  and  $k$  in terms of  $R_{ps}$ ,  $\phi$ , and  $\Delta\theta_{ps}$  are quite complicated.<sup>83</sup> Although the advantages of  $R_p/R_s$  measurements were cited in Section 1.2a, a serious disadvantage is the fact that the entire experimental apparatus must be calibrated for the relative efficiency with which it passes s- and p-polarized radiation. Also, the noise level of a  $R_p/R_s$  spectrum is much higher than for a usual relative reflectance spectrum recorded at near-normal incidence.

Hale *et al.*<sup>84</sup> have used a modified version of the relative reflectance method in which a reference material is chosen whose optical properties are similar to those of the sample under investigation. The phase shift is calculated via a KK-transformation procedure analogous to equation [1.80].

In this case,  $\Delta\theta_{sw} = \theta_s - \theta_w$ , where  $\theta_s$  is the phase angle for

the sample, and  $\theta_w$  is the phase angle for the reference material. In order to determine  $\theta_s$ , supplementary information on the optical constants of the reference material is required.

The KK method has also been extended to transmittance data.<sup>34,85</sup> The appropriate dispersion relation is:

$$\theta(\nu) = \frac{\nu}{\pi} \int_0^{\infty} \frac{\ln T(\nu) - \ln T(\nu') d\nu'}{\nu'^2 - \nu^2} + 2\pi\nu d \quad [1.81]$$

where  $\hat{t} = \sqrt{T} \exp(i\theta)$   
and  $d =$  sample thickness .

Thus,  $\theta(\nu)$  is a function of  $n$ ,  $k$ ,  $\nu$ ,  $\phi$ , and  $d$ . Because these transmittance measurements are necessarily performed on thin films, the Fresnel's equations for  $\hat{t}$ , [1.27] and [1.28], must be modified to include the effect of multiple reflections within the sample. The resultant expressions for  $n$  and  $k$  in terms of  $\theta$  and  $T$  are very complex.<sup>86</sup> Furthermore, the thin film of the sample is usually deposited on a thick transparent substrate, so the refractive index of the substrate material is also needed. It can be readily seen that this procedure involves considerably more experimental and computational time than the reflectance method.

King<sup>87</sup> has recently proposed an alternative formulation of the KK integral relations in which the associated real and imaginary optical quantities are written as conjugate Fourier series. Because of the present availability of fast Fourier transformation procedures (e.g. the Cooley-Tukey

algorithm), this method should significantly reduce the computation time.

Another variation of the KK procedure is the Subtractive Kramers-Kronig (SKK) method.<sup>88,89</sup> This method requires a knowledge of the reflectance and phase at a reference frequency, the so-called "anchor point", although this condition may be relaxed under certain circumstances. For this "anchor point" frequency  $\nu_0$ , the KK dispersion relation is:

$$\theta(\nu_0) = \frac{-\nu_0}{\pi} P \int_0^{\infty} \frac{\ln R(\nu_i) d\nu_i}{\nu_i^2 - \nu_0^2}.$$

Subtraction of this equation from [1.69] gives:

$$\frac{\theta(\nu_j)}{\nu_j} - \frac{\theta(\nu_0)}{\nu_0} = \frac{-1}{\pi} P \int_0^{\infty} \frac{\ln R(\nu_i) d\nu_i}{\nu_i^2 - \nu_j^2} + \frac{1}{\pi} P \int_0^{\infty} \frac{\ln R(\nu_i) d\nu_i}{\nu_i^2 - \nu_0^2}$$

or

$$\theta_{SKK}(\nu_j) = \frac{\nu_j}{\nu_0} \theta(\nu_0) + \frac{\nu_j}{\pi} \left[ P \int_0^{\infty} \frac{\ln R(\nu_i) d\nu_i}{\nu_i^2 - \nu_0^2} - P \int_0^{\infty} \frac{\ln R(\nu_i) d\nu_i}{\nu_i^2 - \nu_j^2} \right]. \quad [1.82]$$

The term in square brackets may also be written as a single integral, i.e.

$$(\nu_0^2 - \nu_j^2) P \int_0^{\infty} \frac{\ln R(\nu_i) d\nu_i}{(\nu_i^2 - \nu_j^2)(\nu_i^2 - \nu_0^2)}.$$

This integral converges much more rapidly than the normal KK expression [1.69], and is less sensitive to the unmeasured spectral regions. This latter property is apparent from the error term due to neglect of the wing regions:

$$\Delta\theta_{\text{SKK}}(v_j) = \frac{v_j}{\pi} \left[ \int_0^{v_{\min}} \frac{\ln R(v_i) dv_i}{v_i^2 - v_o^2} - \int_0^{v_{\min}} \frac{\ln R(v_i) dv_i}{v_i^2 - v_j^2} \right] + \frac{v_j}{\pi} \left[ \int_{v_{\max}}^{\infty} \frac{\ln R(v_i) dv_i}{v_i^2 - v_o^2} - \int_{v_{\max}}^{\infty} \frac{\ln R(v_i) dv_i}{v_i^2 - v_j^2} \right]. \quad [1.83]$$

Thus the contributions from the wing regions largely cancel, and this cancellation is more perfect the closer  $v_j$  is to  $v_o$ .

The first application of this SKK procedure was in 1970 by Bachrach and Brown.<sup>90</sup> They used the analogous n-k form of the SKK integral to obtain the optical constants of solid films of TlCl and TlBr in the visible region. However, it is Ahrenkiel<sup>88</sup> who is largely credited with the development of the SKK method. He derived the expressions for the  $\theta$ -form of the SKK integral, and discussed the attractive features of this modified KK analysis. Since then, this method has been applied to several optical studies conducted over a narrow frequency range.<sup>68,69,91</sup> A more general form of the SKK function, involving multiple anchor points, has also been used.<sup>68</sup>

The second category of indirect methods involves a classical dispersion analysis of reflectance and/or transmittance

data.<sup>92</sup> This method is based on the classical damped harmonic oscillator model, described in Section 1.1d.

From equations [1.50], [1.51], and [1.56], the real and imaginary dielectric constants may be expressed as a sum over N classical oscillators:

$$\epsilon'(\nu) = \epsilon_{\infty} + \sum_{j=1}^N \frac{S_j (\nu_j^2 - \nu^2)}{[(\nu_j^2 - \nu^2)^2 + \gamma_j^2 \nu^2]} \quad [1.84]$$

$$\epsilon''(\nu) = \sum_{j=1}^N \frac{S_j \gamma_j \nu}{[(\nu_j^2 - \nu^2)^2 + \gamma_j^2 \nu^2]} \quad [1.85]$$

where  $S_j$ ,  $\nu_j$ , and  $\gamma_j$  are the strength, frequency, and line-width of the  $j^{\text{th}}$  oscillator. These constants are called the dispersion parameters.

The actual procedure of fitting a reflectance spectrum consists of an initial guess of the dispersion parameters and  $\epsilon_{\infty}$ , subsequent calculation of the normal incidence reflectance from:

$$R_{\text{calc}}(\nu) = \left| \frac{[\hat{\epsilon}(\nu)]^{\frac{1}{2}} - 1}{[\hat{\epsilon}(\nu)]^{\frac{1}{2}} + 1} \right|^2 \quad [1.86]$$

and adjustment of the parameters until the difference between the calculated and measured reflectance is less than some prescribed amount, over the frequency region of interest.

The main motivation for this type of analysis is that, in the case of resonance absorption, the oscillator para-

meters have a physical significance. However, this is not true for a spectrum dominated by electronic transitions.<sup>92</sup> It should be noted that this is an approximate procedure, since it depends upon a particular model for the absorption process. The fact that it worked extremely well for some compounds<sup>93</sup> indicates that it is a good model for these particular situations. The KK method, on the other hand, is exact and does not presuppose any model or band shape. Another shortcoming of the classical dispersion analysis is that the fitting procedure may be very long and tedious, although recent applications employ automatic curve-fitting routines.<sup>94</sup> Also, more than one set of dielectric constants may fit equally well the same portion of a reflectance spectrum, so caution must be exercised.<sup>92</sup>

Recent measurements of optical constants show that a combination of a Kramers-Kronig and classical dispersion analysis may provide complementary information.<sup>11,94,95</sup> A comparison of the results obtained by the two procedures enables the error due to the limited range of experimental data to be estimated.

### 1.3 Properties of $\text{Ba}(\text{ClO}_3)_2 \cdot \text{H}_2\text{O}$

Crystalline compounds suitable for infrared optical study must be available as large, single crystals with well-defined faces, capable of being polished to infrared optical quality. Also, the crystal structure must be well known. A further requirement, imposed by the constant reflectance

extrapolation of the Kramers-Kronig procedure, is that the crystal be transparent in the visible region.

The compound, barium chlorate monohydrate  $\text{Ba}(\text{ClO}_3)_2 \cdot \text{H}_2\text{O}$ , satisfies all these criteria. It is surprising that no detailed infrared reflectance study has been performed on this crystal, since the analogous compounds,  $\text{NaClO}_3$ <sup>96-98</sup> and  $\text{KClO}_3$ ,<sup>99</sup> have been well studied by this method. For all these reasons, and because of the need to supplement earlier studies of this compound in this laboratory,  $\text{Ba}(\text{ClO}_3)_2 \cdot \text{H}_2\text{O}$  was considered an excellent candidate for study. It readily crystallizes from a saturated aqueous solution to give fairly large, colorless crystals of prismatic form.<sup>100</sup> The solubility and density characteristics of  $\text{Ba}(\text{ClO}_3)_2 \cdot \text{H}_2\text{O}$  at various temperatures in aqueous solution<sup>101,102</sup> are given in Table 1.2. Morphological studies<sup>103</sup> have shown that the prismatic axis is the c-crystal axis, that the m planes  $\{110\}$  are the most well-developed, and that cleavage is perfect along  $\{011\}$  and distinct along  $\{100\}$  directions.

The first detailed X-ray study of  $\text{Ba}(\text{ClO}_3)_2 \cdot \text{H}_2\text{O}$  was carried out by Kartha<sup>104</sup> in 1952. From single-crystal rotation and Weissenberg photographs recorded at room temperature, he determined the crystal to be monoclinic, space group  $\text{I}2/\text{c}(\text{C}_{2h}^6)$ , b-axis unique, with 4 molecules per body-centered unit cell, and cell dimensions of:  $a = 8.86 \pm 0.02 \text{ \AA}$ ,  $b = 7.80 \pm 0.02 \text{ \AA}$ ,  $c = 9.35 \pm 0.02 \text{ \AA}$ , and  $\beta = 93^\circ 26'$ . A later single-crystal neutron-diffraction study by Chidambaram

Table 1.2 Solubility and Density Data for  $\text{Ba}(\text{ClO}_3)_2 \cdot \text{H}_2\text{O}$   
at Atmospheric Pressure<sup>101</sup>

$t(^{\circ}\text{C})$	Sp. gr. of Sat. Sol.	Gms. $\text{Ba}(\text{ClO}_3)_2 \cdot \text{H}_2\text{O}$ per 100 gms. of Sat. Sol.
0	1.195	16.90
10	1.234	21.23
20	1.274 <sup>†</sup>	25.26
25	1.263	27.53
30	1.315 <sup>†</sup>	29.43
40	1.355.	33.16
60	1.433	40.05
80	1.508	45.90
100	1.580	51.2

<sup>†</sup>Values obtained from Reference 102.

*et al.*<sup>105</sup> in 1968 confirmed these basic findings, but modified the set of room temperature unit-cell parameters to:  $a = 8.916 \pm 0.010 \text{ \AA}$ ,  $b = 7.832 \pm 0.008 \text{ \AA}$ ,  $c = 9.425 \pm 0.010 \text{ \AA}$ , and  $\beta = 93^\circ 39' \pm 7'$ . These crystal structure results are summarized in Table 1.3.

The projection of the structure of  $\text{Ba}(\text{ClO}_3)_2 \cdot \text{H}_2\text{O}$  on the (010) plane is illustrated in Figure 1.7. The chlorate ions are situated on sites of  $C_1$  symmetry and possess a distorted low pyramidal configuration with an oxygen triangle of average side  $2.377 \text{ \AA}$  and chlorine-oxygen distance of  $1.485 \text{ \AA}$ . The chlorine atom lies at a distance of  $0.57 \text{ \AA}$  from the oxygen plane. These values are in good agreement with those found in  $\text{KClO}_3$  and  $\text{NaClO}_3$ <sup>105</sup> (see Table 1.4).

The  $\text{Ba}^{2+}$  ions and water molecules are both situated on sites of  $C_2$  symmetry. From Figure 1.7, it can be seen that there is only one orientation of the water molecules in  $\text{Ba}(\text{ClO}_3)_2 \cdot \text{H}_2\text{O}$  crystal, in which the proton-proton vectors of the various water molecules all lie parallel to one another. Thus, the water dipole moments are aligned along the two-fold axis; a result which was earlier predicted by pmr findings.<sup>106,107</sup> The crystal structure also shows that the water molecule has an O-H bond distance of  $0.958 \pm 0.011 \text{ \AA}$ , and an H-O-H angle of  $110.7^\circ \pm 1.4^\circ$ . Since these values are very similar to those found in a free water molecule ( $0.9572 \pm 0.0003 \text{ \AA}$  and  $104.52 \pm 0.05^\circ$ ),<sup>108</sup> this suggests that hydrogen bonding is very weak in this crystal hydrate.

Table 1.3 Crystal Structure Data for  $\text{Ba}(\text{ClO}_3)_2 \cdot \text{H}_2\text{O}$ <sup>103-105</sup>

Space Group:  $I2/c$  ( $C_{2h}^6$ ) - monoclinic ( $Z = 4$ )

Habit: prismatic [001]

Cleavage: {011} perfect, {100} distinct

Cell dimensions:  $a = 8.916 \pm 0.010 \text{ \AA}$ ,  $b = 7.832 \pm 0.008 \text{ \AA}$ ,  
 $c = 9.425 \pm 0.010 \text{ \AA}$ ,  $\beta = 93^\circ 39' \pm 7'$

Table 1.4 Average Dimensions of the  $\text{ClO}_3^-$  Ion in Different Chlorates<sup>105</sup>

	$\langle \text{Cl-O} \rangle_{\text{av}}$	$\langle \text{O-O} \rangle_{\text{av}}$	Angle $\langle \text{O-Cl-O} \rangle_{\text{av}}$	Distance of Cl from oxygen plane
$\text{Ba}(\text{ClO}_3)_2 \cdot \text{H}_2\text{O}$	$1.485 \text{ \AA}$	$2.377 \text{ \AA}$	$106.3^\circ$	$0.57 \text{ \AA}$
$\text{KClO}_3$	$1.475 \text{ \AA}$	$2.38 \text{ \AA}$	$107.5^\circ$ <sup>†</sup>	$0.54 \text{ \AA}$
$\text{NaClO}_3$	$1.455 \text{ \AA}$	$2.38 \text{ \AA}$	$109.7^\circ$	$0.48 \text{ \AA}$

<sup>†</sup>These values were incorrectly determined in reference 105.

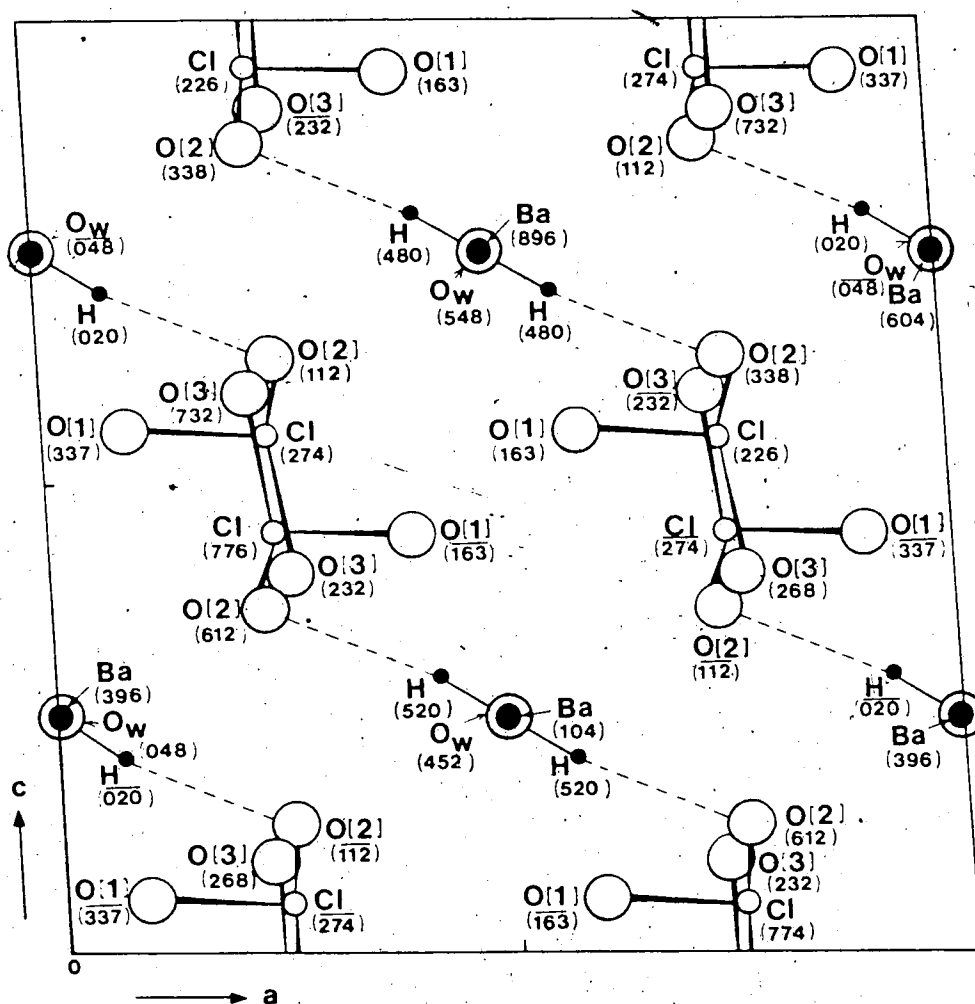


Figure 1.7 Projection of the structure of  $\text{Ba}(\text{ClO}_3)_2 \cdot \text{H}_2\text{O}$  on the (010) plane. The fractional y coordinate ( $\times 10^3$ ) of the atoms are given in parentheses.

Redrawn from Reference 105.

Because there is only one kind of water molecule in the crystal and it is located at a site of relatively simple symmetry,  $\text{Ba}(\text{ClO}_3)_2 \cdot \text{H}_2\text{O}$  has been the subject of extensive proton magnetic resonance,<sup>106,107,109</sup> deuteron<sup>110-112</sup> and oxygen-17<sup>113</sup> nuclear quadrupole resonance, and inelastic neutron scattering<sup>114-116</sup> experiments. These studies were primarily concerned with the dynamics of water motion in the crystal. Several  $^{35}\text{Cl}$  nuclear quadrupole resonance studies<sup>117-121</sup> have also been performed on  $\text{Ba}(\text{ClO}_3)_2 \cdot \text{H}_2\text{O}$  in order to probe the reorientational motion of the chlorate group.

By contrast, very little optical data is available on  $\text{Ba}(\text{ClO}_3)_2 \cdot \text{H}_2\text{O}$ . The crystal is monoclinic and so belongs to the biaxial optical system with only the b-crystal axis coincident with one of the optical indicatrix axes. The remaining two indicatrix axes lie in the ac plane, and their positions can vary with frequency. Only at the sodium D-line, has the relationship between the crystallographic and indicatrix axes been well-defined. At this frequency, the crystal exhibits a strong birefringence of positive optical sign.<sup>103</sup> The optic axial plane<sup>103</sup> is (010), and therefore,  $b \perp \beta$ . Figure 1.4 illustrates the relevant geometry of the ac crystal plane: the acute bisectrix,<sup>103</sup>  $\gamma$ , makes an angle of  $23.75^\circ$  with the c-axis in the acute a:c angle  $86^\circ 21'$ ; and the angle between the two optic axes,<sup>104</sup>  $2V_D$ , is  $55^\circ 30'$ . The principal refractive indices are<sup>103</sup>:  $n_\alpha^D = 1.5622$ ,  $n_\beta^D = 1.5777$ , and  $n_\gamma^D = 1.635$ .

The low frequency dielectric properties of  $\text{Ba}(\text{ClO}_3)_2 \cdot \text{H}_2\text{O}$  single crystal were studied by Khanna and Sobhanadri<sup>122</sup> in 1973. They measured the real dielectric constant,  $\epsilon'$ , and the loss tangent,  $\tan \delta$  (where  $\epsilon'' = \epsilon' \tan \delta$ ) along the three different crystalline axes in the frequency region  $10^2$  to  $10^5$  Hz, and for temperatures ranging from 32 to 325°C. Very little anisotropy was observed in the limiting values of the real dielectric constant at 100 kHz, that is, at room temperature,  $\epsilon' = 6.88, 6.96$  and  $6.86$  along the x-, b-, and c-axis, respectively, where the x-direction is perpendicular to the bc plane. They explained the higher value of  $\epsilon'_b$  as due to the alignment of water dipoles along the b-crystal axis. However, these authors did not investigate the orientation of the optic axes with respect to the crystallographic axes. Thus, no conclusions can be drawn from the relative magnitudes of their measured real dielectric constants. Better evidence for their assertion is found in the different frequency dependence of  $\epsilon''_b$  compared with  $\epsilon''_x$  and  $\epsilon''_c$ . Only in the former case, was a loss tangent peak observed at 4 kHz, which disappeared at temperatures above 130°C. The temperature variation of  $\epsilon'$  revealed a sharp decrease starting around 105°C (95°C for the b-direction), and continuing until 125°C, where it began to increase again. This behavior was attributed to loss of the water of crystallization. A compilation of the currently available optical data on  $\text{Ba}(\text{ClO}_3)_2 \cdot \text{H}_2\text{O}$  is given in Table 1.5.

The structural changes accompanying the dehydration pro-

Table 1.5 Optical Data for  $\text{Ba}(\text{ClO}_3)_2 \cdot \text{H}_2\text{O}$ 


---



---

Monoclinic, class 2/m

at  $\text{Na}_D$ , strong positive birefringence  
 optic axial plane (010)

$b = \beta$

$c:\gamma = 23.75^\circ$  in the acute angle  $86^\circ 21'$

$a:\alpha = 27.4^\circ$

$2V_D = 55.5^\circ$

$n_\alpha^D = 1.5622$ ,  $n_\beta^D = 1.5777$ ,  $n_\gamma^D = 1.635$

at 100 kHz and room temperature<sup>†</sup>:

$\epsilon'(b) = 6.96$

$\epsilon'(c) = 6.86$

$\epsilon'(x) = 6.88$

---

<sup>†</sup>Reference 122. The x-direction is normal to the bc plane. These authors did not investigate the relationship between the indicatrix and crystallographic axes in the ac plane.

cesses in  $\text{Ba}(\text{ClO}_3)_2 \cdot \text{H}_2\text{O}$  were investigated by Vargas *et al.*,<sup>120</sup> who measured the  $^{35}\text{Cl}$  nuclear quadrupole resonance intensity as a function of the loss of water. They observed a steep decline in the intensity of the NQR signal up to approximately 3 mole % loss of water; further water loss resulted in a much less pronounced signal reduction. These findings indicated that the dehydration occurred in two stages. The proposed mechanism was: (1) water vacancies are created at different lattice sites, and after a critical size of cluster is formed, (2) these vacancies act as nuclei around which continuous regions of the anhydrous phase begin to grow. This mechanism was also studied by thermogravimetry, X-ray diffraction, and Raman spectroscopy.<sup>120,123</sup> In the thermogravimetric analysis,<sup>120</sup> the water loss was monitored as the  $\text{Ba}(\text{ClO}_3)_2 \cdot \text{H}_2\text{O}$  samples were heated in a vacuum oven at a fixed temperature and for a fixed duration. They found that at room temperature, the dehydration proceeded slowly, yielding a maximum loss of 0.3 mole % water; at 75°C, the dehydration was suddenly accelerated; and at 135°C, the dehydration was complete. The activation energy for this process was estimated from the isothermal decay times of the  $\nu_1$  line of  $\text{H}_2\text{O}$  in the Raman spectra of powdered  $\text{Ba}(\text{ClO}_3)_2 \cdot \text{H}_2\text{O}$  samples, recorded at various temperatures.<sup>123</sup> For an assumed first order reaction, they obtained an activation energy of 1.41 eV/bond and a frequency factor of  $5.2 \times 10^{14} \text{ sec}^{-1}$ . Unfortunately, they gave no details of this calculation, such as the number of data points, the

temperature range of validity, the estimated uncertainty in these values, or any representative data.

A subsequent kinetic study of thermal dehydration in  $\text{Ba}(\text{ClO}_3)_2 \cdot \text{H}_2\text{O}$  by Guarini *et al.*<sup>124</sup> showed that a single kinetic law could not fully explain the process. Their differential scanning calorimetry experiments also indicated that different kinetic laws applied to the single crystal than to the polycrystalline material.

In order to elaborate the structural differences between  $\text{Ba}(\text{ClO}_3)_2 \cdot \text{H}_2\text{O}$  and  $\text{Ba}(\text{ClO}_3)_2$ , Vargas *et al.*<sup>125</sup> recorded the room temperature X-ray powder photographs of the two compounds. They noted significant differences in the powder patterns, thus confirming their contention that a structural phase transition had occurred. This finding contradicted the results of earlier workers<sup>117,119</sup> who had observed little difference in the powder patterns of the hydrated and anhydrous species. From the measured spacing of the powder lines, Vargas *et al.*<sup>125</sup> deduced that  $\text{Ba}(\text{ClO}_3)_2$  was orthorhombic, space group  $\text{Fd}2\text{d}(\text{C}_{2v}^{19})$ , with lattice parameters of:  $A = 11.74 \pm 0.01 \text{ \AA}$ ,  $B = 7.70 \pm 0.01 \text{ \AA}$ , and  $C = 13.33 \pm 0.01 \text{ \AA}$ . This structure can be considered to arise from a doubling of the slightly deformed unit cell of  $\text{Ba}(\text{ClO}_3)_2 \cdot \text{H}_2\text{O}$ , with the common axis  $\underline{B} = \underline{b}$  and  $\underline{A} = \underline{a} + \underline{c}$ ,  $\underline{C} = \underline{a} - \underline{c}$ .

The infrared absorption and Raman spectra of  $\text{Ba}(\text{ClO}_3)_2 \cdot \text{H}_2\text{O}$  and  $\text{Ba}(\text{ClO}_3)_2$  have been studied by several research groups. Because  $\text{Ba}(\text{ClO}_3)_2 \cdot \text{H}_2\text{O}$  is a centrosymmetric crystal, the rule of mutual exclusion applies, i.e. Raman active

bands are infrared-inactive, and vice versa. Thus a complete vibrational analysis requires both infrared and Raman measurements in order to assign the *ungerade* and *gerade* modes, respectively. In the following account, the relevant spectral investigations carried out after 1952 are briefly surveyed. Unless otherwise specified, the spectra were recorded at room temperature.

Miller *et al.*<sup>126,127</sup> obtained infrared spectra of nujol mulls of  $\text{Ba}(\text{ClO}_3)_2 \cdot \text{H}_2\text{O}$  between 300 and  $5000 \text{ cm}^{-1}$ . This work comprised part of a systematic investigation of the infrared spectra of inorganic substances, and no attempt at vibrational assignments was made. In 1956, Rocchiccioli,<sup>128</sup> measured the spectrum of anhydrous  $\text{Ba}(\text{ClO}_3)_2$  in nujol between 270 and  $1900 \text{ cm}^{-1}$ . However, no spectra are presented in the paper and only the frequencies of the absorption maxima are reported. In 1972, Fukushima *et al.*<sup>129</sup> measured the infrared spectra of polycrystalline samples of  $\text{Ba}(\text{ClO}_3)_2 \cdot \text{H}_2\text{O}$  and  $\text{Ba}(\text{ClO}_3)_2 \cdot \text{D}_2\text{O}$  over the region  $30\text{--}4000 \text{ cm}^{-1}$ . The primary objective of their study was to obtain qualitative spectral data, in order to correlate the nature and strength of hydrogen bonding in various crystal hydrates with the general appearance and frequencies of the rotational vibrations of the water molecules. The water rotational and translational modes were distinguished on the basis of their isotope ratios ( $\nu_{\text{H}}/\nu_{\text{D}}$ ), but no further assignments were made.

In 1973, Bertie *et al.*<sup>130</sup> performed an extensive study

of the infrared and Raman spectra of polycrystalline and single-crystal  $\text{Ba}(\text{ClO}_3)_2 \cdot \text{H}_2\text{O}$  and  $\text{Ba}(\text{ClO}_3)_2 \cdot \text{D}_2\text{O}$  at 90°K and 298°K. The Raman and infrared spectra were recorded over the regions  $40\text{--}4000\text{ cm}^{-1}$  and  $90\text{--}4000\text{ cm}^{-1}$ , respectively. It was found that the Raman bands were generally well-resolved and exhibited clear polarization behavior, so vibrational assignments of the *gerade* modes were made with a great deal of confidence. However, the infrared study was complicated by broad, strong absorption, particularly in the chlorate stretching region ( $900\text{--}1000\text{ cm}^{-1}$ ), which made it difficult to determine the true number of active vibrations and their polarization dependence. It was thought that reflection effects and combination and overtone bands were largely responsible for this spectral distortion. Because the thinnest crystal they were able to prepare was about  $20\text{ }\mu\text{m}$  thick, they were unable to clearly resolve the fundamental absorption.

In 1976, Brink,<sup>131</sup> apparently unaware of the detailed infrared study by Bertie *et al.*,<sup>130</sup> essentially repeated some of their earlier experiments by measuring the spectra of polycrystalline samples of  $\text{Ba}(\text{ClO}_3)_2 \cdot \text{H}_2\text{O}$  and  $\text{Ba}(\text{ClO}_3)_2 \cdot \text{D}_2\text{O}$  at 128°K and 298°K. Brink's main interest was in the assignment of the water vibrational and librational modes. Although his observed frequencies are in good agreement with the values reported by Bertie *et al.*,<sup>130</sup> his assignments of the librational modes are different.

The previously mentioned Raman investigations by

Vargas *et al.*,<sup>120,123</sup> conducted in the late 1970's, were only used as a physical means of monitoring the structural changes in  $\text{Ba}(\text{ClO}_3)_2 \cdot \text{H}_2\text{O}$  during the dehydration process. They also recorded room temperature Raman spectra of  $\text{Ba}(\text{ClO}_3)_2 \cdot \text{H}_2\text{O}$ ,  $\text{Ba}(\text{ClO}_3)_2$ , and  $\text{Ba}(\text{ClO}_3)_2 \cdot x\text{H}_2\text{O}$ , where  $0 < x < 1$ . Their spectrum of  $\text{Ba}(\text{ClO}_3)_2 \cdot \text{H}_2\text{O}$  is consistent with the corresponding spectrum of Bertie *et al.*<sup>130</sup> reported at 298°K. Their spectra of partially dehydrated  $\text{Ba}(\text{ClO}_3)_2 \cdot x\text{H}_2\text{O}$  could be interpreted as a linear superposition of the spectra due to the fully hydrated and anhydrous species, indicating that the two phases coexist. They also found that, when the sample of  $\text{Ba}(\text{ClO}_3)_2 \cdot \text{H}_2\text{O}$  was heated above 85°C, new chlorate stretching and deformation modes appeared shifted to higher and lower frequencies, respectively. In the lattice mode region, the various band intensities decreased steadily with increasing temperature; at ~90°C, the modes were almost completely extinguished; and at higher temperatures, new bands appeared shifted to lower frequency and with less fine structure than those of the room-temperature single-crystal sample.

In 1978, Lindgren *et al.*<sup>132</sup> remeasured the infrared spectra of polycrystalline samples of  $\text{Ba}(\text{ClO}_3)_2 \cdot \text{H}_2\text{O}$  and  $\text{Ba}(\text{ClO}_3)_2 \cdot \text{D}_2\text{O}$  at 90°K, over the region  $2000\text{--}4000\text{ cm}^{-1}$ . This work constituted part of an investigation of several solid hydrates, whose objective was to correlate the isotopic ratios  $\nu_{\text{OH}}/\nu_{\text{OD}}$  of the water stretching frequencies with  $\nu_{\text{OH}}$ . This data was also included in their correlation curves be-

tween deuteron quadrupole coupling constants and  $\nu_{OH}$ .<sup>133</sup> Later that year, Lindgren and Eriksson<sup>134</sup> published a more extensive study on  $Ba(ClO_3)_2 \cdot H_2O$ . They extended the infrared measurements on powdered samples at 100°K and 298°K to 40  $cm^{-1}$ . Of particular note, they observed a weak band at 457  $cm^{-1}$ , which had not been previously detected. Their spectra<sup>132,134</sup> and vibrational assignments<sup>134</sup> are in good agreement with those of Bertie *et al.*<sup>130</sup> However, in the region 105-110  $cm^{-1}$ , Bertie *et al.* observed three strong bands, whereas Lindgren and Eriksson reported only one strong feature at 109  $cm^{-1}$ . This apparent discrepancy may be the result of resolution effects, since the studies were performed at resolutions of 1-2  $cm^{-1}$  and 3  $cm^{-1}$ , respectively. The only other significant discrepancy is found in their different assignments of the water twisting mode. Lindgren and Eriksson assigned the weak band at 457  $cm^{-1}$  to this vibration, while Bertie *et al.*, based on earlier deuteron magnetic resonance results,<sup>110</sup> considered the water twisting and wagging modes to be degenerate at 395  $cm^{-1}$ .

It should be noted that a great deal of controversy has been associated with the identification of the rocking, wagging, and twisting vibrations of the water molecule in  $Ba(ClO_3)_2 \cdot H_2O$ . Figure 1.8 illustrates the form of these vibrations, and Table 1.6 compares the various assignments that have been made based on dmr,<sup>110</sup> inelastic neutron scattering,<sup>115</sup> and infrared<sup>130,131,134</sup> studies. Consideration of Figure 1.8 allows some qualitative predictions to be made

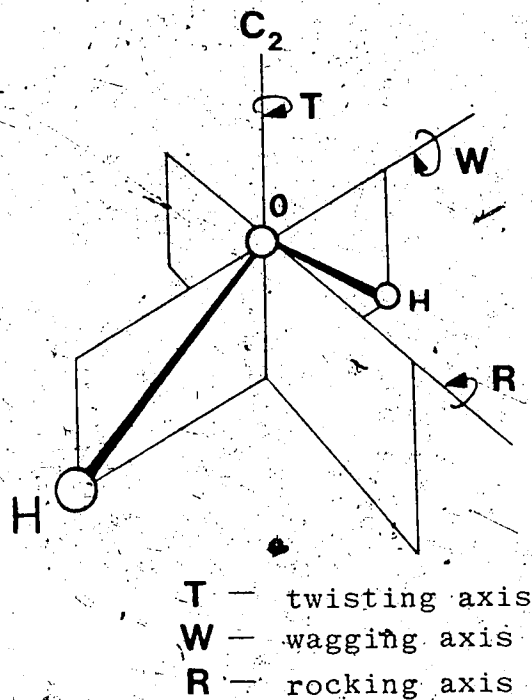


Figure 1.8 Illustration of the librational modes of a water molecule.

Table 1.6 Frequencies Assigned to the Librational Modes of the Water Molecule in  $\text{Ba}(\text{ClO}_3)_2 \cdot \text{H}_2\text{O}$

$\nu/\text{cm}^{-1}$	Ref. 110	Ref. 115	Ref. 130	Ref. 131	Ref. 134
$\nu_{\text{rock}}$	450	477±6	454	456	467
$\nu_{\text{twist}}$	335	395±5 457±5	395	—	457
$\nu_{\text{wag}}$	335		395	395	396

about the expected behavior of these modes. It can be seen that during the twisting motion, the directions of the induced and equilibrium dipole moment are the same. Thus, it might be expected that absorption by this mode would be relatively weak. In fact, for a water molecule located on a site of  $C_{2v}$  symmetry within the unit cell, the twisting mode should be infrared-inactive.<sup>131</sup> In the rocking mode, the hydrogens move in the plane of the water molecule, whereas in the twisting and wagging modes, the hydrogens move out of this HOH plane. A neutron inelastic scattering experiment should be able to distinguish between these two cases by using different directions of the neutron wave vector transfer relative to the proton-proton vector. Thaper *et al.*<sup>115</sup> performed this experiment on a single crystal of  $Ba(ClO_3)_2 \cdot H_2O$  and found that the rocking mode was too high frequency of the other two modes. The water librational assignments can be further assisted by polarized spectral studies on the single crystal. Only in the twisting motion, is the  $C_2$  symmetry preserved. The rocking and wagging modes belong to the same symmetry species under the  $C_{2h}$  unit-cell group and, if they are close in frequency, they can give rise to mixed intramolecular modes. Bertie *et al.*<sup>130</sup> have studied the polarization dependence of these librational modes in single crystal  $Ba(ClO_3)_2 \cdot H_2O$ , but their results did not permit a clear distinction to be made.

Normal coordinate analyses<sup>130,135</sup> have also been performed on the water molecule in  $Ba(ClO_3)_2 \cdot H_2O$ . Bertie

*et al.*<sup>130</sup> calculated the effective intramolecular force field in two ways: directly from the observed stretching and bending frequencies, and after correction to their harmonic values. In this latter calculation, the gas phase anharmonicity constants were used for the stretching modes, and the anharmonicity constants for the bending modes were estimated from the fundamental and overtone frequencies, according to:  $G(v) = (v + \frac{1}{2})\omega_e + (v + \frac{1}{2})^2\omega_e x_e$  where  $\omega_e$  is the harmonic frequency at equilibrium and  $\omega_e x_e$  is the anharmonicity constant. This second force field gave excellent agreement, with an average error of 0.046%. Eriksson *et al.*<sup>135</sup> repeated these calculations but included their observed librational and translational water frequencies in the analysis. These additional frequencies were uncorrected for anharmonicity. Whereas the deformation frequencies were corrected in the same manner employed by Bertie *et al.*,<sup>130</sup> the anharmonicity constants for the stretching vibrations were estimated from the observed OD and OH frequencies of isotopically-dilute HDO molecules in solid  $\text{Ba}(\text{ClO}_3)_2 \cdot \text{H}_2\text{O}$  at 90°K, according to:

$$\nu_{\text{OH}} = \omega_e - 2\omega_e x_e$$

$$\nu_{\text{OD}} = p \omega_e - 2p^2 \omega_e x_e$$

$$\text{where } p = \frac{\omega_e(\text{OD})}{\omega_e(\text{OH})}$$

This procedure gave calculated harmonic frequencies differing by 11-14  $\text{cm}^{-1}$  from the corresponding values of Bertie *et al.*<sup>130</sup>

Using the results of their normal coordinate analysis, Eriksson *et al.*<sup>136</sup> corrected the stationary-state neutron diffraction values<sup>105</sup> of the O-H bond length ( $0.926 \pm 0.010 \text{ \AA}$ ) and H-O-H angle ( $110.7 \pm 1.4^\circ$ ) of the water molecule in  $\text{Ba}(\text{ClO}_3)_2 \cdot \text{H}_2\text{O}$  for the effects of rigid-body librational and anharmonic stretching motions. They computed correction factors of  $0.034 \text{ \AA}$  and  $-2.2^\circ$ , respectively, giving equilibrium values of  $0.960 \text{ \AA}$  and  $108.5^\circ$ . This corrected value of the O-H distance is in good agreement with the neutron diffraction value of  $0.958 \pm 0.011 \text{ \AA}$ , obtained by Chidambaram *et al.*<sup>105</sup> after correction for thermal motion.

#### 1.4 Infrared Optical Constant Studies of Solids

In this section, some of the significant developments in the study of infrared optical properties of solids, in particular, molecular crystals, will be described. This is not intended as a comprehensive review, but as a guide to the type of compounds that have been studied, the information derived from these studies, and how the research has shifted from a qualitative to a more quantitative and definitive approach.

The reasons for obtaining optical constants are highly diverse. In 1953, Robinson and Price<sup>71</sup> outlined the Kramers-Kronig (KK) procedure for the conversion of reflection data to optical constants. The elimination of the tedious graphical analysis generated a renewed interest in such measurements. However, some of the earlier studies were apparently motivated by the novelty of the KK method, rather than a fun-

damental desire for the optical properties. For example, in 1956, Abbott and Elliott<sup>137</sup> measured the infrared absorbance spectrum and dichroism of crystalline acetanilide. Because of the very strong absorbance in the C=O and aromatic C-H stretching regions, they corrected their observed spectra for reflection effects. Acetanilide is an orthorhombic crystal, so the indicatrix axes, which define the directions of the transition moments, are coincident with the crystallographic axes. Thus, Abbott and Elliott measured both the reflectance and the absorbance with the electric vector of the incident light parallel to each of the a-, b- and c- crystal axes. These authors reported that the optical constants were determined in two different ways: from a KK-analysis and directly from the measured reflectance at an air-crystal and a NaCl-crystal interface. They stated that both procedures were in good agreement, but they did not present any data to substantiate this claim.

Early candidates for optical study were compounds which were readily available as large single crystals and whose crystal structure and morphology were well-characterized. An example is gypsum,  $\text{CaSO}_4 \cdot 2\text{H}_2\text{O}$  which occurs as exceptionally large single crystals in nature. It is a monoclinic crystal, belonging to space group  $C_{2h}^6$  ( $C2/c$ ), with the b-axis unique. Thus, as in the case of  $\text{Ba}(\text{ClO}_3)_2 \cdot \text{H}_2\text{O}$ , only the b-crystal axis coincides with one of the indicatrix axes for all frequencies. In 1956, Haas and Sutherland<sup>138</sup> measured the near-normal incidence reflectance of the (010), ( $\bar{1}01$ ) and ( $\bar{2}01$ )

faces of single crystals of  $\text{CaSO}_4 \cdot 2\text{H}_2\text{O}$ . By varying the polarizer angle, they determined the directions of maximum dichroism for the various bands. As expected for the (101) and (201) faces, the  $A_u$  bands exhibited maximum dichroism when the electric vector was parallel to the b-axis. These authors then derived the corresponding optical constants from a KK-analysis. Following the procedure of gas-phase spectroscopists, they determined the band intensities from  $\int k \nu d\nu$ , whereas the relevant quantity in condensed-phase studies is  $\int \epsilon'' \nu d\nu$  (see Section 1.1d). For comparative purposes, they also recorded polarized transmission spectra of the (010) face, using a  $15 \mu\text{m}$  thick sample. These spectra clearly demonstrate the superiority of the reflection method in defining the position and contour of very intense absorption bands.

Another class of compounds whose optical properties have been extensively studied are the alkali halides<sup>27,139-144</sup> because they exhibit a selective reflection of radiation in the infrared region. This is referred to as the reststrahlen band, and is associated with the fundamental optic mode of vibration in which the lattice of alkali ions moves  $180^\circ$  out-of-phase with the lattice of halide ions. A typical reststrahlen spectrum is shown in Figure 1.9. It is interesting to note that for an ideally ionic crystal, with zero damping, the reflectivity would reach 100%; the band of perfect reflection extending from the transverse optic to longitudinal optic frequency.<sup>145</sup> The influence of damping on the

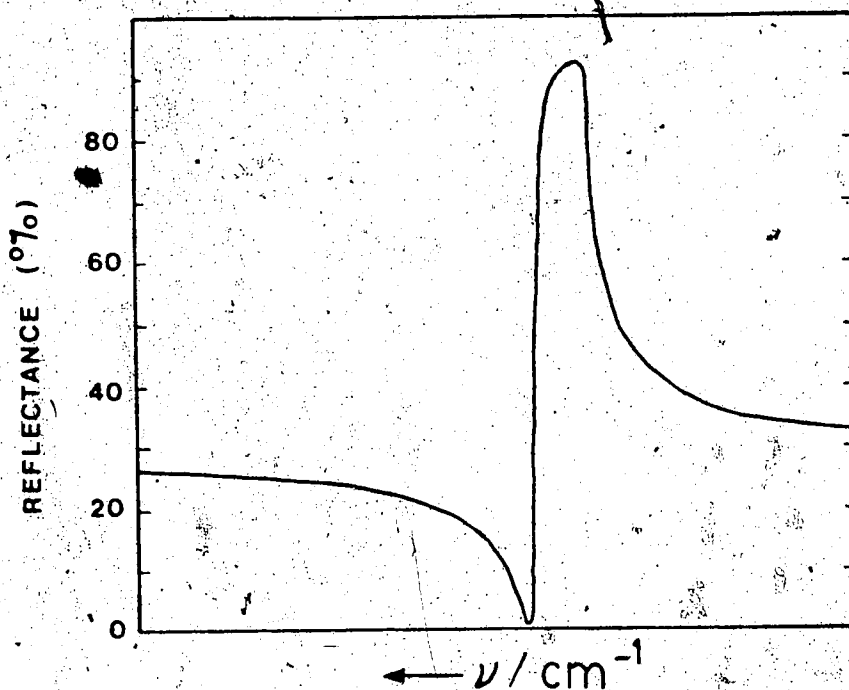


Figure 1.9 A typical reststrahlen spectrum.

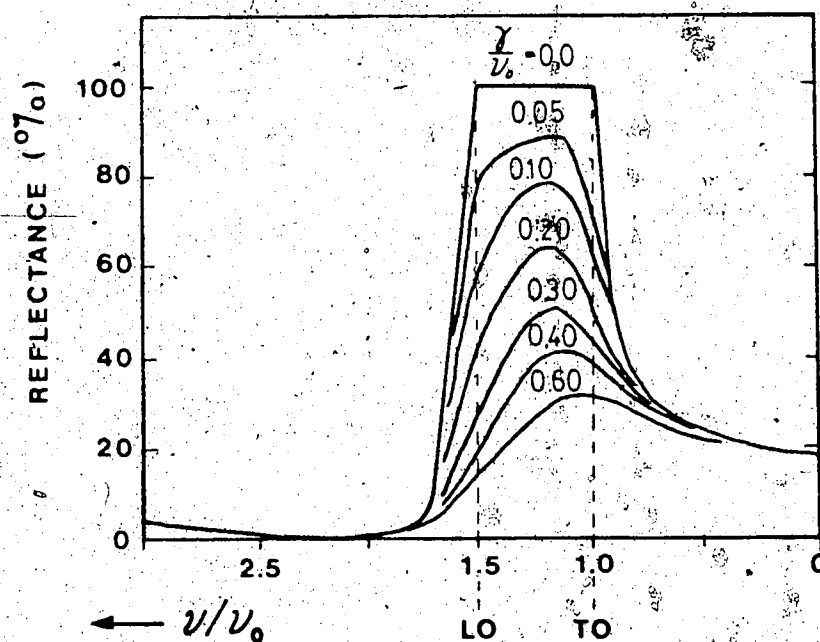


Figure 1.10 Shape of reststrahlen band for different values of the damping constant,  $\gamma$ .

Figures 1.9 and 1.10 redrawn from Reference 145.

reststrahlen peak maximum is illustrated in Figure 1.10. This should be contrasted with the behavior of an absorbance spectrum, for which increased damping primarily affects the peak width.

Because the alkali halides all possess a cubic lattice structure, their optical properties are strikingly similar. For example, they all display subsidiary peaks on the high frequency side of the reflection maximum.<sup>27</sup> The isotropic nature of the alkali halides has considerably simplified the requisite optical experiments: no special preparation of a particular crystal face is necessary; the incident radiation does not have to be polarized at normal incidence; and beam convergence does not pose a problem, as it does in the study of anisotropic crystals.<sup>146</sup> The absence of these complicating factors enables a clearer interpretation of such studies as the temperature dependence of the optical constants.<sup>139,143,144</sup>

Because of the simplicity of the reststrahlen spectrum, many workers have analyzed it in terms of one or two classically damped harmonic oscillators.<sup>139,143,144</sup> In some cases, the determination of the optical constants has been almost incidental; their primary concern being the longitudinal and transverse frequencies,<sup>142</sup> which are readily given by the dielectric function  $\epsilon(\nu)$ . (See Section 1.1d). These frequencies, in turn, define the effective charge of the positive and negative ions, and give a measure of the relative ionicity or covalency of the bond.<sup>147</sup>

Another characteristic feature of the reststrahlen band, and indeed the reflection band associated with any strong absorption process, recorded at near-normal incidence, is a pronounced minimum on the high frequency side of the peak. It has been found that a KK analysis frequently generates physically untenable negative values of the extinction coefficient,  $k$ , in this region.<sup>27,139</sup> Since the KK-integral is acutely sensitive to very small reflectance values, it has been suggested that inaccurate measurements of this  $R_{\min}$  region are the source of this anomaly.<sup>140</sup> A poignant demonstration of how the shape and magnitude of the calculated optical constant spectra are affected by the value of  $R_{\min}$  is given by Hadni *et al.*<sup>144</sup> for the case of KBr.

Other compounds which have been the subject of optical studies include metals,<sup>148,149</sup> semiconductors,<sup>94,150-153</sup> conducting layer compounds, such as  $K_2Pt(CN)_4Br_{0.3} \cdot 3H_2O$ <sup>154</sup> and  $HgI_2$ ,<sup>155,156</sup> and compounds possessing unusual optical characteristics. Some examples of this latter category are: the ferroelectric titanates;<sup>157,158</sup>  $KNiF_3$ , which is antiferromagnetic<sup>159</sup> at temperatures below  $275^\circ K$ ; and thiourea crystal,<sup>160</sup> which undergoes a ferroelectric to paraelectric phase transition at a temperature of approximately  $200^\circ K$ .

Optical studies of molecular crystals are surprisingly few. Representative examples from each of the crystal classes, excluding triclinic, will be given.

The infrared optical properties of the cubic crystal,  $NaClO_3$ , have been investigated by Raman<sup>97</sup> and by external<sup>96</sup>

and internal<sup>98</sup> (ATR) reflection spectroscopy. This crystal contains four molecules per primitive unit cell and both the  $\text{Na}^+$  ions and  $\text{ClO}_3^-$  ions are located on sites of  $C_3$  symmetry. Because of the high crystal symmetry and several molecules per unit cell,  $\text{NaClO}_3$  provides an ideal model compound for studying the effects of factor-group or Davydov splitting. In the infrared reflectance study by Andermann and Dows<sup>96</sup> over the region  $400\text{--}1400\text{ cm}^{-1}$ , the optical constants were calculated via the Kramers-Kronig phase relation. The transition strengths of the various fundamental modes were then computed by four different expressions:

$$S_I = \frac{2}{\pi} \int_{\text{band}} \epsilon'' \nu d\nu = \frac{2}{\pi} \int_{\text{band}} \sigma d\nu \quad [1.87]$$

$$S_{II} = \frac{n_\infty}{\pi^2} \int_{\text{band}} \alpha d\nu \quad [1.88]$$

$$S_{III} = n_\infty^2 (\nu_{LO}^2 - \nu_{TO}^2) \quad [1.89]$$

$$S_{IV} = (\bar{n})^2 (\nu_{LO}^2 - \nu_{TO}^2) \quad \text{where } \bar{n} = \frac{\int_{\text{band}} n \alpha d\nu}{\int_{\text{band}} \alpha d\nu} \quad [1.90]$$

The values obtained from the integrated conductivity ( $S_I$ ) and absorption coefficient ( $S_{II}$ ) measurements gave reasonable agreement. However, the values derived from the measured LO-TO splitting ( $S_{III}$  and  $S_{IV}$ ) were markedly different. The authors explained this discrepancy by stating that the latter two expressions ( $S_{III}$  and  $S_{IV}$ ) are only valid for a single

mode, and therefore, inapplicable to  $\text{NaClO}_3$ . Because of their fundamental interest in understanding how band intensities are affected by a change from the gaseous to the crystalline state, Andermann and Dows also evaluated the dipole moment derivatives for the various  $\text{ClO}_3^-$  internal modes. They basically followed the procedure outlined in Section 1.1d of this thesis, with the assumption of a Lorentz local field. However, they incorrectly determined the vector sum of the molecular dipole moment derivatives, so their resultant crystal dipole derivatives are in error. The correct values are given in Decius and Hexter's book, "Molecular Vibrations in Crystals".<sup>161</sup>

Hartwig, Rousseau, and Porto<sup>97</sup> later measured both the Raman and infrared reflection spectrum of  $\text{NaClO}_3$  from 40-1100  $\text{cm}^{-1}$ . The advantage of Raman spectroscopy is that the TO and LO modes are both excited and appear as distinct bands. In an infrared absorption experiment at normal incidence, the LO modes are never observed; whereas in a reflection spectrum, the LO and TO frequencies can be estimated from the peak inflection points or directly measured from the derived dielectric constant spectrum (see Section 1.1d). Although all of the vibrational modes of  $\text{NaClO}_3$  are Raman-active, some were too weakly active to be apparent. It was for this reason that Porto *et al.* also recorded the reflection spectrum.

The transition strengths, damping constants and longitudinal- and transverse-optic frequencies were determined

for all fourteen F optic modes via a classical dispersion analysis of the reflectance spectrum. An initial set of  $S_j$  were obtained from equation [1.84], with the assumptions of zero damping and  $\epsilon'(\nu = \nu_{LO}) = 0$ , i.e.

$$\epsilon'(\nu_{LO}^k) = \epsilon_\infty + \sum_{j=1}^N \frac{S_j}{(\nu_{TO}^j)^2 - (\nu_{LO}^k)^2} = 0 \quad [1.91]$$

These values of  $S_j$  and estimated values of the damping constant,  $\gamma_j$ , were then substituted into the damped harmonic oscillator equations [1.84] and [1.85]. The theoretical reflectance curve was computed via equation [1.86], and compared with the measured spectrum. The values of  $\nu_{LO}^j$ ,  $\nu_{TO}^j$  and  $\gamma_j$  were adjusted until a satisfactory fit was achieved. The corresponding "best fit" values of  $S_j$  were then compared with the directly measured transition strengths ( $S_I$ ) of Andermann and Dows.<sup>96</sup> The two sets of results are said to be in good agreement (maximum discrepancy ~30%), signifying that the LO-TO frequency splitting can give reliable values of the transition strengths if the various  $S_j$  are evaluated simultaneously. The reason that the isolated mode approximation, implicit in equations [1.89] and [1.90], breaks down for the case of  $\text{NaClO}_3$  is because it has several close-lying transitions which can interact appreciably with one another.

In the optical study of uniaxial crystals, the most common experimental procedure is to measure polarized reflectance spectra with the electric vector vibrating suc-

cessively parallel and perpendicular to the c-crystal axis, which coincides with the optic axis. This is usually followed by a Kramers-Kronig dispersion analysis of each spectrum, giving the extraordinary- and ordinary-ray optical constants, respectively. The c-axis may be determined with a polarizing microscope since no birefringence is viewed along this direction, or from X-ray measurements. Hexagonal, tetragonal, and trigonal crystal classes belong to this optical system. Some examples of uniaxial molecular crystals whose infrared optical properties have been characterized are:  $\text{LiKSO}_4$ ,<sup>11</sup>  $\text{Ca}_{10}(\text{PO}_4)_6\text{F}_2$ <sup>162</sup> (hexagonal);  $\beta\text{-NaN}_3$ ,<sup>163</sup> quartz<sup>93</sup> (trigonal); and  $\text{LiOH}$ ,<sup>164</sup>  $\text{ZrSiO}_4$ ,<sup>165</sup>  $\text{KHF}_2$ <sup>166</sup> (tetragonal). Only the significant aspects of these studies, with general implications to uniaxial systems, will be discussed.

In 1976, Hiraishi *et al.*<sup>11</sup> reported the polarized infrared reflectance spectra ( $\underline{E}||c$  and  $\underline{E}\perp c$ ) of  $\text{LiKSO}_4$  from 100-2000  $\text{cm}^{-1}$ ; the angle of incidence was  $20^\circ$  and the  $R_s$  component was measured. In their KK analysis, they used expressions [1.78] and [1.79] which explicitly allow for the true angle of incidence, instead of using the more common normal-incidence approximation. Strangely, their KK analysis generated large negative values of  $k(\nu)$  in the frequency region below the reflectance maximum at  $\sim 1100 \text{ cm}^{-1}$ . They attributed this result to small distortions in the observed reflectance. These authors also performed a classical dispersion analysis to obtain the oscillator parameters for the

A species ( $\underline{E} \parallel c$ ) and  $E_1$  species ( $\underline{E} \perp c$ ) vibrations. They found that 4 and 5 oscillators, respectively, satisfactorily described the measured reflectance.

In 1968, Kravitz *et al.*<sup>162</sup> studied the polarized infrared reflectance of  $\text{Ca}_{10}(\text{PO}_4)_6\text{F}_2$  over the region  $300\text{--}1600\text{ cm}^{-1}$ , with the radiation incident on the sample at angles of  $30^\circ$ ,  $45^\circ$ , and  $70^\circ$  to the  $c$ -crystal axis. With the electric vector parallel to  $c$  ( $\underline{E} \parallel c$ ), i.e. when exciting extraordinary optical modes, the resonant frequencies were noticeably dependent upon the direction of wave propagation. This demonstrated the general anisotropy of the extraordinary wave normal modes. By contrast, when the polarizer was rotated so that the electric vector was perpendicular to  $c$  ( $\underline{E} \perp c$ ), and pure ordinary waves were excited, no such anisotropy was observed. The authors stated that a KK-analysis met with limited success because of the relatively small frequency range of data. Consequently, they performed a classical dispersion analysis. However, it should be noted that they terminated their low frequency reflection data in the middle of an intense band so their KK-analysis could not be expected to give satisfactory results.

The infrared optical study of quartz by Spitzer and Kleinman<sup>93</sup> in 1961 was significant in that it was the first successful application of classical dispersion theory to a complicated reflectance spectrum. In the frequency region  $300\text{--}2000\text{ cm}^{-1}$ , both the ordinary- and extraordinary-ray spectra were well described by 7 classically damped harmonic oscillators.

Although the technique for extracting optical constants of isotropic materials from reflectance-versus-angle-of-incidence measurements has been well-known for many years (see Section 1.2a), it was not until 1968 that Mosteller and Wooten<sup>167</sup> extended this type of analysis to strongly absorbing uniaxial crystals. They derived the relevant expressions for transverse electric (TE) and transverse magnetic (TM) polarized radiation incident on the basal plane, i.e. for which the optic axis is normal to the reflecting face. These are:

$$R(\text{TE}) = \left| \frac{\cos \phi - (\hat{\epsilon}_{\perp} - \sin^2 \phi)^{\frac{1}{2}}}{\cos \phi + (\hat{\epsilon}_{\perp} - \sin^2 \phi)^{\frac{1}{2}}} \right|^2 \quad [1.92]$$

$$R(\text{TM}) = \left| \frac{\hat{n}_{\perp} \cos \phi - (1 - \sin^2 \phi / \hat{\epsilon}_{\parallel})^{\frac{1}{2}}}{\hat{n}_{\perp} \cos \phi + (1 - \sin^2 \phi / \hat{\epsilon}_{\parallel})^{\frac{1}{2}}} \right|^2 \quad [1.93]$$

where  $\phi$  = angle of incidence

$\hat{\epsilon}_{\perp}$  = ordinary-ray complex dielectric constant

$\hat{\epsilon}_{\parallel}$  = extraordinary-ray complex dielectric constant.

Surprisingly, there are very few applications of this procedure in the literature. Decius appears to be one of its main proponents. In 1975, Decius and Fredrickson<sup>163</sup> measured the TE- and TM-polarized reflectance spectra of the (111) face of  $\beta\text{-NaN}_3$  at several angles of incidence. They then fitted their results to equations [1.92], [1.93] and the classical dispersion expressions, [1.84] and [1.85], in order to obtain the optical, dielectric, and dispersion parameters. Their main concern was in obtaining reliable values

of the transition strengths and dipole moment derivatives.

In addition to  $\beta\text{-NaN}_3$ , Decius has applied this method to  $\text{LiOH}$ <sup>164</sup> and  $\text{CaCO}_3$ <sup>168</sup> (trigonal) single crystals.

In 1971, Wilkinson *et al.*<sup>165</sup> studied the polarized infrared reflectance of  $\text{ZrSiO}_4$ . This work is noteworthy because it discusses qualitatively how various experimental errors and limitations affect the accuracy of the KK-analysis. From model calculations, they found that if the reflectance spectrum was recorded with insufficient resolution to accurately define the  $\epsilon''$  peak maximum, then the KK procedure could generate negative regions of  $\epsilon''(\nu)$ .

Wilkinson *et al.*<sup>166</sup> also performed a theoretically significant optical study of  $\text{KHF}_2$  in 1973. The F-F distance in this compound is 2.26 Å which makes it one of the shortest hydrogen bonds found in nature.  $\text{KHF}_2$  is a centrosymmetric crystal, so the rule of mutual exclusion applies. In the region 20-4000  $\text{cm}^{-1}$ , the Raman-active modes are narrow, symmetrical bands, whereas the infrared-active modes are very broad and unsymmetrical in transmission spectra. The reason for this disparity, in particular, the extraordinary breadth of the  $\text{HF}_2^-$  asymmetric stretching vibration at  $\approx 1400 \text{ cm}^{-1}$ , has been the subject of considerable debate. However, Wilkinson *et al.*, from a combined Kramers-Kronig and classical dispersion analysis, determined the true half-width of this band to be only  $\approx 40 \text{ cm}^{-1}$ . They accounted for the very large widths reported in the earlier literature as due to reflection effects, which completely distorted the true band shape.

In the biaxial optical system, very few molecular crystals have been studied. The orthorhombic crystal, acetanilide has already been discussed. Since the indicatrix axes coincide with the crystal axis directions, the requisite experiments and the interpretation of the optical data are both quite straightforward. The situation is much more complicated in the case of monoclinic crystals. As was noted in Section 1.1c, only the b-crystal axis coincides with one of the indicatrix axes (denoted here the y axis). The complex dielectric tensor then has the form:

$$\hat{\epsilon}(\nu) = \begin{pmatrix} \hat{\epsilon}_{xx}(\nu) & 0 & \hat{\epsilon}_{xz}(\nu) \\ 0 & \hat{\epsilon}_{yy}(\nu) & 0 \\ \hat{\epsilon}_{xz}(\nu) & 0 & \hat{\epsilon}_{zz}(\nu) \end{pmatrix} \quad [1.94]$$

It is generally not possible to diagonalize this matrix since the real part of  $\hat{\epsilon}(\nu)$  may have a different set of principal axes than the imaginary part of  $\hat{\epsilon}(\nu)$ . This is referred to as axial dispersion.<sup>20</sup> Thus  $\hat{\epsilon}(\nu)$  contains eight unknown functions of  $\nu$ . The formidableness of evaluating these quantities has largely inhibited monoclinic optical studies. However, because the largest group of organic molecular compounds crystallize in the monoclinic system, there has been a recent surge of interest in clarifying the dielectric theory of monoclinic crystals.<sup>20,169,170</sup> One of the best descriptions is given by Koch *et al.*<sup>20</sup> They clearly define the experiments necessary for a complete and unambiguous characterization of the dielectric tensor.

The dielectric function  $\hat{\epsilon}_{yy}(\nu)$  may be obtained from a TE-polarized reflectance spectrum of a crystal face containing the b-axis (e.g. (001)) and with plane of incidence (010), followed by a Kramers-Kronig analysis. The quantities  $\hat{\epsilon}_{xx}$ ,  $\hat{\epsilon}_{zz}$ , and  $\hat{\epsilon}_{xz}$  may be derived in either of two ways: from normal incidence reflectance from the (010) face, with various angular settings of the polarizers in the incident and reflected beam, followed by a KK-analysis; or from TM-polarized reflectance at various oblique angles of incidence, with (010) as the plane of incidence, followed by a direct solution of a system of simultaneous equations. In the event of negligible axial dispersion, the experiments are simplified by the removal of the polarization analyzer ( $\hat{\epsilon}_{xz} = 0$ ).

In the light of this discussion, it is interesting to critically review some of the earlier monoclinic studies to assess their theoretical significance.

Haas and Sutherland<sup>138</sup> in their optical study of  $\text{CaSO}_4 \cdot 2\text{H}_2\text{O}$ , correctly determined  $\hat{\epsilon}_{yy}(\nu)$  from measurements of  $E||b$  on the ( $\bar{1}01$ ) and ( $201$ ) crystal faces. Although they used the former data to derive  $\hat{\epsilon}_{yy}$  for the region 450-1200  $\text{cm}^{-1}$ , and the latter data for the region 1400-3700  $\text{cm}^{-1}$ , they state that essentially the same reflectance spectra were obtained for the two faces. They also measured the reflectance from the (010) face for different polarizations of the incident electric vector. In the case of the  $B_u$  components of the  $\text{SO}_4^{2-}$  ion fundamental modes, maximum dichroism

was observed with  $\underline{E}$  at  $9^\circ$  and  $99^\circ$  to the a-crystal face. If axial dispersion is negligible, these latter spectra define  $\hat{\epsilon}_{xx}$  and  $\hat{\epsilon}_{zz}$  for the sulphate bands.

Frindi *et al.*,<sup>171</sup> in 1980, measured the polarized reflectance of single crystal  $\text{Li}_2\text{SO}_4 \cdot \text{H}_2\text{O}$  over the region  $40\text{--}660\text{ cm}^{-1}$ , with  $\underline{E} \parallel b$  and  $\underline{E} \perp b$ , followed by a classical dispersion analysis. They did not identify which crystal face was the reflecting plane, but from a polarized light study, they determined the directions of the x and z indicatrix axes. Their  $\underline{E} \perp b$  reflection experiments were referenced to this visible light x-principal axis, i.e. the B species vibrational modes were observed with  $\underline{E} \perp b$  and  $\underline{E} \parallel x$ . Since the x-direction is frequency-dependent, this type of specification is ambiguous. These spectra only define  $\hat{\epsilon}_{xx}$  and  $\hat{\epsilon}_{zz}$  if the indicatrix axes directions are the same for all bands in the visible and infrared regions. This is highly unlikely.

Another monoclinic crystal whose optical properties have been recently investigated is sodium formate. In 1981, Tajima *et al.*<sup>172</sup> recorded its near-normal incidence ( $\phi = 20^\circ$ ) reflectance spectra over the region  $30\text{--}4000\text{ cm}^{-1}$ , with  $\underline{E} \parallel b$  for the (001) face and  $\underline{E} \perp c$  for the (010) face. They derived the corresponding optical constants from a Kramers-Kronig analysis. Dispersion parameters were then estimated from the dielectric constant spectra, as described in Section 1.1d, and these values were further refined by a classical dispersion analysis. This type of combined Kramers-Kronig-classical dispersion analysis has become increasingly popular in

infrared optical studies. In more recent applications, the error in the derived optical constants has been estimated from the two sets of results.<sup>94</sup> The first experiment of Tajima *et al.* ( $\underline{E} \parallel b$  for (001)) only determines  $\epsilon_{yy}$  unambiguously if the crystal was oriented with the b-axis normal to the plane of incidence. Otherwise, because of the fairly large angle of incidence, there will be considerable admixture of the other dielectric components. Unfortunately, the authors did not give this information. Also, their second experiment ( $\underline{E} \perp c$  for (010)) has no fundamental significance, unless this polarization direction was coincidentally aligned along one of the indicatrix axes.

The organic crystals, naphthalene<sup>55,56</sup> and anthracene<sup>173-175</sup> have been the subject of numerous optical studies. Most of the work on anthracene has been carried out in the ultra-violet region, where it exhibits an intense  $\pi-\pi^*$  transition. Of particular note is the optical reflection study of anthracene single crystals by Koch and Otto,<sup>175</sup> over the energy range 4-10.5 eV. From only three well-defined experiments, they completely determined the complex dielectric tensor (assuming negligible axial dispersion).

One of the earliest polarized infrared reflectance studies of naphthalene was by Person *et al.*<sup>176</sup> in 1955. They measured the normal incidence reflectance spectra of naphthalene and naphthalene- $d_8$  from the bc and ab crystal planes, respectively. Although they did not derive the optical constants, this work is mentioned for the fact that it discusses

why light, which is polarized either parallel or perpendicular to the b-axis and striking at normal incidence on a crystal face containing the b-axis, is not elliptically polarized on reflection. Thus, an experiment with  $\underline{E} \parallel b$ , or  $\underline{E} \perp b$  on any ( $h_1 0 h_2$ ) face of a monoclinic crystal, provides definitive results. In the case of the ATR measurements of single crystal naphthalene by Tsuji and Yamada,<sup>55</sup> spectra were recorded for the ab plane and  $\underline{E} \parallel b$  at  $\phi = 44.2^\circ$  and  $54.6^\circ$ . Solution of Fresnel's equations gave  $\epsilon_{yy}$  directly.

Because of the difficulty in preparing large, single crystals of many compounds of interest, there has been a recent effort to obtain useful information from polycrystalline samples. However, the number of these studies is still quite small, and no completely satisfactory theory has yet explained the observed polycrystalline spectra. A few examples will illustrate the particular difficulties associated with polycrystalline optical studies.

In 1964, Hunt *et al.*<sup>177</sup> measured the near-normal incidence reflectance of polycrystalline  $\text{MgF}_2$  and, from a KK-analysis, determined the vibrational frequencies. Later that year, Barker<sup>178</sup> recorded polarized infrared reflectance spectra of the single crystal  $\text{MgF}_2$ , with  $\underline{E} \parallel c$  and  $\underline{E} \perp c$ . Since  $\text{MgF}_2$  is tetragonal, these two experiments completely specify its optical properties. A KK-analysis of these spectra gave significantly different frequencies from those reported by Hunt *et al.*<sup>177</sup> Also, some of Hunt's assignments were in

error; a consequence of the fact that polycrystalline spectra provide no information on the mode symmetries. Barker makes the observation that since reflectivity is a non-linear function of the dielectric constant, then an analysis of the average reflectivity, as was performed by Hunt *et al.*, cannot yield an average dielectric constant.

Another difficulty with polycrystalline studies is that the samples may not be truly isotropic. For example, Painter *et al.*<sup>179</sup> found that their polycrystalline samples of anthracene, prepared by vacuum deposition onto a substrate, gave reflection spectra remarkably similar to those obtained from the ab plane of the single crystal.<sup>175</sup> This type of preferred orientation problem was also encountered by Tsuji and Yamada<sup>55</sup> in their preparation of polycrystalline naphthalene. They found that if molten naphthalene was poured onto a flat glass plate and allowed to cool, the reflecting surface was approximately the ab plane. However, by compressing a powder of less than 300 mesh particle size, they were able to obtain completely isotropic discs. These authors then attempted to correlate their derived intensities for the polycrystalline and single crystal extinction coefficient spectra. The relative intensities of a particular vibration excited along each of the three axial directions (a:b:c) were calculated from the crystal structure, using the oriented gas model. The ratio of the intensity of the b-axis component of the single crystal to that of the polycrystal was then determined from  $b/^{1/3}(a+b+c)$ , i.e. they

assumed the polycrystalline extinction coefficient spectrum to be a superposition of the three derived  $k(\nu)$  spectra for the single crystal:  $\underline{E}||a$ ,  $\underline{E}||b$  and  $\underline{E}||c$ . However, only the bands belonging to  $B_{1u}$  symmetry gave good agreement between the observed and calculated intensity ratios. This precise agreement might be fortuitous, although it was noted that bands belonging to a particular symmetry species behaved in a similar manner.

To summarize, infrared optical studies have gradually progressed from simple, isotropic crystals to more complex systems. The theoretical development has typically lagged the experimental advances, but with the recent emphasis on obtaining definitive optical quantities, such as band intensities and dipole moment derivatives, there has been a growing effort to understand the molecular nature of the optical constants. This, in turn, has promoted the clearer definition of optical experiments. However, our current understanding of polycrystalline samples is still quite poor.

### 1.5 Objectives of this Work

The purpose of this work was to obtain the infrared optical and dielectric parameters of a molecular hydrogen-bonded crystal. These systems are of particular interest to this laboratory, and compounds such as the clathrate hydrates, simple carboxylic acids, and ordered phases of ice, have been the subject of numerous infrared transmission and

Raman studies. These compounds generally exhibit very broad O-H stretching bands and part of the motivation for our optical study was to define a technique which would enable us to eventually determine whether reflection effects contributed to this extraordinary breadth. However, our primary concern was in a complete description of the infrared optical constants. The fundamental significance of these quantities was detailed in previous sections. Of particular interest was the evaluation of related molecular properties, such as the vibrational frequencies, absolute intensities, damping constants, and dipole moment derivatives for the various infrared-active crystal modes.

Before embarking on this project, it was necessary to develop the experimental and computational methods for deriving optical constants. The procedure adopted was to measure the near-normal incidence reflectance, followed by a Kramers-Kronig analysis. This technique has the advantages of simplicity and general validity. Due to the frequent problem of overlapping bands, the KK method was used in conjunction with a classical dispersion analysis. The inorganic hydrate,  $\text{Ba}(\text{ClO}_3)_2 \cdot \text{H}_2\text{O}$ , was selected as the subject of study, for the reasons enumerated in Section 1.3. Because of the paucity of data available on polycrystalline samples, it was considered that a comparative study of single crystal and polycrystalline  $\text{Ba}(\text{ClO}_3)_2 \cdot \text{H}_2\text{O}$  would be a valuable undertaking. It was also noted from the literature on the infrared optical properties of solids, that very few

studies clearly defined all of the relevant experimental parameters and theoretical approximations used. Also, many of the earlier studies were hampered by the poor signal-to-noise performance of the grating instruments. However, Fourier transform infrared spectrometers of very high signal-to-noise are currently available to us, so we have the capability of obtaining reliable, quantitative optical constant data. In order to achieve this goal, our work was directed at analyzing, and reducing where possible, all sources of experimental and computational error.

## CHAPTER II.

### EXPERIMENTAL

#### 2.1 Introduction

The experimental objectives were to prepare samples of  $\text{Ba}(\text{ClO}_3)_2 \cdot \text{H}_2\text{O}$ , which were of sufficient size and optical quality for study in the infrared region, and to develop the techniques necessary for obtaining reliable reflectance data. This chapter describes the means used to achieve these two goals.

#### 2.2 Sample Preparations

The  $\text{Ba}(\text{ClO}_3)_2 \cdot \text{H}_2\text{O}$  used in the preparation of the polycrystalline and single crystal samples was used as supplied by Allied Chemicals and Matheson Co. Inc.

##### 2.2a Preparation of Polycrystalline $\text{Ba}(\text{ClO}_3)_2 \cdot \text{H}_2\text{O}$

Polycrystalline samples of 1" diameter were prepared by compacting the powdered material in a laboratory press, using the apparatus illustrated in Figure 2.1. Briefly, the apparatus consisted of a 1" tapered compression cell resting on a 2.25" piston which floats in an oil chamber. When pressure was applied to the oil by means of a hand-pump, the 2.25" piston exerted an equivalent force on the compression cell. The pressures delivered to the oil and to the cell were thus related by:

$$P_{\text{cell}} = \left( \frac{2.25}{1.00} \right)^2 P_{\text{oil}} \approx 5.06 \times P_{\text{oil}}$$

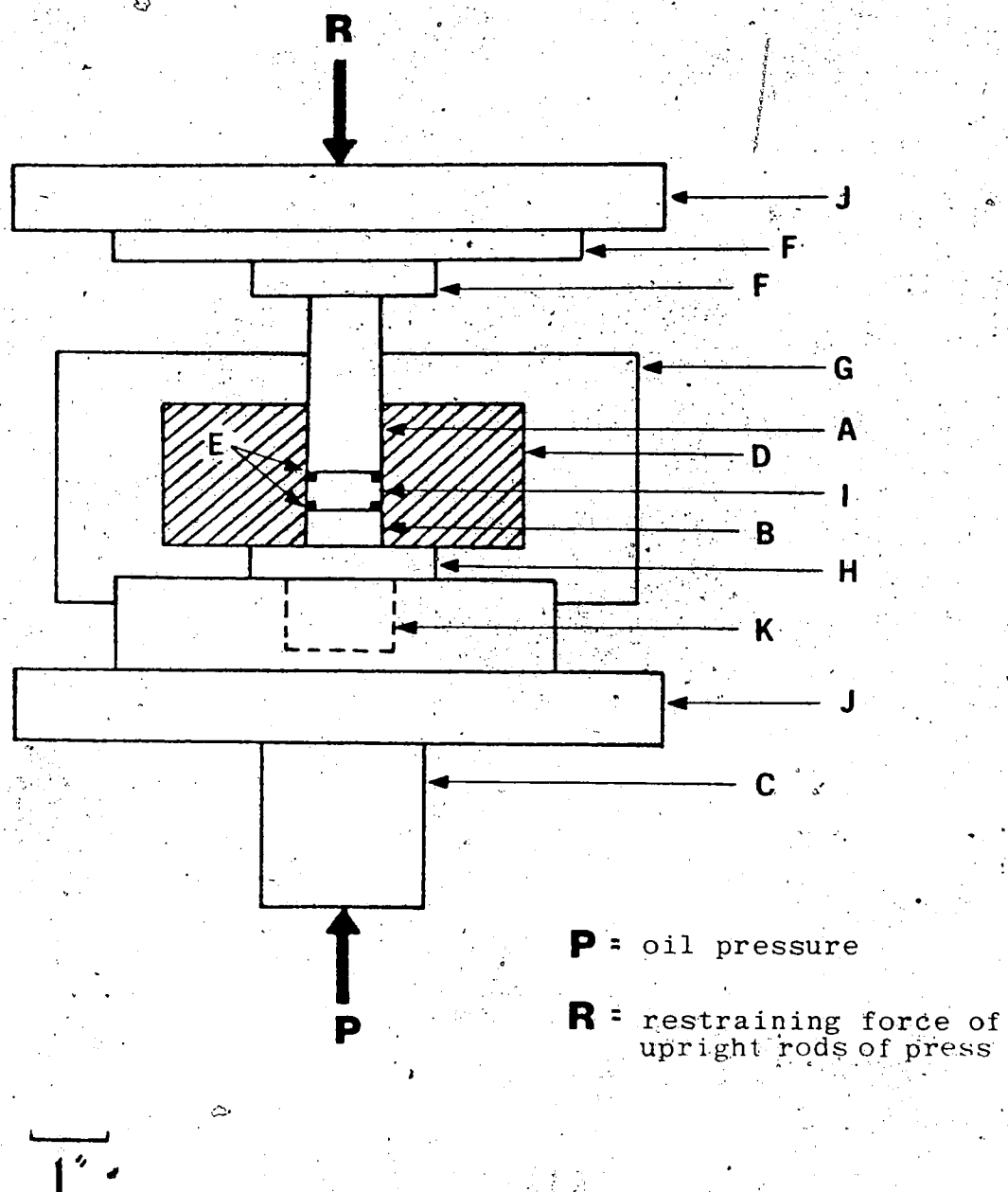


Figure 2.1 The pressure vessel used to prepare polycrystalline samples of  $\text{Ba}(\text{ClO}_3)_2 \cdot \text{H}_2\text{O}$ .

A, top piston; B, bottom piston; C, 2.25" piston of the press  
 D, ~1" tapered i.d., 5" o.d., cylinder;  
 E, brass back-up rings; F, pressure distributing block;  
 G, stainless steel jacket; H, support block; I, sample;  
 J, platen of the press; K, sample cup

A, B, and D comprise the compression cell

In a typical experiment, a known quantity of powdered  $\text{Ba}(\text{ClO}_3)_2 \cdot \text{H}_2\text{O}$  was placed in the cylinder (D) on top of the bottom piston (B). The sample was bracketted by the back-up rings (E) so that it did not extrude between the cylinder and pistons. The top piston (A) was then manually pushed onto the sample and this assembly was positioned on the platen (J) of the press, as indicated in Figure 2.1. Pressure was slowly applied to the vessel; first, in small increments, to take advantage of the sample's better flow characteristics at low pressures and, then, in larger increments, to compact the sample.

To extract the prepared disc from the bore of the compression cell, the support block (H) was removed and pressure was gradually applied until the sample dropped into the cup (K). Damage to the disc's faces was minimized by wrapping a rubber band around the top piston to prevent it from dropping onto the sample, and by placing pieces of kim-wipe in the sample cup to cushion the disc's fall. The samples obtained in this manner were powdery and readily fractured if not handled with care. Occasionally, a face of the disc stuck to the piston. This latter problem was remedied by polishing the piston faces: they were mechanically polished to an 8 $\mu$  inch finish, then further hand polished on 600 grit sandpaper with distilled water as a lubricant, prior to each sample preparation.

Approximately 10 g of  $\text{Ba}(\text{ClO}_3)_2 \cdot \text{H}_2\text{O}$  were used in the disc preparations. This provided a minimum sample thickness

of 6 mm, which ensured that reflection from the back surface was negligible.

Several different pressure application schemes were followed in order to determine the optimum method for making sample discs. The main criterion for this selection was the reflectance of the disc exhibited after a strengthening and polishing procedure, which will be described shortly. The following sample pressures and lengths of application provided the discs with the best optical quality:

Table 2.1 Applied Pressure Timetable for the Preparation of  $\text{Ba}(\text{ClO}_3)_2 \cdot \text{H}_2\text{O}$  Pellets

---

---

<u>P<sub>sample</sub> (bar)</u>	<u>Time (min)</u>
51	20
101	90
202	20
405	25
810	60

---

...the diameter of the hydraulic ram of the press = 2.25"

...the diameter of the bore of the compression cell = 0.9998"

---

Compared with the method of Table 2.1, it was found that lower final pressures resulted in more crumbly discs, which possessed insufficient strength; while higher final pressures resulted in harder discs, whose initial infrared reflectivities were higher, but whose final reflectivities measured after the strengthening and polishing steps, were

not as good.

Attempts to directly polish a face of these samples caused the samples to rapidly disintegrate. For this reason, it was necessary to strengthen the desired reflecting face of the disc, prior to polishing.

This was accomplished by repeated applications of a saturated solution of  $\text{Ba}(\text{ClO}_3)_2 \cdot \text{H}_2\text{O}$  in distilled water. The solution was saturated at  $40^\circ\text{C}$ , allowed to cool to slightly above room temperature, then applied by means of an eye-dropper. In order to wet the disc's face and have the solution absorbed into its pores, the tip of the dropper had to brush the solution over the face. Excess solution was carefully scraped off with the straight edge of a microscope slide. The disc was then supported on two glass rods and allowed to dry for one hour. This sequence of events was repeated until crystals began depositing on the disc's face.

The samples were then polished by a conventional window polishing technique. This involved initial grinding on a flat glass plate with a slurry of 1000 grit aluminum oxide and iso-propanol. This step was continued until the shiny surface crystallites were ground flat, as determined under 15X magnifying power. The discs were then polished on a chamois-covered board with a slurry of cerium oxide and iso-propanol. To maintain the flatness of the disc's face, it was moved in a figure-eight pattern over the surface of the chamois and frequently rotated about its axis. Finally, the discs were polished on a clean chamois with

either iso-propanol or Skelly-B (hexanes). These latter two polishing stages were continued until no further increase in the infrared reflectance of the disc was obtained. The fact that two independent discs displayed the same ultimate reflectivities provides confidence in this empirical evaluation of optical quality.

## 2.2b Preparation of Single Crystal $\text{Ba}(\text{ClO}_3)_2 \cdot \text{H}_2\text{O}$

The most common procedures for the growth of large, good quality, single crystals involve crystal growth from solution. These methods require a knowledge of the compound's solubility characteristics. From Table 1.2, we see that  $\text{Ba}(\text{ClO}_3)_2 \cdot \text{H}_2\text{O}$  is readily soluble in water at room temperature and atmospheric pressure, and its solubility increases significantly with increase in temperature. For these reasons, the following three methods were employed in the preparation of single crystals of  $\text{Ba}(\text{ClO}_3)_2 \cdot \text{H}_2\text{O}$ :

- i) slow evaporation of a solution of  $\text{Ba}(\text{ClO}_3)_2 \cdot \text{H}_2\text{O}$ , saturated in distilled water at room temperature.
- ii) slow cooling of a solution of  $\text{Ba}(\text{ClO}_3)_2 \cdot \text{H}_2\text{O}$ , saturated in distilled water at  $80^\circ\text{C}$ .
- iii) circulation method.

The first two methods did not provide large, optical quality single crystals. However, seed crystals of suitable size and quality were obtained for later use in the circulation method. The major drawback, common to the first two procedures, is their susceptibility to external temperature

fluctuations. The evaporation method also proved to be a very slow process, while the cooling method required the temperature to be decreased according to a very exact schedule. Another complication besetting the cooling method was the necessity of a constant temperature bath filled with a light paraffin oil. A small pump circulated the oil in order to ensure uniformity in the bath's temperature. However, it is suspected that the pump's buffeting action may have disturbed the seed crystals' growth.

i) Production of seeds by evaporation

81 g of  $\text{Ba}(\text{ClO}_3)_2 \cdot \text{H}_2\text{O}$  were dissolved in 275 ml of distilled water at room temperature. To ensure saturation, the solution was slowly stirred with a Fischer Dyna Mix mechanical stirrer for a period of two days, then filtered through a coarse sintered funnel. The filtrate was transferred to a 650 ml beaker, covered with a watch glass, and left undisturbed for one month. Although some fairly large (>1 cm) crystals were obtained, there were several smaller crystals embedded in their faces, thereby making them useless for reflection studies. The small, faultless crystals were washed with a water-moistened kimwipe, patted dry on filter paper, and stored in a covered petri dish. The remaining crystals were stored in stoppered glass bottles and were later used as the polycrystalline starting material in the circulation method.

### ii) Production of seeds by cooling

86 g of  $\text{Ba}(\text{ClO}_3)_2 \cdot \text{H}_2\text{O}$  were dissolved in 114 ml distilled water at  $80^\circ\text{C}$ . The solution was contained in a closed tubular flask, insulated by two beakers filled with a light paraffin oil. This assembly was secured to the table of a Colera bath. The oil in the bath was equilibrated at  $80^\circ\text{C}$  until its temperature matched that of the oil in the inner beaker. The recrystallization solution was then cooled to room temperature at the rate of  $4^\circ\text{C}$  per day, under manual control.

The residual solution was decanted off and the best single crystals were stored in a covered petri dish.

### iii) Production of single crystals by circulation method

The circulation method proved to be the most reliable for the production of large, good quality single crystals. The experimental apparatus for this procedure is illustrated in Figure 2.2.

The method<sup>180</sup> involves placing both a seed crystal and a saturated solution of the material to be crystallized in a closed container. The upper part of the crystallization vessel is maintained at a slightly higher temperature than the lower part of the vessel. A simple means of accomplishing this requirement is to use a water bath, whose evaporating action creates a constant temperature differential of  $0.1 - 0.2^\circ\text{C}$  with the surrounding air.

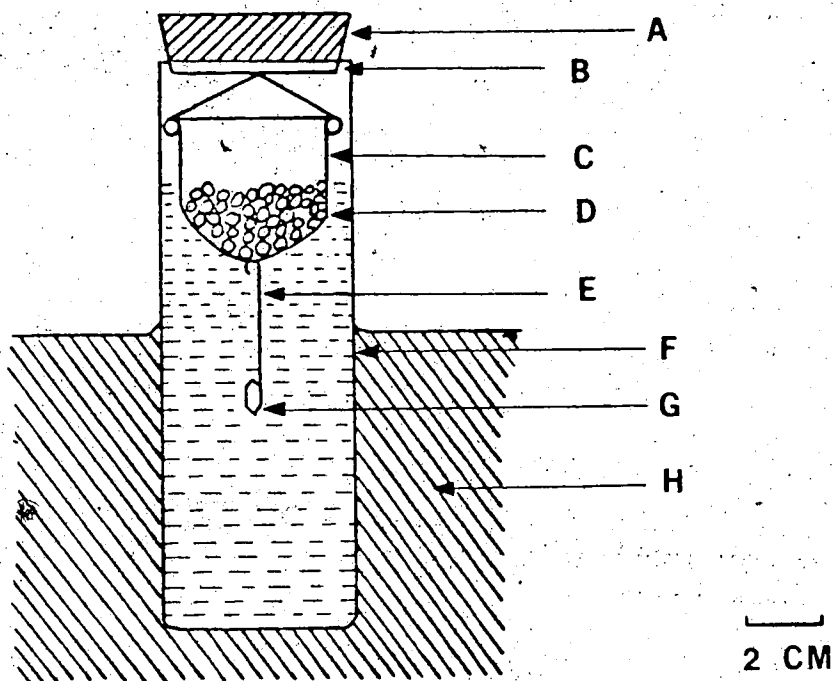


Figure 2.2 Growth of  $\text{Ba}(\text{ClO}_3)_2 \cdot \text{H}_2\text{O}$  single crystals by circulation method.

A, cork stopper; B, teflon tape; C, nylon pouch used as polycrystalline material holder; D, polycrystalline material; E, glass fiber; F, crystallization vessel; G, seed crystal; H, water bath.

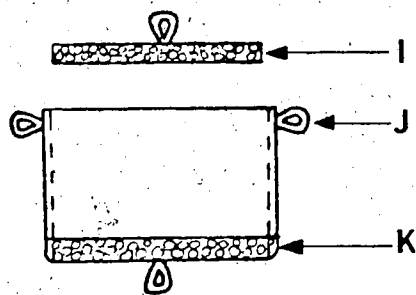


Figure 2.2a Glass crucible used as polycrystalline material holder.

I, lid; J, hooks; K, coarse frit.

1 CM

A nylon or glass holder, containing the polycrystalline starting material is held in the upper part of the container and the seed crystal is situated in the lower part of the container. The circulation of the solution occurs if the density of the saturated solution increases with temperature. The solution of the warmer, upper part of the tube then sinks to the bottom, where it becomes supersaturated, and some of the dissolved material deposits on the seed crystal. As a result, the solution surrounding the seed becomes less dense. This solution then streams upward, where it dissolves more of the polycrystalline material and the process continues.

For the preparation of single crystals of  $\text{Ba}(\text{ClO}_3)_2 \cdot \text{H}_2\text{O}$ , the following experimental procedure was used (with slight modifications, as noted):

The crystallization vessel was a 15 cm long glass tube, 5 cm in diameter, with a flat bottom. A saturated solution of  $\text{Ba}(\text{ClO}_3)_2 \cdot \text{H}_2\text{O}$  was prepared from 47 g of  $\text{Ba}(\text{ClO}_3)_2 \cdot \text{H}_2\text{O}$  in 150 ml distilled water. This solution was stirred with a glass rod for 1-2 hours, then filtered twice through a coarse sintered glass funnel, to ensure saturation at room temperature. The material holder was filled with polycrystalline  $\text{Ba}(\text{ClO}_3)_2 \cdot \text{H}_2\text{O}$ , which had been previously recrystallized by the evaporation method. Initial preparations used a densely woven nylon stocking as the material holder, while later preparations used a glass crucible with a coarse frit bottom and a loose-fitting lid, as illustrated

in Figure 2.2 a. The saturated solution was then poured through the holder in order to wash out any small grains, and refiltered. This step was carried out in order to avoid the formation of parasite crystals, which act as secondary nuclei and inhibit the growth of the seed crystal.

The seed crystal was supported from the holder either by tying it to a cotton thread or by glueing it to a fine glass fiber with glyptal cement.

The saturated solution was then warmed slightly ( $\approx 28^{\circ}\text{C}$ ) and poured into the crystallization tube. The material holder and suspended seed crystal were immersed in the solution, and the mounted crystallization vessel was carefully placed in a water bath. The water level was set to a height approximately half-way between the material holder and the seed crystal, and this level was maintained daily. It was important to allow the water to equilibrate to room temperature, prior to its addition. The whole assembly was then placed in a quiet, undisturbed location, in order to minimize vibrations which induce defects in the growing crystal.

The crystal growth was terminated when the polycrystalline material in the holder was exhausted, or when the formation of parasite crystals was severely retarding the seed crystal's growth.

The apparent growth rate was not predictable. Starting with seed crystals measuring 1-2 mm, a crystal 2 cm long was obtained after two weeks, while a crystal 3 cm long was

only obtained after six weeks. All of the crystals grown by the circulation method exhibited a prismatic habit.

### 2.3. Crystal Cutting and Polishing

With the assistance of Dr. R. Morton of the Geology Department, at the University of Alberta, the single crystals of  $\text{Ba}(\text{ClO}_3)_2 \cdot \text{H}_2\text{O}$  were cut on a Buehler diamond saw, using paraffin oil as a lubricant. The crystals were supported in an aluminum chuck, and cut perpendicular to the prismatic axis. In order to minimize mechanical deformation of the single crystals, a slow cutting speed was used. Two parallel slices were cut from each crystal. The first slice ( $\approx 6$  mm thick), containing the prismatic cap, was used in the reflection studies. The second slice ( $\approx 1$  mm thick) was used to confirm the orientation of the crystal axes by the X-ray precession method.

The cut face of the prismatic cap was polished to optical flatness by a procedure similar to that described for the polycrystalline samples. Initial polishing was performed with a slurry of cerium oxide in iso-propanol upon a Buehler AB Microcloth which was affixed to a flat glass plate. The crystal face was continually rotated in a figure-eight pattern. After polishing for approximately five minutes, the crystal was thoroughly cleaned with a kimwipe, moistened with iso-propanol, then polished on a clean Buehler pad with either iso-propanol or distilled Skelly-B. By repeated application of these two polishing

stages, a surface was produced with fewer and fewer visible flaws. The mid-infrared reflectance was monitored after each session, and polishing was continued until no further improvement in the sample's reflectance was obtained.

#### 2.4 Precession X-Ray Study of the Single Crystals

The orientation of the single crystal axes was determined by the precession method. The chief advantage of this technique over the Weissenberg method is that it provides an undistorted map of the reciprocal-lattice layer.<sup>181</sup> This is accomplished by coupling the motion of the reciprocal-lattice net and the film so that they are always parallel.

The basic experimental procedure is as follows. The 1 mm thick platelet (see Section 2.3) was affixed to a glass fiber with molten shellac, so that the fiber axis was approximately bisecting the acute angle of this crystal face. The fiber was then attached to a rotatable goniometer head, and adjusted so that the plane of the crystal slice was parallel to one of the arcs. The crystal was then mounted on a Nonius precession camera, and aligned as indicated by alignment photographs. Absorption problems were minimized by arranging the X-ray beam to impinge on the edge of the crystal face, and by using Mo K $\alpha$  radiation.

The alignment photographs were taken without the use of a filter, while the zero level and first level photographs were taken with a zirconium filter. The sample-to-

film distance was 60 mm, and a precession angle of  $25^\circ$  was used to collect the reciprocal-lattice layer data. Typically, an exposure time of six hours provided sufficiently intense diffraction spots for measurement purposes.

## 2.5 Instrumentation

Specular reflection measurements on  $\text{Ba}(\text{ClO}_3)_2 \cdot \text{H}_2\text{O}$  were performed over the spectral range  $20\text{--}7000\text{ cm}^{-1}$  for the polycrystalline samples, and over the region  $100\text{--}7000\text{ cm}^{-1}$  for the single crystal samples. In order to cover the range  $20\text{--}7000\text{ cm}^{-1}$ , two Fourier transform infrared (FTIR) instruments were used. Below  $100\text{ cm}^{-1}$ , a Beckman R.I.I.C. model FS 720 interferometer was utilized; while for the region  $100\text{--}7000\text{ cm}^{-1}$ , a Nicolet model 7199 interferometer was used.

The principle of FTIR spectroscopy is the differentiation of frequency elements by division of amplitude, whereas conventional grating instruments distinguish frequency elements spatially. The essential components of an FTIR instrument are depicted schematically in Figure 2.3. Division of amplitude is accomplished by means of a Michelson interferometer. Each incident frequency is partially reflected and transmitted at the beamsplitter boundary. A phase difference, or retardation, is introduced into the recombined beam by the different path lengths to the moving and stationary mirrors. This results in a cosinusoidal dependence of intensity on retardation, whose characteristic

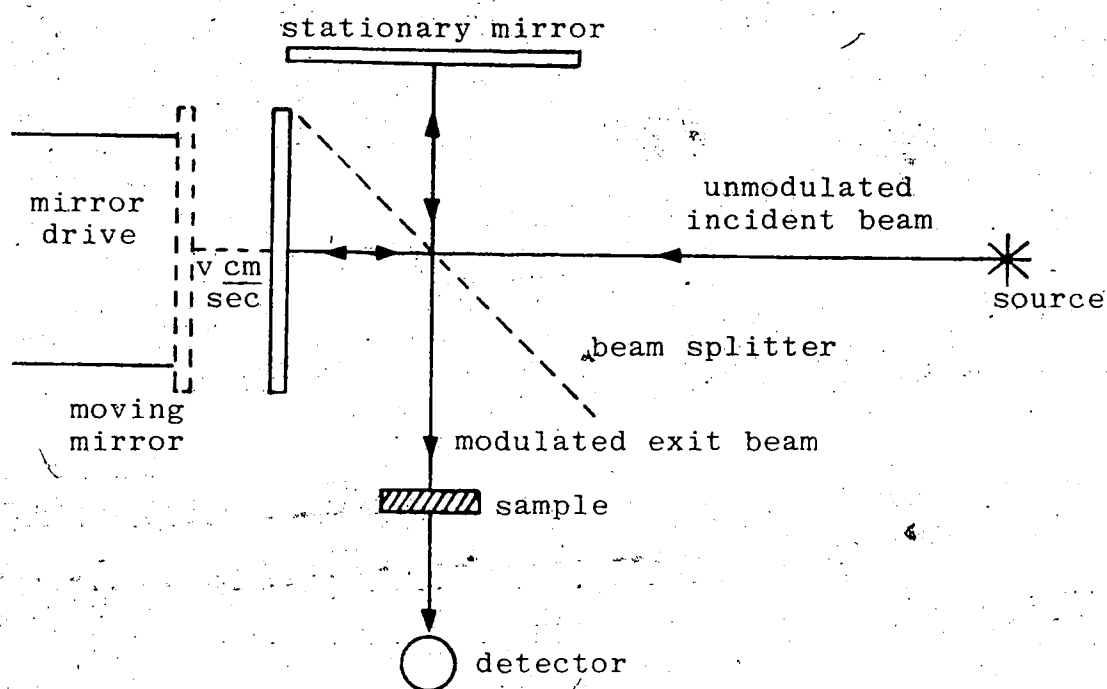


Figure 2.3 Schematic diagram of an FTIR instrument.

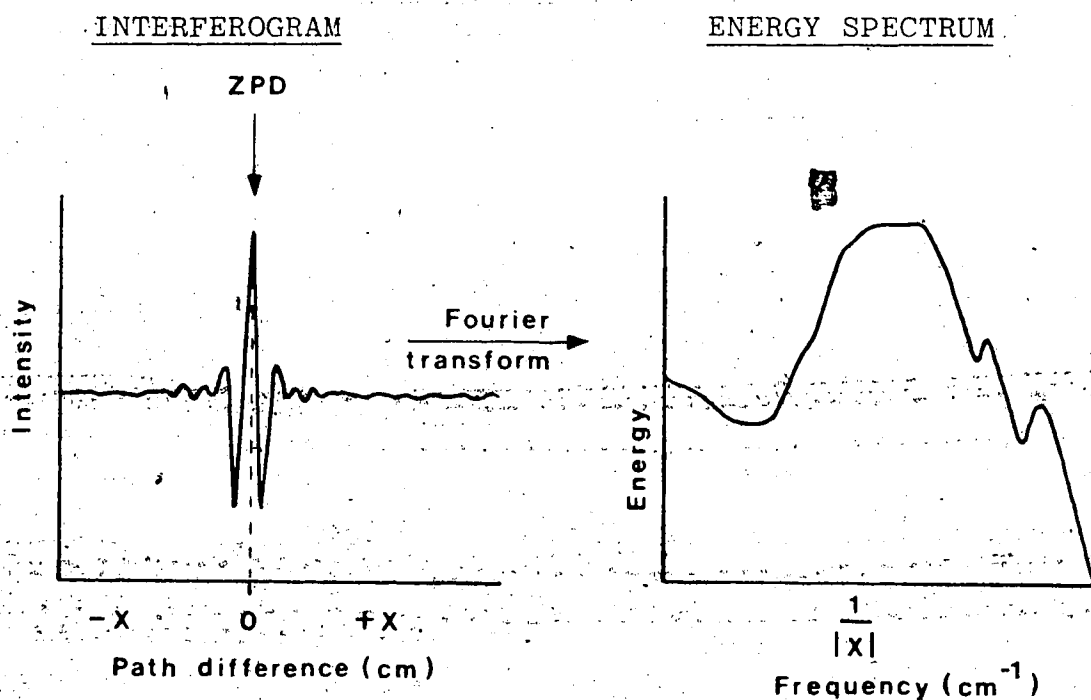


Figure 2.4 The relationship between an interferogram and a single-beam energy spectrum.

frequency,  $f_v$ , is given by:

$$f_v = 2 v \nu$$

$v$  = velocity of moving mirror ( $\text{cms}^{-1}$ )  
 $\nu$  = incident frequency ( $\text{cm}^{-1}$ )

The experiment measures the intensity of this radiation reaching the detector as a function of the retardation and this record is called the interferogram. For a broad-band source, the different cosine waves add together to give a beat pattern and the measured interferogram is the resultant of the interferograms corresponding to each incident frequency. The Fourier transform of this function is the single-beam energy spectrum (see Figure 2.4), and the ratio of the sample to the background energy spectra gives the transmittance or reflectance spectrum.

When the moving and stationary mirrors are equidistant, all of the modulated infrared frequencies are in-phase. This produces a maximum in the interferogram, which is known as the zero path difference (ZPD) peak, and its peak-to-peak voltage is a measure of the total intensity incident on the detector.

For two frequencies separated by  $\Delta\nu = \nu_1 - \nu_2$ , it is necessary to translate the moving mirror a distance  $X = 1/\Delta\nu$ , in order to observe one complete cycle of the beat pattern and therefore, to discriminate between the two frequencies. The nominal spectral resolution,  $\Delta\nu$ , is thus related to the maximum retardation by  $X_{\text{max}} = 1/\Delta\nu$ .

Because of instrumental limitations, the interferogram cannot be recorded as a continuous function, but must be

digitized, and can only be collected over a finite retardation range. These physical realities can cause significant distortion in the computed spectrum. To reduce this distortion, the procedures of apodization and phase correction are carried out.

Apodization is a process which improves the instrument line shape, i.e. the computed shape of a single, sharp, spectral line. Because the interferogram is only collected over a finite range, the computed spectrum is not a sharp line, but a band with several secondary minima or "pods". Multiplication of the interferogram by an apodization function before Fourier transformation suppresses these "pods", but with some broadening of the peak. The choice of apodization function is determined by the relative importance of these two opposing considerations.

Phase errors result from digitization errors and the frequency-dependent characteristics of the electronics and the beamsplitter optical properties. An excellent discussion of the various phase correction procedures can be found in several references.<sup>182,183</sup>

The signal-to-noise ratio of the computed spectrum is affected by various parameters. Noise is reduced by optical and electronic filtering. Optical filtering restricts the range of frequencies, or bandwidth incident on the detector; while electronic filtering restricts the bandwidth of the amplifier. Amplification of the signal enables greater precision in the analogue-to-digital conversion process and

may improve the signal-to-noise ratio, when signal averaging is performed. A selective amplification, called gain-ranging or gain-switching, enables greater amplification of points at large retardations than of points in the vicinity of zero retardation. This is often desirable when the signal is small at large path differences. The nature of the interferogram dictates the type of gain-ranging to be used. An interferogram due to a broad-band continuous source has the appearance of a sharp spike at ZPD about which can be seen modulations which rapidly decrease to an unobservably low amplitude; whereas, an interferogram caused by a sample with very narrow absorption lines shows appreciable intensity even at large retardations. In the former case, a large gain-ranging factor is used; whereas in the latter case, little or no gain-ranging is possible. The moving mirror velocity should also be selected to optimize the signal-to-noise ratio of the computed spectrum. The choice depends upon the frequency range of interest and the detector's response as a function of modulation frequency.

The three variable components of the FTIR instrument are the: source, beamsplitter and detector.

The R.I.I.C. interferometer was used with a water-cooled, 125 W, high-pressure mercury vapour lamp, mylar beamsplitters of various thicknesses (12, 25 and 50  $\mu\text{m}$ ), and a Molelectron silicon bolometer which operates at 1.3°K.

The Nicolet interferometer was used with a water-cooled Globar source, and either a liquid nitrogen cooled, type B,

HgCdTe detector, sensitive over the range  $400-7000\text{ cm}^{-1}$ , or a room temperature triglycine sulfate (TGS) detector, with polyethylene window, sensitive over the range  $100-700\text{ cm}^{-1}$ . Several different dielectric-coated and mylar beamsplitters were used, depending upon the frequency region of interest. These various components and their range of use are given in Table 2.2.

The R.I.I.C. and the Nicolet 7199 interferometers are different in several aspects of data collection and processing. Since these differences are relevant to any comparative discussion of spectra collected on these two instruments, they are briefly listed in Table 2.3.

Of particular note, is the fact that the power spectrum, i.e. the square root of the sum of the squares of the sine and cosine transforms, is computed from the R.I.I.C. data. Thus, the noise is computed to be always positive, rather than randomly positive and negative. For a noisy spectrum then, the height of the baseline is shifted above its true value. The Nicolet 7199, on the other hand, uses the Mertz multiplicative method<sup>182,183</sup> in which the Fourier-transform of the apodized interferogram is multiplied by a phase error function calculated by Fourier-transforming a short, double-sided portion of the interferogram. The power spectrum and the spectrum computed by the Mertz method, can be represented as:

Table 2.2 Source, Beamsplitters and Detectors Used on the  
Nicolet 7199 FTIR Instrument

<u>Source</u>	<u>Range of Use</u>
water-cooled Globar	100-7000 $\text{cm}^{-1}$
<u>Beamsplitters</u>	
Ge on KBr substrate	400-4800 $\text{cm}^{-1}$
Si on $\text{CaF}_2$ substrate	1150-7000 $\text{cm}^{-1}$
3 micron mylar	250-700 $\text{cm}^{-1}$
6.25 micron mylar	140-390 $\text{cm}^{-1}$
12.5 micron mylar	100-230 $\text{cm}^{-1}$
<u>Detectors</u>	
HgCdTe-B ( $\ell$ . $\text{N}_2$ cooled)	400-7000 $\text{cm}^{-1}$
TGS detector with polyethylene window	100-700 $\text{cm}^{-1}$

Table 2.3 Differences in Operation and Data Processing  
for R.I.I.C. and Nicolet 7199 Instruments

R.I.I.C.	Nicolet 7199
slow-scanning interferometer	rapid-scanning interferometer
uses remote computer (Amdahl 470)	has its own dedicated mini- computer (Nicolet 1180)
data is collected from $-X_{\max}$ to $+X_{\max}$	data is collected from $-X_{\min}$ to $+X_{\max}$
(resolution, $\Delta\nu=1/X_{\max}$ )	(resolution, $\Delta\nu=1/X_{\max}$ )
triangular apodization	Happ-Genzel apodization
computes power spectrum	uses Mertz multiplicative phase correction procedure

$$|S(v)| = \{T_{\cos}(v)^2 + T_{\sin}(v)^2\}^{\frac{1}{2}}$$

and  $B(v) = T_{\cos}(v)t_{\cos}(v) + T_{\sin}(v)t_{\sin}(v)$

where  $|S(v)|$  = power spectrum

$B(v)$  = spectrum calculated via Mertz multiplicative method

$T_{\cos}(v)$ ,  $T_{\sin}(v)$  are the cosine and sine transforms of the apodized, full interferogram

$t_{\cos}(v)$ ,  $t_{\sin}(v)$  are the cosine and sine transforms of the apodized, short, double-sided interferogram.

## 2.6 Reflectance Measurements

The infrared reflectance spectra were measured with a modified version of the Harrick retro-mirror assembly (RMA), versatile reflection accessory (VRA). The RMA enables reflectance measurements to be made over a continuous range of angles of incidence. Since this capability was not required, the RMA was used simply as a sample holder mount, for a fixed angle of incidence. The optical pathway through this accessory is illustrated schematically in Figure 2.5. The precise angle of incidence used was measured with the Nicolet instrument's alignment laser and the details of this procedure are given in Section 2.6a. By dispensing with the retro-mirror system, it was possible to eliminate one plane mirror from the optical path, and thereby improve the accessory's energy throughput.

Initial optical alignment of the reflectance accessory was achieved in two stages. First, a crude adjustment of

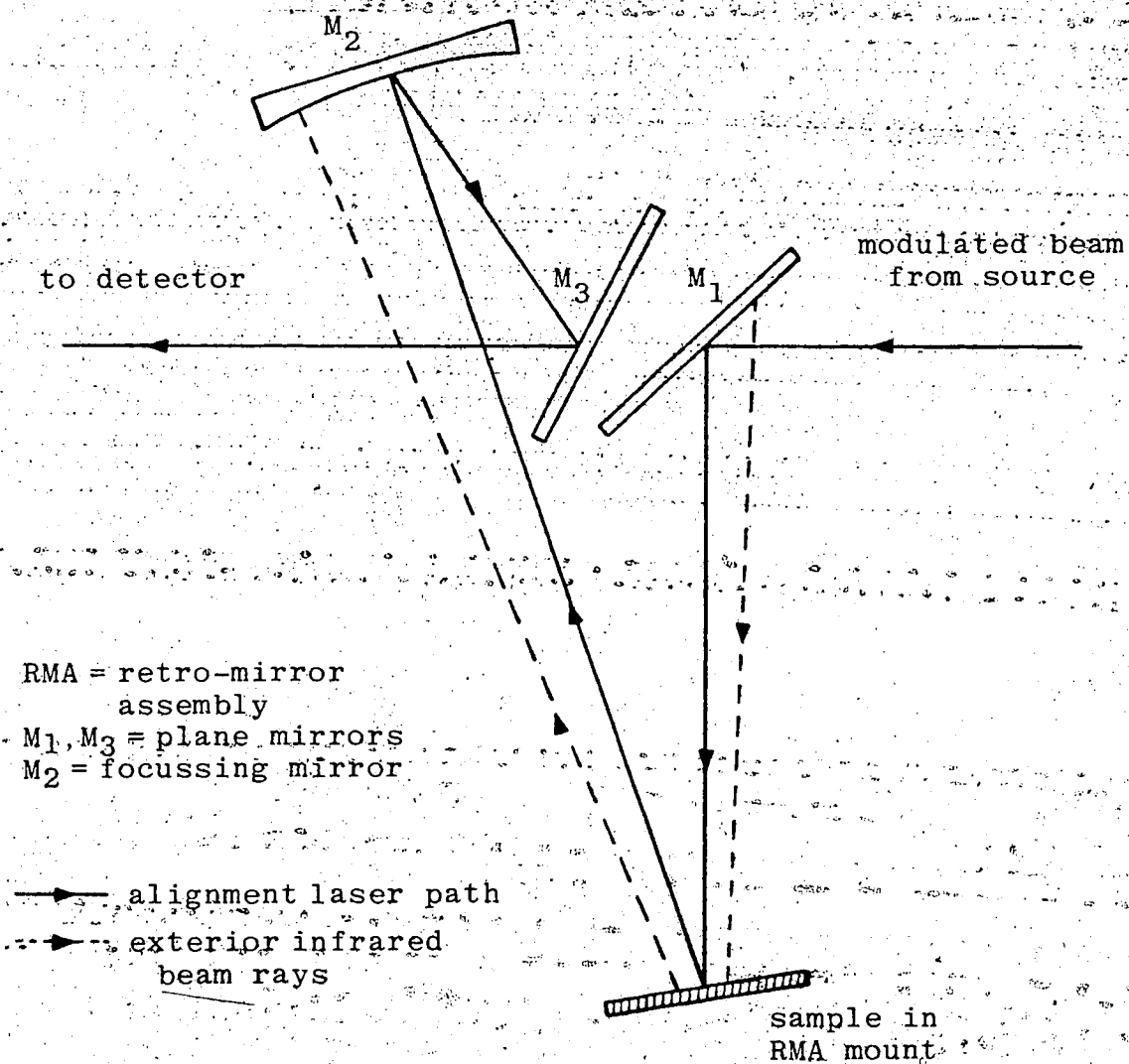


Figure 2.5 Harrick Variable Angle Reflectance Accessory, modified to operate at a fixed angle of incidence ( $I = 9.5^\circ$ ).

the mirrors was made so that a horizontal beam passed undisturbed through the accessory. This was accomplished with an auxiliary 5 mW Metrologic He-Ne laser, mounted on a tilting trough support with vertical and transverse slide adjustments.

The height of the laser was adjusted to correspond to the center of mirror  $M_1$ , and a spirit level was used to check that the laser beam's path was horizontal. The image of the beam at some point across the room was noted. The reflectance accessory was then positioned so that the front edge of its metal base was normal to the laser beam, and this configuration was secured with masking tape. A 1.5" x 2.5" front-surface aluminized,  $\text{SiO}_2$ -coated mirror was used as the sample reflecting surface. The angular scale on the RMA was set at  $15^\circ$ . Mirror  $M_1$  was adjusted so that the laser beam impinged at near-normal incidence on the sample. Mirror  $M_3$  was then adjusted so that the beam followed the correct vertical plane. The tilt of the laser path was corrected by means of focussing mirror  $M_2$ . By small systematic adjustments of these three variables, the laser beam was brought into coincidence with its original path.

The reflectance accessory was then transferred to the sample compartment of the Nicolet FTIR instrument and mounted on sliding rails which ran parallel to the infrared beam. The unit was translated until a maximum infrared signal was obtained. This was achieved when the accessory was moved

to the extreme right of the sample compartment, with the beam travelling from right to left. The energy throughput was further optimized by slight adjustments of mirrors  $M_1$ ,  $M_2$ , and  $M_3$ . When optimally aligned, the energy responded to a throughput of 80-90%. A throughput spectrum is the ratio of spectra recorded with, and without, the reflectance accessory in the beam. A typical throughput spectrum with a 0.25" diameter reflecting surface is shown in Figure 2.6. The sharp peaks are due to water vapour.

#### 2.6a Determination of Angle of Incidence

Since the reflectivity is a function of the angle of incidence, it was important to know this quantity accurately. Its measurement was facilitated by the use of the Nicolet instrument's alignment laser. When properly set, the laser simulates the infrared beam and gives a visible light source for mapping the optical pathway through the Harrick reflectance accessory (HRA). With the aid of a clear plastic triangle, the light incident and reflected at the reference mirror surface was traced onto a piece of white paper horizontally fixed to the base plate of the accessory. The angle between the entrance and exit beams was measured with a protractor. By repeating this procedure, the angle of incidence was determined to be  $9.5^\circ$  with an estimated precision of  $\pm 0.1^\circ$ . After this measurement was made, mirror  $M_1$  and the RMA angular setting were never further adjusted.

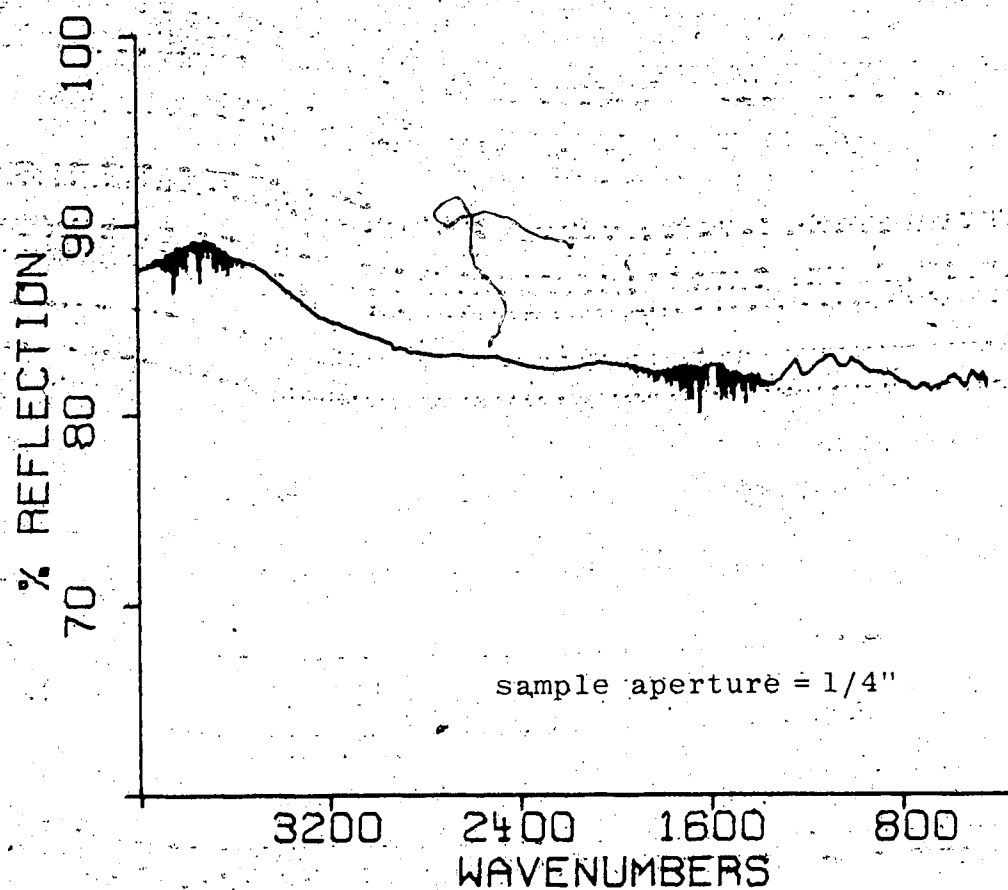


Figure 2.6 Typical mid-infrared throughput curve for Harrick reflectance accessory with gold reference mirror and  $9.5^\circ$  incidence.

Sharp features are due to water vapour.

## 2.6b Design of Sample Holders

The design of a component in an optical accessory requires an accurate knowledge of the radiation beam's path and dimensions as it traverses the system. Thus, before designing holders for the polycrystalline and single crystal samples, it was necessary to measure the size and position of the infrared beam impinging on the reflecting surface. This was accomplished in the following manner. A 1" by 2" front-surface aluminized mirror was placed in the sample mount and its position was noted. A 1" by 2" microscope slide was then covered with black paper (used to protect photographic film from light exposure) and markings 0.10" apart were made along its bottom and side edges. This blackened microscope slide was used as an adjustable mask in front of the aluminum mirror. The vertical and horizontal positions of the mask, corresponding to the onset of signal attenuation, were recorded by monitoring the size of the ZPD peak. In this way, the beam size at the reflecting surface was determined to be 6 mm. To confirm this finding and check the beam's location, a 6 mm diameter aperture was cut out of a piece of the black paper. This was taped to the front surface of the mirror, at the position determined from the previous measurements. It was noted that the infrared signal was only reduced to 96% of its former value, thus verifying the measurement procedure.

The polycrystalline sample holder was fabricated from  $\frac{1}{4}$ " thick brass. Its design is illustrated in Figure 2.7.

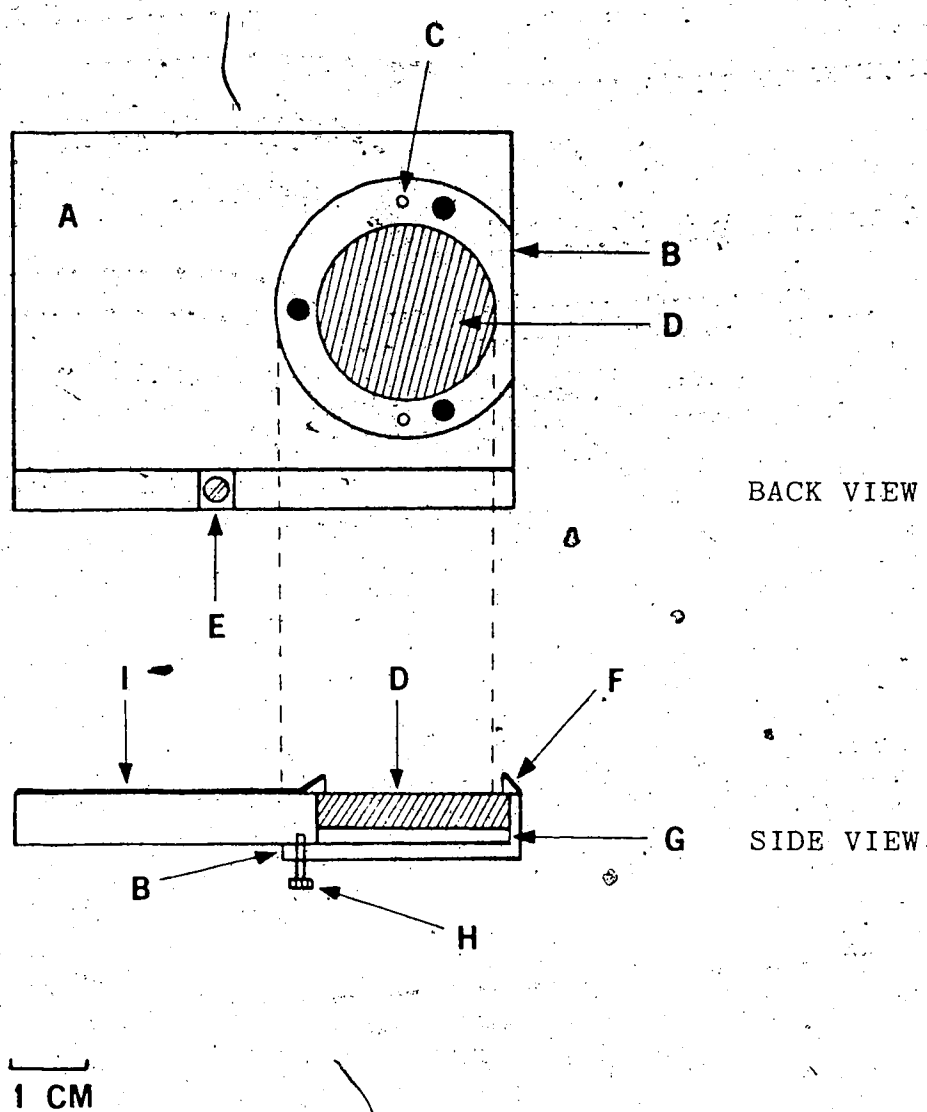


Figure 2.7 Design of polycrystalline sample holder.

A, brass holder; B, retaining plate; C, positioning pin; D, sample or reference mirror; E, brass stop; F, 45° conical rim; G, teflon spacer; H, Allen screw; I, black velvet material.

The 1" diameter sample was seated on a 1 mm lip, so that its front face coincided with the requisite reflecting plane. A teflon spacer and an open-ring retaining plate held the sample securely in place, and a brass stop enabled reproducible positioning of the sample holder. The 45° sloping rim, encircling the sample aperture, was designed to deflect any radiation not incident on the sample from reaching the detector. However, the measured reflectance with no sample was significant, particularly in the far-infrared region, where it was approximately 2.0%. This was due to the high reflectance of brass, which is a monotonically increasing function with decreasing frequency. Various procedures were tried in order to reduce this background reflection from the holder, including: sandblasting, blackening by anodization, and painting with a black absorbing paint. Measurable success was finally achieved by using a black velvet material, affixed to the front face of the holder with contact cement. The percent reflectance contributed by the holder was then reduced to approximately 0.15% in the far-infrared region.

The design of the single crystal sample holder proved to be more difficult. Initially, it was desired to have two matched sample holders which could accommodate the single crystal sample and reference mirror, respectively. However, the constraints imposed by the need for exact optical coplanarity of the reference mirror and the crystal proved too demanding. For this reason, the same sample

holder was used for the sample and background measurements.

The precision of this procedure will be discussed in Chapter V of this thesis.

The design of the single crystal sample holder is shown in Figure 2.8. It was fashioned from 0.125" thick aluminum. A  $3/8$ " hole was drilled so that various cone-shaped pieces could be inserted. This allowed some flexibility in the size of crystal that could be studied. For the majority of the single crystal measurements, a  $7/32$ " diameter sample aperture was used. The inside walls of the conical piece were tapered at  $20^\circ$  so that the converging, incident infrared beam was not significantly attenuated. A second groove was made in the RMA sample mount, parallel to the existing groove for the polycrystalline sample holder. This acted as a physical stop for the single crystal sample holder and positioned the sample in the correct reflecting plane. A piece of black paper (used to protect photographic film), taped to the front face of the holder, reduced the extraneous background reflectance to 0.02% in the mid-infrared region, and to approximately 0.03% in the far-infrared region.

#### 2.6c Design of R.I.I.C. Sample Compartment

In order to perform reflectance measurements on the R.I.I.C., it was necessary to design a sample compartment that could house the Harrick reflectance accessory. In con-

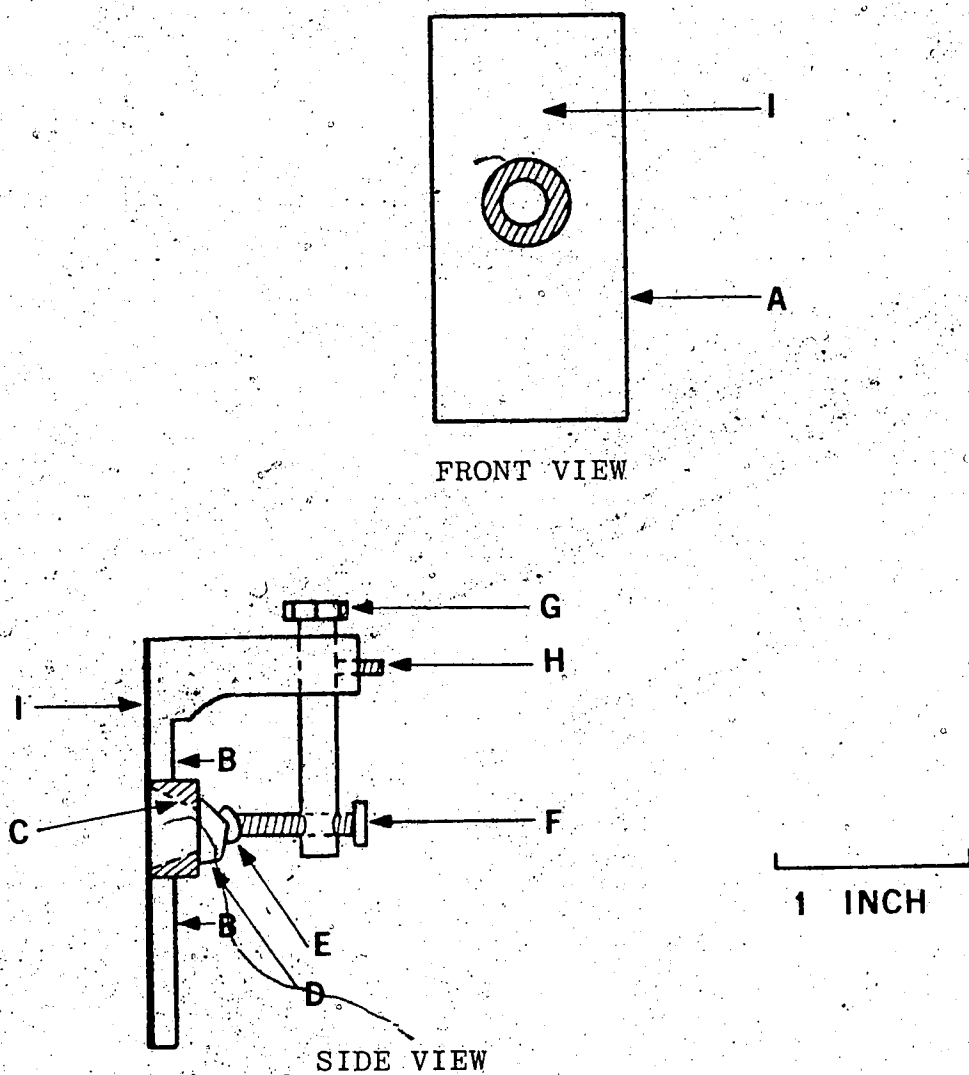


Figure 2.8 Design of single crystal sample holder.

A, Aluminum holder; B, reference markings; C, cone-shaped insert; D, single crystal or reference mirror; E, plasticine; F, nylon screw; G, positioning pin; H, teflon securing screw; I, black paper.

sultation with the Chemistry Department's machine shop, the design illustrated in Figure 2.9 was adopted.

The sample compartment is comprised of 3 main pieces:

- i) a top plate.
- ii) a rectangular box with entrance and exit ports, having vacuum seal fittings to the interferometer and detector, respectively.
- iii) a bottom plate.

All pieces were constructed of 1/2" thick aluminum. A vacuum tight seal between these three components was provided by 3/16" thick O-rings. The reflectance attachment was mounted on a stainless steel sliding rail support which was bolted to the bottom plate. This feature permitted a slight lateral adjustment of the accessory and optimization of the energy throughput. However, the horizontal positioning of the accessory was fixed so that the incident infrared beam was directed at the center of the first plane mirror,  $M_1$ .

The sample compartment was also fitted with two brass holders. One was used for the various polyethylene filters, and the other enabled the use of a polarizer.

#### 2.6d Reference Mirror and Calibration Standard

The measurement of a sample's specular reflectance on an infrared spectrometer is a relative measurement. The power reflected from the sample ( $R_s I_0$ ) is compared to that reflected from a metal surface ( $R_m I_0$ ). Thus, the ratio of the two detected powers gives the relative power reflectance

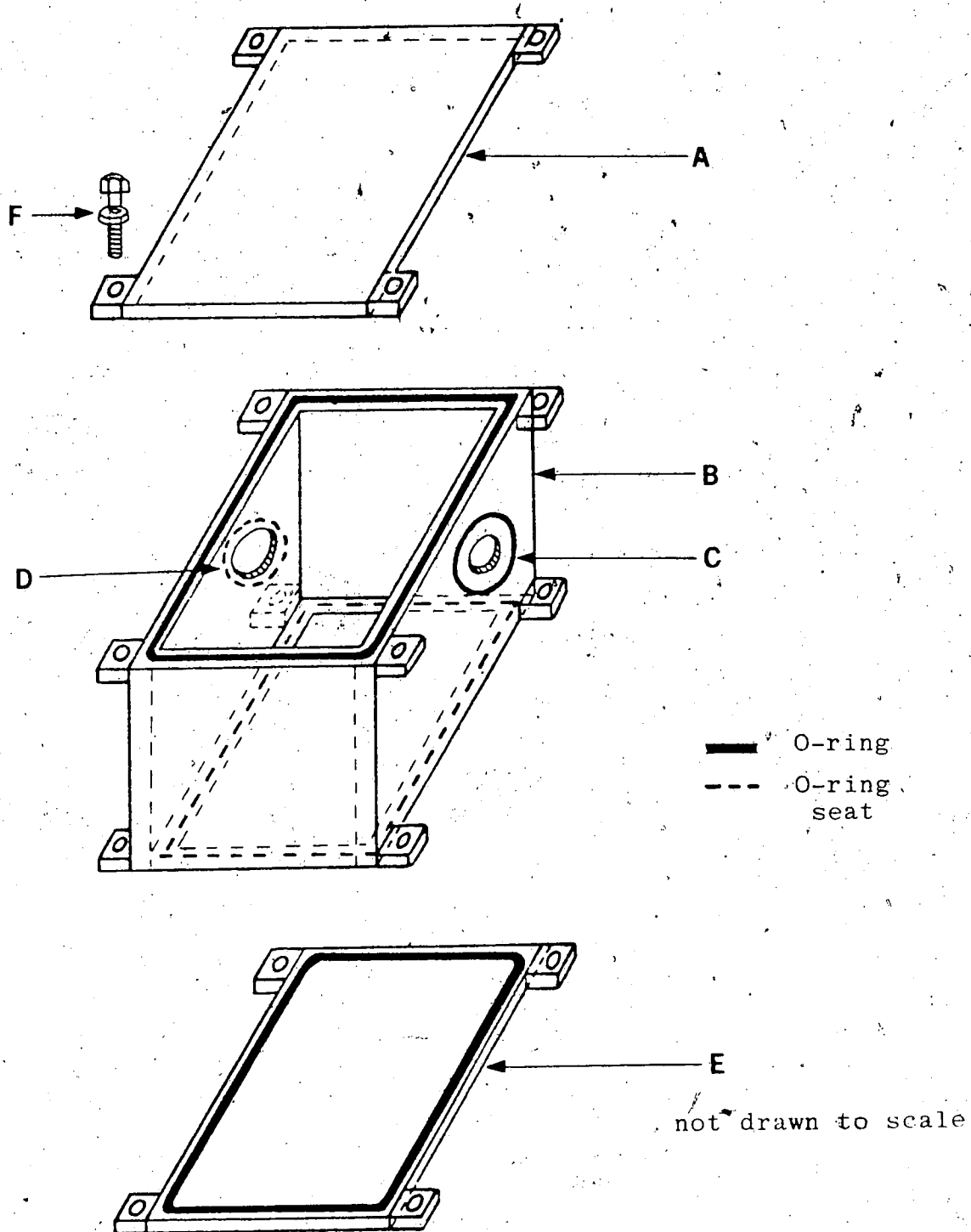


Figure 2.9 Design of R.I.I.C. sample compartment.

A, top plate; B, rectangular box; C, interferometer interface; D, detector interface; E, bottom plate; F, screw and washer.

of the sample ( $R_s/R_m$ ). Ideally, the reference surface is perfectly reflecting; in which case, this ratio gives the sample's absolute reflectance ( $R_s$ ). The term reflectivity is only used to express the ideal absolute reflectance of a sample.<sup>184</sup> Typically, the metal reflector is a thin film of aluminum, silver, or gold vacuum-evaporated onto a glass substrate.

For my reflectance measurements, the reference mirror was either a gold coated pyrex mirror or a hard gold (occluded nickel on copper) mirror. Both mirrors were 1.0" diameter flats purchased from Oriel Corporation. Although they have a purported reflectivity of >98% in the infrared region, it was not expected that this reflectivity remain constant with the mirrors' frequent usage. Therefore, for precise measurements, it was necessary to calibrate the reference mirror's reflectance.

The reflection standard had to satisfy the following requirements:

- i) its optical constants must be well known.
- ii) it must be optically and mechanically stable.
- and
- iii) it must be capable of being optically worked into a plane form.

Several pure, elemental semi-conductors meet these requirements and, of these, silicon was adopted in this study. Its optical constants have been studied by several workers over the entire infrared region.<sup>38,150,185</sup>

A 1" diameter boule of silicon was provided by Dr. F. Weichman, of the Physics Department, at the University of Alberta. Unfortunately, its purity is not known. With the assistance of Dr. C. Scarfe, of the Geology Department, the boule was cut on a Buehler diamond saw, using distilled water as a lubricant. To eliminate multiple reflection effects, the back face of the silicon sample was wedged at  $10^\circ$  to the cylinder axis. The minimum sample thickness was 0.28" (see Figure 2.10).

The optical polishing of the silicon standard was a long and tedious procedure. Mr. B. Arnold, of the Electrical Engineering Department, instructed me on the technique.

The sample was first ground on a flat glass plate with successively smaller grit sizes of alumina (15, 9, and  $5\text{ }\mu\text{m}$ ) using water as a lubricant. Each grinding session was approximately 5 min in duration and each grit size was used until a uniform finish was obtained. After each grinding stage, the glass plate was checked for flatness and re-ground, if necessary, and the sample was thoroughly washed with running water. Polishing was then done on a hard-pitch lap. First,  $1\text{ }\mu\text{m}$  alumina dispersed in a soap solution was used. This polishing stage was continued for several hours;

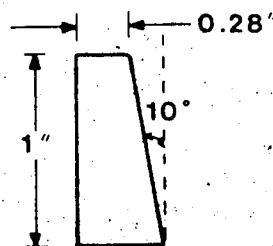


Figure 2.10 Dimensions of silicon calibration standard

again, each session lasting 5 min. Between sessions, the pitch lap was flattened by rubbing its surface with a slurry of the polishing compound and a warm plate, then pressing the plate on the lap with a brass weight for 5 min. Final polishing was performed on a clean pitch lap with a slurry of 0.3  $\mu\text{m}$  alumina and distilled water.

This procedure produced an almost scratch-free, mirror-like surface. The optical flatness was determined to be  $1/4 \lambda$  at the Helium wavelength,  $\lambda = 0.59 \mu\text{m}$ .

## 2.7 Operating Procedures and Parameters

The objective of this research project was to obtain quantitative reflection results. For this reason, considerable time was devoted to optimizing the various operating conditions and to adopting a systematic approach. The basic experimental procedure will be briefly outlined for reflectance measurements on the Nicolet 7199 instrument. This procedure was followed after the initial alignment, described in Sections 2.6 and 2.6a.

All measurements were made at room temperature. Since surface condition greatly affects a sample's reflectance, special care was taken to minimize surface contamination by always wearing surgical gloves whenever handling the samples or mirrors. Any dust was blown off the mirrors with compressed air.

The Harrick reflection accessory was positioned to the extreme right of the sample compartment and secured by means

of a retaining plate. The gold reference mirror was placed in the sample holder and this assembly was inserted into the sample mount of the RMA. The previously optimized operating parameters were then set, and the infrared signal was monitored on a CRT display. By small adjustments of mirrors  $M_2$  and  $M_3$  (see Figure 2.5), the signal was maximized. For all experiments, the gain was set so that the ZPD peak measured 5-10 V. Instrument stability was then checked via 100% lines. A 100% line is a simple ratio of two successively collected spectra taken with the gold mirror in place. The deviation from 100% gives a measure of the signal-to-noise ratio and the instrumental drift. If the 100% lines were satisfactory and the energy throughput of the accessory high (i.e. 80-90% of the open-beam value), then no further tuning was done. However, in some cases, the instrumental performance could be improved by a slight realignment of the stationary mirror of the interferometer.

The instrument was then purged with dry nitrogen gas from a liquid nitrogen reservoir in order to remove atmospheric water vapour and carbon dioxide from the optical path. After collecting several background spectra, the gold mirror was replaced with the silicon calibration standard. A series of silicon reflectance spectra were taken in order to check the reproducibility of the positioning of the sample and sample holder. The spectrum used for calibration purposes was the average of these various spectra.

The polycrystalline sample of  $\text{Ba}(\text{ClO}_3)_2 \cdot \text{H}_2\text{O}$  was polished on a chamois with iso-propanol or Skelly-B, and allowed to dry. The sample then replaced the silicon standard. Two successive 250 scan collections were taken immediately, without purging. It was found that prolonged purging caused significant deterioration of the sample's reflectance. This phenomenon is discussed more fully in Chapter III. The sample was then repolished and a further set of spectra were collected.

For reflectance measurements on the single crystal samples, the above procedure was slightly modified. Because of the anisotropic nature of the single crystals, it was desired to probe the dependence of the optical constants on the direction and polarization of the incident light, relative to the crystal orientation. Therefore, it was important to have these quantities well-defined for a given experiment. Polarized infrared radiation was produced by various wire grid polarizers. The different substrates were:  $\text{BaF}_2$  (near-infrared),  $\text{AgBr}$  (mid-infrared), and polyethylene (far-infrared). The spectra of the gold mirror reference surface and of the single crystal's reflecting face were measured with  $0^\circ$  (TE) polarization, i.e. with the electric vector perpendicular to the plane of incidence. The single crystals were rotated so that the desired crystal axis was aligned parallel to this direction. The reasons for rotating the sample, rather than the polarizer, were two-fold:

- i) for our Nicolet 7199 interferometer, it was noted that the energy throughput was generally greater for  $0^\circ$  polarization than for  $90^\circ$  polarization, particularly in the far-infrared region.
- ii)  $0^\circ$  polarized radiation is always parallel to the sample surface, whereas  $90^\circ$  polarized radiation is only parallel to the sample surface at normal incidence. Therefore, for an angle of incidence of  $9.5^\circ$ , some polarization information is lost if  $90^\circ$  polarized light is used.

Although the basic procedure for obtaining reflectance measurements was the same for the various spectral regions, the particular operating parameters were different, as detailed below.

#### 2.7a Near-Infrared ( $1800-7000\text{ cm}^{-1}$ )

The globar source,  $\text{CaF}_2$ -Si beamsplitter and HgCdTe-B detector were used in this region. The spectral bandwidth was set at  $15798.0\text{ cm}^{-1}$  and the high-pass (HPS) and low-pass (LPS) electronic filter settings (at which they attenuate by 3dB) were set at 250 Hz and 100 kHz, respectively. The source aperture was 6.35 mm in diameter and the moving mirror velocity was 0.783 cm/sec.

It was found that careful alignment of the interferometer stationary mirror was necessary for efficient operation in this region. It was also necessary to allow the system to equilibrate for several hours after alignment, otherwise the high-frequency performance significantly deteriorated with time.

Because the  $\text{Ba}(\text{ClO}_3)_2 \cdot \text{H}_2\text{O}$  samples exhibited very weak, broad-featured, reflectivity in this region, the spectra

were collected at  $8\text{ cm}^{-1}$  resolution, and with a gain-range factor of 8.

#### 2.7b Mid-Infrared ( $400\text{--}4000\text{ cm}^{-1}$ )

The globar source, KBr-Ge beamsplitter, and HgCdTe-B detector were used in this region. The spectral bandwidth was set at  $7899.0\text{ cm}^{-1}$ , and the HPS and LPS electronic filters were set at 100 Hz and 50 kHz, respectively. The source aperture and moving mirror velocity were the same as for the near-infrared region. However, no gain-ranging was used because the sample interferogram displayed large alternating intensity over the entire sampling interval.

Spectra were collected at  $2\text{ cm}^{-1}$  resolution.

#### 2.7c Far-Infrared on Nicolet ( $100\text{--}400\text{ cm}^{-1}$ )

The globar source, mylar beamsplitters ( $6.25\text{--}12.5\text{ }\mu\text{m}$ ), and TGS detector with polyethylene window were used in this region. A black polyethylene filter prevented the unwanted modulated energy above  $1300\text{ cm}^{-1}$  from reaching the detector, and resulted in a significant improvement in the signal-to-noise ratio.

The spectral bandwidth was set at  $7899.0\text{ cm}^{-1}$  and the HPS and LPS electronic filters were set at 10 Hz and 2 kHz, respectively. The source aperture was 10 mm in diameter and the moving mirror velocity was approximately 0.15 cm/sec. No gain-ranging was used for the reason given in Section 2.7 b.

Because the unsupported mylar films are very susceptible to pressure fluctuations which can cause variable optical path lengths, it was important to decrease the instrument's purge rate. Since the data collections were necessarily longer in this spectral region, the reduced purge rate also helped to minimize surface deterioration effects of the  $\text{Ba}(\text{ClO}_3)_2 \cdot \text{H}_2\text{O}$  samples (Chapter III).

Spectra were collected at  $2 \text{ cm}^{-1}$  resolution.

#### 2.7d Far-Infrared on R.I.I.C. ( $20\text{-}250 \text{ cm}^{-1}$ )

The Hg lamp, mylar beamsplitters (12, 25 and  $50 \mu\text{m}$ ), and Si bolometer were used in this region. Filtering was accomplished by various Beckman cut-off filters, which are listed in Table 2.4.

Table 2.4 Frequency Range Covered by the Mylar Beamsplitters on the R.I.I.C.

<u>Beamsplitter</u>	<u>Filter #</u>	<u>(Cut-off frequency)</u>	<u>Range of Use</u>
12 $\mu\text{m}$	#4	( $250 \text{ cm}^{-1}$ )	60-200 $\text{cm}^{-1}$
25 $\mu\text{m}$	#2	( $125 \text{ cm}^{-1}$ )	40-100 $\text{cm}^{-1}$
50 $\mu\text{m}$	#1	( $80 \text{ cm}^{-1}$ )	20-50 $\text{cm}^{-1}$

Prior to collecting the interferogram data, the sample compartment was evacuated to  $\approx 0.05$  torr. Three successive backgrounds were recorded with the gold mirror, followed by three successive sample collections. The resultant reflect-

ance spectrum was the average of these three sample runs ratioed against the corresponding background runs. The resolution obtained after apodization was either  $8\text{ cm}^{-1}$  or  $2\text{ cm}^{-1}$ .

## CHAPTER III.

### SAMPLE CHARACTERIZATION, DATA HANDLING PROCEDURES, AND REFLECTION RESULTS FOR $\text{Ba}(\text{ClO}_3)_2 \cdot \text{H}_2\text{O}$

This chapter describes the treatment and evaluation of the experimental reflection results for polycrystalline and single crystal  $\text{Ba}(\text{ClO}_3)_2 \cdot \text{H}_2\text{O}$ . This involved sample characterization via X-ray methods, to determine crystal axes orientation; optical quality checks, as measured by ultimate reflectance; and consistency of sample preparation, by a comparative study of two samples (Section 3.1). The reflectance data were then averaged, scaled, and calibrated to obtain a high signal-to-noise ratio, smooth overlap between spectral regions, and accurate results, respectively (Section 3.2). The final composite reflectance spectra are presented in Section 3.3.

#### 3.1 Sample Characterization

##### 3.1a Characterization of Single Crystal $\text{Ba}(\text{ClO}_3)_2 \cdot \text{H}_2\text{O}$

Large, single crystals of  $\text{Ba}(\text{ClO}_3)_2 \cdot \text{H}_2\text{O}$  were grown from a saturated, aqueous solution by the circulation method (Section 2.2b). These crystals all exhibited a prismatic habit and, from morphological studies,<sup>103</sup> we know that the prismatic axis coincides with the c-crystal axis. A typical single crystal and its dimensions are shown in Figure 3.1. The relationship between the external morphology and the crystal's point-group symmetry is depicted in Figure 3.2; the two-fold rotation axis is shown coming out of the page. It can be

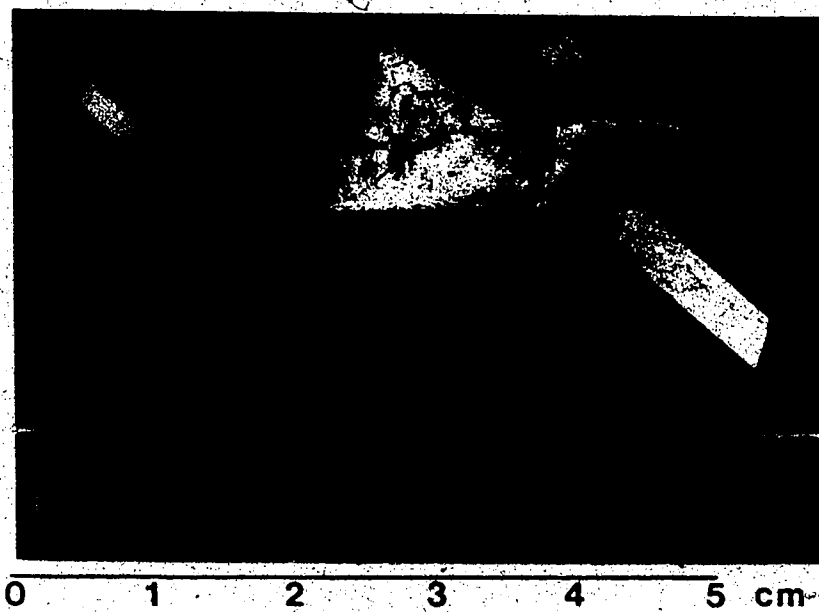


Figure 3.1 A typical single crystal of  $\text{Ba}(\text{ClO}_3)_2 \cdot \text{H}_2\text{O}$

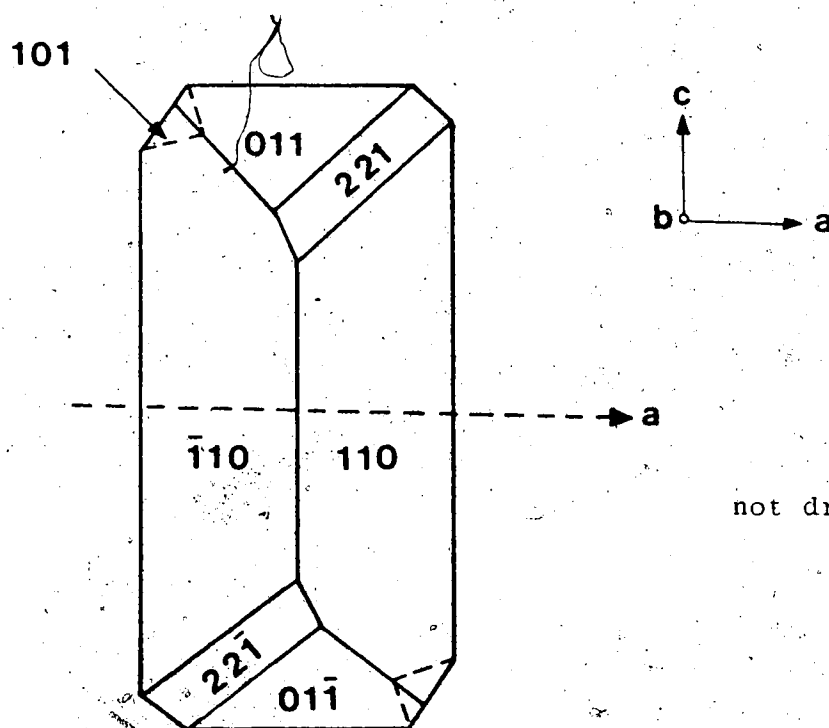


Figure 3.2 Crystal habit of  $\text{Ba}(\text{ClO}_3)_2 \cdot \text{H}_2\text{O}$

Class 2/m

seen that the crystal has well-developed (101), (011), (221), and (110) faces. These faces were identified from the known lattice parameters<sup>105</sup> and measurements of the included angle between symmetry-related adjacent faces.

The crystal was cut perpendicular to the prismatic axis (Section 2.3) and this cut face was used in the reflection studies. A second parallel slice (~1 mm thick) was used to determine the orientation of the crystal axes in this a'b reflection plane. The a' direction defines the projection of the a-axis onto the plane normal to the c-axis. A preliminary visual examination showed that this face was a parallelogram with measured edge angles of  $82 \pm 1^\circ$  and  $98 \pm 1^\circ$ . Comparison with Figure 3.3, which describes the geometry of the a'b plane, based on neutron-diffraction values<sup>105</sup> of the lattice constants, shows that the a' axis bisects the  $82^\circ$  angle. Since the observed crystal morphology does not always mirror the crystal symmetry, this assignment was checked by X-ray precession measurements (Section 2.4).

The zero level (hk0) precession photographs displayed mm symmetry, i.e. mirror symmetry with respect to both axes. The observed systematic absences were hk0:  $h+k=2n+1$ . This indicated that the crystal was either C- or I- centered. The reflections were indexed and the axial lengths determined from the standard equations:

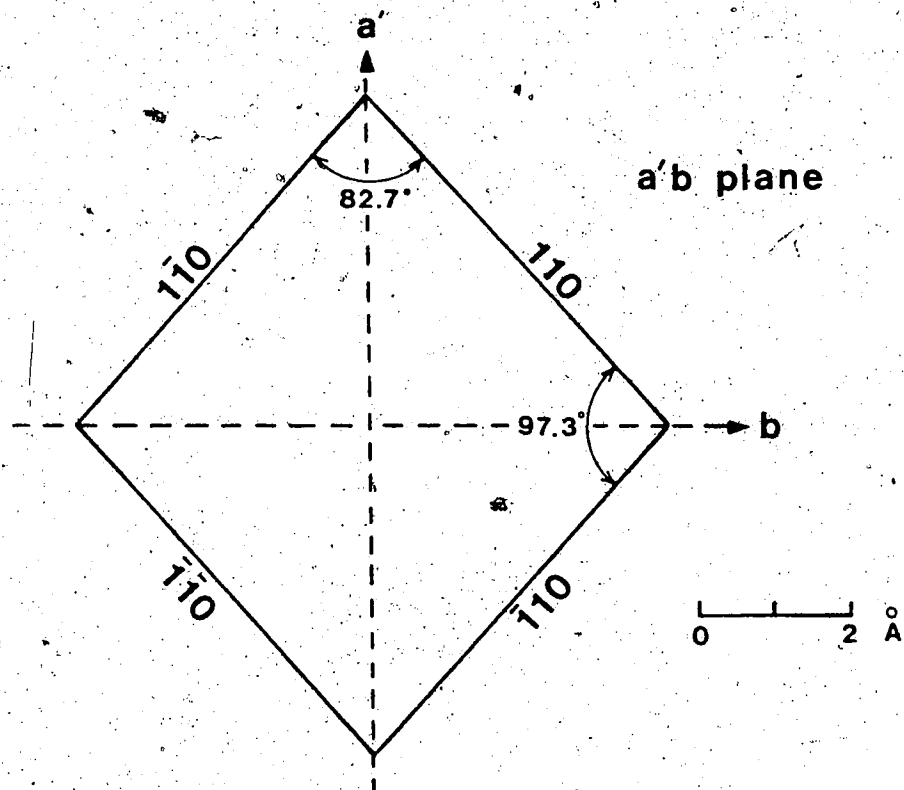


Figure 3.3 Crystal face of  $\text{Ba}(\text{ClO}_3)_2 \cdot \text{H}_2\text{O}$  obtained on cutting single crystal perpendicular to prismatic c-axis.<sup>105</sup>  
 $a' = a \cos(\beta - 90^\circ)$

Table 3.1 Comparison of Literature<sup>105</sup> and Measured Axial Lengths for  $a'b$  Crystal Face of  $\text{Ba}(\text{ClO}_3)_2 \cdot \text{H}_2\text{O}$

Literature <sup>105</sup> (Å)	Measured (Å)		
	SC-BCL·H2O-01		SC-BCL·H2O-02
$a' = 8.898$	8.86	8.92	8.91
$b = 7.832$	7.79	7.80	7.75

$$\zeta = \frac{\sum y_n}{\sum n \times 60.0 \text{ mm} \times 0.7107 \text{ \AA}}$$

where  $n = h$  or  $k$  index for reflections along  $a$  or  $b$  axis, respectively

$y_n$  = separation (in mm) between  $+n$  and  $-n$  layer lines

$\zeta$  = reciprocal-lattice axial length ( $a^*$  or  $b^*$ )

$$b = \frac{1}{b^*}$$

$$a' = \frac{1}{a^* \sin \beta}$$

The literature<sup>105</sup> and measured results are compared in Table 3.1 for the two single crystals studied (denoted SC-BCL-H20-01 and SC-BCL-H20-02). Because every second reflection is absent, these results are the average of only three or four measurements. In the case of sample SC-BCL-H20-01, the axial lengths were determined for two different photographs, recorded with exposure times of six hours and eleven hours, respectively. These X-ray findings confirmed the tentative identification of the crystal axes based on measurements of the edge angles.

Because it is not possible to distinguish mirror symmetry from two-fold rotation symmetry in a zero-level photograph, a first level ( $hkl$ ) photograph was also obtained. It was found that the mirror symmetry was conserved about the  $a^*$  axis, but not about the  $b^*$  axis; the intensity of the spots differed for corresponding  $hkl$  and  $hk\bar{l}$  reflections. This indicated that there was a two-fold rotation axis along  $b$ . The observed systematic absences were:

h0l for all values of h, and hkl for even values of the sum,  $h+k$  (i.e.  $h+k+l=2n+1$ ). These absences, in conjunction with the diffraction symmetry observed in the zero-level photograph, indicated that there was a c-glide plane perpendicular to b, and that the crystal was I-centered; giving the total diffraction symmetry as  $I2/c$ , the expected space group for  $Ba(ClO_3)_2 \cdot H_2O$  (see Section 1.3).

After confirming the orientation of the crystal axes in the a'b plane, the cut sections, containing the prismatic cap, were polished according to the procedure described in Section 2.3. Polishing with cerium oxide and iso-propanol was terminated, when no further increase in the sample's reflectance was apparent. Figures 3.4 and 3.5 compare the polarized, mid-infrared reflectance spectra of samples, SC-BCL.H2O-01 and SC-BCL.H2O-02, at a similar stage of optical finish. It can be seen that the agreement is extremely good. However, it was possible to ultimately obtain a slightly better finish for sample -02 than sample -01. The only significant discrepancy between the two samples was evident in the region  $750-850\text{ cm}^{-1}$ , which has been expanded for clarity in the insets. Sample -02 (Curves B) exhibited several weak reflectance features: at 788, 809, and  $816\text{ cm}^{-1}$  in the b-polarized spectrum, and at  $786\text{ cm}^{-1}$  in the a'-polarized spectrum; whereas, sample -01 (Curves A) displayed only a smooth reflectance edge in this region, under both polarizations. This may be explained by the fact that sample SC-BCL.H2O-01 was prepared from

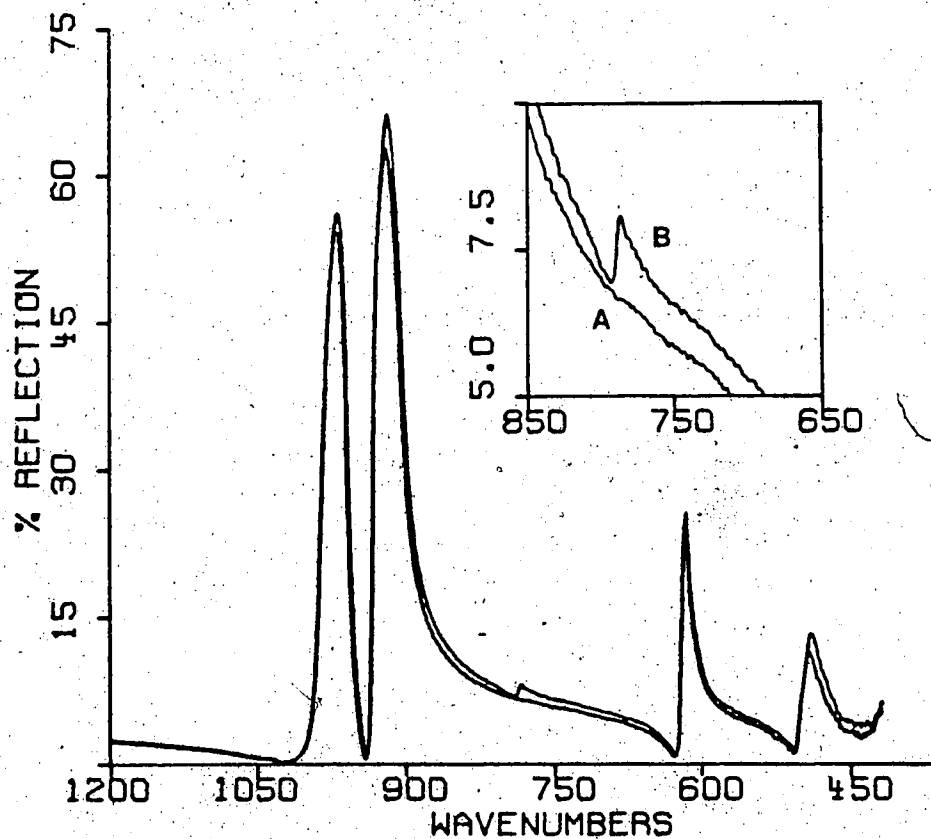
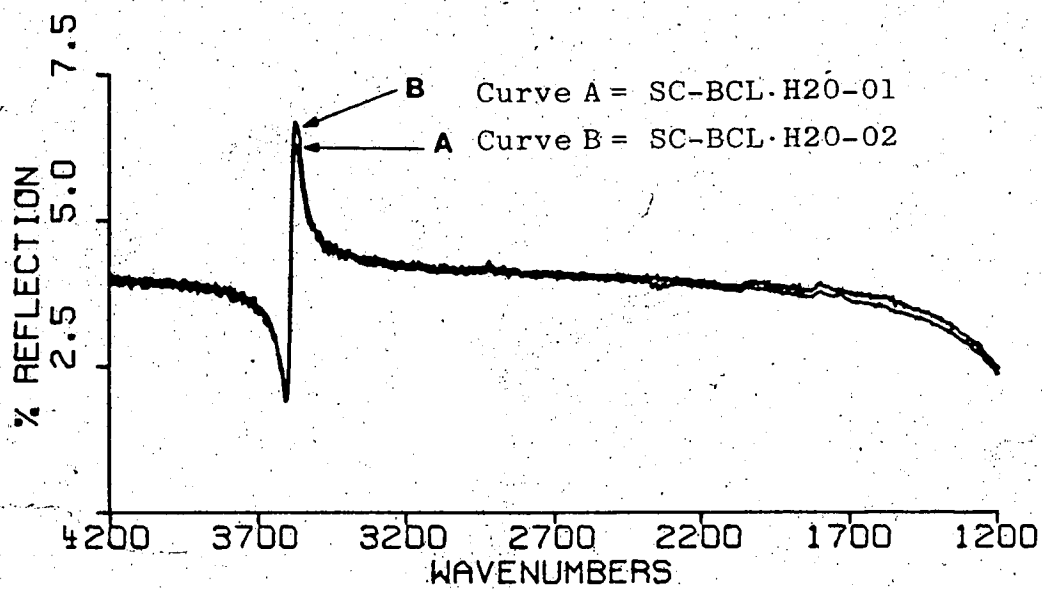


Figure 3.4 Comparison of a'-polarized reflectance from (001) face of two different samples of single crystal  $\text{Ba}(\text{ClO}_3)_2 \cdot \text{H}_2\text{O}$ .

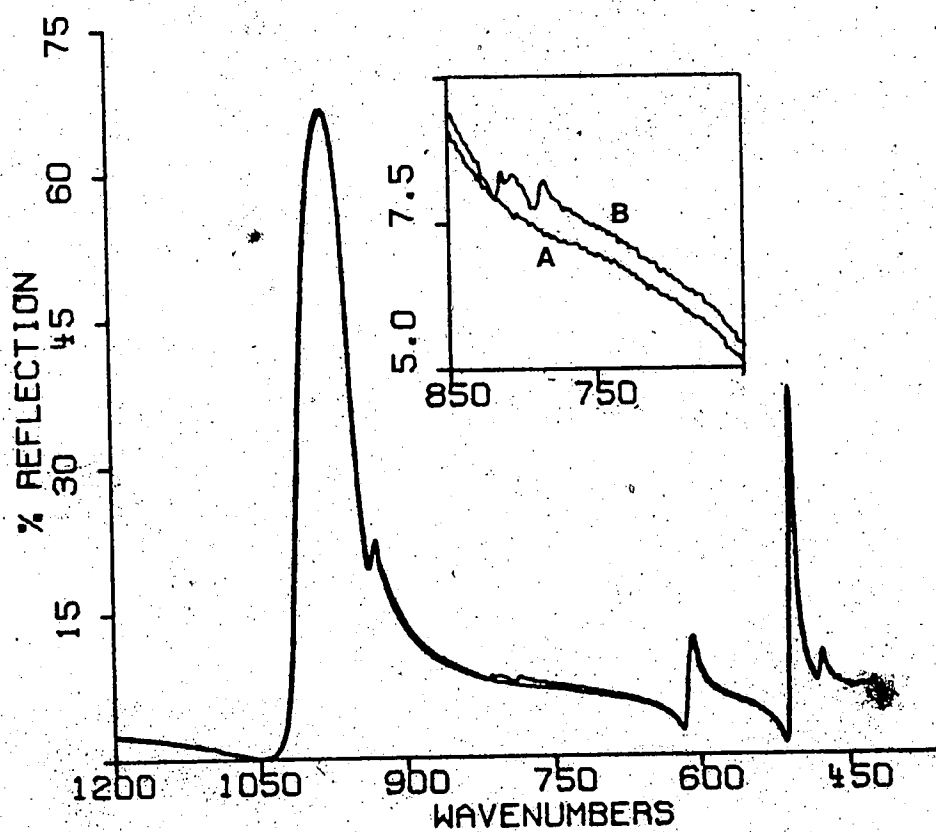
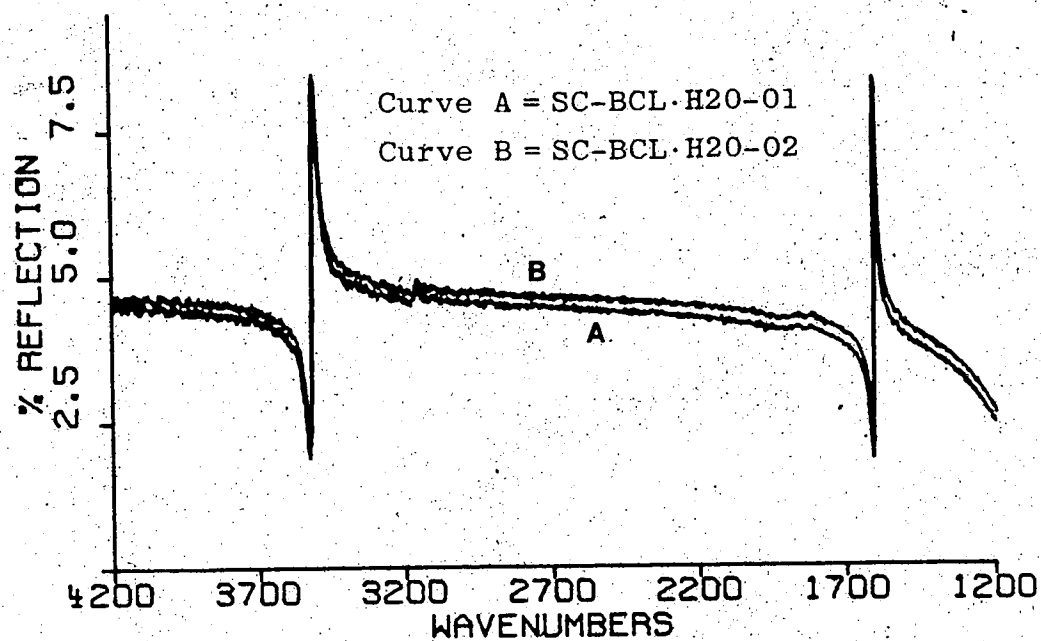


Figure 3.5 Comparison of b-polarized reflectance from (001) face of two different samples of single crystal  $\text{Ba}(\text{ClO}_3)_2 \cdot \text{H}_2\text{O}$ .

$\text{Ba}(\text{ClO}_3)_2 \cdot \text{H}_2\text{O}$  obtained from Allied Chemicals, whereas the starting material for sample SC-BCL-H2O-02 was supplied by Matheson Co. Inc., and was undoubtedly slightly impure. This trace impurity is most likely  $\text{Ba}(\text{BrO}_3)_2 \cdot \text{H}_2\text{O}$ , which is isomorphous<sup>106</sup> with  $\text{Ba}(\text{ClO}_3)_2 \cdot \text{H}_2\text{O}$ , and which according to Rocchiccioli,<sup>186</sup> exhibits infrared absorption peaks at 784, 810 and 816  $\text{cm}^{-1}$ . Since the corresponding reflectance peaks show a polarization dependence, this suggests that  $\text{Ba}(\text{BrO}_3)_2 \cdot \text{H}_2\text{O}$  co-crystallizes with  $\text{Ba}(\text{ClO}_3)_2 \cdot \text{H}_2\text{O}$  in a regular manner.

### 3.1b Characterization of Polycrystalline $\text{Ba}(\text{ClO}_3)_2 \cdot \text{H}_2\text{O}$

The polycrystalline samples of  $\text{Ba}(\text{ClO}_3)_2 \cdot \text{H}_2\text{O}$  were made by compacting the powder into a disc using a hydraulic press (Section 2.2a). A final sample pressure of ~800 bar gave the best quality discs, as appraised by their ultimate reflectivities, after a strengthening and polishing procedure. Although a polycrystalline sample holder was specifically designed to accommodate these 1" diameter discs (see Figure 2.7), it was found that more reproducible results were obtained with the single crystal holder and an aperture of 7/32" (Figure 2.8). Thus, all final reflectance spectra, reported for  $\text{Ba}(\text{ClO}_3)_2 \cdot \text{H}_2\text{O}$  in this thesis, were measured with this single crystal holder.

To ensure that the polishing procedure did not induce structural changes in the samples, the reflectance was monitored prior to, and after each polishing stage. Fig-

ure 3.6 illustrates the dramatic improvement in the optical quality of the sample, achieved after only a few polishing sessions. It is suspected that the features at  $1850\text{ cm}^{-1}$  and  $2900\text{ cm}^{-1}$  in Curve B of Figure 3.6 are spurious, since they disappeared upon further polishing. The other spectral features, however, remained fairly constant in relative magnitude, so they are considered genuine.

Two samples were studied in detail, and these are denoted POLY-BCL·H<sub>2</sub>O-02 and POLY-BCL·H<sub>2</sub>O-05. The final reflectivities exhibited by these two samples were in excellent agreement, as can be seen from Figure 3.7.

To confirm the sample's polycrystalline nature, its reflectance spectrum was recorded with polarized radiation (Figure 3.8). It was found that, for a particular sample orientation, all spectral features observed under TE polarization were retained in the same relative proportion under TM polarization. Thus, the sample was truly composed of randomly oriented microcrystals. The only difference between the two spectra was a higher reflectance in the case of TE polarization. This is a consequence of the fact that the angle of incidence was  $9.5^\circ$ , and not  $0^\circ$ . From equations [1.36]-[1.40], it can be determined that if the normal incidence reflectance,  $R_0$  is 0.05, and the sample is non-absorbing, then at  $9.5^\circ$  incidence, the s-(TE) and p-(TM) polarized reflectances are:  $R_s = 0.052$  and  $R_p = 0.048$ , giving an expected difference of  $\Delta R_{sp} = 0.004$  or

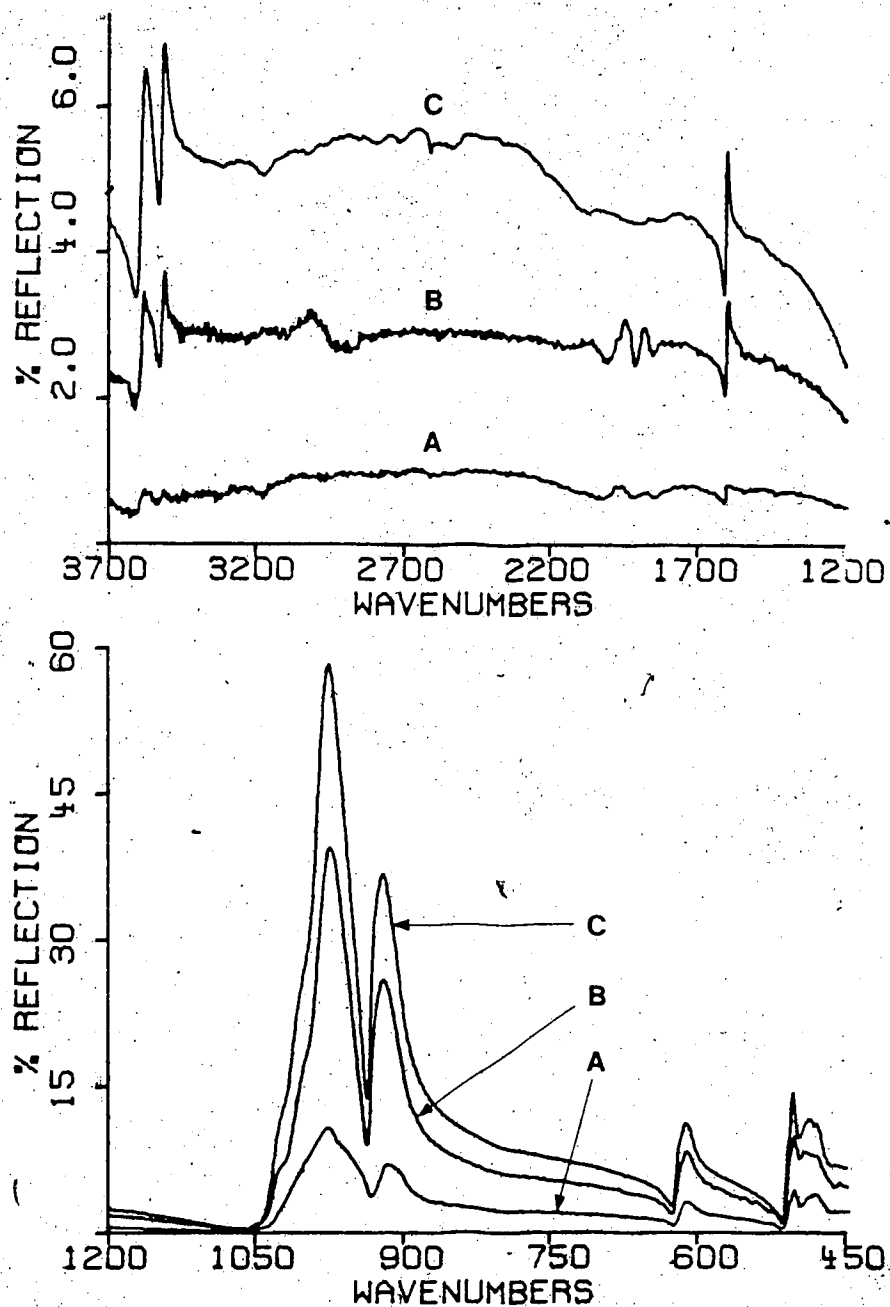


Figure 3.6 Reflectance spectra of polycrystalline  $\text{Ba}(\text{ClO}_3)_2 \cdot \text{H}_2\text{O}$  before and after polishing treatments.

Curve A: strengthened sample, before polishing

Curve B: same sample, after polishing with cerium oxide and iso-propanol

Curve C: same sample, after further polishing with cerium oxide and iso-propanol

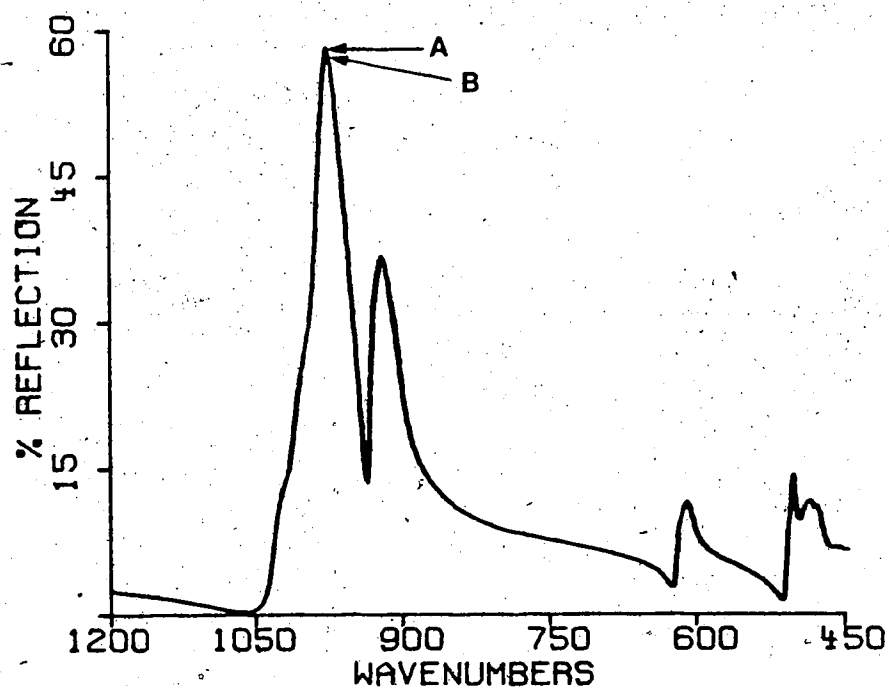
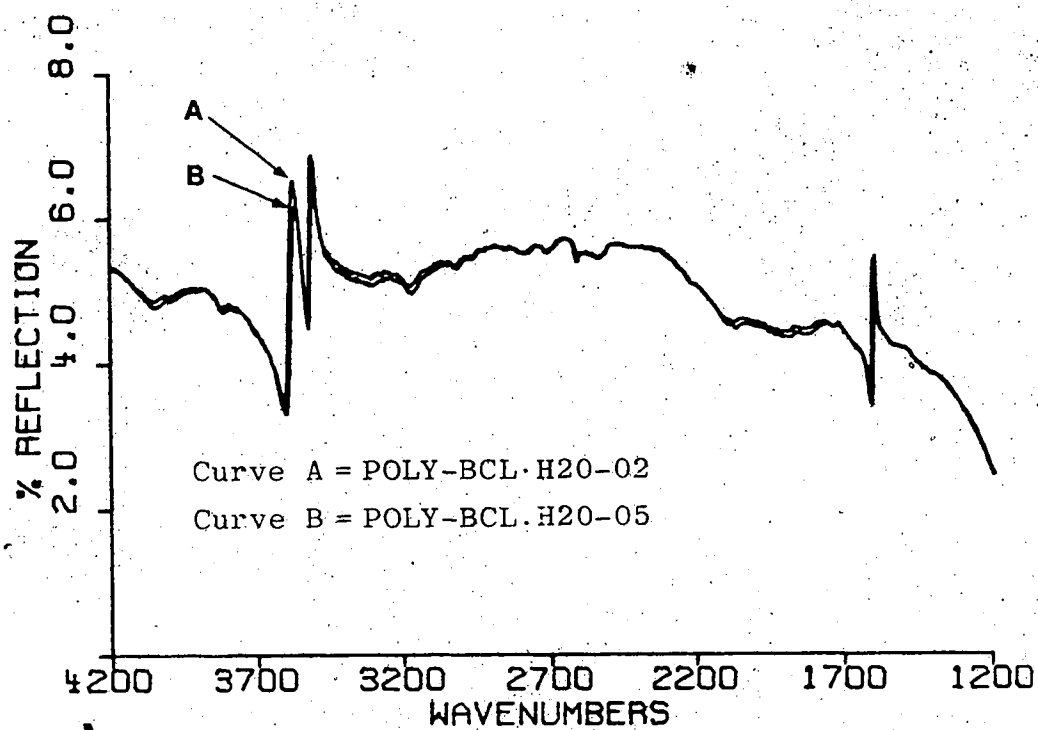


Figure 3.7 Comparison of unpolarized reflectance of two different samples of polycrystalline  $\text{Ba}(\text{ClO}_3)_2 \cdot \text{H}_2\text{O}$ .

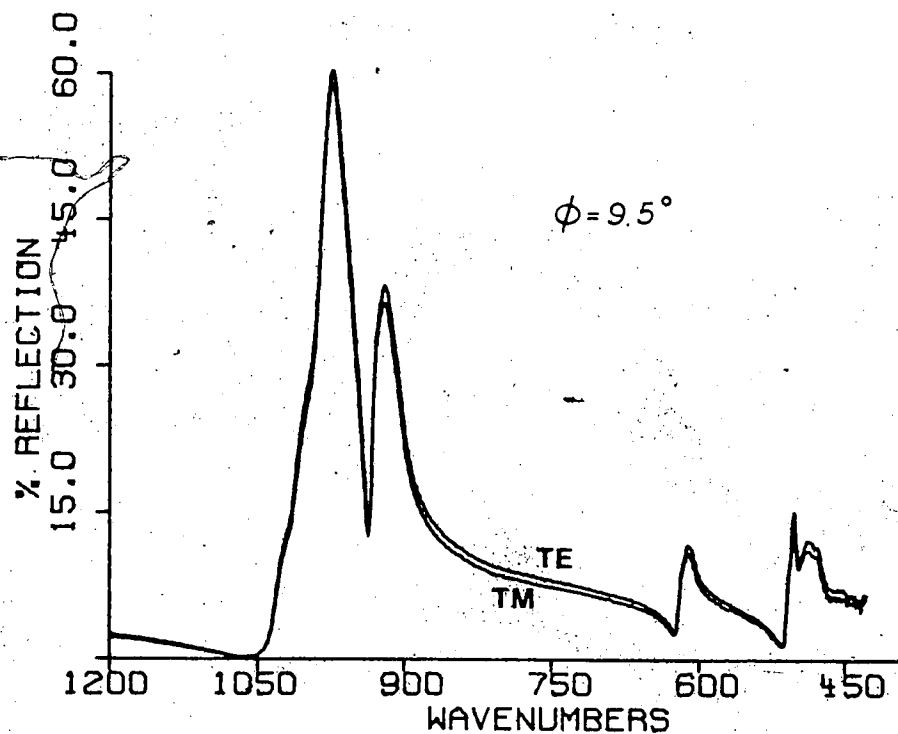
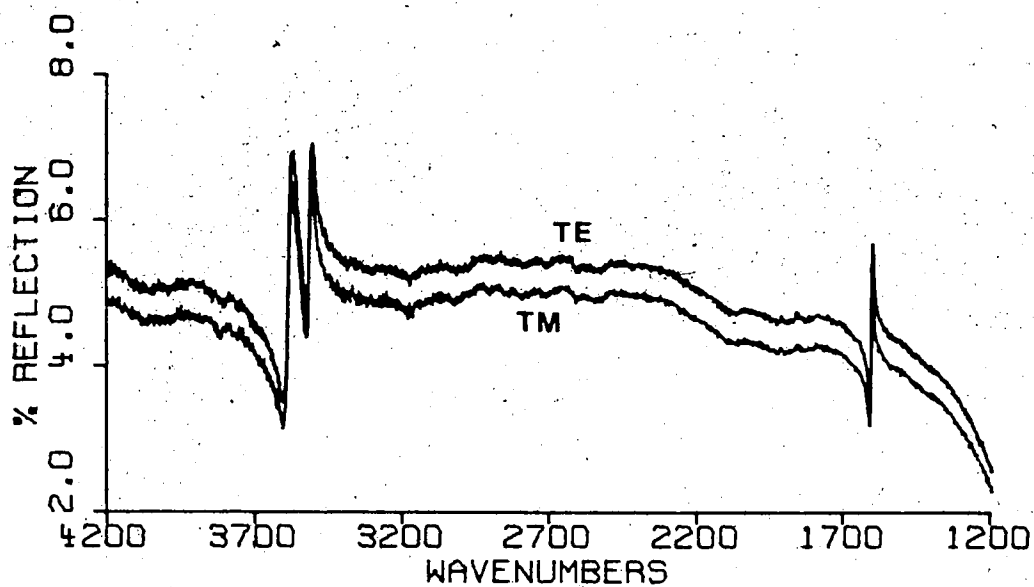


Figure 3.8 Polarized reflectance spectra of polycrystalline  $\text{Ba}(\text{ClO}_3)_2 \cdot \text{H}_2\text{O}$  with electric vector parallel (TM) and perpendicular (TE) to the plane of incidence, at  $\phi = 9.5^\circ$ .

0.4% reflection. This corresponds exactly with our measured difference of 0.4% reflection in the region 1800-3200  $\text{cm}^{-1}$ , where this calculation is roughly applicable.

A problem peculiar to the near-infrared investigation of polycrystalline  $\text{Ba}(\text{ClO}_3)_2 \cdot \text{H}_2\text{O}$  was an apparent day-dependence of the absolute reflectance. This phenomenon is illustrated in Figure 3.9. Comparison of the unpolarized near-infrared reflectance spectra of both samples POLY-BCL.H20-02 and POLY-BCL.H20-05 recorded on two different days shows that, on a given day, the two samples were in very good agreement. However, depending upon the day the spectra were recorded, the absolute magnitude of the spectral features changed significantly. Several possible contributing factors were investigated, such as sample positioning, apparatus polarization, and deterioration of reference mirror performance, but the source of this experimental anomaly has not yet been determined.

Although our initial reaction was that the higher reflectance was due to a better polished sample, this was not found to be the case. In fact, the lower reflectance curves (e.g. Curves 1 in Figure 3.9) gave a closer correspondence with the mid-infrared results, in their region of spectral overlap ( $\approx 1200\text{--}4800 \text{ cm}^{-1}$ ).

It is also expected that the polycrystalline  $\text{Ba}(\text{ClO}_3)_2 \cdot \text{H}_2\text{O}$  possesses a reflectance of  $\approx 0.052$  in the visible region, based on the principal refractive indices of the single crystal <sup>103</sup> at the sodium D-line. From Figure

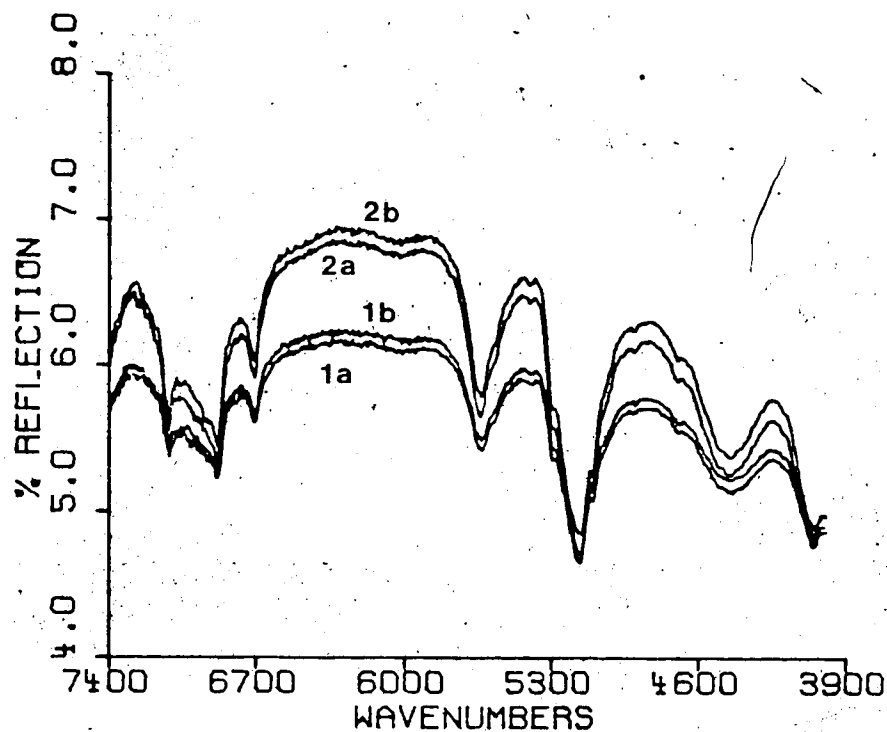


Figure 3.9 Day-dependence of near-infrared reflectance of polycrystalline  $\text{Ba}(\text{ClO}_3)_2 \cdot \text{H}_2\text{O}$ .

Curves 1 and 2 represent spectra taken on different days.

The a and b symbols refer to samples: POLY-BCL-H2O-02 and POLY-BCL-H2O-05, respectively.

3.9, it can be seen that the lower reflectance curves are in better agreement with this anticipated result.

For these reasons, the near-infrared spectra which gave the best overlap with the more reproducible, averaged mid-infrared spectra, were used in the merging procedure.

The reflectance of  $\text{Ba}(\text{ClO}_3)_2 \cdot \text{H}_2\text{O}$  was found to depend upon the length of time that the sample was purged with dry nitrogen gas, before the spectrum was recorded (see Sections 2.7 and 3.2a). This prompted an investigation of whether exposure to vacuum in the R.I.I.C. sample compartment similarly affected the  $\text{Ba}(\text{ClO}_3)_2 \cdot \text{H}_2\text{O}$  reflectance. This test was conducted in the following manner. A sample of polycrystalline  $\text{Ba}(\text{ClO}_3)_2 \cdot \text{H}_2\text{O}$  was freshly polished with iso-propanol on a chamois, and its mid-infrared reflectance spectrum was recorded on the Nicolet FTIR instrument. The sample was then evacuated for 20 minutes in the R.I.I.C. at  $\approx 0.07$  torr. Immediately thereafter, the sample's mid-infrared reflectance spectrum was re-recorded. It can be seen from curves A and B of Figure 3.10 that no significant change had occurred. However, if the sample was evacuated for a period of  $1\frac{1}{2}$  hours in the R.I.I.C., its mid-infrared reflectance decreased, particularly for frequencies greater than  $1800 \text{ cm}^{-1}$  (Curves C and D of Figure 3.10). In the region below  $1800 \text{ cm}^{-1}$ , the changes were sufficiently small to suggest that the sample's far-infrared reflectance was not affected by evacuation. Thus, the R.I.I.C.

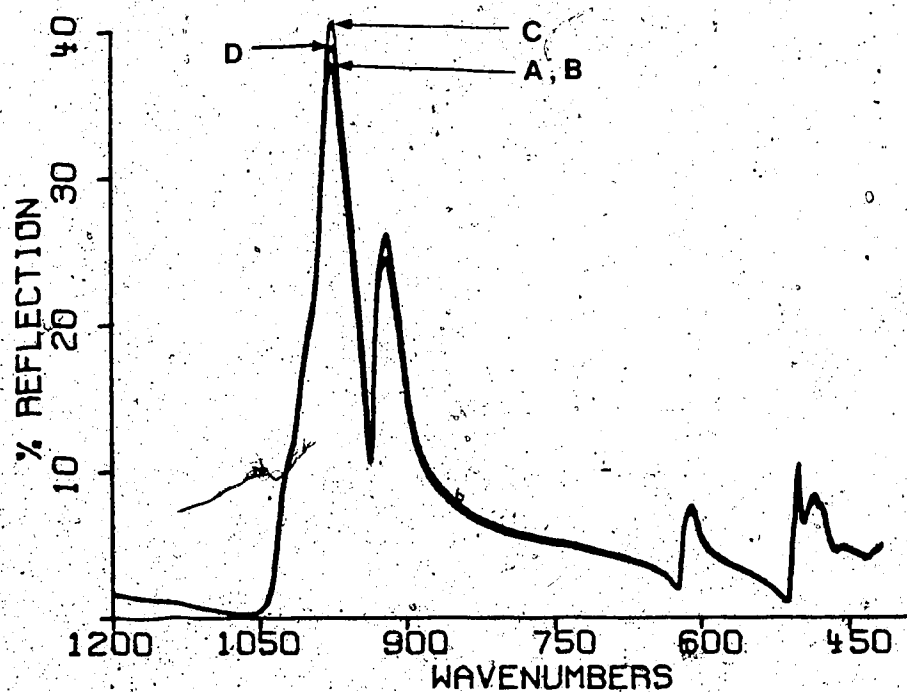
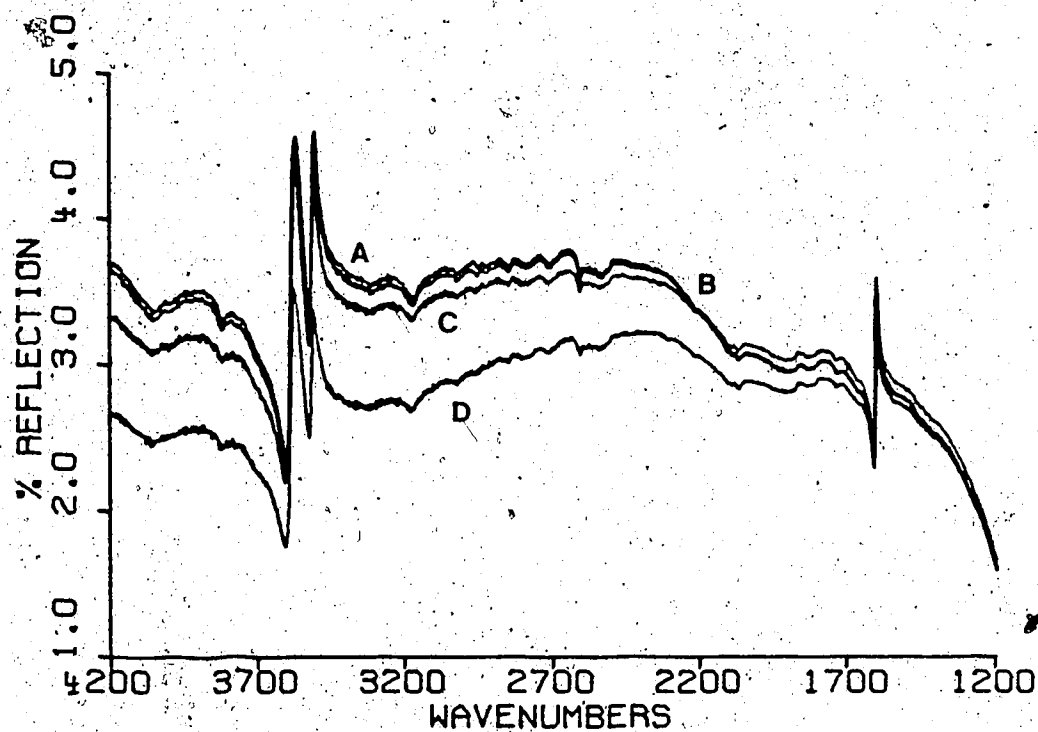


Figure 3.10 Effect of sample evacuation on mid-infrared reflectance of polycrystalline  $\text{Ba}(\text{ClO}_3)_2 \cdot \text{H}_2\text{O}$ .

Curve A: sample freshly polished

Curve B: after 20 min. evacuation in R.I.I.C. (0.07 torr)

Curve C: sample freshly polished

Curve D: after 1.5 hr. evacuation in R.I.I.C. (0.045 torr)

data is considered representative of an undistorted sample of  $\text{Ba}(\text{ClO}_3)_2 \cdot \text{H}_2\text{O}$ .

### 3.2 Data Handling

In this section, the data handling procedures required to analyze the  $\text{Ba}(\text{ClO}_3)_2 \cdot \text{H}_2\text{O}$  spectra, are described in detail. Representative examples have been included to illustrate these techniques, and the spectral information used to construct the composite reflectance spectra is tabulated.

#### 3.2a Subtraction of Water Vapour and Carbon Dioxide

##### Features

Preliminary spectra of both polycrystalline and single crystal  $\text{Ba}(\text{ClO}_3)_2 \cdot \text{H}_2\text{O}$ , indicated that the spectral features changed with prolonged instrument purging. Figure 3.11 illustrates this for polycrystalline  $\text{Ba}(\text{ClO}_3)_2 \cdot \text{H}_2\text{O}$ . Comparison of Curves A and B clearly shows that the changes did not involve a gradual deterioration of the surface, since this would have been characterized by a reduction in the reflectance, at all frequencies. Instead, the changes were most pronounced at the peak maxima. Although the intensity of most peaks decreased with time, the peak at  $920 \text{ cm}^{-1}$  increased, and a new feature appeared at  $\approx 1020 \text{ cm}^{-1}$ . If the sample was repolished with iso-propanol and its reflectance spectrum immediately recorded, the spectrum (Curve C of Figure 3.11) was essentially the same as that observed prior to purging (Curve A).

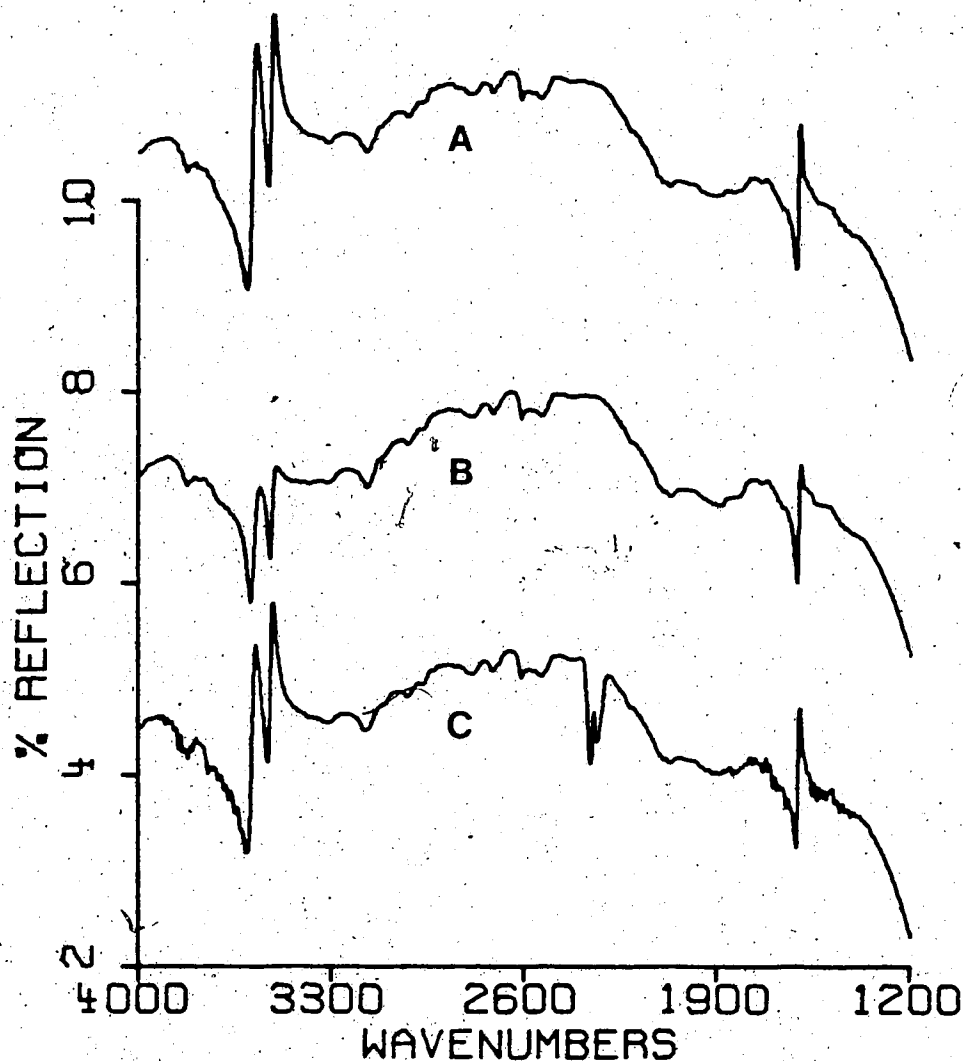


Figure 3.11 Effect of sample purging with dry nitrogen gas on mid-infrared reflectance of polycrystalline  $\text{Ba}(\text{ClO}_3)_2 \cdot \text{H}_2\text{O}$ .

Curve A: before purging  
Curve B: after purging 2 hours  
Curve C: after sample was repolished with iso-propanol and chamois

For clarity of presentation, the Curves A and B have been offset by 6.0% and 3.0% reflection, respectively.

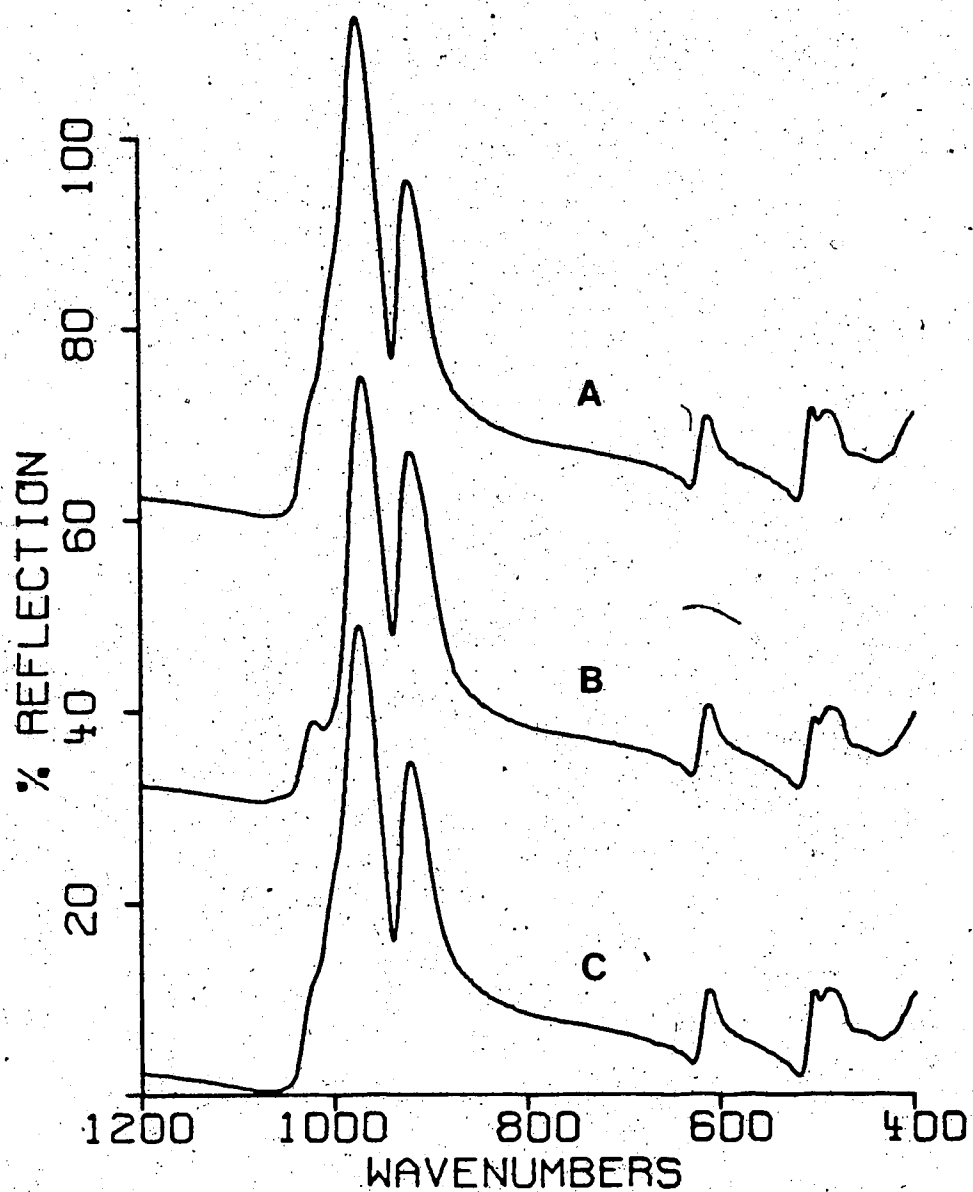


Figure 3.11a Continuation of Figure 3.11.

Curves A and B have been offset by 30.0% and 60.0% reflection, respectively.

Single crystal samples of  $\text{Ba}(\text{ClO}_3)_2 \cdot \text{H}_2\text{O}$  also exhibited a preferential reduction in peak intensities with extended purging, and a restoration of the original spectrum with repolishing. However, because of our previous experience with the polycrystalline samples, the single crystals were never purged long enough to observe the appearance of any new features.

Since  $\text{Ba}(\text{ClO}_3)_2 \cdot \text{H}_2\text{O}$  is relatively insoluble in alcohol, these findings suggest that purging only affects a very thin surface layer. The most probable explanation is that the surface dehydrates when the surrounding atmosphere becomes very dry. Consequently, the reflectance spectra used in this thesis were measured for freshly polished samples, immediately after they were positioned in the instrument. The rate of any spectral change was approximately gauged from the difference between two successive 250 scan collections. In the mid- and near-infrared regions, this collection period (~10 minutes) was sufficiently short that insignificant change took place. The background spectra of the reference mirror, on the other hand, were always recorded under well-purged instrumental conditions.

A problem associated with this procedure is that atmospheric water vapour and carbon dioxide features were superimposed on the  $\text{Ba}(\text{ClO}_3)_2 \cdot \text{H}_2\text{O}$  reflection spectra. Before conducting a Kramers-Kronig analysis of this data, it was necessary to remove these extraneous features. This was accomplished in the following manner. Recall that a

reflection experiment measures the relative intensities of incident radiation reflected from the sample and from a reference mirror, *i.e.*  $R_s/R_m$ , where the subscripts  $s$  and  $m$  refer to the sample and mirror, respectively. The presence of air in the sample compartment modifies this measured ratio,  $R_{\text{meas}}$ , to  $R_s/R_m[\exp(-\alpha l)]_{\text{H}_2\text{O}}[\exp(-\alpha l)]_{\text{CO}_2}$ , where the two bracketted terms define the transmittance of water vapour and carbon dioxide. The other symbols are:

$\alpha$  = sample absorptivity ( $\text{cm}^{-1}$ )

$l$  = optical path length (cm).

If the negative logarithm of this quantity is taken, *i.e.*  $-\log_{10}(R_{\text{meas}})$ , it becomes possible to remove the water vapour and carbon dioxide features by linearly subtracting weighted absorbance spectra of these interfering species. The reflection spectrum of the "pure"  $\text{Ba}(\text{ClO}_3)_2 \cdot \text{H}_2\text{O}$  can then be recovered by taking the antilogarithm of this corrected spectrum. This was the technique used.

Since the relative amounts of carbon dioxide and water vapour in the  $\text{Ba}(\text{ClO}_3)_2 \cdot \text{H}_2\text{O}$  spectra were not constant, these spectral features were isolated from a transmittance spectrum of air and stored in separate files. In order to reduce the level of noise generated in the subtracted spectrum, the regions devoid of water vapour (or  $\text{CO}_2$ ) absorption in the reference spectrum were replaced by horizontal lines of zero absorbance. The subtractions were performed by viewing a region of unambiguous absorption by water vapour (or  $\text{CO}_2$ ) in the sample spectrum, and adjusting the

scale factor of the reference spectrum until complete subtraction of this feature was noted. This stepwise subtraction procedure is illustrated in Figure 3.12 for the mid-infrared reflectance spectrum of polycrystalline  $\text{Ba}(\text{ClO}_3)_2 \cdot \text{H}_2\text{O}$ . In the mid- and near-infrared regions, this method was quite straightforward; but in the far-infrared region, where there is significant absorption by water vapour, it proved to be considerably more difficult.

### 3.2b Calibration of the Reference Mirror

In order to obtain accurate reflectance values, it is necessary that the reflectance of the reference mirror be well-defined for all frequencies of interest. This was accomplished by a comparison of the known and measured reflectances of a calibration standard; in this case, silicon.<sup>150</sup> Because of the gradual deterioration of the gold mirror, this calibration was only strictly valid for the day on which it was carried out. The cutting and polishing of the wedged silicon standard were described in detail in Section 2.6d. Although the purity of our silicon is not known, it is believed that the resistivity exceeds  $0.12 \, \Omega \text{ cm}$ . According to Runyan,<sup>187</sup> silicon samples possessing lower resistivities, display a marked increase in their reflectance with decreasing frequency. The reflectance of our silicon was measured down to  $100 \text{ cm}^{-1}$ , and no such increase was apparent.

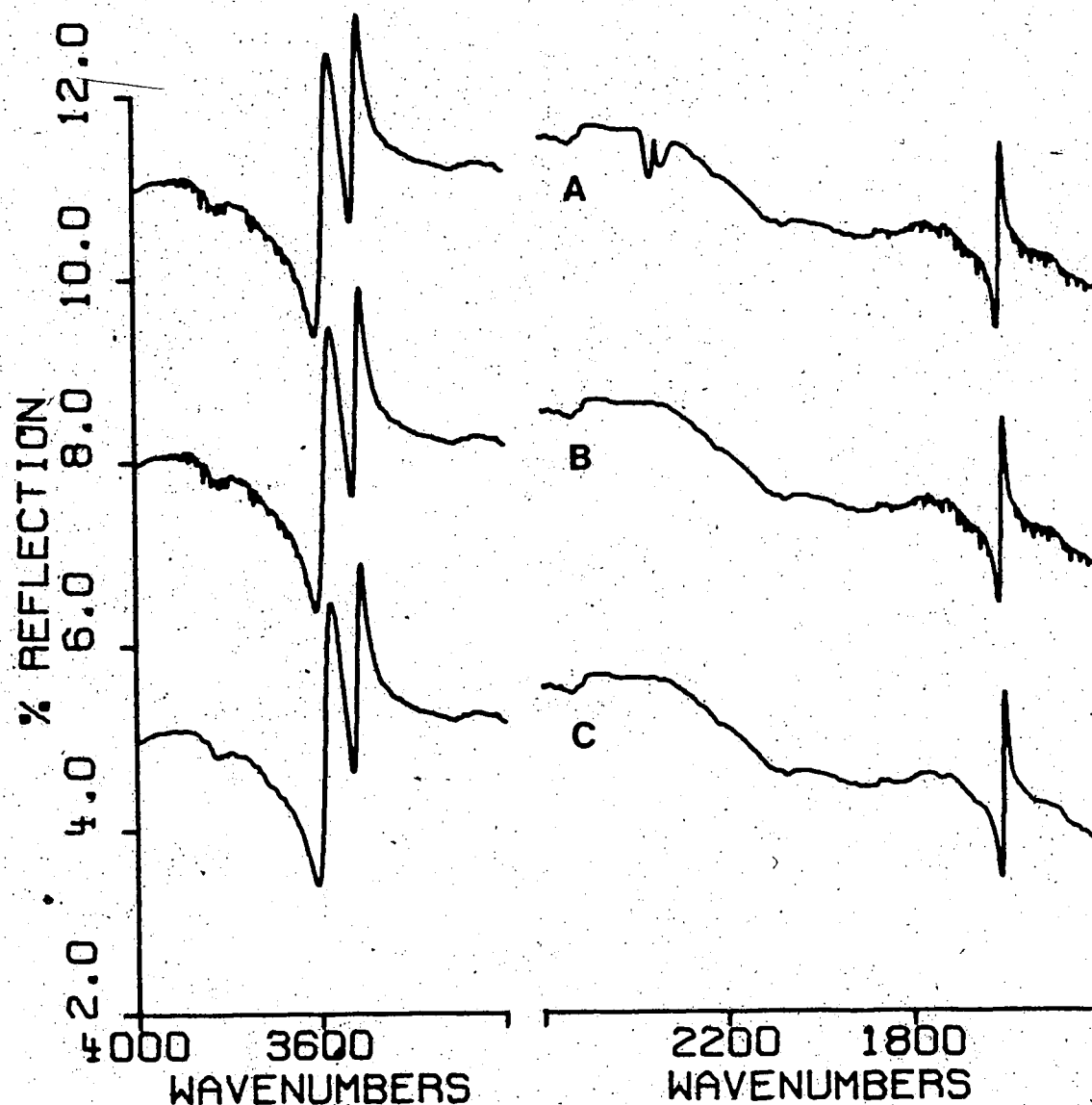


Figure 3.12 Subtraction of water vapour and carbon dioxide features from observed reflectance spectra.

Curve A: measured reflectance of polycrystalline  $\text{Ba}(\text{ClO}_3)_2 \cdot \text{H}_2\text{O}$

Curve B: after subtraction of  $\text{CO}_2$

Curve C: after subtraction of  $\text{H}_2\text{O}$  vapour and  $\text{CO}_2$

Curves A and B have been offset by 6.0% and 3.0% reflection, respectively.

The calibration procedure we employed involved several steps. First, the extent of apparatus polarization was determined by measuring the relative contributions of s- and p-polarized reflectance to the reflectance measured with unpolarized light. These measurements were made from transmission curves, such as those shown in Figure 3.13, which were recorded at  $9.5^\circ$  incidence, with the gold mirror as the reflecting surface, and with the wire grid polarizer set to transmit either s- or p-polarized light. The background spectrum in each case was recorded without the polarizer in the beam. The relative s- and p-polarized reflectance contributions:  $R_s/R_t$  and  $R_p/R_t$ , where  $R_t = R_s + R_p$ , are given in Table 3.2 for several frequencies in the mid-infrared. For an ideal system, at  $0^\circ$  incidence, both these quantities would be 0.50 for all frequencies. The non-ideality of our particular system is clearly demonstrated in Figure 3.13 by the oscillatory behavior of the s- and p-polarized reflectance, with the s-polarized (TE) component increasing dramatically at low frequencies.

Since the infrared extinction coefficients of silicon at room temperature are very small,<sup>188</sup> its expected normal-incidence reflectance can be determined, to a good approximation, from literature values of the refractive index,  $n$ , according to  $R_0 = (n-1)^2 / (n+1)^2$ . In the mid-infrared region, these values were obtained from Edward's and Ochoa's<sup>150</sup> room-temperature channel spectrum measurements on n-type silicon ( $\rho = 3-4 \Omega\text{cm}$ ), and are listed for several frequencies in

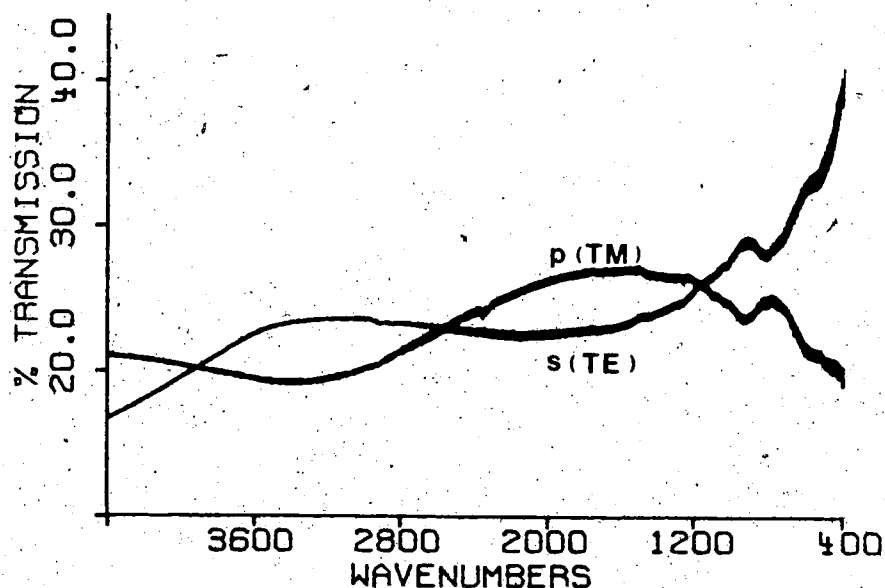


Figure 3.13 Percent transmission curves for s-(TE) and p-(TM) polarized light through Harrick reflectance accessory ( $\phi = 9.5^\circ$ ) in Nicolet 7199 instrument.

Table 3.2 Infrared Reflectance of Silicon for  $10^\circ$  Incidence and Corrected for Apparatus Polarization

$\nu(\text{cm}^{-1})$	Literature <sup>150</sup>			Experimental		Calculated
	$R_o$	$R_s^+$	$R_p^+$	$R_s/R_t$	$R_p/R_t$	$R_{10}$
4000	0.3023	0.3077	0.2969	0.481	0.519	0.302
2925	0.3012	0.3066	0.2958	0.534	0.466	0.302
2000	0.3005	0.3058	0.2951	0.461	0.539	0.300
1000	0.2999	0.3053	0.2946	0.531	0.469	0.300
800	0.2999	0.3053	0.2946	0.511	0.489	0.300
600	0.2998	0.3052	0.2945	0.601	0.399	0.301
500	0.2998	0.3052	0.2945	0.618	0.382	0.301

<sup>+</sup> values for  $10^\circ$  incidence.

Table 3.2. The corresponding s- and p-polarized reflectances for  $\approx 10^\circ$  incidence, were calculated via equations [1.36] and [1.38], *i.e.*

$$R_s = \left( \frac{a - \cos 10^\circ}{a + \cos 10^\circ} \right)^2 \quad R_p = \left( \frac{a - \sin 10^\circ \tan 10^\circ}{a + \sin 10^\circ \tan 10^\circ} \right)^2$$

where  $a = \sqrt{n^2 - \sin^2 10^\circ}$ ,

and these values are also given in Table 3.2.

The reflectance of silicon expected for the unpolarized conditions of the instrument, at  $10^\circ$  incidence, and for a perfectly reflecting reference mirror, was then derived from the sum of the s- and p-polarized reflectances, weighted by their respective contributions:

$$R_{10} = \left( \frac{R_s}{R_t} \right) R_s + \left( \frac{R_p}{R_t} \right) R_p$$

A comparison of the  $R_0$  and  $R_{10}$  values in Table 3.2 shows that an assumption of normal-incidence entails negligible error; the maximum error is  $\approx 0.3\%$  at  $500 \text{ cm}^{-1}$ .

The second step in the calibration procedure involved recording several unpolarized reflectance spectra of silicon, to obtain an estimate of the experimental reproducibility. The gold mirror to be calibrated was used as the reference reflector and, in the first instance, was assumed to be 100% reflecting. The reflectance spectra were then coadded to produce an average spectrum. The term coadding refers to the process of taking a weighted average of a

number of spectra; the weighting factor for each spectrum being determined by the relative number of associated interferograms (scans). Figure 3.14 shows the average mid-infrared reflectance of silicon measured on the 13/01/82, and in Table 3.3, these reflectance values are tabulated for several frequencies. For this particular experiment, the sample and background spectra were collected with gain settings of 2 and 1, respectively. It was later (20/01/82) found that an error existed in the gain settings of the Nicolet instrument (see Chapter V), and that for a sample-to-background gain ratio of 2/1 (all other parameters the same), the resultant reflectance was too large by a factor of 1.013. Therefore, it was necessary to scale the measured reflectance by the factor  $1/1.013$ , before comparison with the calculated  $10^\circ$  incidence reflectance values. These corrected reflectances are given in Table 3.3 as  $R_{\text{corr}}$ . The actual reflectance of the gold mirror was then computed from:  $R_{\text{mir}} = R_{10}/R_{\text{corr}}$ . These mid-infrared calibration results for gold mirror #3 on the 13/01/82 are summarized in Table 3.3 and represented graphically in Figure 3.15.

Since this calibration curve is strictly only applicable to reflectance spectra of  $\text{Ba}(\text{ClO}_3)_2 \cdot \text{H}_2\text{O}$  recorded on the same day, it was of interest to compare the calibrated  $\text{Ba}(\text{ClO}_3)_2 \cdot \text{H}_2\text{O}$  reflectance with the averaged results from several determinations on different days, to see if the reproducibility justified the labour of calibration. The

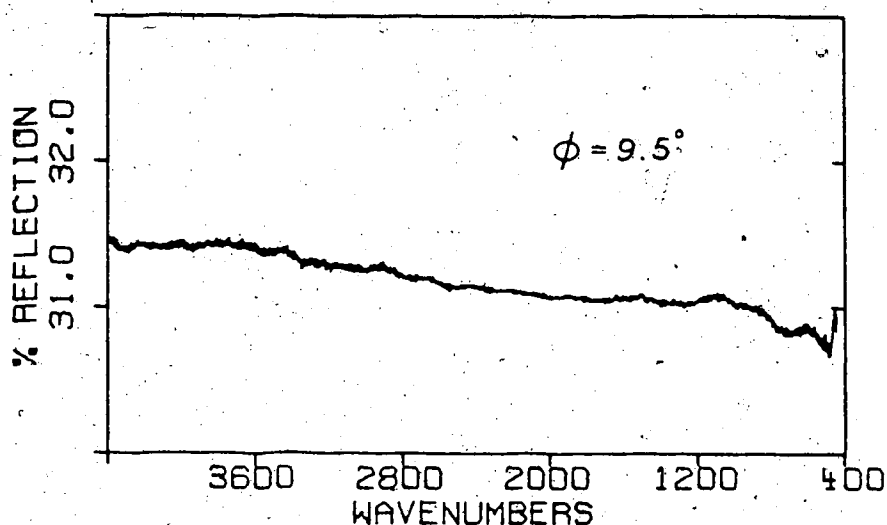


Figure 3.14 Average mid-infrared reflectance spectrum of silicon calibration standard, on 13/01/82.

Table 3.3 Calibration of Mid-Infrared Reflectance of Gold Mirror #3 for 13/01/82

$\nu(\text{cm}^{-1})$	$R_{\text{meas}}^{\S}$	$R_{\text{corr}}^{*}$	$R_{10}^{\dagger}$	$\% R_{\text{mir}}^{\ddagger}$
4000	0.3144	0.3104	0.302	97.3
2925	0.3130	0.3090	0.302	97.6
2000	0.3109	0.3069	0.300	97.8
1000	0.3104	0.3064	0.300	98.0
800	0.3092	0.3052	0.300	98.3
600	0.3087	0.3047	0.301	98.8
500	0.3076	0.3037	0.301	99.1

\* corrected for amplification error; factor = 1/1.013 (Chapter V).

$\dagger$  calculated values for  $10^\circ$  incidence are from Table 3.2.

$\ddagger R_{\text{mir}} = R_{10}/R_{\text{corr}}$

$\S R_{\text{meas}} =$  averaged silicon spectrum (see Figure 3.14).

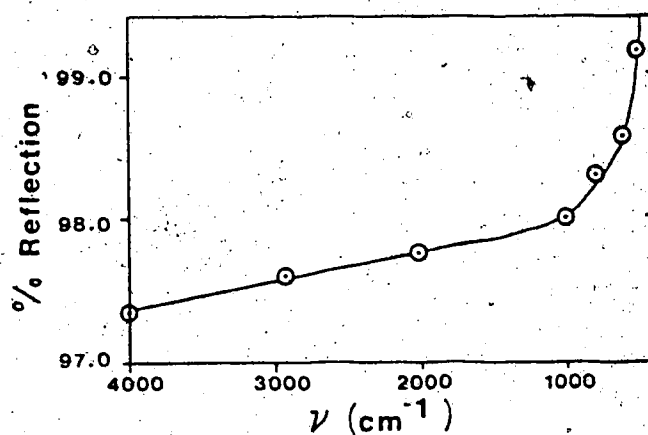


Figure 3.15 Mid-infrared calibration curve for gold mirror #3 on 13/01/82.

Table 3.4 Comparison of Calibrated and Averaged b-Polarized Mid-Infrared Reflectance of Single Crystal  $\text{Ba}(\text{ClO}_3)_2 \cdot \text{H}_2\text{O}$

$\nu(\text{cm}^{-1})$	% $R_{\text{meas}}$	% $R_{\text{mir}}^*$	% $R_{\text{cal}}$	% $R_{\text{av}}^{\dagger}$	$\Delta^{\ddagger}$
4400	5.03	97.3	4.89	4.87	-0.004
3529	1.97	97.5	1.92	1.96	+0.021
3510	9.36	97.5	9.13	9.04	-0.010
2800	4.95	97.6	4.83	4.89	+0.012
2200	4.70	97.7	4.59	4.64	+0.011
1614	2.05	97.8	2.00	2.04	+0.020
1604	9.00	97.8	8.80	8.82	+0.002
1049	0.0648	98.0	0.0635	0.0625	-0.016
979	71.54	98.0	70.1	70.72	+0.009
932	24.38	98.1	23.9	23.99	+0.004
609	13.14	98.7	13.0	12.93	-0.005
508	41.07	99.1	40.7	40.92	+0.005
479	11.71	99.3	11.6	11.43	-0.015

\* calibration results are for 13/01/82; estimated uncertainty in %  $R_{\text{mir}} = \pm 0.4\%$  reflection.

<sup>†</sup> Averaged data is the result of 6 independent spectra, collected on 3 different days.

<sup>‡</sup>  $\Delta = (R_{\text{av}} - R_{\text{cal}}) / R_{\text{cal}}$

results of such a study are presented in Table 3.4 for the b-polarized mid-infrared reflectance of single crystal  $\text{Ba}(\text{ClO}_3)_2 \cdot \text{H}_2\text{O}$ . The reflectance was measured at several peak and trough frequencies. These values were not corrected for amplification error since both the calibration and averaged spectra were recorded with the same sample-to-background gain ratio of 32/4.

It can be seen that the measured  $\text{Ba}(\text{ClO}_3)_2 \cdot \text{H}_2\text{O}$  reflectance on the 13/01/82, after correction for the reference mirror's reflectance according to  $R_{\text{cal}} = R_{\text{meas}} \times R_{\text{mir}}$ , agrees very well with the averaged  $\text{Ba}(\text{ClO}_3)_2 \cdot \text{H}_2\text{O}$  results, which were obtained from six independent collections on three different days. The fractional differences are tabulated in the last column of Table 3.4. This error is not systematic, since the differences are randomly positive and negative, with a maximum absolute value of 0.020. However, if our comparison is confined to reflectance values greater than 5.0%, and if the  $479 \text{ cm}^{-1}$  measurement is excluded because of poor reference mirror calibration in this region, then the maximum difference is reduced to  $\pm 0.010$ . This compares with an estimated fractional error of  $\pm 0.004$  in the calibration of the reference mirror above  $500 \text{ cm}^{-1}$ , and an overall fractional reproducibility in the  $\text{Ba}(\text{ClO}_3)_2 \cdot \text{H}_2\text{O}$  reflectance values of  $\pm 0.030$ . Thus, it was decided that the averaged polarized reflectance of single crystal  $\text{Ba}(\text{ClO}_3)_2 \cdot \text{H}_2\text{O}$  in the mid-infrared region, represented the "true" reflectance, within the experimental uncertainty.

This same conclusion was arrived at from calibration experiments in the far-infrared region. For example, with the 3  $\mu\text{m}$  mylar beamsplitter, the gold reference mirror's reflectance was determined to be  $0.994 \pm 0.016$ . This large uncertainty was due primarily to the poor reproducibility of successive data collections with the DTGS detector. The maximum fractional difference between the calibrated and averaged  $\text{Ba}(\text{ClO}_3)_2 \cdot \text{H}_2\text{O}$  results was  $\pm 0.03$  (based on eight determinations, where the measured reflectance was greater than 5.0%). This compares with a fractional overall reproducibility of  $\pm 0.07$ .

The calibration of the reference mirror proved to be more important in the near-infrared region. Figure 3.16 shows the near-infrared reflectance of gold mirror #3 determined on the 03/02/82. The equation of this line, determined from a least-squares fit, was  $R(\nu) = -1.823\text{E}-0.6\nu + 0.976$ . This calibration function was then used to correct the  $\text{Ba}(\text{ClO}_3)_2 \cdot \text{H}_2\text{O}$  reflectance spectra, measured on the same day. The results of this procedure are illustrated in Figure 3.17 for the near-infrared a'-polarized reflectance from the (001) face of single crystal  $\text{Ba}(\text{ClO}_3)_2 \cdot \text{H}_2\text{O}$ . Curve A shows the measured spectrum; Curve B is the spectrum after correction for the reference mirror's reflectance; and Curve C shows the corresponding averaged mid-infrared spectrum. The overlap of Curves B and C in the region  $1200\text{--}4800\text{ cm}^{-1}$  is excellent, thus verifying this calibration procedure.

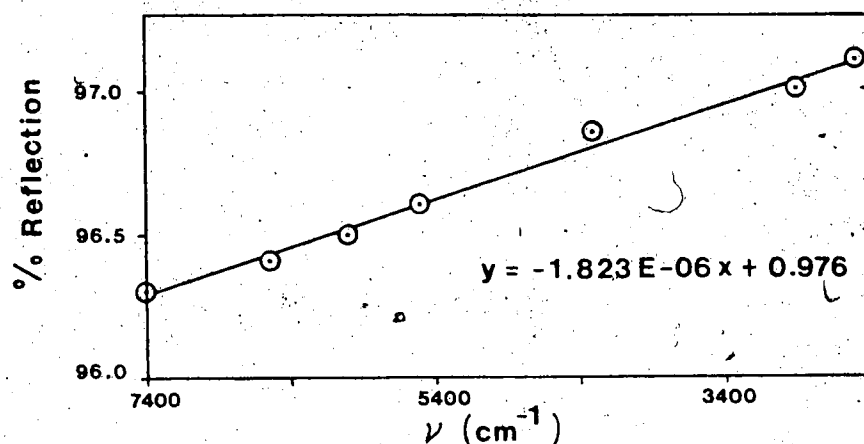


Figure 3.16 Near-infrared region calibration curve for gold mirror #3 on 03/02/82.

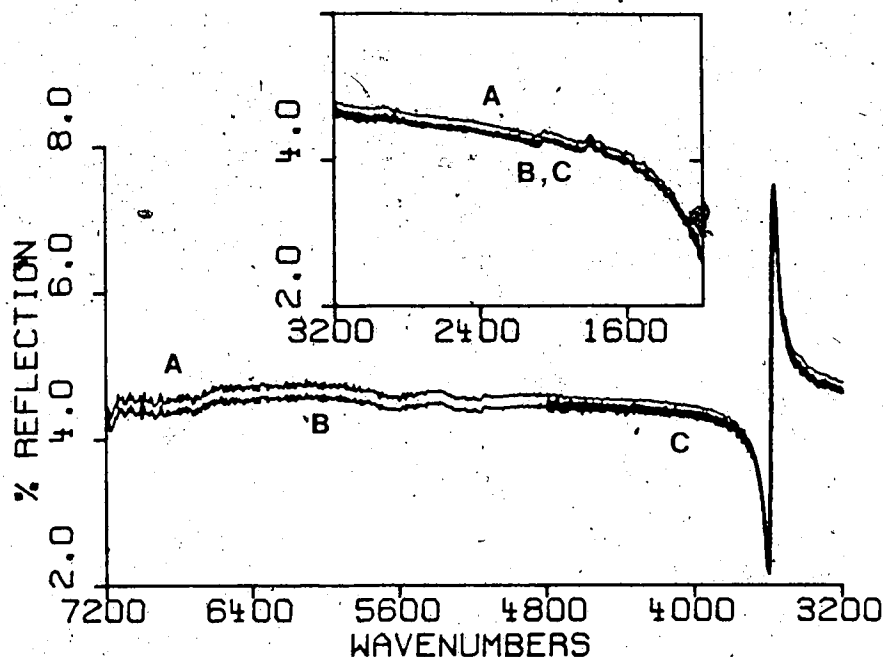


Figure 3.17 Comparison of overlap region for calibrated near-infrared and averaged mid-infrared results for a'-polarized reflectance from (001) face of single crystal  $\text{Ba}(\text{ClO}_3)_2 \cdot \text{H}_2\text{O}$ .

- Curve A: uncalibrated, near-infrared spectrum
- Curve B: calibrated, near-infrared spectrum (see Figure 3.16)
- Curve C: averaged, mid-infrared spectrum

### 3.2c Merging of Data from Various Spectral Regions

In order to obtain infrared reflectance data over a wide frequency range, several beamsplitters and two different FTIR instruments were used. The experimental details for these various spectral ranges are described in Section 2.7. To simplify the following discussion, the spectra collected for a particular experimental set of conditions, will be denoted sub-spectra. These sub-spectra were merged to produce a composite reflectance spectrum. In this section, a brief technical description of this procedure will be given, followed by illustrative examples, details of the merging process for the various composite spectra, and an evaluation of the spectral overlap achieved by this method.

The Nicolet sub-spectral data were stored in separate FTIR integer files. These integer files are characterized by the fact that the first block of memory (352 decimal words) contains the file status information such as the sample spacing interval (SSP) and the number of data points (NDP); the remainder of the file contains the reflectance data, with each data element occupying one word of memory. The corresponding frequency elements are calculated from the He/Ne laser frequency of  $15798.0 \text{ cm}^{-1}$  and the values of SSP and NDP used to record the spectrum.

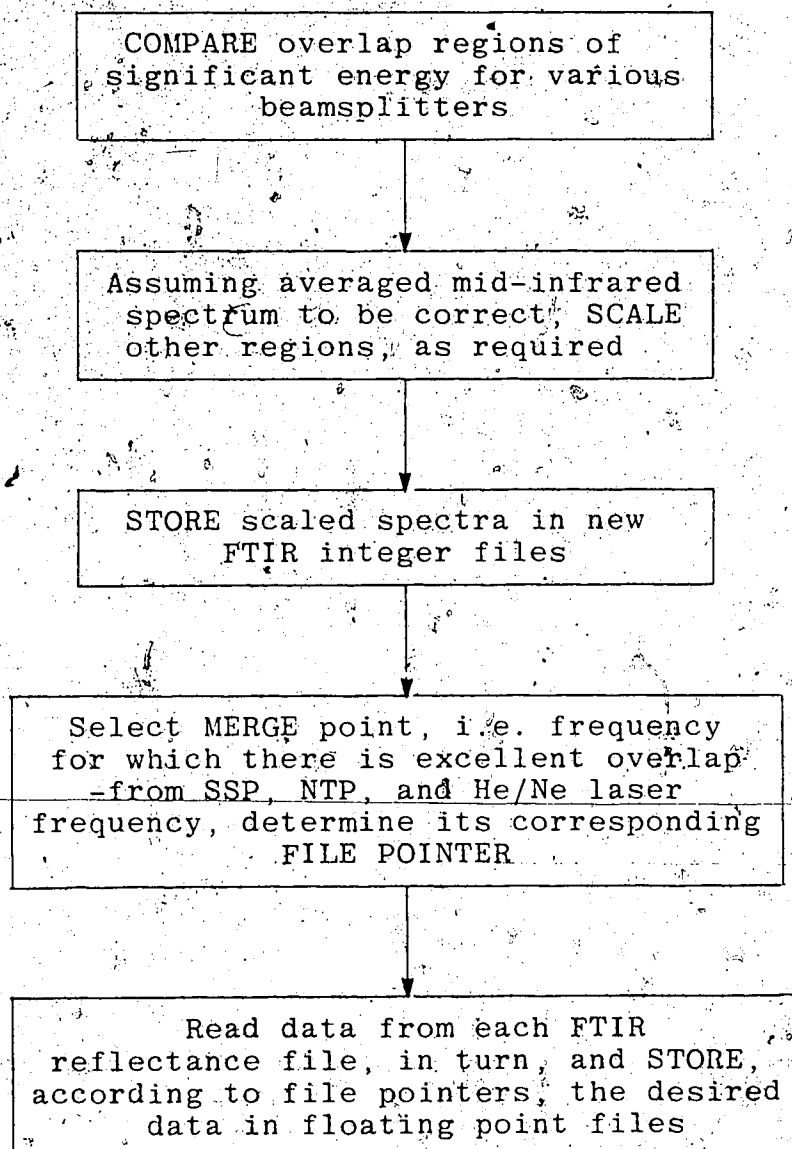
The first step in the merging procedure involved plotting and comparing the frequency regions of significant energy common to a given pair of beamsplitters. On the

basis of a previous comparison of calibrated and averaged reflectance results (see, for example, Table 3.4), it was assumed that the mid-infrared sub-spectrum was correct, and all other sub-spectra were scaled, if necessary, to provide smooth, continuous overlap of the spectral regions. Scaled spectra were stored in new integer files. A merge point was then chosen at a frequency of excellent overlap, and its corresponding file pointer was determined. A "Merge" program was written in BASIC to combine these sub-spectra at the selected merge points. Since BASIC can only operate on floating point data, it was first necessary to make this data conversion. After merging, the composite reflectance data and associated frequency data were stored in separate floating-point files. This procedure for merging data collected on the Nicolet 7199 instrument is summarized schematically in Figure 3.18.

The method for merging the far-infrared reflectance data from the R.I.I.C. was slightly more complicated. As was noted in Table 2.3, the R.I.I.C. intensity data were processed via a remote Amdahl 470 computer. The three successive sample and background collections were Fourier-transformed and ratioed to give three reflectance spectra. The averaged result was then punched onto paper tape and terminated by a Ctrl/D character. This format permitted the tape to be interpreted by a high-speed reader, interfaced with the Nicolet 1180 computer, and stored in an ASC code file. The Nicolet DEDIT routine was used to correct

Figure 3.18

Procedure for Merging Data from Various  
Spectral Regions - on Nicolet 7199 Instrument



any erroneous characters generated by this procedure. After this data file was redefined to one of the sixteen available file units, it could be accessed by the BASIC "Merge" program via an "Input #e" statement, where 'e' refers to the unit assignment number.

An illustration of this merge procedure is shown in Figure 3.19. These spectra are of the a'-polarized (001) face of single crystal  $\text{Ba}(\text{ClO}_3)_2 \cdot \text{H}_2\text{O}$ . The upper curves demonstrate the excellent agreement between the KBr and 3  $\mu\text{m}$  mylar data, without scaling, over the region 700-450  $\text{cm}^{-1}$ . The merge point was chosen at 500  $\text{cm}^{-1}$ . The 6.25  $\mu\text{m}$  mylar data, after scaling by a factor of 1.04, was also in good agreement over the range 700-520  $\text{cm}^{-1}$ , which corresponds to the mylar's second interference fringe, or "window". In the lower plot, the overlap is shown for the 3  $\mu\text{m}$  and scaled 6.25  $\mu\text{m}$  mylar data. Again, the agreement is extremely good; the merge point being chosen at 250  $\text{cm}^{-1}$ . It was considered justifiable to scale-up the far-infrared spectra, since they were obtained for much longer sample collection periods than the mid- or near-infrared data, and therefore, the concomitant risk of sample deterioration was much greater.

Figure 3.20 illustrates the overlap of the Nicolet and R.I.I.C. far-infrared data. The agreement is again fairly good. A constant value of 0.015 has been subtracted from the R.I.I.C. measured reflectance. This value was estimated as the contribution of noise to the spectrum. Recall

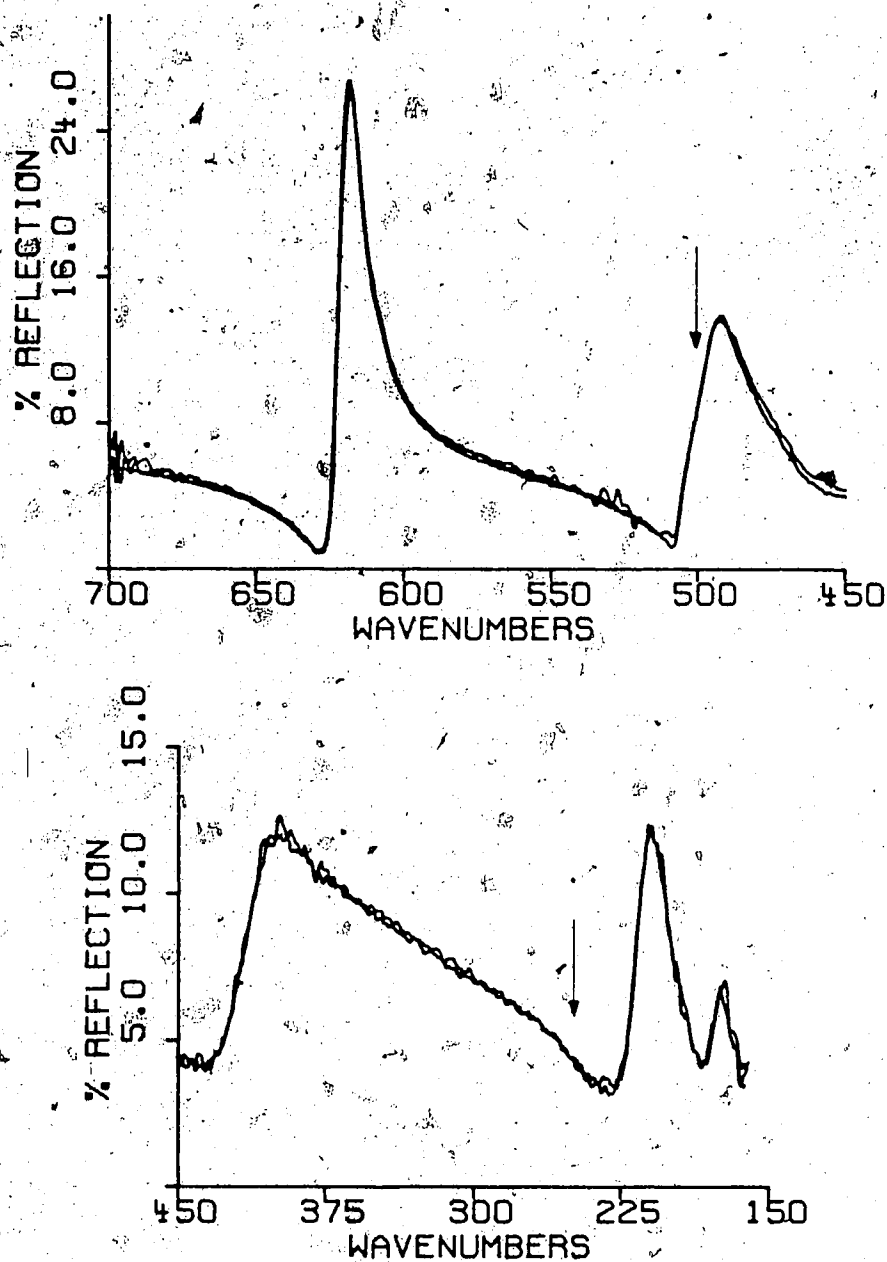


Figure 3.19 Overlap of mid- and far-infrared reflectance data for a'-polarized (001) face of single crystal  $\text{Ba}(\text{ClO}_3)_2 \cdot \text{H}_2\text{O}$ .

Upper plot: overlap of KBr, 3  $\mu\text{m}$  and 6.25  $\mu\text{m}$  (scaled) mylar spectra

Lower plot: overlap of 3  $\mu\text{m}$  and 6.25  $\mu\text{m}$  (scaled) mylar data

Arrows indicate position of merge points.

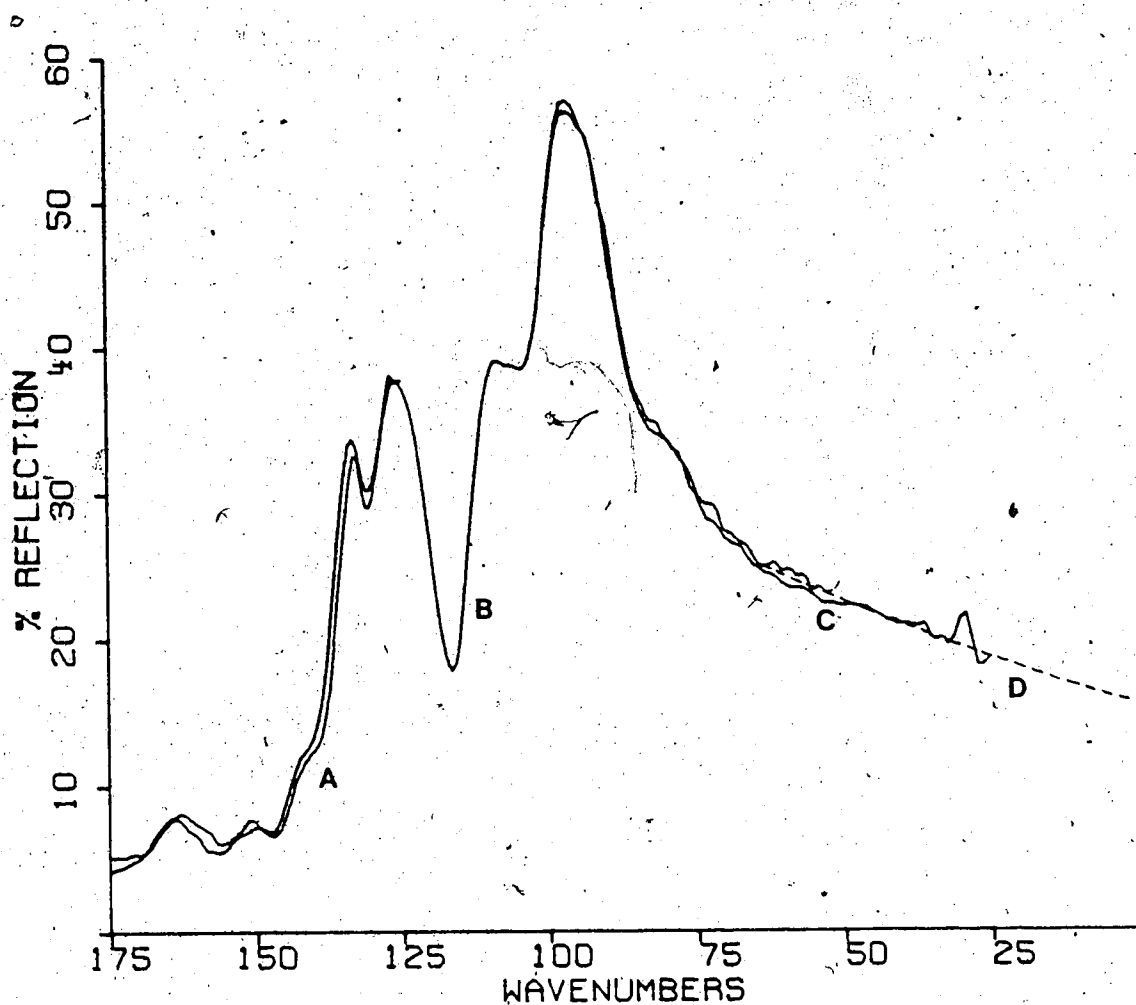


Figure 3.20 Overlap of far-infrared Nicolet and R.I.I.C. data for polycrystalline  $\text{Ba}(\text{ClO}_3)_2 \cdot \text{H}_2\text{O}$ .

Curve A ( $175\text{--}125\text{ cm}^{-1}$ ):  $12.5\text{ }\mu\text{m}$  mylar spectrum on Nicolet

Curve B ( $175\text{--}50\text{ cm}^{-1}$ ):  $12\text{ }\mu\text{m}$  mylar spectrum on R.I.I.C. (-1.5% for background noise)

Curve C ( $100\text{--}25\text{ cm}^{-1}$ ):  $25\text{ }\mu\text{m}$  mylar spectrum on R.I.I.C. (-1.5%)

Curve D ( $70\text{--}0\text{ cm}^{-1}$ ): artificial wing generated from  $R(\nu) = a \exp(b\nu) - 0.015$ ; where  $a = 0.17$ ,  $b = 0.007$ .

from Section 2.5 that the R.I.I.C. intensity data is transformed to a power spectrum, for which the noise is always computed to be positive. The low frequency 25  $\mu\text{m}$  mylar reflectance data exhibited an apparent exponential decay to zero frequency. This observation was verified by fitting the region from 25-75  $\text{cm}^{-1}$  to  $R(\nu) = a \exp(b\nu)$ , with  $a = 0.17$  and  $b = 0.007$ . It can be seen that this artificial wing (Curve D) simulates extremely well the low frequency 12  $\mu\text{m}$  (Curve B) and 25  $\mu\text{m}$  (Curve C) mylar reflectance data.

The merging data used to construct the composite reflectance spectra of polycrystalline and single crystal  $\text{Ba}(\text{ClO}_3)_2 \cdot \text{H}_2\text{O}$ , are compiled in Tables 3.5 and 3.6. The relevant information includes: frequency region employed, the number of averaged spectra, the total number of scans, and the scale factor used in the merging. The validity of this procedure was ultimately assessed by the maximum fractional errors ( $\Delta R/R$ ) observed in the peak and trough reflectance values for a given pair of merged sub-spectra. These fractional discrepancies are listed in Table 3.7. It can be seen that the overlap is generally very good, except in regions of very weak reflectance.

### 3.3 Reflection Results for $\text{Ba}(\text{ClO}_3)_2 \cdot \text{H}_2\text{O}$

In the previous sections (3.1 and 3.2), the techniques for characterizing the  $\text{Ba}(\text{ClO}_3)_2 \cdot \text{H}_2\text{O}$  samples, and treating the primary reflectance spectra, were detailed. The final composite reflection spectra, which were obtained after

Table 3.5 Merging Data for the Composite Reflectance  
Spectra of Polycrystalline  $\text{Ba}(\text{ClO}_3)_2 \cdot \text{H}_2\text{O}$

<u>Beamsplitter</u>	<u>Frequency region employed (<math>\text{cm}^{-1}</math>)</u>	<u>#Averaged Spectra</u>	<u>Total #Scans</u>	<u>Scale Factor</u>
$\text{CaF}_2/\text{Si}$	4000-7200	5	(1250)	1.0
$\text{KBr}/\text{Ge}$	550-4000	7	(3100)	1.0
<u>or</u>	<u>or</u>			
$\text{KBr}/\text{Ge}$	550-4400	7	(3100)	1.0
3 $\mu\text{m}$ mylar	203-550	4	(2500)	1.0
12.5 $\mu\text{m}$ mylar (Globar)	170-203	4	(3500)	1.0
12 $\mu\text{m}$ mylar (Hg lamp)	50-170	3	(3)	1.0*
<u>or</u>	<u>or</u>			
12 $\mu\text{m}$ mylar (Hg lamp)	64-170	3	(3)	1.0*
artificial wing <sup>†</sup>	0-64	3	(3)	1.0*

<sup>†</sup> wing generated from  $R(\nu) = a \exp(b\nu)$ , where  $a = 0.17$ ,  
 $b = 0.007$ .

\* a constant background reflectance of 0.015 was subtracted,  
before merging.

Table 3.6 Merging Data for the Composite Reflectance  
Spectra of Single Crystal  $\text{Ba}(\text{ClO}_3)_2 \cdot \text{H}_2\text{O}$

<u>a'-polarized</u>				
<u>Beamsplitter</u>	<u>Frequency region employed (<math>\text{cm}^{-1}</math>)</u>	<u>#Averaged Spectra</u>	<u>( Total #Scans )</u>	<u>Scale Factor</u>
KBr/Ge	500-4400	6	(1344)	1.00
3 $\mu\text{m}$ mylar	250-500	6	(1500)	1.00
6.25 $\mu\text{m}$ mylar	105-250	8	(2000)	1.04
<u>b-polarized</u>				
KBr/Ge	500-4400	6	(1375)	1.00
3 $\mu\text{m}$ mylar	250-500	6	(1500)	1.00
6.25 $\mu\text{m}$ mylar	160-250	6	(1500)	1.05
12.5 $\mu\text{m}$ mylar	115-160	6	(1500)	1.07

Table 3.7 Maximum Discrepancies Between Merged  $\text{Ba}(\text{ClO}_3)_2 \cdot \text{H}_2\text{O}$  Sub-Spectra, After Scaling

polycrystalline		$\Delta R/R$ †		
Beamsplitter pair	Frequency range (cm <sup>-1</sup> )*	Merge point (cm <sup>-1</sup> )	Peaks	Troughs
KBr/3μm mylar	490-670	550	0.1/11.3	0.1/1.5
3μm/12.5μm mylar	180-215	203	0.6/10.5	0.2/4.8
KBr/12.5μm mylar	605-700	-	0.05/11.4	0.05/2.8
12.5μm mylar (Globar)/ 12μm mylar (Hg lamp)	125-175	170	1.3/34.0	0.4/6.0
a'-polarized				
KBr/3μm mylar	490-670	500	0.4/13.6	0.6/1.2
3μm/6.25μm mylar	180-430	250	0.6/12.6	0.4/3.2
	540-680	-	0.4/26.5	0.1/0.8
b-polarized				
KBr/3μm mylar	490-670	500	2.6/41.2	0.3/1.2
3μm/6.25μm mylar	180-430	250	0.75/9.5	0.35/1.2
6.25μm/12.5μm mylar	145-240	160	1.6/20.0	0.6/3.0
3μm/12.5μm mylar	415-540	-	0.4/11.9	0.4/1.2

\* overlap frequency region for which both beamsplitters gave significant energy throughput.

† the maximum fractional discrepancies between the merged data.

these data handling procedures, are presented in this section along with a tabulation of the fundamental peak reflectance values.

### 3.3a Near-Infrared Results

The room-temperature, near-infrared reflectance spectra of both polycrystalline and single crystal  $\text{Ba}(\text{ClO}_3)_2 \cdot \text{H}_2\text{O}$ , recorded at  $9.5^\circ$  incidence and with a resolution of  $8 \text{ cm}^{-1}$ , are shown in Figure 3.21.

Curves A and B were measured with the electric vector perpendicular and parallel, respectively, to the b-axis in the (001) crystal face; polarized radiation was produced by a barium fluoride wire grid polarizer. Both of these reflectance spectra represent the average of four independent measurements made on the same day for samples, SC-BCL-H20-01 and SC-BCL-H20-02, and calibrated according to the procedure of Section 3.2b.

Curve C depicts the unpolarized near-infrared reflectance of polycrystalline  $\text{Ba}(\text{ClO}_3)_2 \cdot \text{H}_2\text{O}$ . Because of the apparent day-dependence of this spectrum (see Figure 3.9), the experiment which gave the best agreement with the averaged mid-infrared results, was selected for the merging procedure. Since the mid-infrared results were highly reproducible, this selection criterion was considered to be reasonably valid. This "best" near-infrared spectrum is shown in Curve C of Figure 3.21 and also in Figure 3.22, where it is compared with the averaged mid-infrared spec-

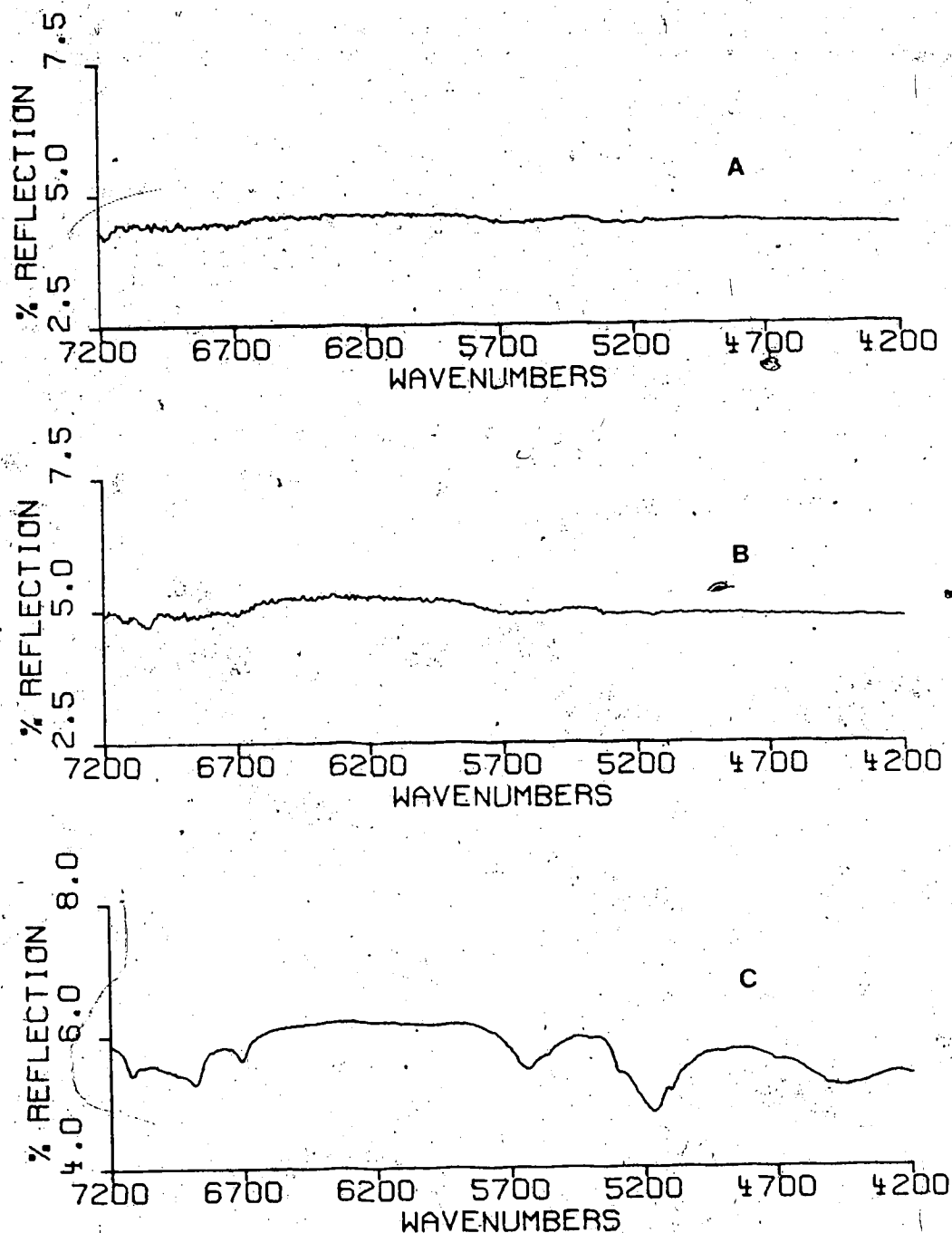


Figure 3.21 Near-infrared reflectance spectra of polycrystalline and polarized (001) face single crystal  $\text{Ba}(\text{ClO}_3)_2 \cdot \text{H}_2\text{O}$ , at  $-298^\circ\text{K}$  and  $8 \text{ cm}^{-1}$  resolution.

Curve A: a'-polarized spectrum of (001) face

Curve B: b-polarized spectrum of (001) face

Curve C: unpolarized spectrum of polycrystalline sample

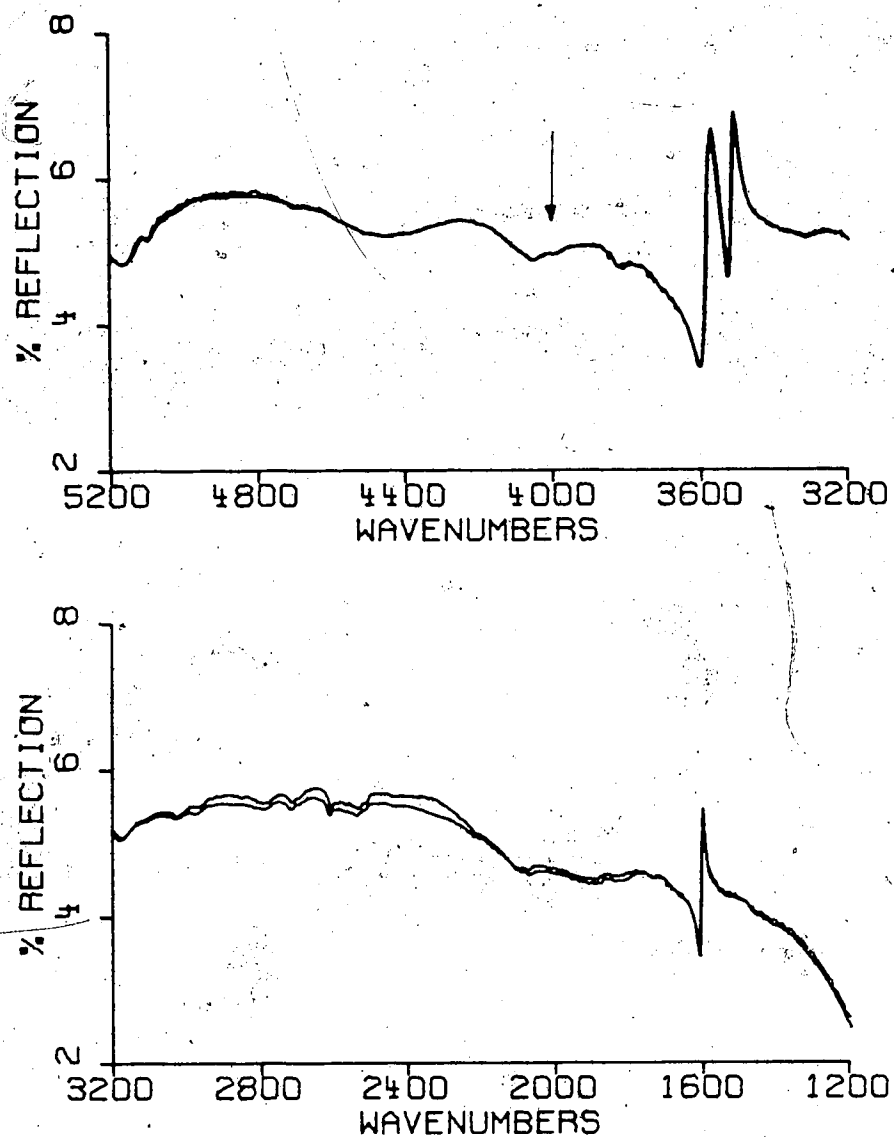


Figure 3.22 Comparison of overlap region for "best" near-infrared and averaged mid-infrared results for polycrystalline  $\text{Ba}(\text{ClO}_3)_2 \cdot \text{H}_2\text{O}$ .

Arrow indicates merge point for composite spectrum.

trum. It represents the average of five independent sets of reflectance measurements on samples POLY-BCL·H2O-02 and POLY-BCL·H2O-05, recorded on the same day. The spectral overlap with the mid-infrared data, in the frequency region where the  $\text{CaF}_2/\text{Si}$  and  $\text{KBr}/\text{Ge}$  beamsplitters both possess significant energy, is excellent.

It is interesting to note that the spectra obtained for the (001) face were relatively featureless, whereas the polycrystalline spectrum exhibited several broad reflectance peaks and a high frequency reflectivity greater than that found for either single crystal spectrum.

### 3.3b Polycrystalline $\text{Ba}(\text{ClO}_3)_2 \cdot \text{H}_2\text{O}$ ---Mid- and Far Infrared

The room-temperature, unpolarized reflectance of polycrystalline  $\text{Ba}(\text{ClO}_3)_2 \cdot \text{H}_2\text{O}$ , over the range  $50\text{--}4200\text{ cm}^{-1}$ , is shown in Figure 3.23. This spectrum was recorded at  $9.5^\circ$  incidence and with a spectral resolution of  $2\text{ cm}^{-1}$ . Other data pertaining to the production of this composite reflectance spectrum are summarized in Table 3.5.

The fundamental reflection bands are characterized by their peak and trough reflectance values in Table 3.8. The minimum reflectance of 0.002 at  $1063.5\text{ cm}^{-1}$  occurs to high frequency of the maximum observed reflectance of 0.586 at  $976.7\text{ cm}^{-1}$ . A more detailed compilation of the measured reflectances is given in Appendix B, where data are tabulated at frequency intervals corresponding to a change in reflection of 1.0% below  $1200\text{ cm}^{-1}$ , and 0.2% above  $1200\text{ cm}^{-1}$ .

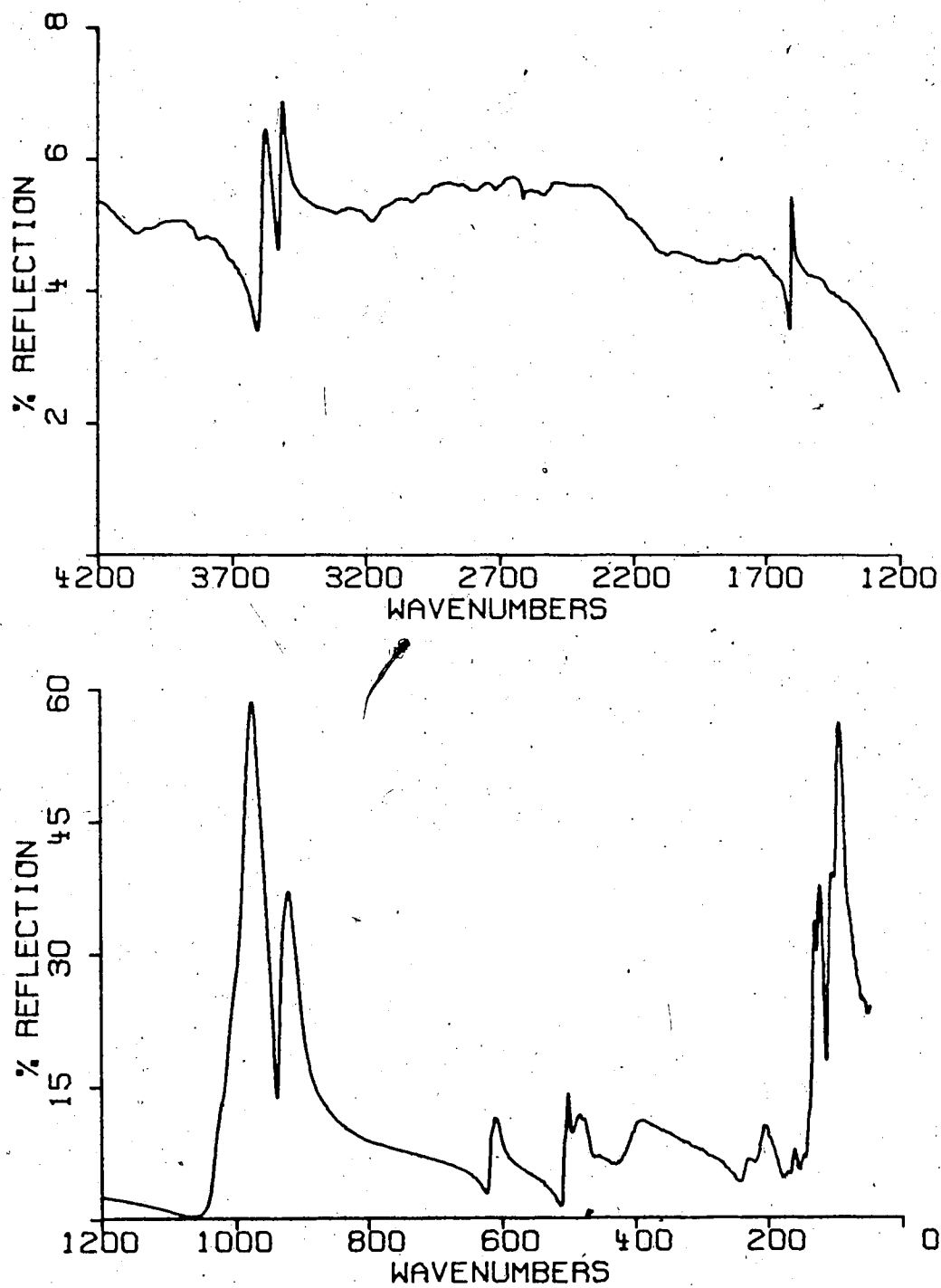


Figure 3.23 Composite reflectance spectrum of polycrystalline  $\text{Ba}(\text{ClO}_3)_2 \cdot \text{H}_2\text{O}$  at  $-298^\circ\text{K}$  and  $2\text{ cm}^{-1}$  resolution.

Table 3.8 Peak and Trough Reflectance Values for Fundamental Bands of Polycrystalline  $\text{Ba}(\text{ClO}_3)_2 \cdot \text{H}_2\text{O}$  at 298°K; resolution = 2  $\text{cm}^{-1}$

PEAK		TROUGH	
$\nu_{\text{max}} (\text{cm}^{-1})$	$R_{\text{max}}$	$\nu_{\text{min}} (\text{cm}^{-1})$	$R_{\text{min}}$
96.3	0.562	104.3	0.385
108.5	0.390	116.5	0.178
126.2	0.377	131.1	0.302
133.5	0.337	147.6	0.068
149.4	0.072	157.3	0.055
164.0	0.078	170.1	0.049
173.5	0.052	180.3	0.045
206.3	0.105	244.9	0.041
255.0	0.050	273.3	0.064
391.4	0.111	433.9	0.061
458.0	0.071	463.8	0.069
480.1	0.114	482.1	0.112
486.9	0.119	498.5	0.097
504.2	0.143	514.9	0.014
613.2	0.114	626.7	0.028
921.8	0.371	938.2	0.136
976.7	0.586	1063.5	0.002
1603.5	0.054	1613.1	0.034
3511.7	0.069	3529.1	0.046
3576.3	0.065	3608.1	0.034

### 3.3c Single Crystal $\text{Ba}(\text{ClO}_3)_2 \cdot \text{H}_2\text{O}$ ---Mid- and Far-Infrared

The room-temperature reflectance spectra of the (001) crystal face of  $\text{Ba}(\text{ClO}_3)_2 \cdot \text{H}_2\text{O}$ , over the region 100-4200  $\text{cm}^{-1}$ , are presented in Figures 3.24 and 3.25. These a'- (Figure 3.24) and b- (Figure 3.25) polarized spectra were measured with the electric vector perpendicular and parallel to the b-axis, respectively. Both spectra were recorded at  $9.5^\circ$  incidence with a resolution of 2  $\text{cm}^{-1}$ . The polarized radiation was produced either by a silver bromide (500-4400  $\text{cm}^{-1}$ ) or polyethylene (100-500  $\text{cm}^{-1}$ ) wire grid polarizer. The weak feature at 786  $\text{cm}^{-1}$  in the a'-polarized spectrum is most likely due to a trace impurity of  $\text{Ba}(\text{BrO}_3)_2 \cdot \text{H}_2\text{O}$  (see Section 3.1a).

Merging data, relevant to the production of these composite spectra, are compiled in Table 3.6. The peak and trough reflectance values of the fundamental reflection bands are listed in Table 3.9. The minimum observed reflectance of 0.0004 at 1048.1  $\text{cm}^{-1}$  in the b-polarized spectrum indicates that the contribution of stray radiation to the measured reflectance is negligible. The maximum observed reflectances in the b- and a'-polarized spectra were 0.714 at 979.6  $\text{cm}^{-1}$  and 0.679 at 921.8  $\text{cm}^{-1}$ , respectively. A more complete tabulation of the measured reflectances is given in Appendix C in which the data define changes in the reflection of 1.0% below 1200  $\text{cm}^{-1}$  and 0.2% above 1200  $\text{cm}^{-1}$ .

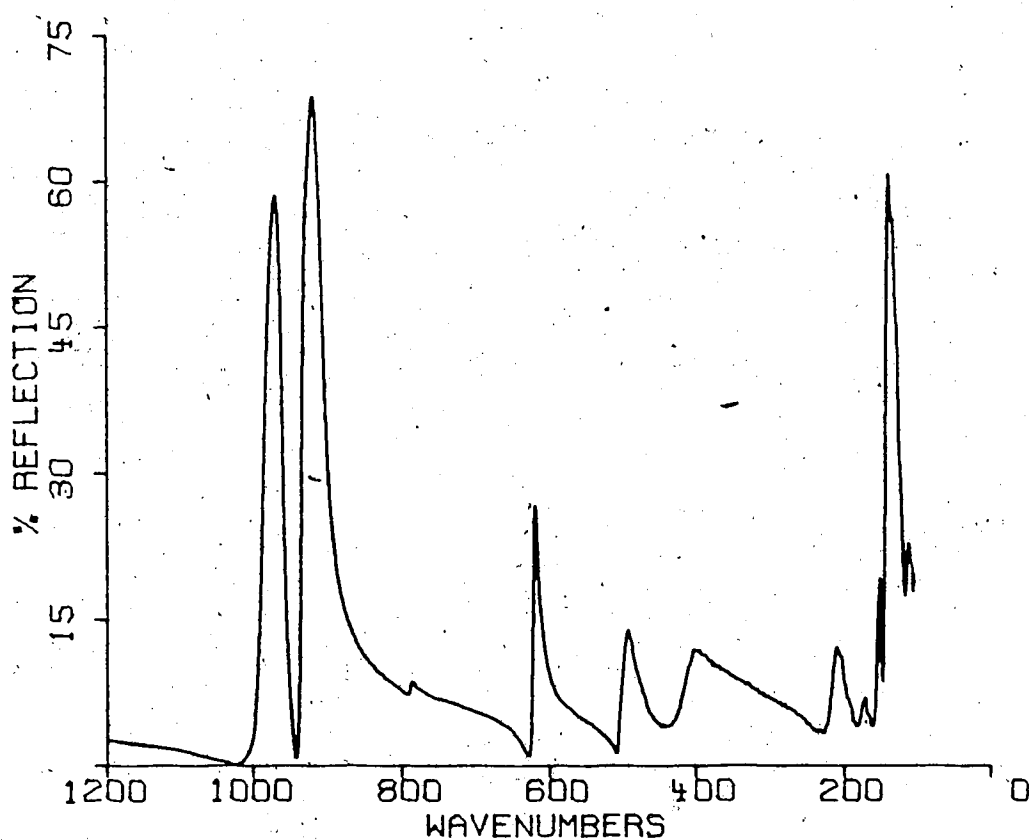
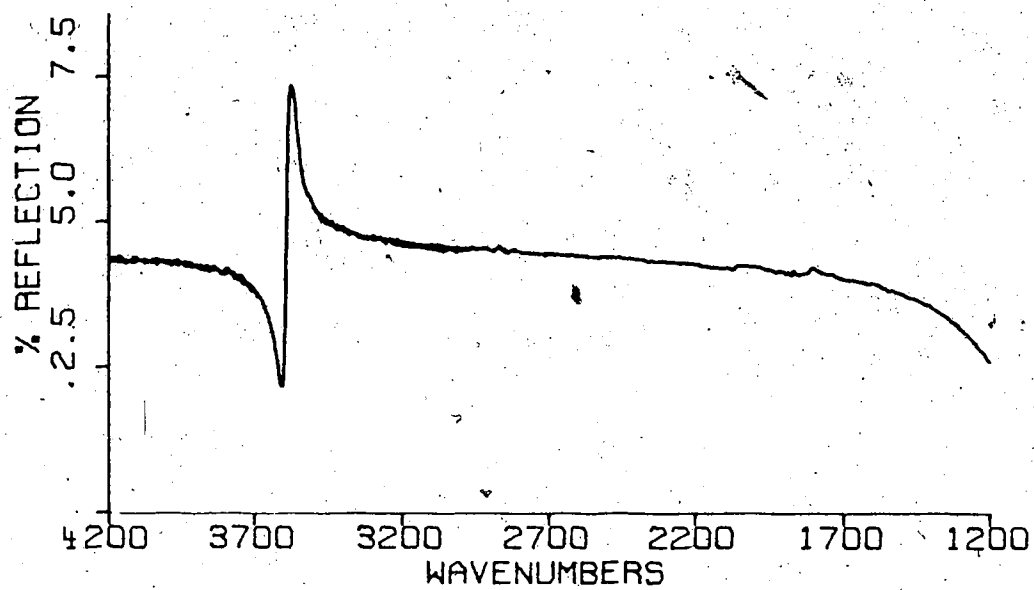


Figure 3.24 Composite a'-polarized reflectance spectrum of (001) face of single crystal  $\text{Ba}(\text{ClO}_3)_2 \cdot \text{H}_2\text{O}$  at  $-298^\circ\text{K}$  and  $2 \text{ cm}^{-1}$  resolution.

The feature at  $786 \text{ cm}^{-1}$  is most likely due to a trace impurity of  $\text{Ba}(\text{BrO}_3)_2 \cdot \text{H}_2\text{O}$ .

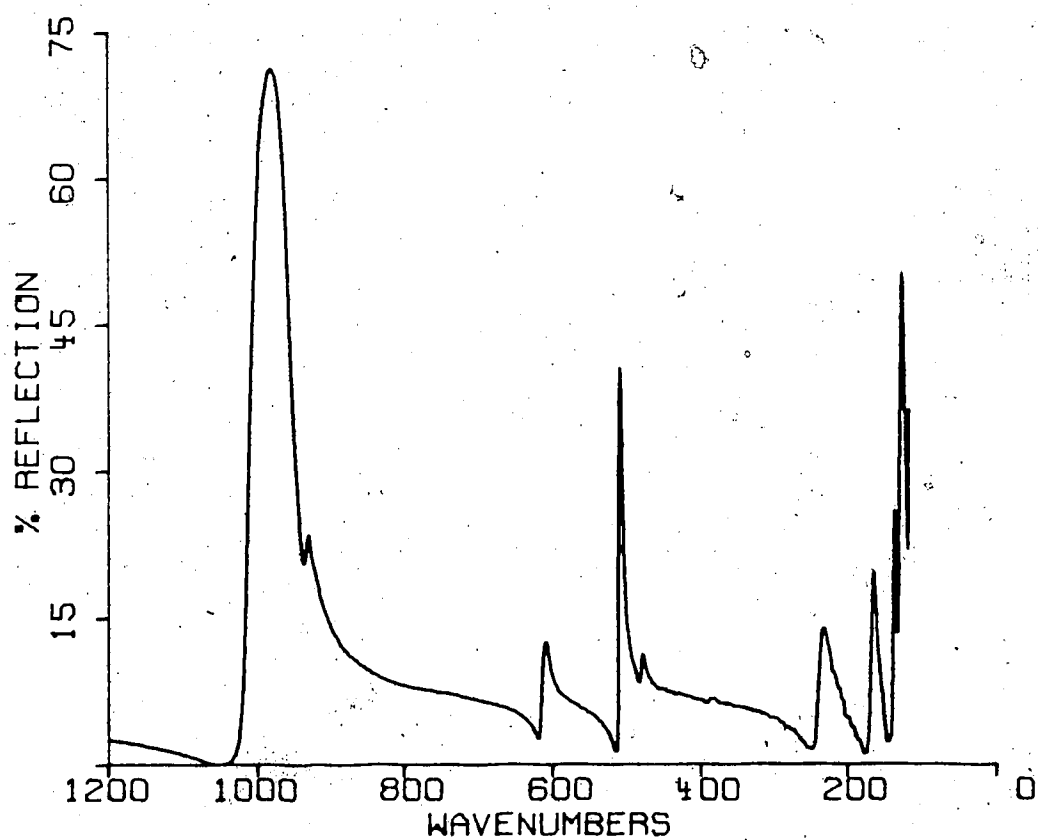
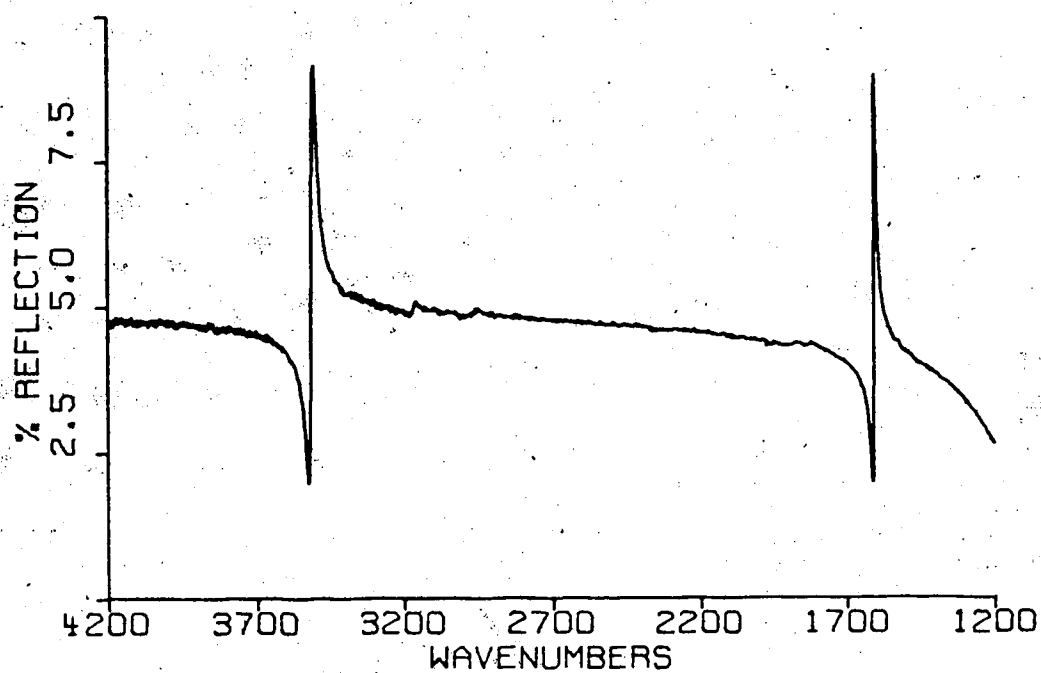


Figure 3.25 Composite b-polarized reflectance spectrum of (001) face of single crystal  $\text{Ba}(\text{ClO}_3)_2 \cdot \text{H}_2\text{O}$  at  $-298^\circ\text{K}$  and  $2 \text{ cm}^{-1}$  resolution.

Table 3.9 Peak and Trough Reflectance Values for (001)

Face of Single Crystal  $\text{Ba}(\text{ClO}_3)_2 \cdot \text{H}_2\text{O}$  at 298°K;  
 resolution = 2  $\text{cm}^{-1}$

$\underline{E} \parallel b$			
PEAK		TROUGH	
$\nu_{\text{max}} (\text{cm}^{-1})$	$R_{\text{max}}$	$\nu_{\text{min}} (\text{cm}^{-1})$	$R_{\text{min}}$
123.4	0.504	131.1	0.134
134.9	0.261	143.6	0.023
162.9	0.199	173.5	0.011
231.4	0.140	247.8	0.016
383.7	0.068	393.4	0.064
479.2	0.115	483.0	0.084
509.1	0.408	515.8	0.013
609.4	0.128	620.0	0.026
931.4	0.237	937.2	0.207
979.6	0.714	1048.1	0.0004
1604.4	0.088	1614.1	0.020
$\underline{E} \perp b$			
112.8	0.230	117.6	0.175
139.8	0.608	147.5	0.087
151.3	0.194	161.9	0.042
171.6	0.071	182.2	0.042
210.2	0.123	227.5	0.034
398.1	0.119	440.6	0.041
491.7	0.140	509.1	0.015
618.0	0.275	628.6	0.009
921.8	0.679	942.0	0.008
970.9	0.588	1026.9	0.002
3571.5	0.073	3610.0	0.022

## CHAPTER IV:

### THE OPTICAL AND DIELECTRIC PROPERTIES OF POLYCRYSTALLINE AND SINGLE CRYSTAL $\text{Ba}(\text{ClO}_3)_2 \cdot \text{H}_2\text{O}$

This chapter presents the optical and dielectric constants derived from the measured polycrystalline and polarized single crystal reflectance spectra of  $\text{Ba}(\text{ClO}_3)_2 \cdot \text{H}_2\text{O}$ . In the case of the single crystal data, these parameters were obtained from both a Kramers-Kronig (Section 4.2b) and a combined Kramers-Kronig/classical dispersion analysis (Section 4.3). For the polycrystalline data, only the former method was used (Section 4.2a). These results are prefaced by a description of the Kramers-Kronig computer program (Section 4.1a) and an assessment of its accuracy with simulated reflectance data (Section 4.1b).

#### 4.1 Kramers-Kronig Method for Obtaining Optical Constants

The Kramers-Kronig (KK) procedure for the conversion of measured reflectance to optical constants was described in Section 1.2b and its general mathematical basis is outlined in Appendix A. This section describes the implementation of this KK method in the analysis of the  $\text{Ba}(\text{ClO}_3)_2 \cdot \text{H}_2\text{O}$  reflectance data. Details of the computer program are given, including how the KK-integral was evaluated, and any approximations involved in the calculation. The program's accuracy, and the effect of the finite integration range are illustrated with theoretical reflection

data, for which the optical constants are accurately known.

#### 4.1a Description of Method

The Kramers-Kronig program was written in Fortran for general use on the Nicolet 1180 computer. The following form of the Kramers-Kronig integral was employed:

$$\theta(\nu_j) = \frac{\nu_j}{\pi} \int_0^{\infty} \frac{\ln R(\nu_j) - \ln R(\nu_i) d\nu_i}{\nu_i^2 - \nu_j^2} \quad [4.1]$$

Because experimental data is only available over the finite frequency range  $(\nu_{\min}, \nu_{\max})$ , this integral was rewritten as the sum of three integrals with integration bounds of  $[0, \nu_{\min}]$ ,  $[\nu_{\min}, \nu_{\max}]$ , and  $[\nu_{\max}, \infty]$ , respectively. This formulation is shown in Equation [1.76]. The contributions from the regions  $(0, \nu_{\min})$  and  $(\nu_{\max}, \infty)$  are unknown, thereby making it necessary to assume some form of reflectance behavior beyond the measured frequency limits.

Since the near-infrared reflectance of  $\text{Ba}(\text{ClO}_3)_2 \cdot \text{H}_2\text{O}$  is relatively constant, and the crystal is transparent to visible light, it is reasonable to make an extrapolation of constant reflectance from  $\nu_{\max}$  to infinity, with the reflectance equal to  $R(\nu_{\max})$ . Although a constant reflectance extrapolation of the low frequency data, with the reflectance equal to that of  $R(\nu_{\min})$  is more tenuous, the range of extrapolation is very narrow (less than  $100 \text{ cm}^{-1}$ ). It is expected that the error incurred by these approximations is small because of the local character of the KK-

integral (see Section 1.2b), and the fact that the region of prominent infrared absorption was measured.

The assumption of  $R(\nu)$  equal to  $R(\nu_{\max})$  for frequencies greater than  $\nu_{\max}$  and equal to  $R(\nu_{\min})$  for frequencies less than  $\nu_{\min}$ , enables the contribution of these wing regions to be determined by rigorous integration according to equation [1.77]. For the measured region  $(\nu_{\min}, \nu_{\max})$ , the integral was evaluated by a 3-point Simpson's rule. This procedure is illustrated schematically in Figure 4.1 and the relevant mathematical expressions are summarized in Table 4.1. The only difficulty arose when the frequencies  $\nu_i$  and  $\nu_j$  were equal. It can be seen from equation [4.1], that the integrand is undefined for this limiting condition. This problem was circumvented by assigning the average value of the integrand function for the next-neighbouring points,  $\nu_{i+1}$  and  $\nu_{i-1}$ , to the frequency  $\nu_i = \nu_j$ . This procedure is merely an application of l'Hopitals rule. When this condition occurred at the border of two integration sub-intervals of different grid spacings,  $\delta$  and  $\Delta$ , then the *weighted* average value of the next-neighboring points was assigned to the integrand function, i.e.:

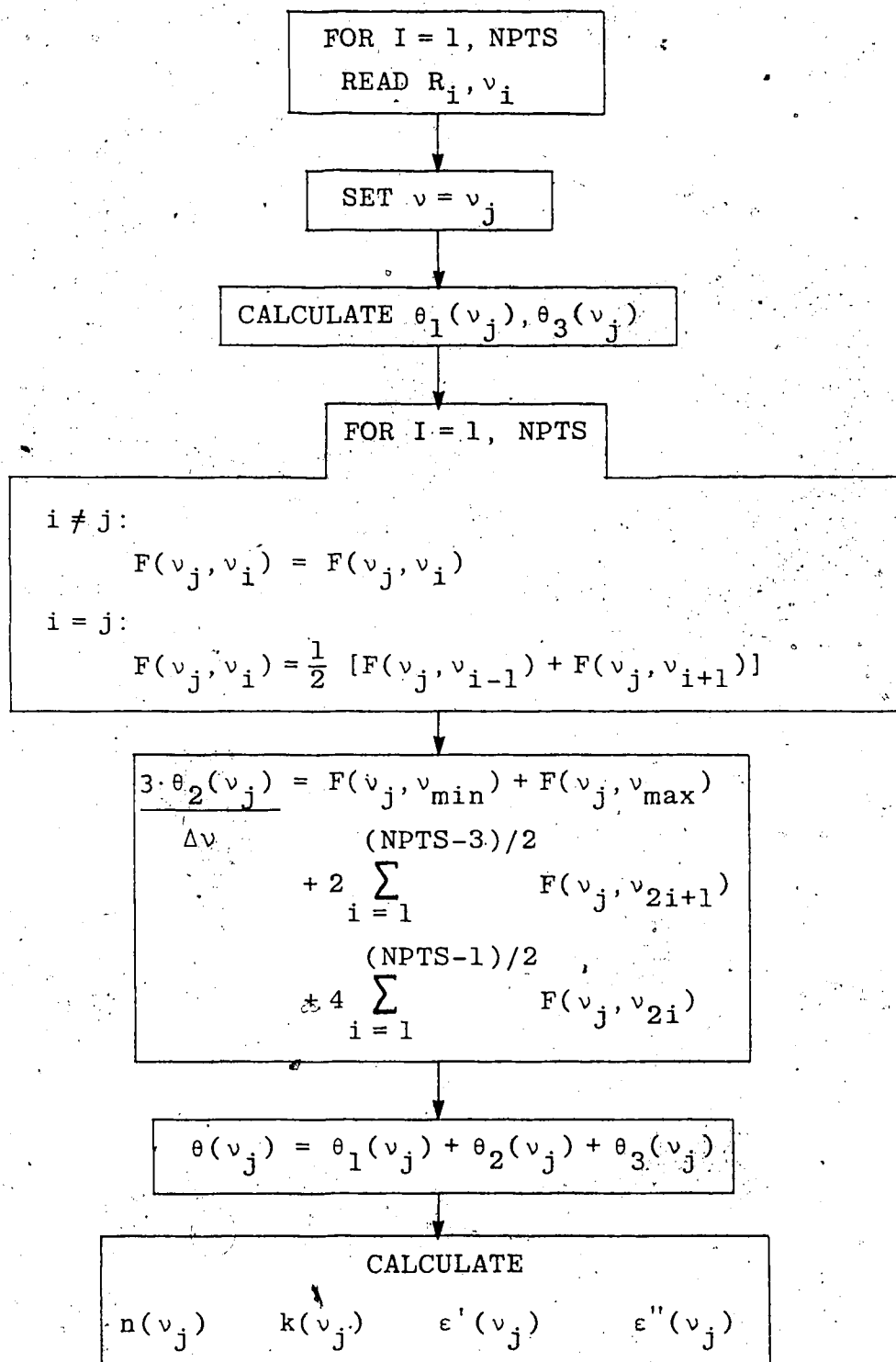
$$F(\nu_j, \nu_i) = \frac{\delta F(\nu_j, \nu_{i+1}) + \Delta F(\nu_j, \nu_{i-1})}{\delta + \Delta}$$

where

$$\Delta = |\nu_{i+1} - \nu_i|$$

$$\delta = |\nu_i - \nu_{i-1}|.$$

Figure 4.1 Schematic of Kramers-Kronig computer program, with Simpson's rule integration procedure.



Because of the Simpson's rule algorithm, each distinct integration sub-interval must contain an odd number of data points. A check for this condition and a suitable corrective measure were therefore included in the program.

It was found that the program execution required typically six hours for the calculation of the phase at every point in a 4500 data point array, that is  $(4500)^2$  evaluations of the integrand function. To permit more rapid, qualitative checks of the KK-derived spectra, provision was made to calculate the phase at only certain specified frequencies.

From the derived phase angle and the measured reflectance, the corresponding optical constants  $n$  and  $k$  were obtained from equations [1.71] and [1.72], which have been rewritten in Table 4.1. These equations assume normal incidence, although our experimental measurements were performed at  $9.5^\circ$  incidence. However, it was previously shown in Section 3.2b that the error introduced by this approximation is generally very small.

#### 4.1b Analysis of Method

Before the Kramers-Kronig program was applied to experimental reflection data, its integrity was checked with theoretical reflectance data, for which the optical constants were accurately known. Since the uncertainty in the measured reflectance was eliminated, it was possible to focus on the errors due to the constant reflectance extrapolation and the mathematical approximations.

Table 4.1 Definition of Terms in Kramers-Kronig Program

$$\theta_1(v_j) = \frac{1}{2\pi} \ln \left[ \frac{R(v_{\min})}{R(v_j)} \right] \ln \left[ \frac{v_j + v_{\min}}{v_j - v_{\min}} \right]$$

$$\theta_3(v_j) = \frac{1}{2\pi} \ln \left[ \frac{R(v_{\max})}{R(v_j)} \right] \ln \left[ \frac{v_{\max} - v_j}{v_{\max} + v_j} \right]$$

$$F(v_j, v_i) = \frac{v_j}{\pi} \left[ \frac{\ln R(v_i) - \ln R(v_j)}{v_j^2 - v_i^2} \right]; \quad \theta_2(v_j) = \int_{v_{\min}}^{v_{\max}} F(v_j, v_i) dv_i$$

$$n(v_j) = \frac{1 - R(v_j)}{1 - 2\sqrt{R(v_j)} \cos \theta(v_j) + R(v_j)}$$

$$k(v_j) = \frac{2\sqrt{R(v_j)} \sin \theta(v_j)}{1 - 2\sqrt{R(v_j)} \cos \theta(v_j) + R(v_j)}$$

$$\epsilon'(v_j) = n^2(v_j) - k^2(v_j)$$

$$\epsilon''(v_j) = 2n(v_j)k(v_j)$$

The classical dispersion method, described in Section 1.2b, was used to generate synthetic reflection spectra. Recall that this model assumes that the real and imaginary dielectric constants can be expressed as the sum of damped harmonic oscillator functions. The band profiles of  $\epsilon'(\nu)$  and  $\epsilon''(\nu)$  are then determined by the oscillator strengths  $S_j$ , the resonance frequencies  $\nu_j$ , the damping constants  $\gamma_j$ , and the assumed constant contribution from all unobserved oscillators to high frequency  $\epsilon_\infty$ . The appropriate relations for  $\epsilon'(\nu)$  and  $\epsilon''(\nu)$  in terms of  $\epsilon_\infty$ ,  $S_j$ ,  $\gamma_j$ , and  $\nu_j$  for  $N$  oscillators, are given in equations [1.84] and [1.85]. The reflectance spectrum  $R(\nu)$  is then calculated from the complex dielectric function,  $\hat{\epsilon}(\nu) = \epsilon'(\nu) + i\epsilon''(\nu)$ , according to:

$$R(\nu) = \left| \frac{\sqrt{\hat{\epsilon}(\nu)} - 1}{\sqrt{\hat{\epsilon}(\nu)} + 1} \right|^2 = \frac{(n-1)^2 + k^2}{(n+1)^2 + k^2}$$

where

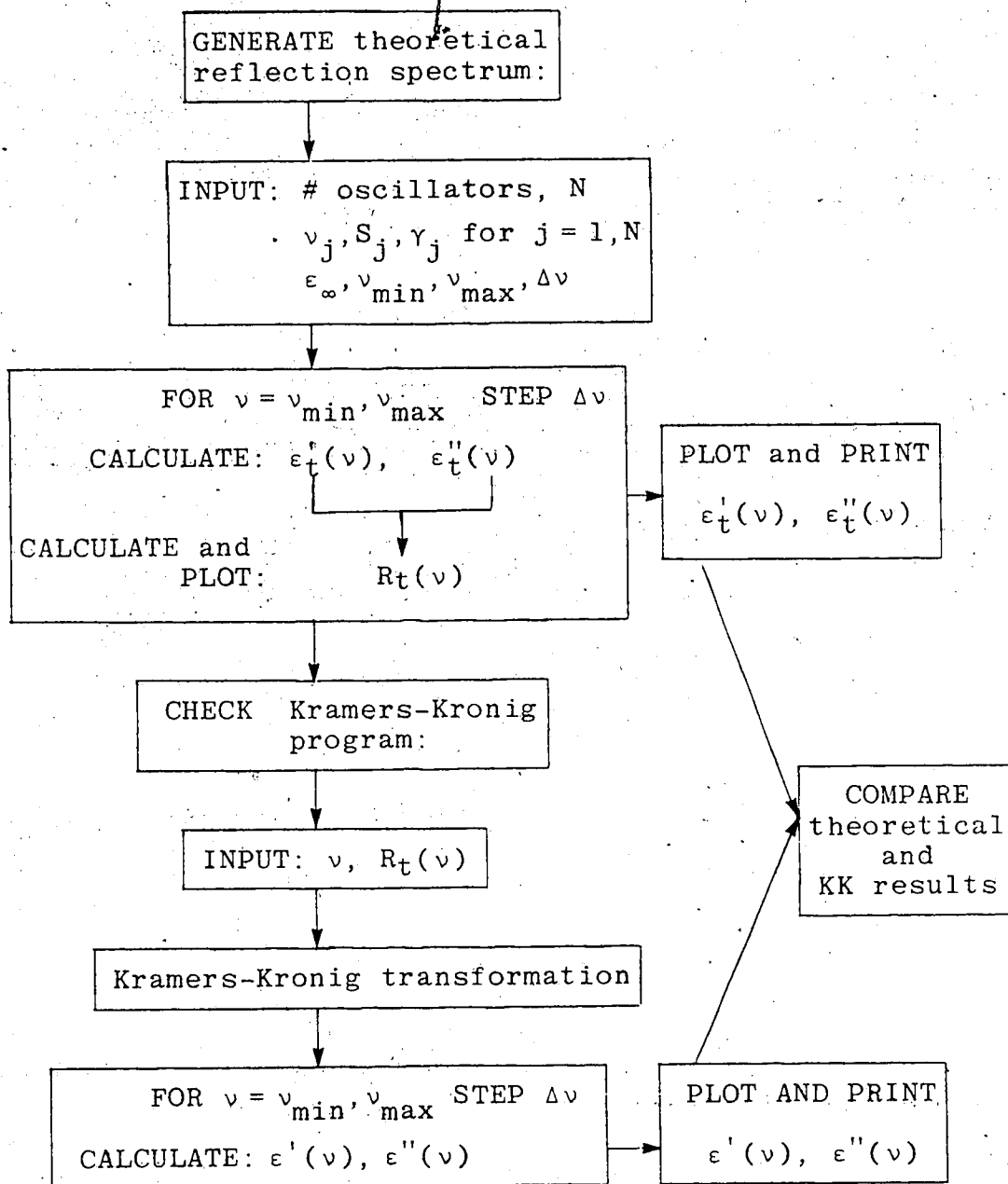
$$n = \frac{1}{2} \sqrt{[\sqrt{\epsilon'^2 + \epsilon''^2} + \epsilon']}$$

and

$$k = \frac{1}{2} \sqrt{[\sqrt{\epsilon'^2 + \epsilon''^2} - \epsilon']} \quad [4.2]$$

These steps in the generation of a synthetic reflection spectrum are summarized in Figure 4.2. To distinguish this data as theoretical, it is denoted with a subscript 't'.

Figure 4.2 Schematic for checking Kramers-Kronig program with theoretical reflection data



In our case, the assumed oscillator parameters were obtained from Spitzer and Kleinman's<sup>93</sup> dispersion fit to the ordinary ray ( $E \perp c$ ) reflectance spectrum of quartz, and are listed in Table 4.2. The reflectance spectrum computed from this set of parameters on a  $1 \text{ cm}^{-1}$  grid over the frequency region  $200\text{--}2000 \text{ cm}^{-1}$  is shown in Figure 4.3. It can be seen that it bears a superficial resemblance to the infrared reflectance spectra of  $\text{Ba}(\text{ClO}_3)_2 \cdot \text{H}_2\text{O}$  and, therefore, should provide a realistic analytical model.

In order to understand the effect of the finite integration limits on the accuracy of the derived optical constants, the Kramers-Kronig analysis was performed for three different frequency ranges:

- i) 1801 points encoded at  $1 \text{ cm}^{-1}$  intervals from  $200\text{--}2000 \text{ cm}^{-1}$  (Spectrum A)
- ii) Spectrum A + 39 points encoded at  $5 \text{ cm}^{-1}$  intervals from  $10\text{--}200 \text{ cm}^{-1}$  (Spectrum B)
- iii) Spectrum B + 401 points encoded at  $5 \text{ cm}^{-1}$  intervals from  $2000\text{--}4000 \text{ cm}^{-1}$  (Spectrum C)

The real dielectric constant spectra  $\epsilon'(\nu)$ , computed for these various integration ranges, are compared in Figure 4.4 with the "theoretical"  $\epsilon'(\nu)$  spectrum, and a list of the  $\epsilon'(\nu)$  and  $\epsilon''(\nu)$  peak and trough values is given in Table 4.3. The theoretical values are underscored for easy comparison. It can be seen that the choice of integration limits has little effect on the calculated frequencies of optical structure, but has a significant effect on the amplitudes of these features. The narrowest integration range, Curve A ( $200\text{--}2000 \text{ cm}^{-1}$ ), gave relatively poor agreement with the

Table 4.2 Parameters for a 7-Band Simulated Spectrum Generated from a Set of Damped Harmonic Oscillator Functions

Resonance Frequency $\nu_j(\text{cm}^{-1})$	Oscillator Strength $S_j(\text{cm}^{-2})$	Damping Constant $\gamma_j(\text{cm}^{-1})$
1227	$1.35 \times 10^4$	135.0
1163	$1.35 \times 10^4$	6.98
1072	$7.70 \times 10^5$	7.61
797	$6.98 \times 10^4$	7.17
697	$8.73 \times 10^3$	8.36
450	$1.66 \times 10^5$	4.05
394	$5.13 \times 10^4$	2.76

$\epsilon_\infty = 2.3559$ ; frequency range = 200-2000  $\text{cm}^{-1}$ ; resolution = 2  $\text{cm}^{-1}$ .

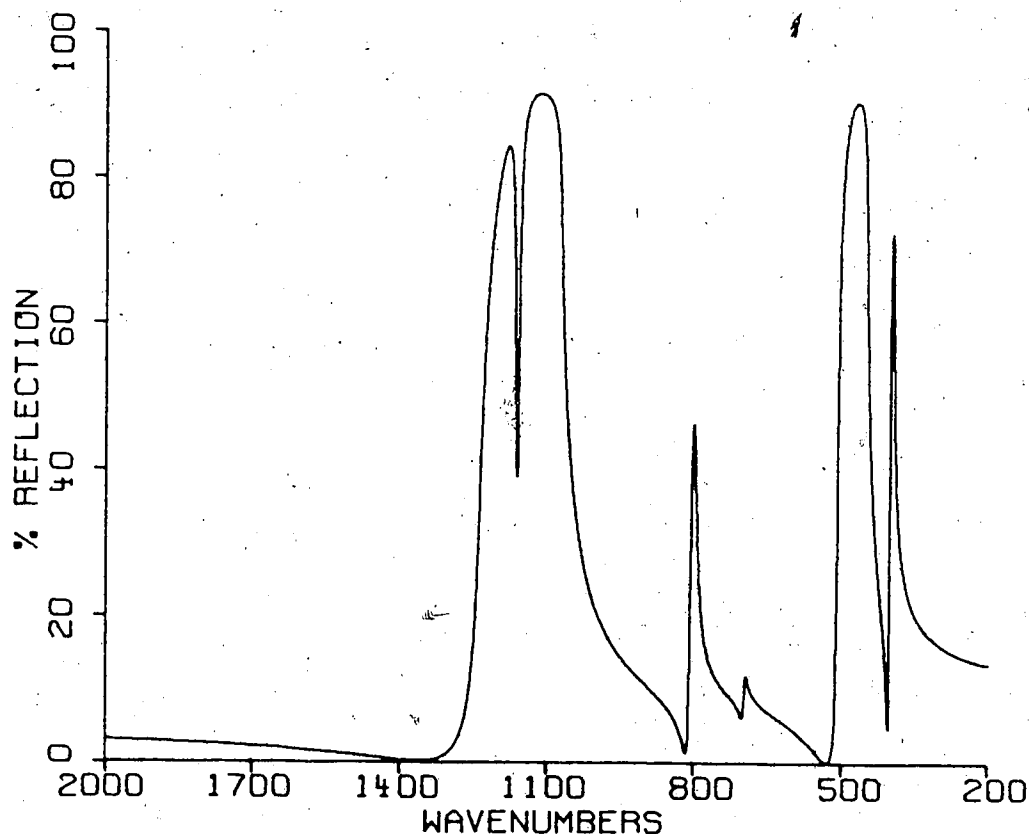


Figure 4.3 Theoretical reflection spectrum derived from dispersion parameters of Table 4.3.

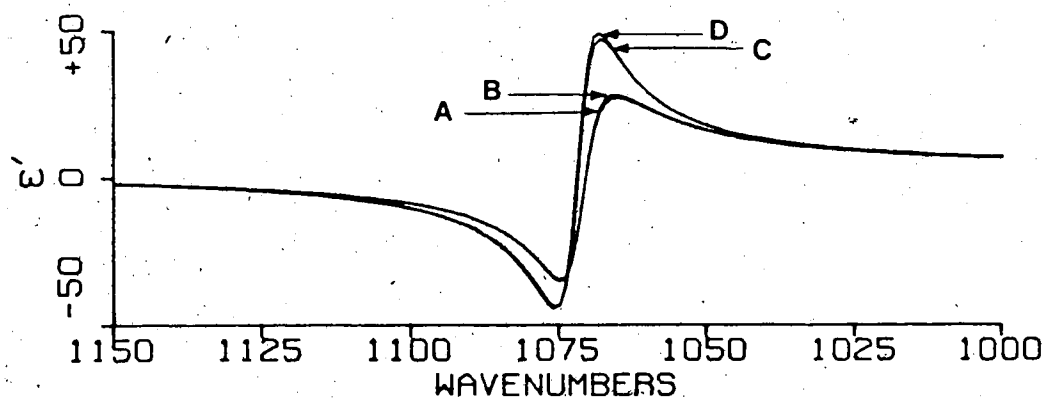
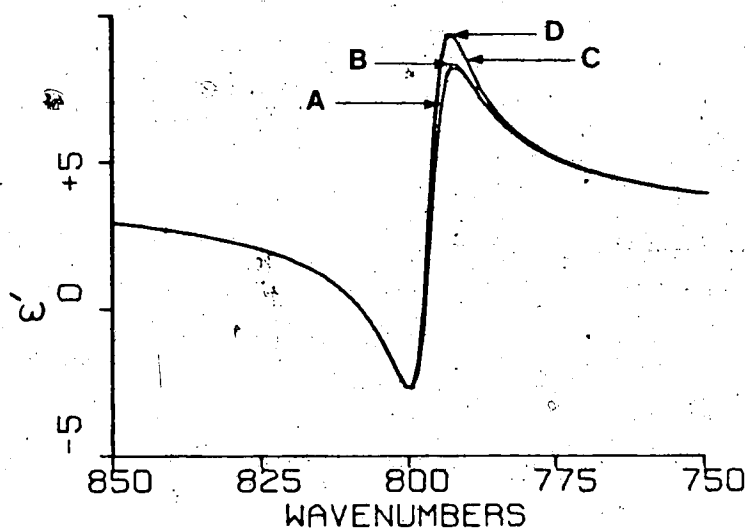
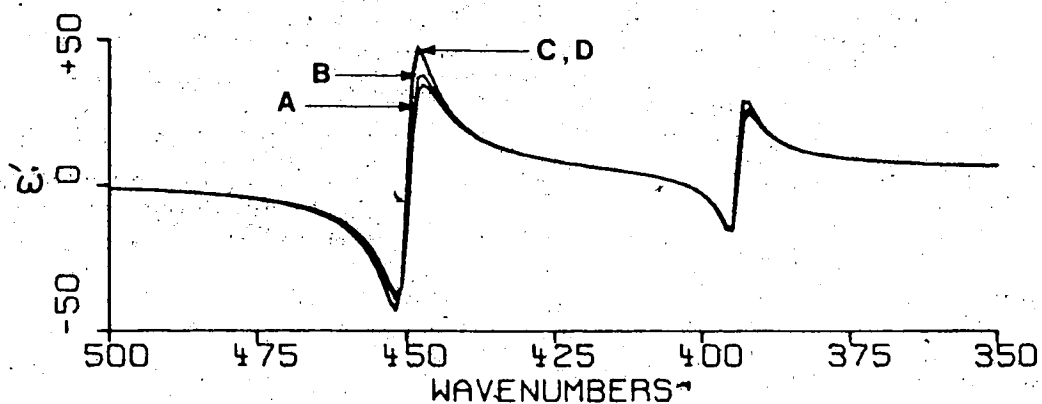


Figure 4.4 Comparison of theoretical  $\epsilon'$  spectrum and Kramers-Kronig derived  $\epsilon'$  spectra for various integration ranges.

Curve A: 200-2000  $\text{cm}^{-1}$ ; data at 1  $\text{cm}^{-1}$  intervals

Curve B: 10-2000  $\text{cm}^{-1}$ ; 10-200  $\text{cm}^{-1}$  at 5  $\text{cm}^{-1}$  intervals, 200-2000  $\text{cm}^{-1}$  at 1  $\text{cm}^{-1}$  intervals

Curve C: 10-4000  $\text{cm}^{-1}$ ; 10-200  $\text{cm}^{-1}$  and 2000-4000  $\text{cm}^{-1}$  at 5  $\text{cm}^{-1}$  intervals, 200-2000  $\text{cm}^{-1}$  at 1  $\text{cm}^{-1}$  intervals

Curve D: theoretical  $\epsilon'$  spectrum

Table 4.3 Comparison of Theoretical and Calculated Dielectric Constants for Various Integration Ranges

		$\epsilon'(\nu)$				$\epsilon''(\nu)$	
Integration range (cm <sup>-1</sup> )		$\nu_{\max}$	$\epsilon'_{\max}$	$\nu_{\min}$	$\epsilon'_{\min}$	$\nu_{\max}$	$\epsilon''_{\max}$
D		393	29.259	395	-15.456	394	47.301
A	200-2000	392	24.795	395	-15.476	394	41.303
B	10-2000	392	26.356	395	-15.548	394	43.464
C	10-4000	392	28.687	395	-15.464	394	46.862
D		448	48.042	452	-43.040	450	91.209
A	200-2000	447	34.992	452	-37.496	450	72.511
B	10-2000	447	38.035	452	-39.141	450	77.917
C	10-4000	448	47.121	452	-42.746	450	89.998
D		693	3.982	701	2.568	697	1.531
A	200-2000	693	3.877	701	2.493	697	1.667
B	10-2000	693	3.894	701	2.505	697	1.648
C	10-4000	693	3.975	701	2.563	697	1.540
D		793	9.413	801	-2.679	797	12.248
A	200-2000	793	8.234	800	-2.720	797	11.257
B	10-2000	793	8.376	800	-2.715	797	11.377
C	10-4000	793	9.335	801	-2.677	797	12.179
D		1068	49.359	1076	-44.859	1072	94.370
A	200-2000	1065	27.476	1075	-34.856	1071	63.709
B	10-2000	1065	28.457	1075	-35.439	1071	65.351
C	10-4000	1068	47.299	1076	-44.005	1072	91.652
D		1160	-0.982	1166	-2.368	1163	1.877
A	200-2000	1160	-0.883	1166	-2.070	1163	1.605
B	10-2000	1160	-0.889	1166	-2.085	1163	1.618
C	10-4000	1160	-0.977	1166	-2.346	1163	1.848

Theoretical data are underscored. Frequencies are in cm<sup>-1</sup>.

"theoretical" spectrum, Curve D. Including reflectance data down to  $10 \text{ cm}^{-1}$  made a slight improvement, particularly for the low frequency features. However, extending the high frequency reflectance data to  $4000 \text{ cm}^{-1}$  (Curve C) made a dramatic improvement to all calculated features. Visual comparison of Curves C and D shows excellent agreement, although the discrepancy increases with increasing frequency. The most likely source of this residual error is the constant reflectance extrapolation from  $4000 \rightarrow \infty \text{ cm}^{-1}$ .

#### 4.2 Kramers-Kronig Derived Optical Constants for $\text{Ba}(\text{ClO}_3)_2 \cdot \text{H}_2\text{O}$

This section presents the results of the Kramers-Kronig analysis of the measured polycrystalline and single crystal  $\text{Ba}(\text{ClO}_3)_2 \cdot \text{H}_2\text{O}$  reflectance spectra. The basic procedure was that outlined in Section 4.1 for the transformation of the theoretical reflectance data. However, since the R.I.I.C. far-infrared data and the Nicolet near-infrared data were obtained with a different spectral resolution than the Nicolet mid- and far-infrared reflection results, it was necessary to treat these different frequency regions as distinct integration sub-intervals. Furthermore, because of the requirement of an odd number of points per sub-interval, there was usually no frequency common to neighboring integration regions. Thus, trapezoidal integration was used between the lowest frequency data point of one region and the highest frequency point of its neigh-

bor. These integration sub-intervals are defined in Figure 4.5, and the method of integration employed in each region is indicated.

#### 4.2a. Polycrystalline $\text{Ba}(\text{ClO}_3)_2 \cdot \text{H}_2\text{O}$

The polycrystalline  $\text{Ba}(\text{ClO}_3)_2 \cdot \text{H}_2\text{O}$  reflectance data were processed in three different ways:

- i) using measured reflectance data from 50-4000  $\text{cm}^{-1}$  (Range A)
- ii) using measured reflectance data from 64-4400  $\text{cm}^{-1}$  and an artificial wing generated from  $R(\nu) = a \exp(b\nu) - 0.015$ , where  $a = 0.17$  and  $b = 0.007$ , in the region 1-64  $\text{cm}^{-1}$  (Range B)
- iii) using measured reflectance data from 50-7200  $\text{cm}^{-1}$  (Range C)

The input data to the KK-calculations are summarized in Table 4.4, which gives the number of data points, the extrapolated high and low frequency reflectance values, and the modes of integration.

The optical and dielectric constant spectra derived for integration range A are shown in Figures 4.6 and 4.7, respectively. A detailed compilation of the  $\epsilon'(\nu)$  and  $\epsilon''(\nu)$  values is given in Appendix D at frequency intervals corresponding to a change in  $\epsilon''(\nu)$  of 0.2 units below 1200  $\text{cm}^{-1}$  and 0.04 units above 1200  $\text{cm}^{-1}$ . Spurious negative dips are evident in the  $k(\nu)$  and  $\epsilon''(\nu)$  spectra at  $\approx 830$ -900  $\text{cm}^{-1}$  (-0.55), 1900-2450  $\text{cm}^{-1}$  (-0.14) and 3700-4200  $\text{cm}^{-1}$  (-0.06). The numbers in parentheses are the maximum values of the dips in  $\epsilon''(\nu)$  over the specified region. This physically unacceptable result has been en-

Figure 4.5 Definition of integration sub-intervals for Kramers-Kronig integration procedure.

Sub-intervals	Description
I	- R.I.I.C. $2\text{ cm}^{-1}$ resolution far-infrared data (+ artificial wing)
III	- Nicolet $2\text{ cm}^{-1}$ resolution mid- and far-infrared data
V	- Nicolet $8\text{ cm}^{-1}$ resolution near-infrared data
II, IV	- merge zones

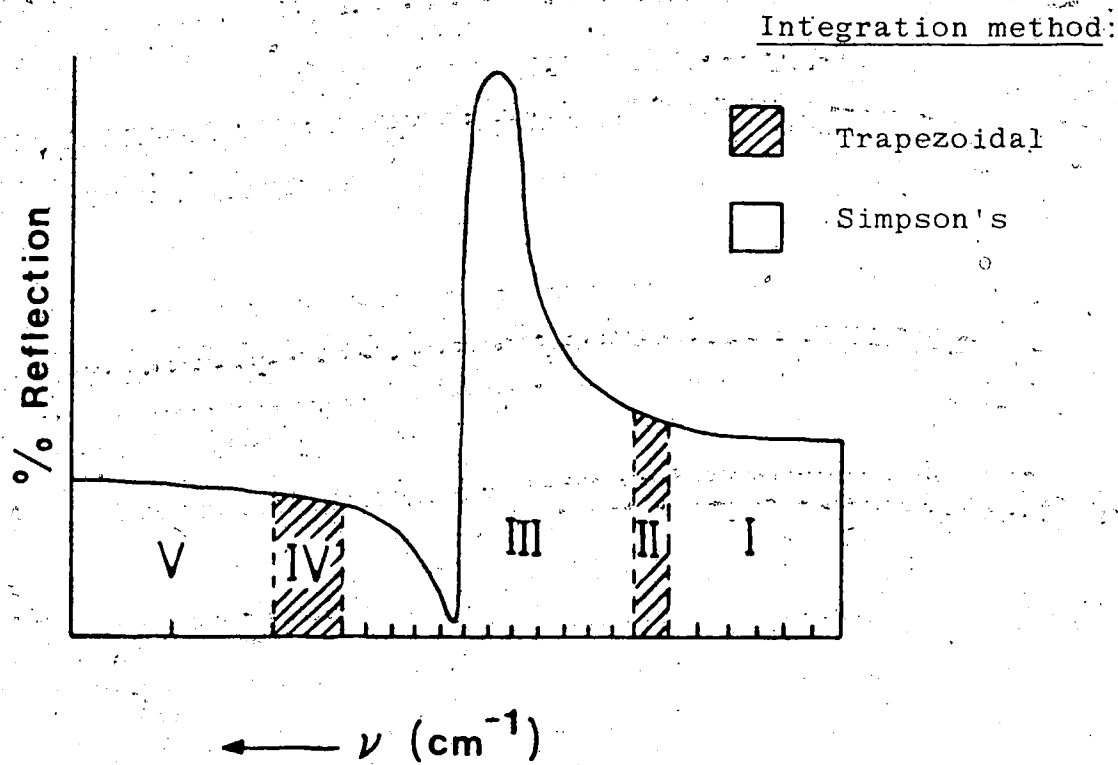


Table 4.4 Integration Range Data for Kramers-Kronig Transformation of  $\text{Ba}(\text{ClO}_3)_2 \cdot \text{H}_2\text{O}$  Reflectance Spectra

	<u>Frequency range(<math>\text{cm}^{-1}</math>)</u>	<u>#Points</u>	<u><math>R(\nu_{\min})</math></u>	<u><math>R(\nu_{\max})</math></u>	<u>Sub- intervals*</u>
<u>Single crystal</u>					
<u>E</u>    b	115-4400	4445	0.363	0.049	III
<u>E</u> ⊥ b	105-4400	4455	0.205	0.044	III
	105-6500	4534	0.205	0.045	III, IV, V
<u>Poly- crystal</u>	1-4400	4664	0.156	0.053	I, II, III
	50-4400	4584	0.236	0.053	I, II, III
	50-7200	5009	0.236	0.059	I-V

\* See description of integration sub-intervals in Figure 4.5.

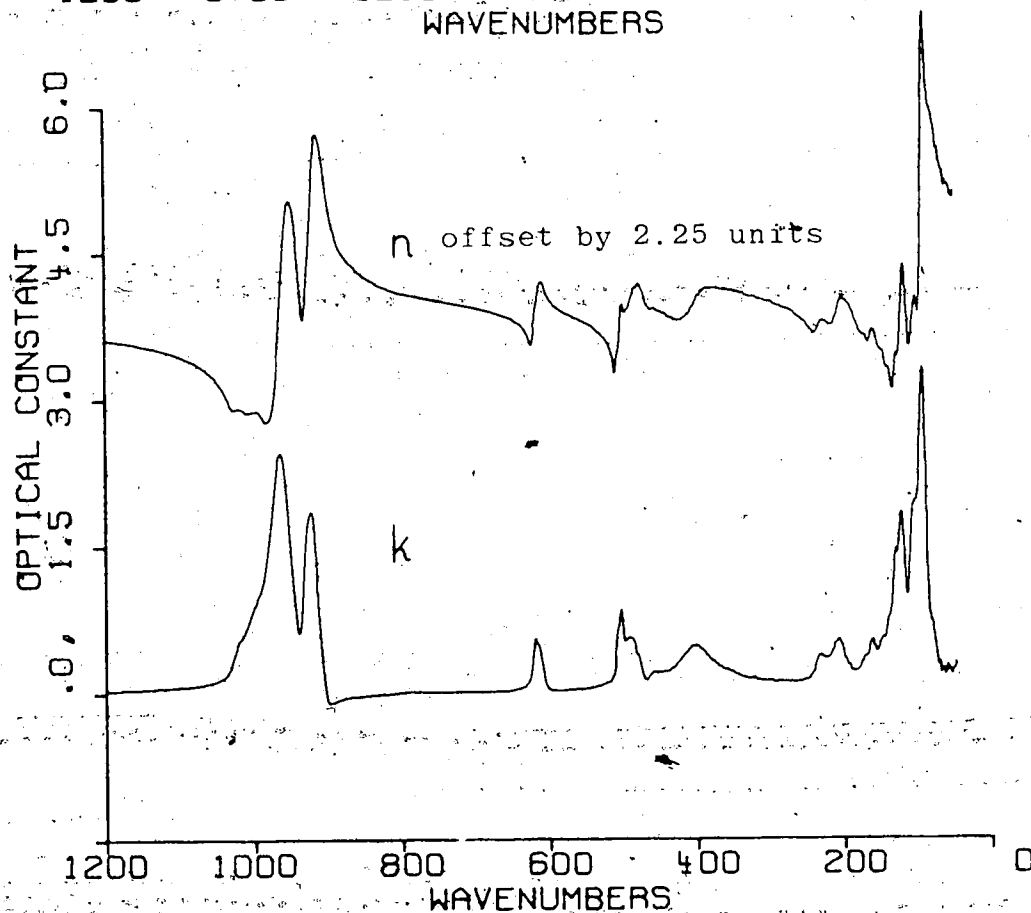
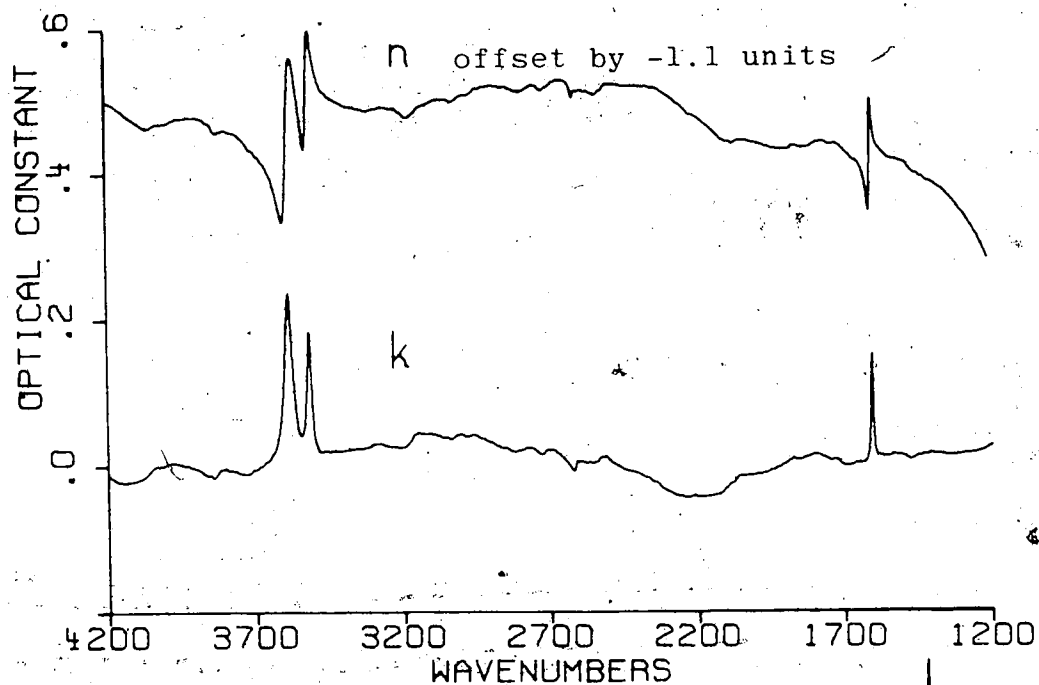


Figure 4.6 Optical constants  $n$  and  $k$  for polycrystalline  $\text{Ba}(\text{ClO}_3)_2 \cdot \text{H}_2\text{O}$  at 298°K; resolution = 2  $\text{cm}^{-1}$ .

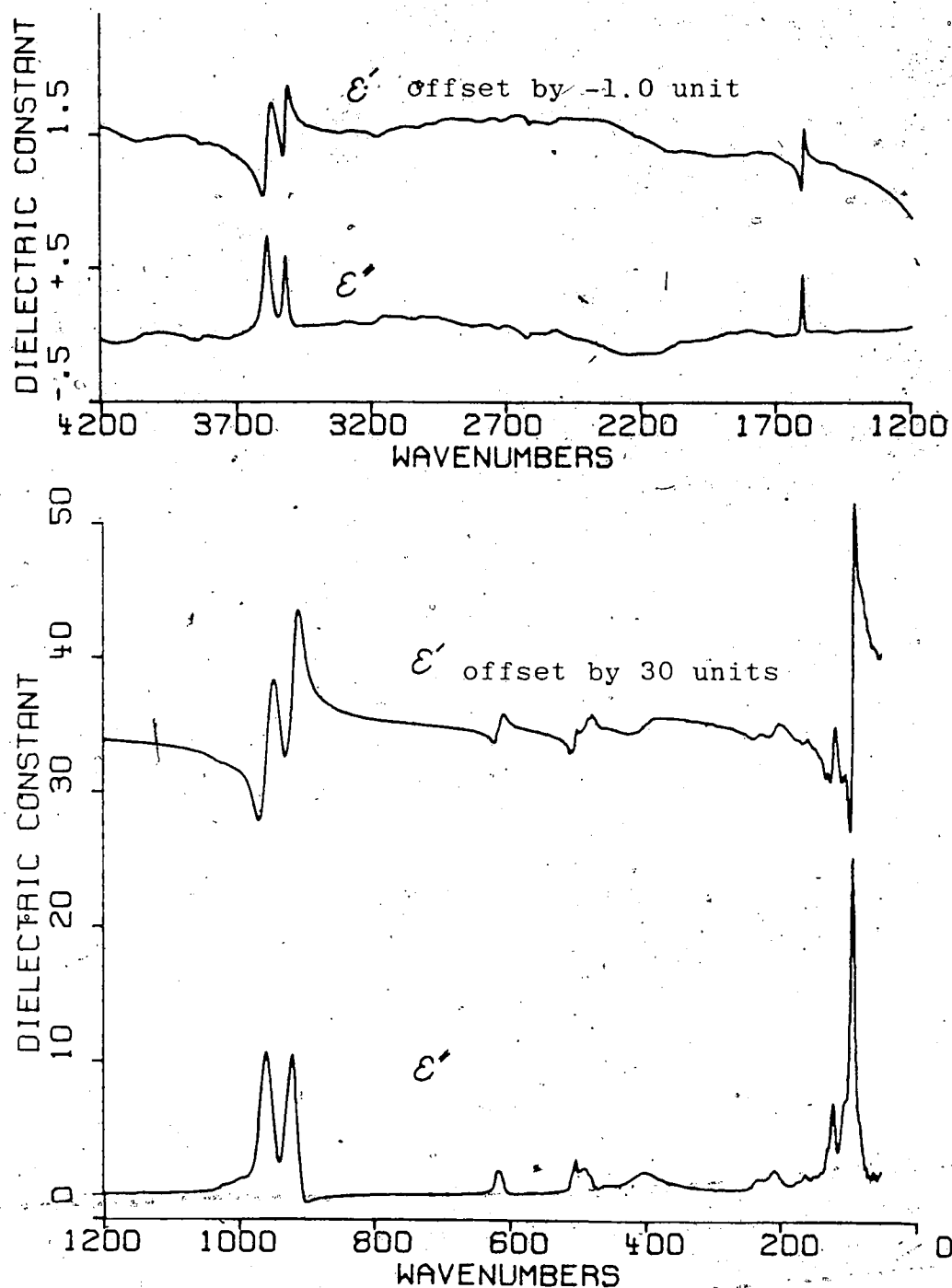


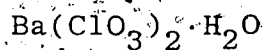
Figure 4.7: Dielectric constants  $\epsilon'$  and  $\epsilon''$  for polycrystalline  $\text{Ba}(\text{ClO}_3)_2 \cdot \text{H}_2\text{O}$  at 298°K; resolution = 2  $\text{cm}^{-1}$ .

countered by several other workers in the Kramers-Kronig analysis of reflection data (see, for example, Section 1.4).

In Table 4.5, the KK-derived values of  $\epsilon'(\nu)$  and  $\epsilon''(\nu)$  for integration ranges B and C are compared with those of range A for several frequencies. Consistent with our theoretical model calculations, the positions of optical structure were little affected by the choice of integration range. However, inclusion of the simulated reflectance wing for the region  $1-64 \text{ cm}^{-1}$  (range B) introduced a fairly large negative dip in the  $\epsilon''(\nu)$  spectra from  $1-72 \text{ cm}^{-1}$ , and increased the negative dip at  $\sim 900 \text{ cm}^{-1}$  by  $\sim 12\%$ . Above  $1000 \text{ cm}^{-1}$ , the derived optical results were in close agreement with those of range A. For these reasons, it is believed that the artificial wing, although it reproduces the observed reflectance in the region  $30-70 \text{ cm}^{-1}$  extremely well, does not accurately describe the reflectance behavior for frequencies below  $30 \text{ cm}^{-1}$ . The results for integration range B are therefore considered less reliable than those of range A.

When the measured near-infrared reflectance data was included in the transformation procedure (range C), there was little change in the derived  $\epsilon'(\nu)$  and  $\epsilon''(\nu)$  results for frequencies below  $800 \text{ cm}^{-1}$ . However, in the region of the strong  $\text{ClO}_3^-$  absorption, from  $\sim 900-1000 \text{ cm}^{-1}$ , there were significant differences with the results of range A; in particular, the negative dip in the  $\epsilon''(\nu)$  spectrum at  $\sim 900 \text{ cm}^{-1}$  increased by  $\sim 20\%$ . The range C data also pro-

Table 4.5 Effect of Integration Range on Calculated Dielectric Constants for Polycrystalline



Frequency $\nu$ ( $\text{cm}^{-1}$ )	$\epsilon'$ ( $\nu$ )			$\epsilon''$ ( $\nu$ )		
	A*	B*	C*	A	B	C
62.2	8.84	8.88	8.84	1.58	-0.37	1.57
92.7	8.26	10.10 <sup>†</sup>	8.34	25.19	27.19 <sup>†</sup>	25.22
122.6	0.97	1.44	0.98	6.87	7.24	6.88
164.1	1.80	1.87	1.81	1.56	1.55	1.56
209.2	2.60	2.67	2.60	1.85	1.81	1.84
402.1	2.91	2.95	2.92	1.74	1.72	1.73
490.8	2.83	2.86	2.85	2.02	2.00	2.01
503.3	2.12	2.16	2.14	2.66	2.67	2.67
619.0	2.30	2.33	2.32	1.77	1.76	1.76
898.7	7.17	7.41 <sup>†</sup>	7.40 <sup>†</sup>	-0.55	-0.62 <sup>†</sup>	-0.66 <sup>†</sup>
921.8	5.57	5.73	5.83	10.51	10.53	10.55
932.4	0.60	0.63	0.65	5.09	5.12	5.15
939.2	3.17	3.19	3.21	2.50	2.49	2.48
948.8	6.32	6.40	6.46	5.74	5.70	5.68
959.4	1.28	1.38	1.47	10.65	10.74	10.81
971.0	-4.19	-4.21	-4.24	5.14	5.21	5.27
1607.4	2.31	2.31	2.32	0.46	0.46	0.44
3518.5	2.61	2.61	2.65	0.61	0.60	0.52
3586.9	2.40	2.40	2.41 <sup>§</sup>	0.75	0.75	0.68 <sup>§</sup>

\* Range A = 50-4400  $\text{cm}^{-1}$ ; Range B = 1-4400  $\text{cm}^{-1}$ ; Range C = 50-7200  $\text{cm}^{-1}$ .

<sup>†</sup> values are for  $\nu = 93.3 \text{ cm}^{-1}$  (calculated position of local  $\epsilon''_{\text{max}}$ ).

<sup>‡</sup> values are for  $\nu = 899.6 \text{ cm}^{-1}$  (calculated position of local  $\epsilon''_{\text{min}}$ ).

<sup>§</sup> values are for  $\nu = 3587.9 \text{ cm}^{-1}$  (calculated position of local  $\epsilon''_{\text{max}}$ ).

duced negative values of  $\epsilon''(\nu)$  over a wider frequency interval: from 1850-2650  $\text{cm}^{-1}$  (-0.17) and from 3400-3500  $\text{cm}^{-1}$  and 3600-7200  $\text{cm}^{-1}$  (-0.24). Again, the maximum values are given in parentheses. These observations provided strong evidence that the range C optical results were less reliable than those of range A. It is expected that these spurious negative regions of  $\epsilon''(\nu)$  are primarily caused by a too large reflectance value being extrapolated from  $\nu_{\text{max}}$  to infinity. Other possible explanations, such as difficulty in measuring the low reflectance regions (Section 4.2b), and anisotropy of the polycrystalline sample (Section 3.1b), have been discounted. It can be seen from Table 4.4 that for ranges A and B, a constant reflectance of 0.053 was used for frequencies greater than  $\nu_{\text{max}}$ , whereas, for range C, a value of 0.059 was used. This compares with the expected visible region reflectance of 0.052 (see Section 3.1b).

#### 4.2b Single Crystal $\text{Ba}(\text{ClO}_3)_2 \cdot \text{H}_2\text{O}$

This section presents the results of a Kramers-Kronig analysis of polarized reflectance spectra from the (001) crystal face of  $\text{Ba}(\text{ClO}_3)_2 \cdot \text{H}_2\text{O}$  (Figures 3.24 and 3.25).

The room-temperature optical constants,  $n(\nu)$  and  $k(\nu)$ , calculated for the b-polarized data over the range 115-4200  $\text{cm}^{-1}$ , are illustrated in Figure 4.8. The corresponding dielectric constant spectra,  $\epsilon'(\nu)$  and  $\epsilon''(\nu)$ , are shown in Figure 4.9. It should be noted that the  $n(\nu)$  and  $\epsilon'(\nu)$  spectra have been offset for clarity of presentation,

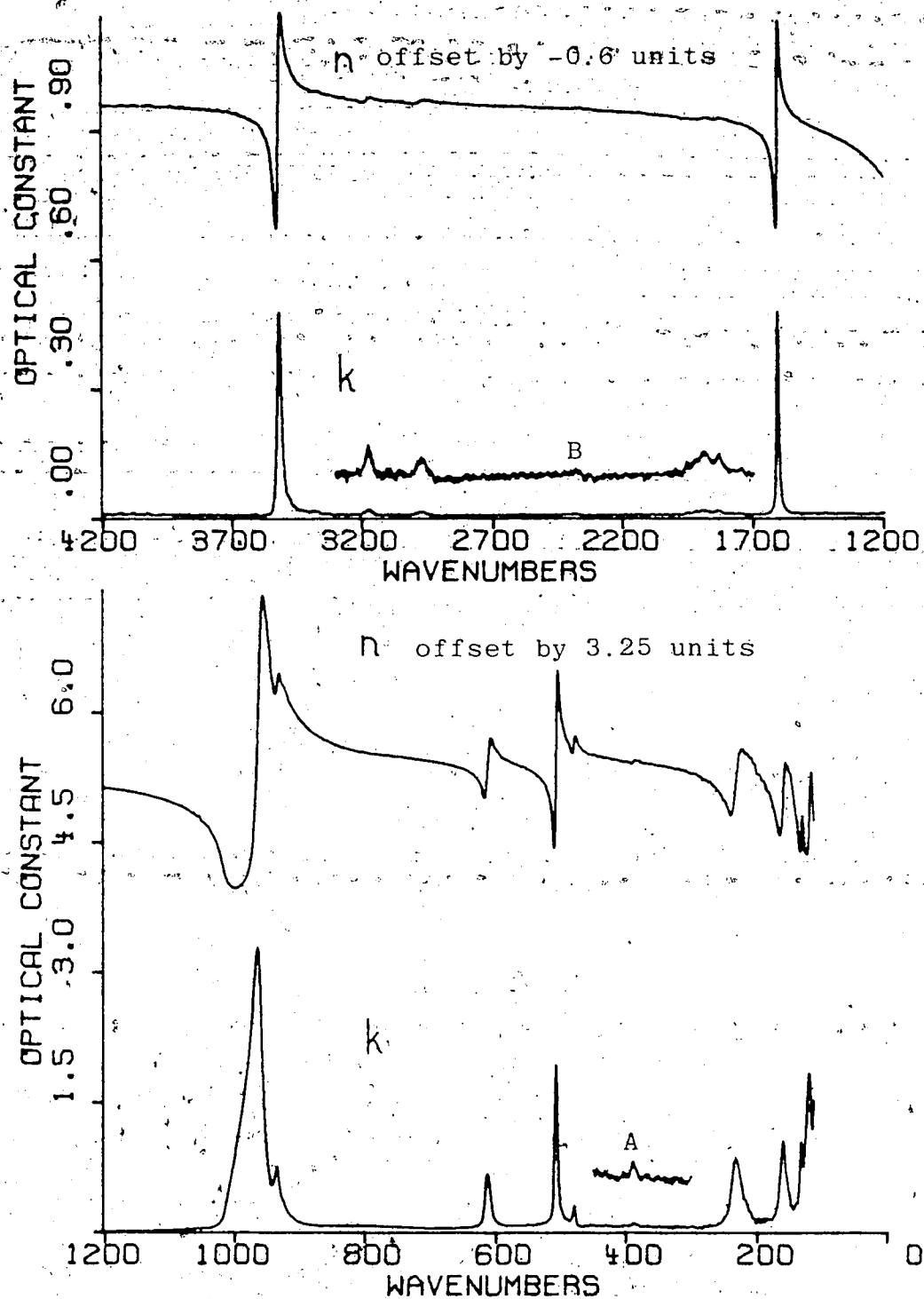


Figure 4.8 Optical constants  $n$  and  $k$  for (001) face of  $\text{Ba}(\text{ClO}_3)_2 \cdot \text{H}_2\text{O}$  measured with the electric vector parallel to the  $b$ -axis at 298°K; resolution = 2  $\text{cm}^{-1}$ .

Inset A:  $n$  offset by 0.06 units; scale = 5x.

Inset B:  $n$  offset by 0.012 units; scale = 5x.

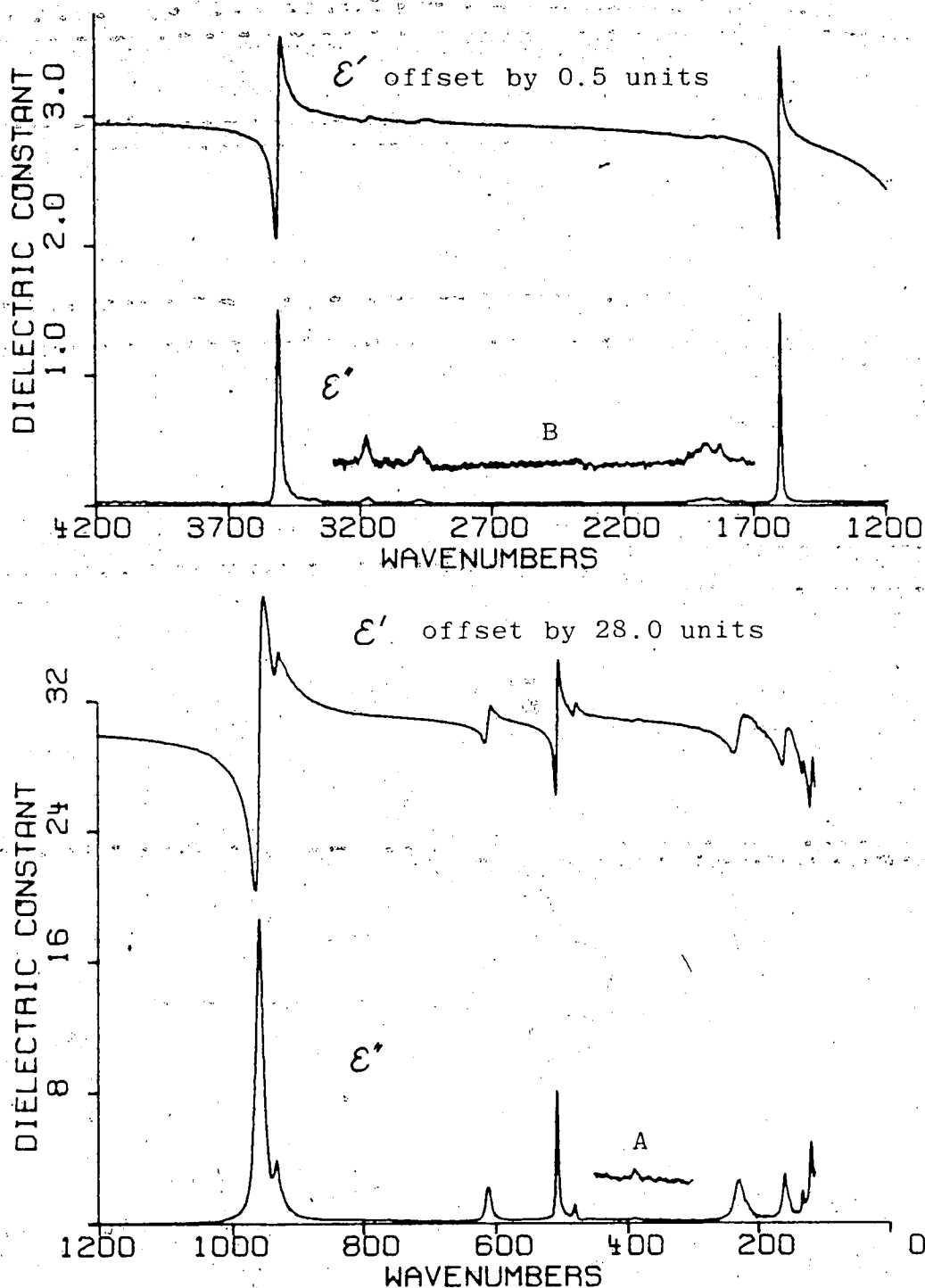


Figure 4.9 Dielectric constants  $\epsilon'$  and  $\epsilon''$  for (001) face of  $\text{Ba}(\text{ClO}_3)_2 \cdot \text{H}_2\text{O}$  measured with the electric vector parallel to the b-axis at 298°K; resolution = 2  $\text{cm}^{-1}$ .

Inset A: offset by 0.32 units; scale = 5 $\times$ .

Inset B: offset by 0.04 units; scale = 5 $\times$ .

and that the weaker features have been scaled by factor of five in the insets. These spectra were derived from measurements at 4445 data points in the range  $115\text{--}4400\text{ cm}^{-1}$ . The high frequency data, from  $4400\text{--}\infty\text{ cm}^{-1}$ , were approximated by a constant reflectance of 0.049; this compares with an expected visible reflectance of 0.050 along the b-crystal axis<sup>103</sup> (assuming zero absorption). In Table 4.4, this input data to the KK-program is summarized, and in Appendix D, the values of  $\epsilon'(\nu)$  and  $\epsilon''(\nu)$  are compiled for changes in  $\epsilon''(\nu)$  of 0.2 units below  $1200\text{ cm}^{-1}$  and 0.04 units above  $1200\text{ cm}^{-1}$ .

To illustrate the effectiveness of the reflectance method for measuring the optical properties of a strongly absorbing compound such as  $\text{Ba}(\text{ClO}_3)_2 \cdot \text{H}_2\text{O}$ , the corresponding transmittance was calculated via

$$T(\nu) = \frac{[1-R(\nu)]^2 A(\nu)}{1-[A(\nu)R(\nu)]^2}$$

where  $A(\nu) = 4\pi\nu k(\nu)b$

$b$  = sample thickness (cm).

In Figure 4.10, the calculated transmittance for single crystal  $\text{Ba}(\text{ClO}_3)_2 \cdot \text{H}_2\text{O}$  polarized along  $b$  in the (001) plane, is shown for several sample thicknesses. It can be seen that for a crystal  $0.2\text{ }\mu\text{m}$  thick, the minimum percent transmission at  $960\text{ cm}^{-1}$  is only 5%; this accounts for the difficulty encountered by previous workers<sup>130</sup> in the measurement of the single crystal's transmission spectrum.

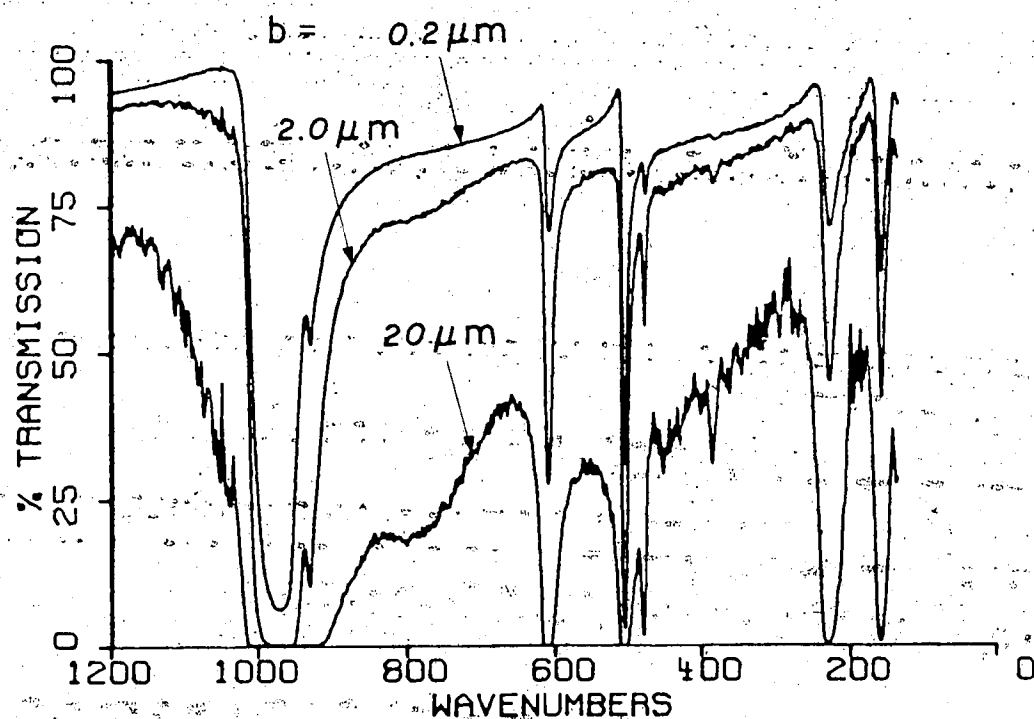
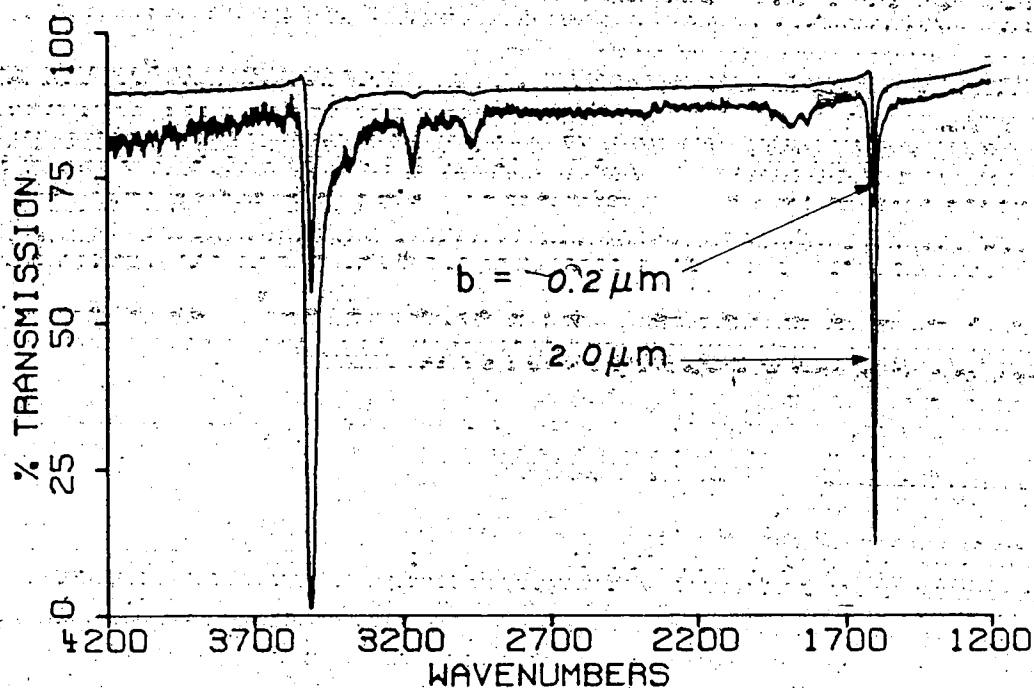


Figure 4.10 Calculated b-polarized transmittance spectra of the (001) face of  $\text{Ba}(\text{ClO}_3)_2 \cdot \text{H}_2\text{O}$  for sample thicknesses of 0.20, 2.0 and 20  $\mu\text{m}$ .

Since any distortions in the measured reflectance affect the derived optical constants, it was necessary to remove the spurious feature at  $786\text{ cm}^{-1}$  in the composite  $a'$ -polarized reflectance spectrum (Figure 3.24), before processing this data. This was accomplished by substituting a scaled spectrum of sample SC-BCL.H20-01 in the region  $500\text{--}1100\text{ cm}^{-1}$  (see Section 3.1a). The Kramers-Kronig calculations were then performed at each data point in a 4455 point array over the range  $105\text{--}4400\text{ cm}^{-1}$ . A value of 0.044, corresponding to the measured reflectance at  $4400\text{ cm}^{-1}$ , was extrapolated from  $4400$  to  $\infty\text{ cm}^{-1}$ ; this compares with an expected visible reflectance of 0.048 along the  $a$ -crystal axis.<sup>103</sup>

The resultant real and imaginary optical and dielectric constant spectra are presented in Figures 4.11 and 4.12. A detailed compilation of the  $\epsilon'(\nu)$  and  $\epsilon''(\nu)$  values is given in Appendix E for changes in  $\epsilon''(\nu)$  of 0.2 units below  $1200\text{ cm}^{-1}$  and 0.04 units above  $1200\text{ cm}^{-1}$ .

It is a significant result that no negative values of the imaginary dielectric constant were calculated for either the  $a'$ - or  $b$ -polarized spectra. One of the most common explanations for the negative values of  $\epsilon''(\nu)$  being generated by the KK-procedure, is the difficulty in accurately measuring small reflectance values.<sup>140</sup> In our study of  $\text{Ba}(\text{ClO}_3)_2 \cdot \text{H}_2\text{O}$ , the minimum reflectance observed for the polycrystalline samples was 0.002, whereas the minimum in the  $b$ -polarized reflectance spectrum was only 0.0004. This suggests that error in the measured reflectance is not re-

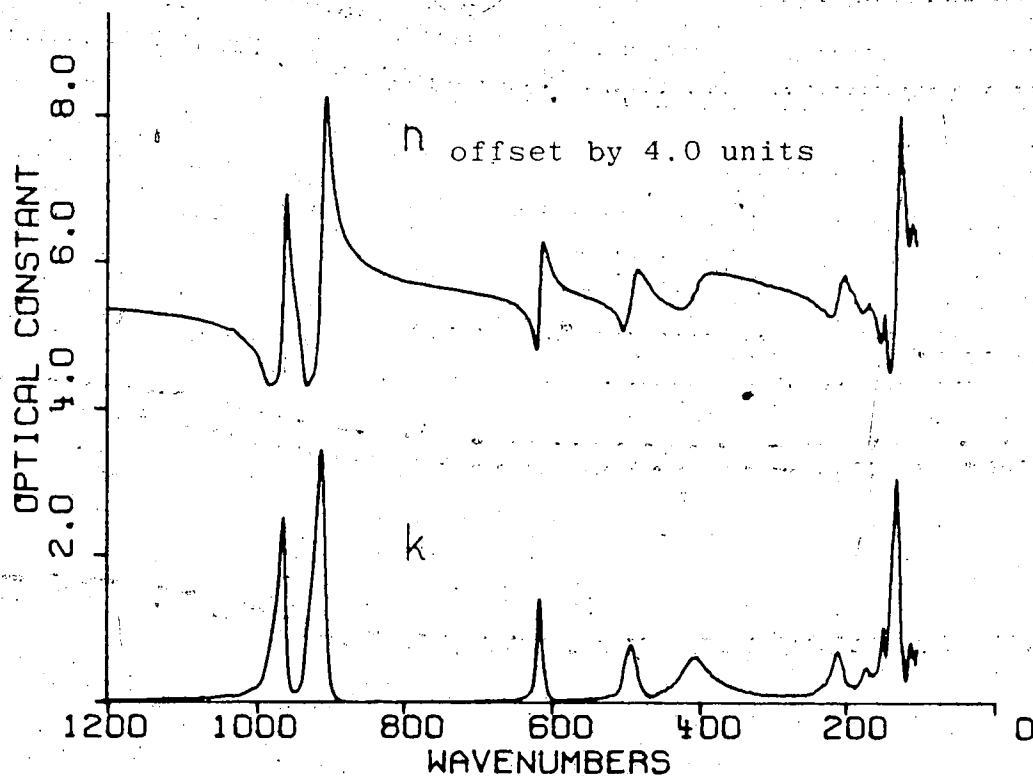
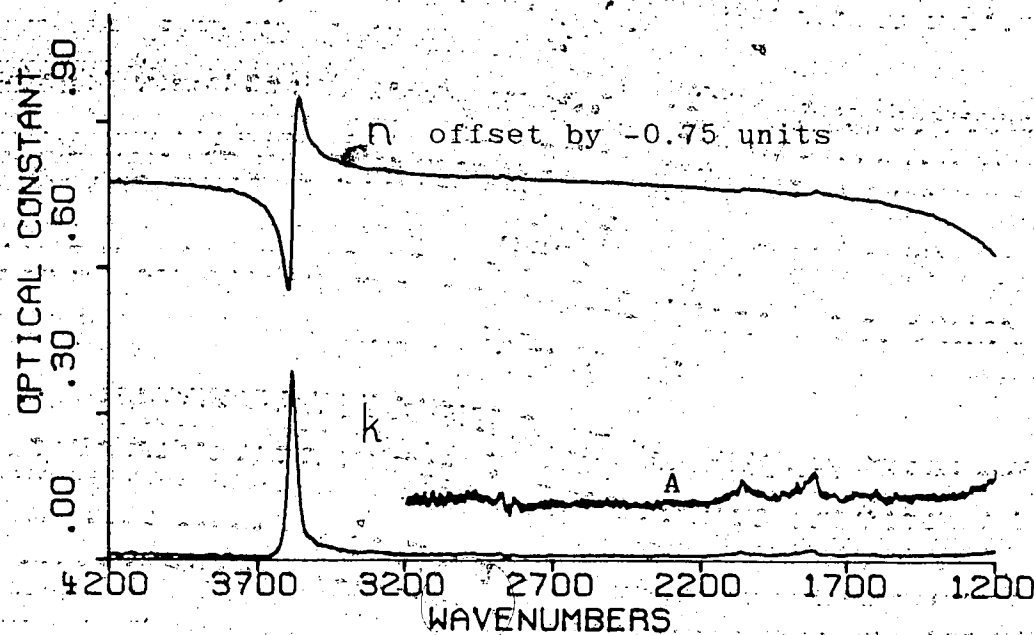


Figure 4.11 Optical constants  $n$  and  $k$  for (001) face of  $\text{Ba}(\text{ClO}_3)_2 \cdot \text{H}_2\text{O}$  measured with the electric vector parallel to the  $a'$ -axis at 298°K; resolution = 2  $\text{cm}^{-1}$ .

Inset A: offset by 0.012 units; scale = 5x.

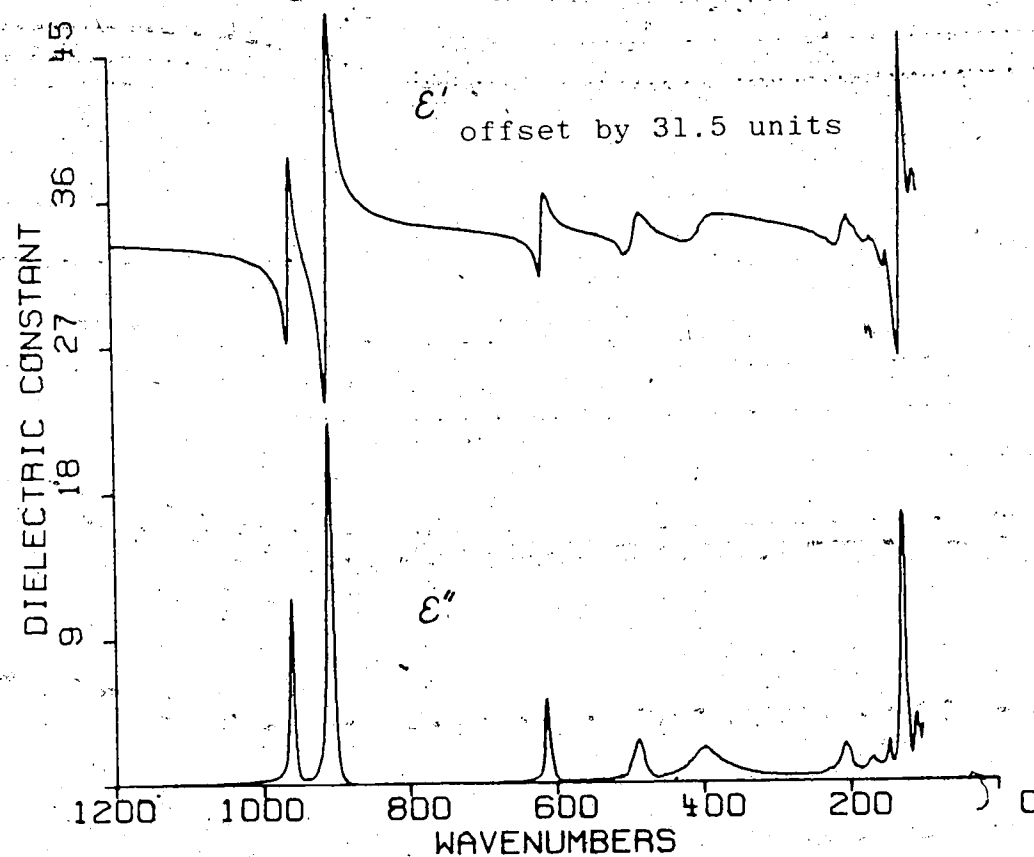
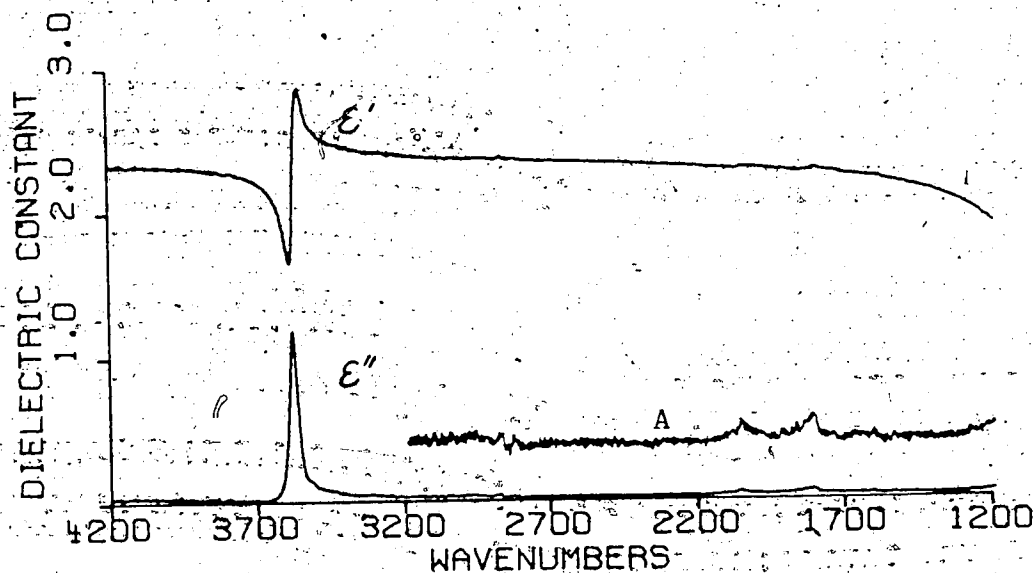


Figure 4.12 Dielectric constants  $\epsilon'$  and  $\epsilon''$  for (001) face of  $\text{Ba}(\text{ClO}_3)_2 \cdot \text{H}_2\text{O}$  measured with the electric vector parallel to the  $a'$ -axis at 298°K; resolution = 2  $\text{cm}^{-1}$ .

Inset A: offset by 0.04 units; scale = 5x.

sponsible for the anomalous negative values of  $\epsilon''(\nu)$  being computed for the polycrystalline data.

In the preceding calculations, polarized reflectance data was only included to  $4400\text{ cm}^{-1}$ , although it was measured to  $7200\text{ cm}^{-1}$ . This simplification was made since the near-infrared reflectance of single crystal  $\text{Ba}(\text{ClO}_3)_2 \cdot \text{H}_2\text{O}$  was relatively constant (see Curves A and B of Figure 3.21). To ensure that this procedure was valid, the Kramers-Kronig calculation was repeated for the a'-polarized data, for frequencies up to  $6500\text{ cm}^{-1}$ . This upper limit was chosen since the spectrum becomes quite noisy for higher frequencies. The excellent overlap of this calibrated near-infrared spectrum with the averaged mid-infrared results was demonstrated in Figure 3.24; the merge point was selected at  $3800\text{ cm}^{-1}$ . Phase calculations were performed at every point in the 4534 data point array, and a constant reflectance of 0.045 was extrapolated from  $6500$  to  $\infty\text{ cm}^{-1}$ . This value corresponds to the measured reflectance at  $6500\text{ cm}^{-1}$  and is slightly closer to the expected visible reflectance of 0.048, than the value of 0.044 at  $4400\text{ cm}^{-1}$ . In Table 4.6, the derived  $\epsilon'(\nu)$  and  $\epsilon''(\nu)$  results are compared for several frequencies with the values obtained for the more limited integration range  $105\text{--}4400\text{ cm}^{-1}$ . It can be seen that the discrepancies are very small, thereby justifying the use of the narrower integration range in the KK calculations.

Table 4.6 Integration Range-Dependence of Calculated Dielectric Constant Values for a'-Polarized (001) Face of  $\text{Ba}(\text{ClO}_3)_2 \cdot \text{H}_2\text{O}$

Frequency $\nu(\text{cm}^{-1})$	$\epsilon'(\nu)$			$\epsilon''(\nu)$		
	A*	B*	$\Delta\epsilon'$ <sup>†</sup>	A	B	$\Delta\epsilon''$
104.1	5.18	5.18	0.00	3.50	3.49	-0.01
127.2	14.63	14.64	+0.01	11.04	11.04	0.00
401.1	2.88	2.88	0.00	2.08	2.08	0.00
616.1	3.07	3.07	0.00	5.21	5.21	0.00
906.3	16.20	16.25	+0.05	10.81	10.76	-0.05
910.2	6.52	6.61	+0.09	22.37	22.41	+0.04
916.0	-7.91	-7.92	-0.01	10.45	10.49	+0.04
934.3	-0.42	-0.42	0.00	0.54	0.54	0.00
963.2	1.00	1.02	+0.02	11.64	11.66	+0.02
966.1	-4.24	-4.25	-0.01	6.27	6.29	+0.02
3582.1	2.40	2.41	+0.01	1.16	1.16	0.00
3673.7	2.16	2.16	0.00	0.02	0.01	-0.01

\* Range A =  $105\text{--}4400\text{ cm}^{-1}$ ;  $\epsilon'(4400\text{ cm}^{-1}) = 2.35$

Range B =  $105\text{--}6500\text{ cm}^{-1}$ ;  $\epsilon'(6500\text{ cm}^{-1}) = 2.37$

$$^{\dagger} \Delta\epsilon' = \epsilon'_B - \epsilon'_A ; \Delta\epsilon'' = \epsilon''_B - \epsilon''_A$$

In the introductory chapter (Section 1.1d), it was shown that the optical property of fundamental significance in the study of solids is  $\epsilon''$ . Figure 4.13 illustrates the conductivity spectra,  $\sigma(\nu) = \nu \epsilon''(\nu)/2$ , derived for the incident electric vector parallel and perpendicular to the b-axis in the (001) crystal face of  $\text{Ba}(\text{ClO}_3)_2 \cdot \text{H}_2\text{O}$ . Complete polarization is exhibited by these conduction bands. This fact is most clearly demonstrated by the peak at  $1606 \text{ cm}^{-1}$  in the  $\underline{E} \parallel b$  spectrum, which is completely absent in the  $\underline{E} \perp b$  spectrum. Thus, no change in the polarization character of the incident wave can have occurred on reflection.

The peak characteristics of the  $\sigma(\nu)$  spectra are described in Table 4.7, that is, the band center frequency, the peak height, and the full width at half maximum (FWHM). Because some of the bands are overlapping, these parameters were roughly estimated by drawing a peak symmetrical about the band center, whose envelope matched that of the unencumbered side of the peak. The positions of peak inflections are indicated in Table 4.7 by a shoulder (sh) designation.

#### 4.3 Combined Kramers-Kronig/Classical Dispersion Method for Obtaining Optical Constants

This section describes the technique for obtaining a set of dispersion parameters by a combined Kramers-Kronig analysis and classical oscillator fit. The attractiveness of this procedure resides in its ability to determine the

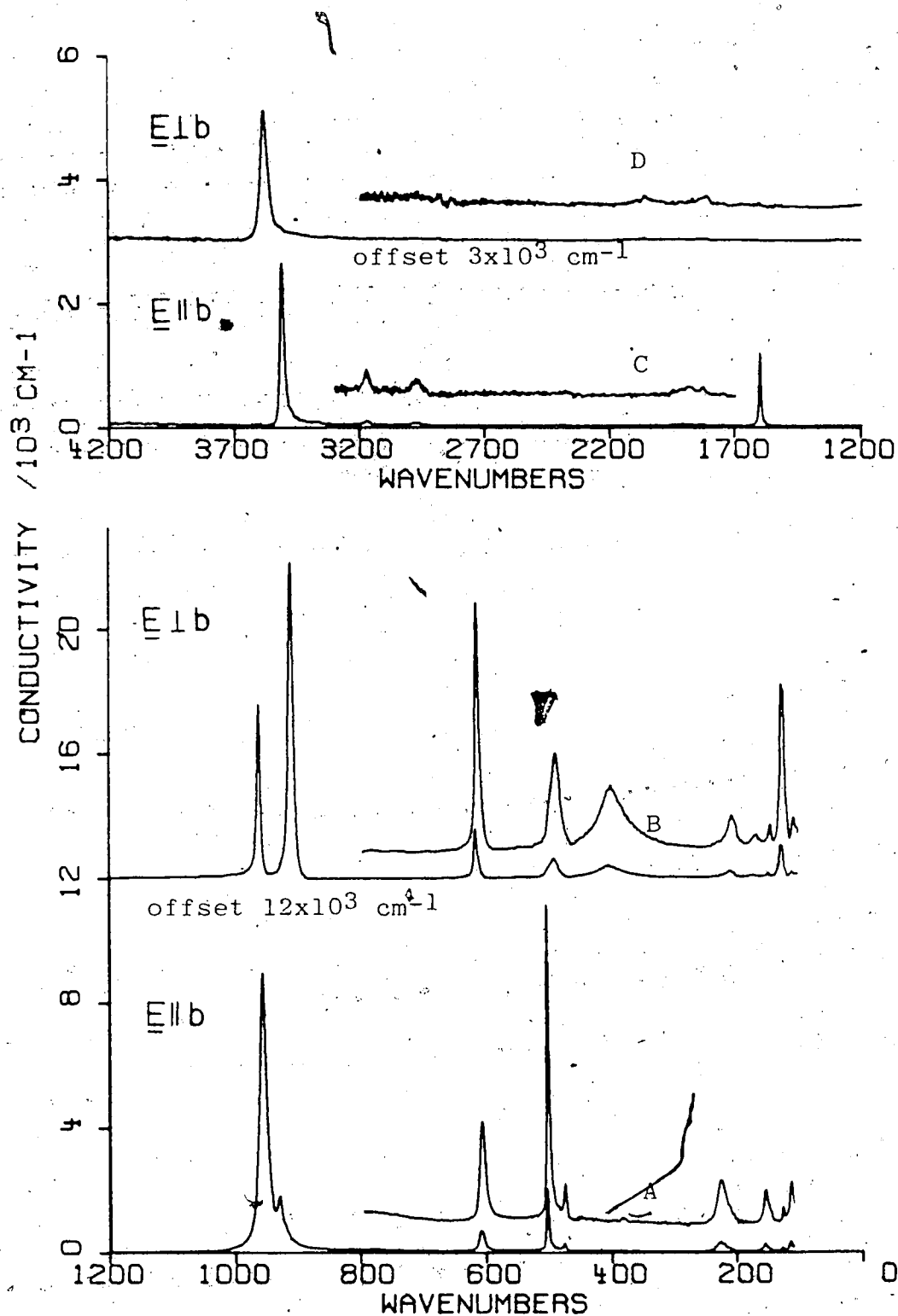


Figure 4.13 Conductivity spectra,  $\nu\epsilon''/2$ , for (001) face of  $\text{Ba}(\text{ClO}_3)_2 \cdot \text{H}_2\text{O}$  measured with the electric vector parallel and perpendicular to the b-axis at 298°K.

Insets A and B: offset  $160 \text{ cm}^{-1}$ ; scale = 5x.  
 Insets C and D: offset  $80 \text{ cm}^{-1}$ ; scale = 5x.

Table 4.7 Peak Characteristics of Conductivity Spectra for (001)

Crystal Face of  $\text{Ba}(\text{ClO}_3)_2 \cdot \text{H}_2\text{O}$ 

<u>E    b</u>		
<u>Band Center(<math>\text{cm}^{-1}</math>)</u>	<u>Peak Height(<math>\times 10^3 \text{cm}^{-1}</math>)</u>	<u>FWHM(<math>\text{cm}^{-1}</math>)</u>
119	0.304	7.5
133	0.138	6.5
159	0.247	11.5
230	0.305	18
389	0.025	8
480	0.290	6.5
507	2.08	4
611	0.690	10
927(sh), 933	1.66	11
959	9.00	13
1606	1.20	9
3514	2.67	19
<u>E ⊥ b</u>		
110(sh), 114	0.240	11
126(sh), 128(sh), 130, 132(sh), 138(sh)	1.09	8
150	0.190	7
173	0.120	19
210	0.240	20
404	0.440	52
487(sh), 492, 500(sh)	0.650	19
616	1.74	7.5
909	10.2	9.5
963	5.61	6
3584	2.14	34

parameters for overlapping bands. As previously discussed, the Kramers-Kronig method suffers from its sensitivity to truncation effects, while the classical dispersion method frequently does not produce a unique solution because of high correlation between the dispersion terms. The error in the dispersion parameters is minimized by requiring them to simultaneously satisfy the Kramers-Kronig derived results and reproduce the observed reflectance.

Good initial estimates of the dispersion parameters are obtained from the conductivity spectrum  $\sigma(\nu)$  by the procedure described in Section 1.1d. The number of oscillators  $N$ , the resonance frequencies  $\nu_j$ , the damping constants  $\gamma_j$ , and the oscillator strengths  $S_j$ , are approximated from:

- i) the number of peaks in  $\sigma(\nu) \rightarrow N$
- ii) the frequencies of  $\sigma_{\max} \rightarrow \nu_j$
- iii) the FWHM of  $\sigma$  bands  $\rightarrow \gamma_j$
- iv)  $2\sigma_{\max} \gamma_j \rightarrow S_j$

These parameters are then refined by a two-step process.

First, they are adjusted by trial-and-error so that the dispersion-calculated  $\epsilon''(\nu)$  spectrum matches the KK-derived  $\epsilon''(\nu)$  spectrum. Secondly, this improved set of oscillator parameters is further refined to bring the dispersion-calculated  $R(\nu)$  spectrum into coincidence with the observed  $R(\nu)$  spectrum. This method was adopted since the peaks in the  $\epsilon''(\nu)$  spectrum are better resolved than those in the  $R(\nu)$  spectrum and, therefore, the correlation between the

dispersion terms is smaller. This should, in turn, reduce the number of iterations required for an adequate fit. A schematic description of this combined Kramers-Kronig/classical dispersion procedure is given in Figure 4.14.

Only the polarized single crystal results were subjected to this type of analysis. Table 4.8 lists the dispersion parameters computed for the major peaks in the conductivity spectra of Figure 4.13. The  $E \parallel b$  and  $E \perp b$  ( $a'b$  plane) spectra were modelled with twelve and eleven oscillators, respectively, and the values of  $\epsilon_\infty$  were assigned to the Na-D line value of  $\epsilon'$  along the appropriate axial direction.<sup>103</sup>

This initial set of parameters was then checked for its ability to reproduce the observed reflectance and KK-derived imaginary dielectric constant spectra. The results of this comparison are shown in Figures 4.15 and 4.16 for the  $a'$ -polarized data, and in Figures 4.17 and 4.18 for the  $b$ -polarized data. The theoretical curves can usually be distinguished by their smoother band profiles but, where ambiguity exists, the different spectra are clearly identified in the figure. It can be seen that the agreement between the dispersion-calculated and KK-derived  $\epsilon''(\nu)$  spectra is exceedingly good, although theory generally underestimates the background level between the bands. In the regions where several strong bands overlap, there is obvious disagreement between the observed and calculated reflectance spectra; this illustrates the greater sensitivity

Figure 4.14 Combined ~~Kramers-Kronig~~/Classical dispersion procedure for obtaining a classical oscillator fit to reflection data.

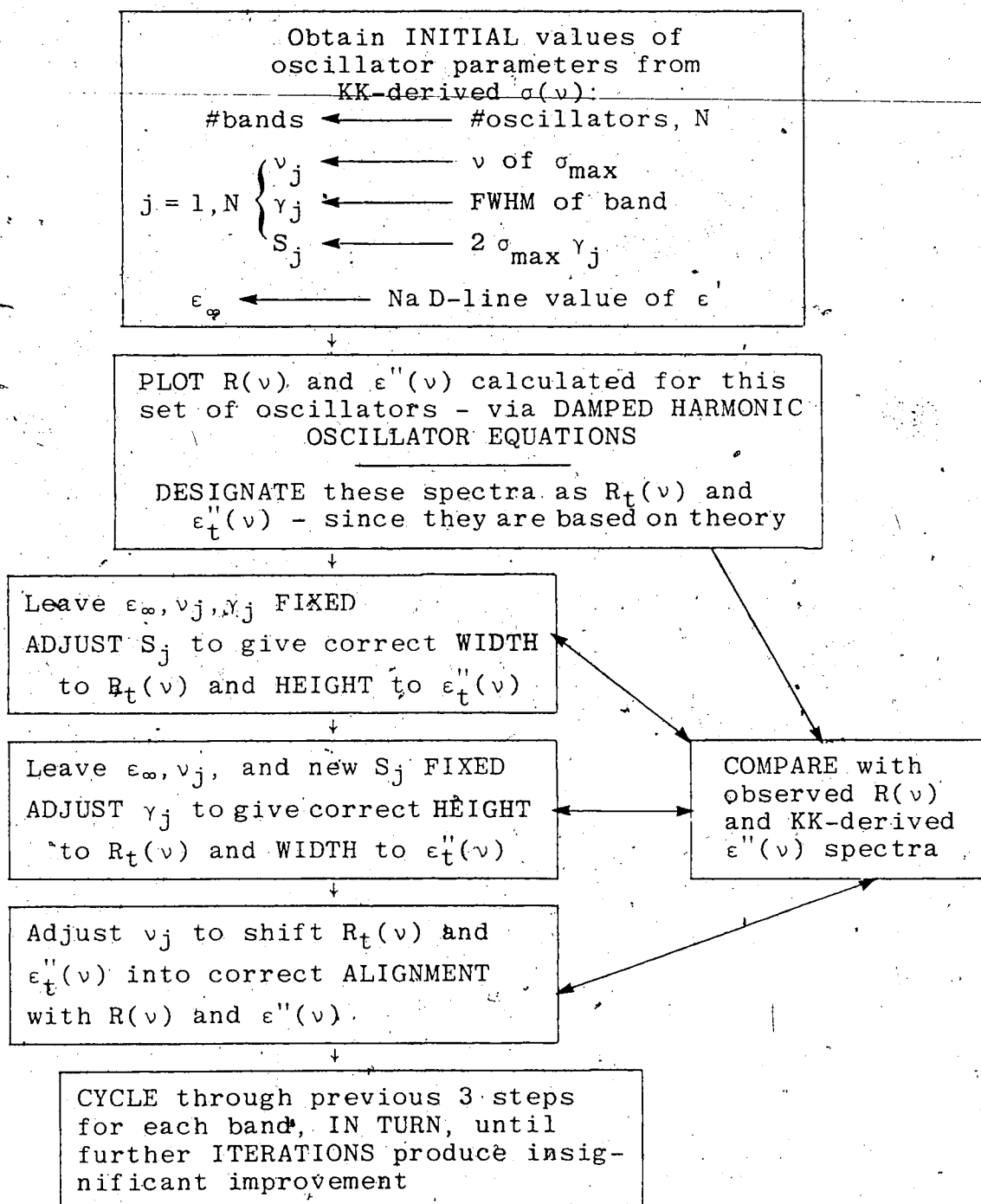


Table 4.8 Initial Set of Classical Oscillator Parameters  
for Polarized Single Crystal  $\text{Ba}(\text{ClO}_3)_2 \cdot \text{H}_2\text{O}$  Data

$\underline{E} \parallel b$			
$j$	$\nu_j (\text{cm}^{-1})$	$S_j (\times 10^4 \text{cm}^{-2})$	$\gamma_j (\text{cm}^{-1})$
1	119	0.456	7.5
2	133	0.179	6.5
3	159	0.568	11.5
4	230	1.10	18
5	389	0.040	8
6	480	0.377	6.5
7	507	1.66	4
8	611	1.38	10
9	933	3.65	11
10	959	23.4	13
11	1606	2.16	9
12	3514	10.1	19
$\epsilon_\infty = 2.49$			
$\underline{E} \perp b$			
1	114	0.528	11
2	130	1.74	8
3	150	0.266	7
4	173	0.456	19
5	210	0.960	20
6	404	4.58	52
7	492	2.47	19
8	616	2.61	7.5
9	909	19.4	9.5
10	963	6.73	6
11	3584	14.6	34
$\epsilon_\infty = 2.44$			

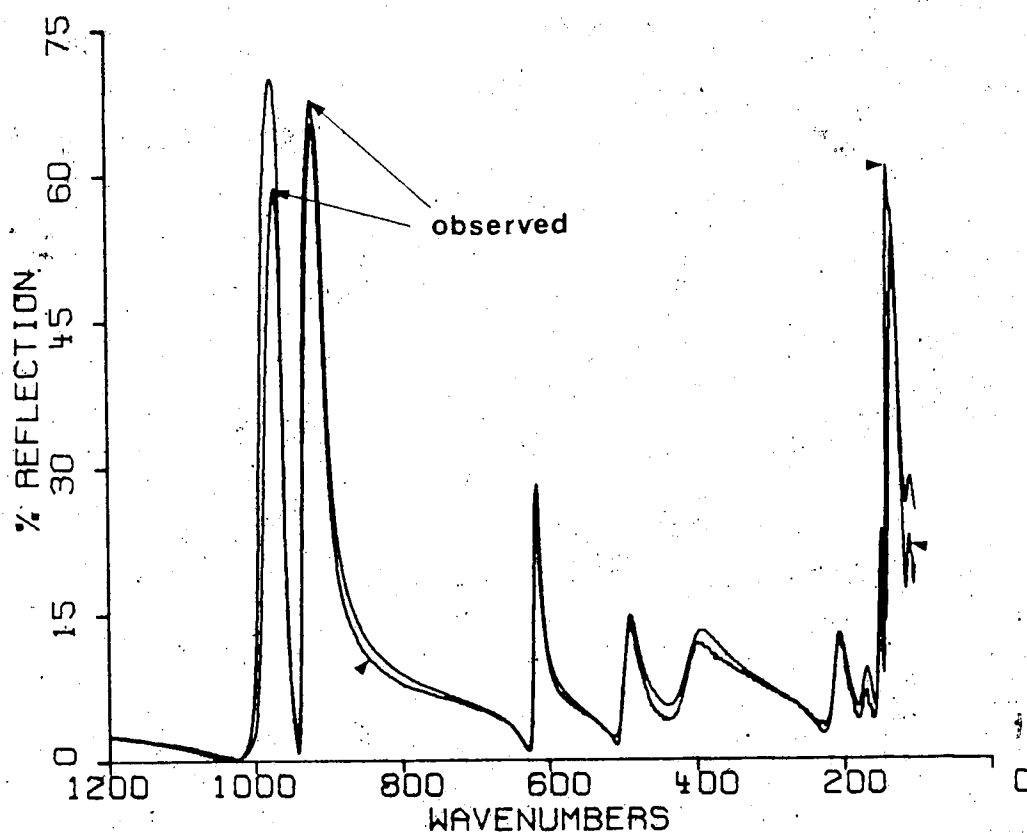
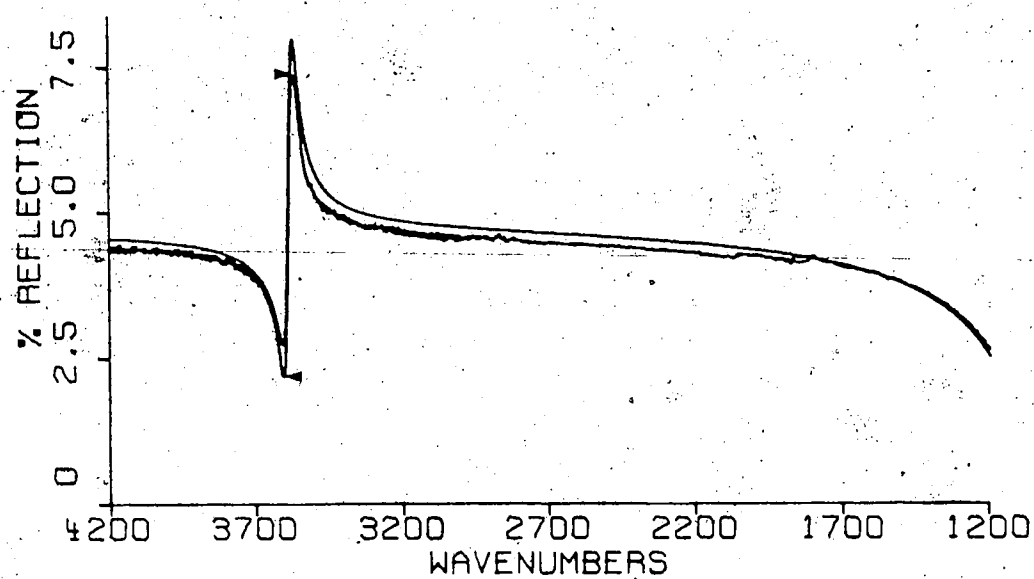


Figure 4.15 Comparison of observed  $a'$ -polarized reflectance from (001) face of  $\text{Ba}(\text{ClO}_3)_2 \cdot \text{H}_2\text{O}$  and theoretical reflectance, based on initial set of dispersion parameters (from Table 4.8).

Observed spectra are distinguished by small arrowheads.

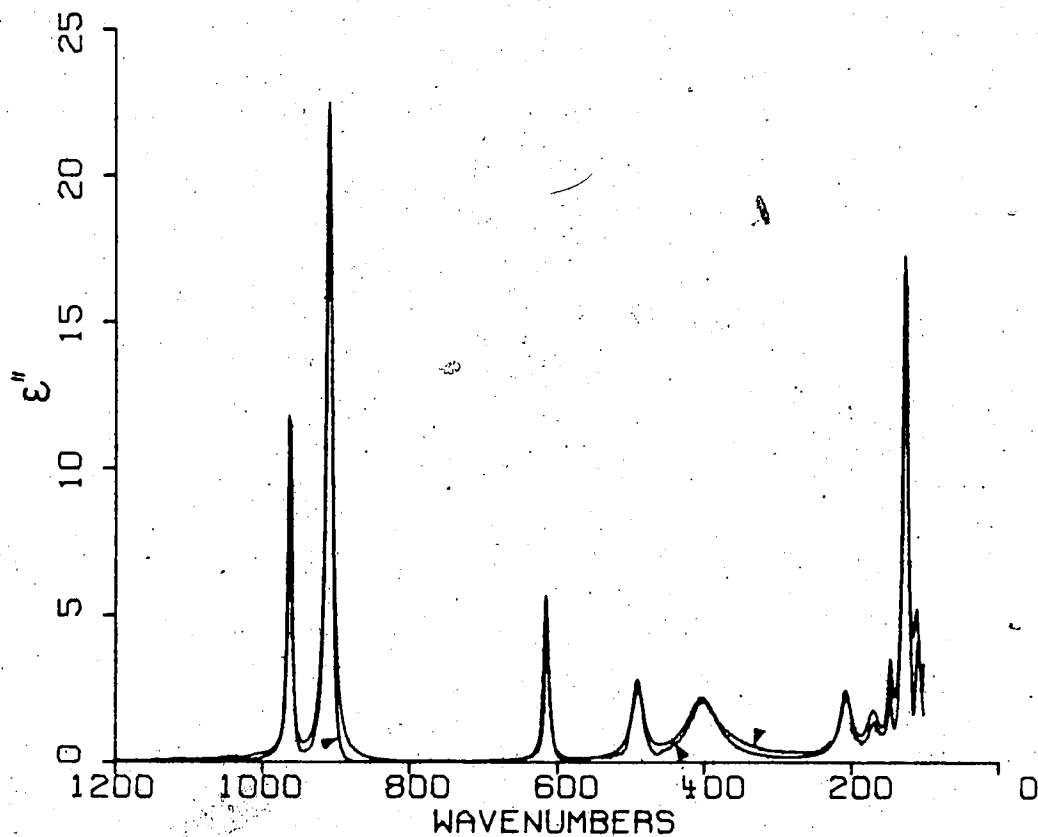
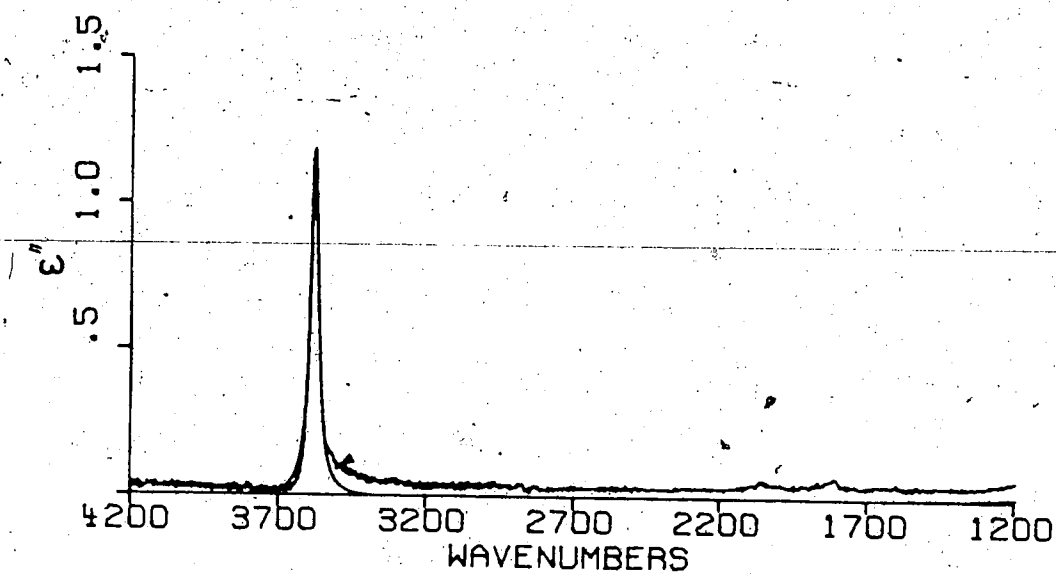


Figure 4.16 Comparison of KK-derived  $\epsilon''(\nu)$  spectrum for  $a'$ -polarized reflectance from (001) face of  $\text{Ba}(\text{ClO}_3)_2 \cdot \text{H}_2\text{O}$  and theoretical  $\epsilon''(\nu)$  spectrum, based on initial set of dispersion parameters (from Table 4.8).

KK-derived spectra are distinguished by small arrowheads.

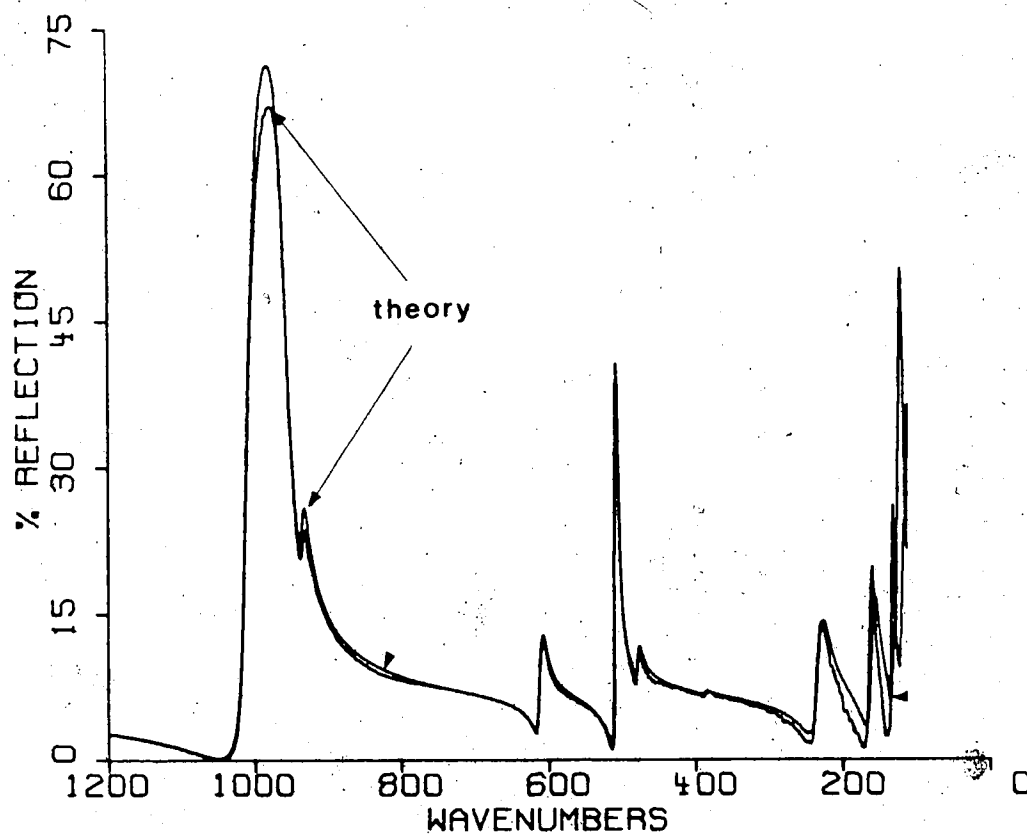
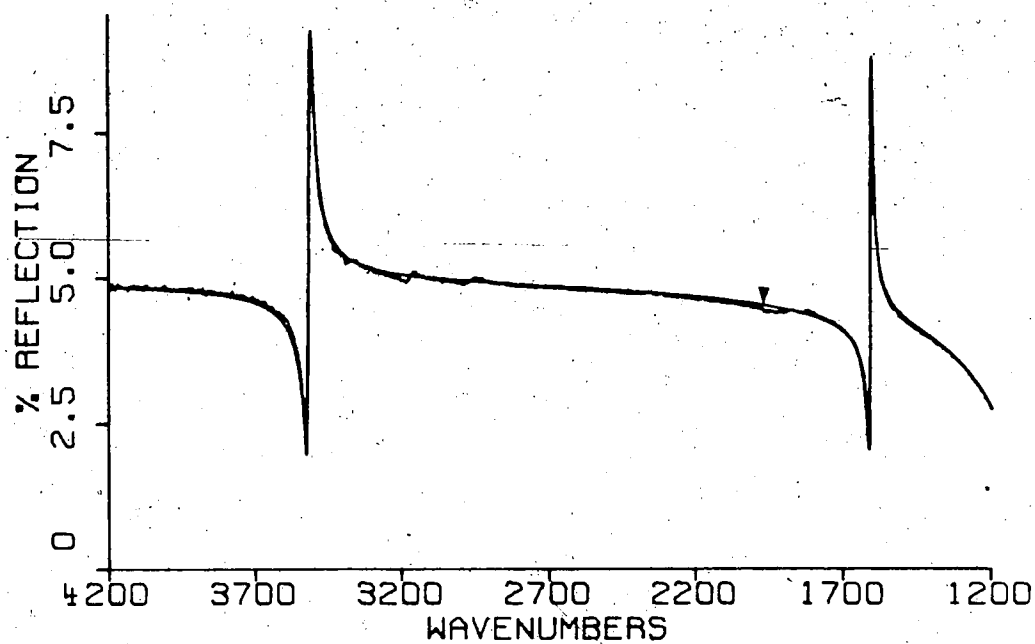


Figure 4.17 Comparison of observed b-polarized reflectance from (001) face of  $\text{Ba}(\text{ClO}_3)_2 \cdot \text{H}_2\text{O}$  and theoretical reflectance, based on initial set of dispersion parameters (from Table 4.8).

Theoretical spectra are distinguished by small arrowheads.

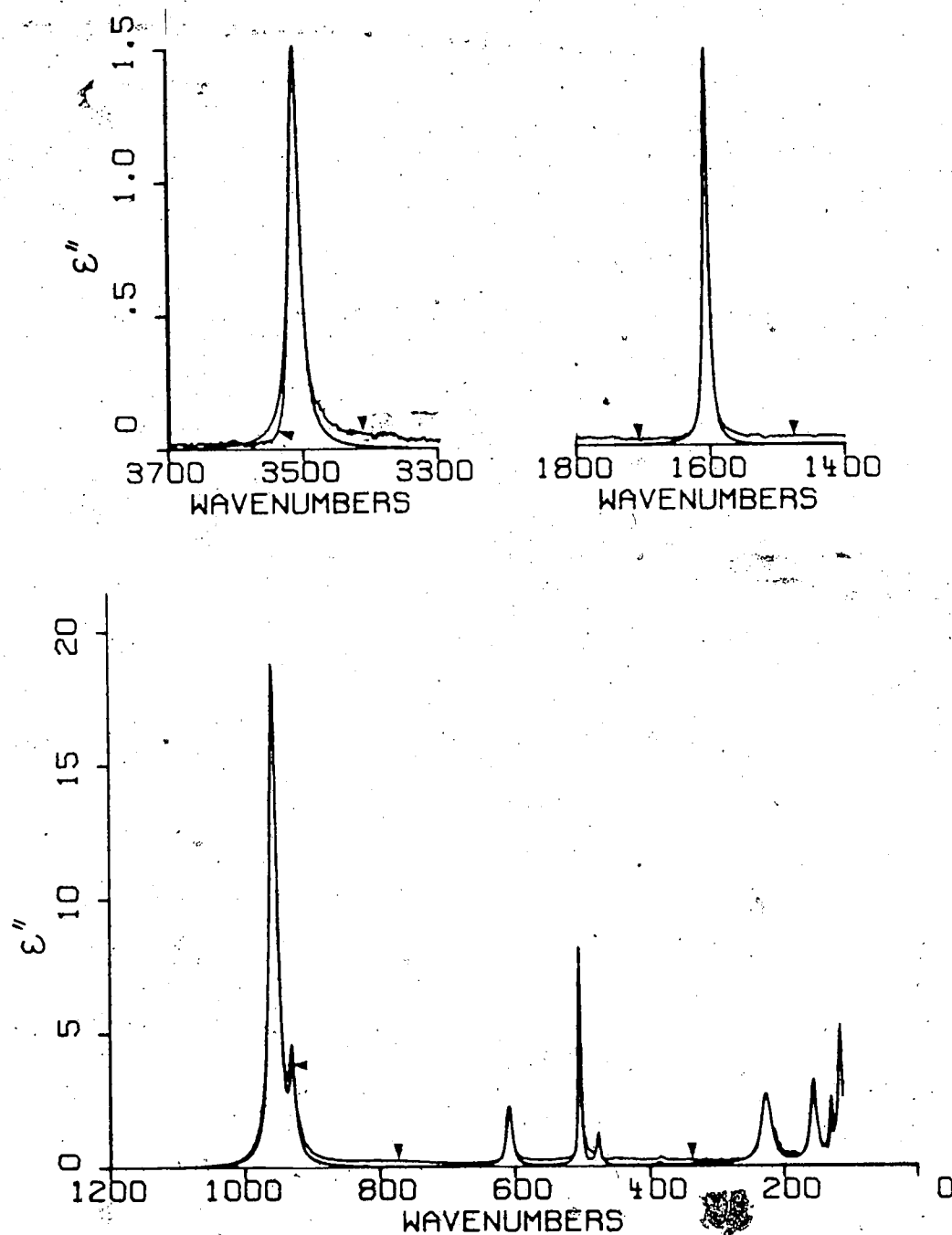


Figure 4.18 Comparison of KK-derived  $\epsilon''(\nu)$  spectrum for b-polarized reflectance from (001) face of  $\text{Ba}(\text{ClO}_3)_2 \cdot \text{H}_2\text{O}$  and theoretical  $\epsilon''(\nu)$  spectrum, based on initial set of dispersion parameters (from Table 4.8).

KK-derived spectra are distinguished by small arrowheads.

of the reflectance spectra to errors in the dispersion parameters and/or dispersion model. The exact coincidence of the observed and calculated high frequency reflectance for the b-polarized data verifies our choice of  $\epsilon_{\infty}$ . However, for the a'-polarized data, the high frequency reflectance is slightly overestimated, suggesting that a smaller value of  $\epsilon_{\infty}$  be used in the fitting procedure.

Next began the task of refining the dispersion parameters. This trial-and-adjustment method is succinctly described in Figure 4.14, and employed the following observations as guidelines:

- i) the number of oscillators required for an adequate fit and their approximate frequencies were estimated from the positions of significant peaks, dips, and shoulders in the KK-derived conductivity spectra (see Table 4.7).
- ii) the width of the  $\epsilon''(\nu)$  peak and the height of the  $R(\nu)$  peak were primarily affected by the damping constant,  $\gamma_j$ .
- iii) the height of the  $\epsilon''(\nu)$  peak and the width of the  $R(\nu)$  peak were most sensitive to the value of the oscillator strength.

A minimum number of oscillators were used to satisfy guideline i). However, in order to simulate the low frequency reflectance behavior, it was necessary to assign an oscillator to a frequency below the measured region. This was the sole function of this additional oscillator and no physical significance was ascribed to its dispersion parameters.

In each adjustment cycle, only one parameter was varied. The effect of each change was monitored by comparison

with either the KK-derived  $\epsilon''(\nu)$  spectrum (in the first approximation) or the observed reflectance (in the second approximation), and the process was terminated when further iterations produced insignificant improvement in the fitted result. If, after exhaustive study, it was found not possible to simultaneously satisfy the Kramers-Kronig  $\epsilon''(\nu)$  spectra and reproduce the observed reflectance, only the former data were used in the fitting procedure. This choice is based on our earlier observation that the shape and position of the  $\epsilon''(\nu)$  peaks were almost insensitive to changes in the oscillator parameters of remote bands, whereas the  $R(\nu)$  peaks changed dramatically. It is therefore expected that neglect of the contribution from the weak background continuum will more seriously affect the reflection spectra and prevent the achievement of a good fit. Thus, the  $\epsilon''(\nu)$  spectra are considered to be a more reliable fitting constraint.

The final theoretical fits for the reflectance and  $\epsilon''(\nu)$  spectra of  $\text{Ba}(\text{ClO}_3)_2 \cdot \text{H}_2\text{O}$  are compared with the corresponding experimental results in Figures 4.19 (b-polarized) and 4.20 (a'-polarized); the theoretical curves being distinguished by small arrowheads. The measured b-polarized data was modelled quite well with 14 oscillators and a high frequency dielectric constant,  $\epsilon_\infty$  of 2.49, which corresponds with the sodium D-line value. The a'-polarized data was successfully modelled with 17 oscillators and an  $\epsilon_\infty$  value of 2.40. This fitted result is 0.04 units less

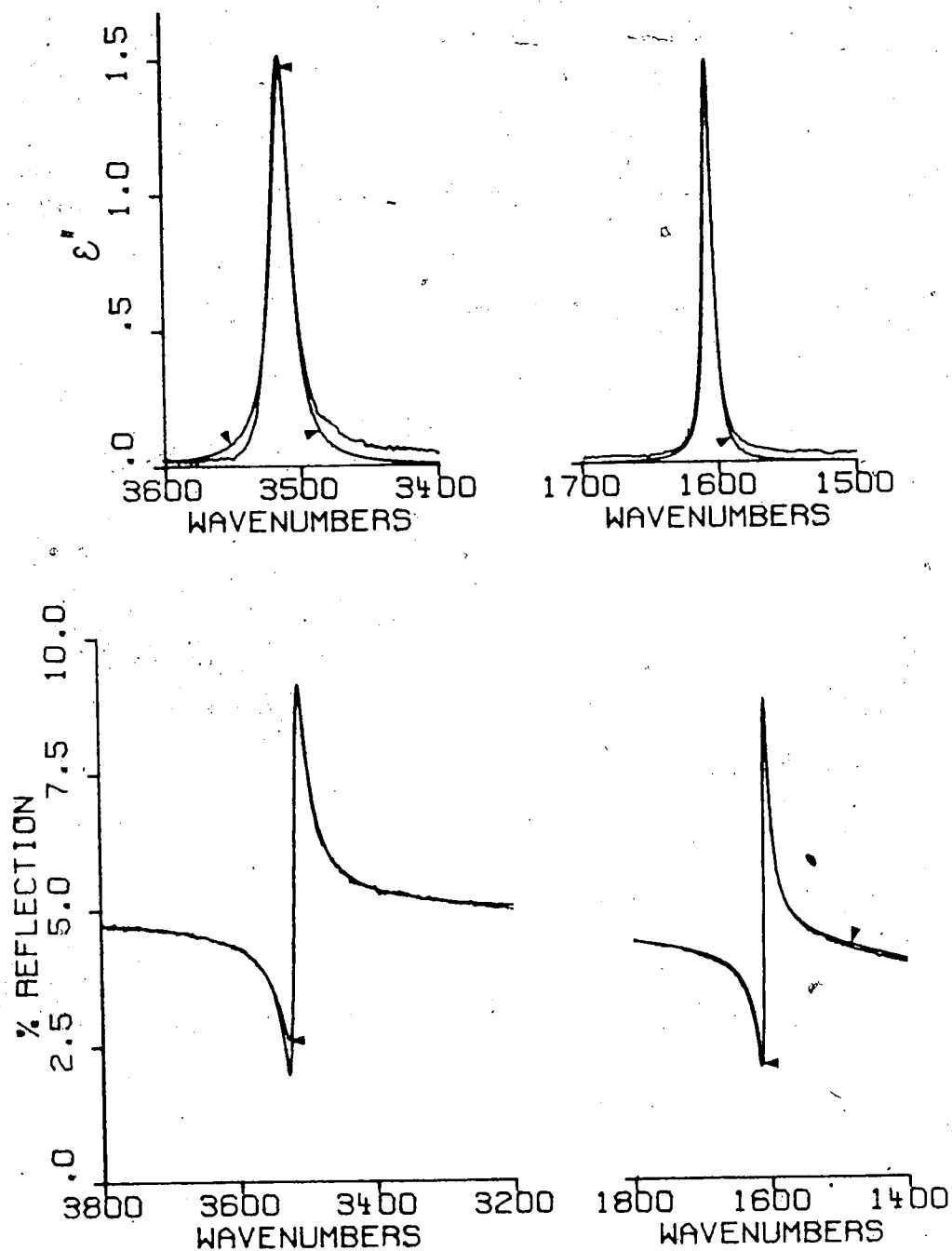


Figure 4.19 Comparison of experimental b-polarized reflectance from (001) crystal face of Ba(ClO<sub>3</sub>)<sub>2</sub>·H<sub>2</sub>O and KK-derived  $\epsilon''(\nu)$  spectrum with corresponding theoretical spectra from combined Kramers-Kronig/classical dispersion fit.

Arrows indicate the theoretical curves.

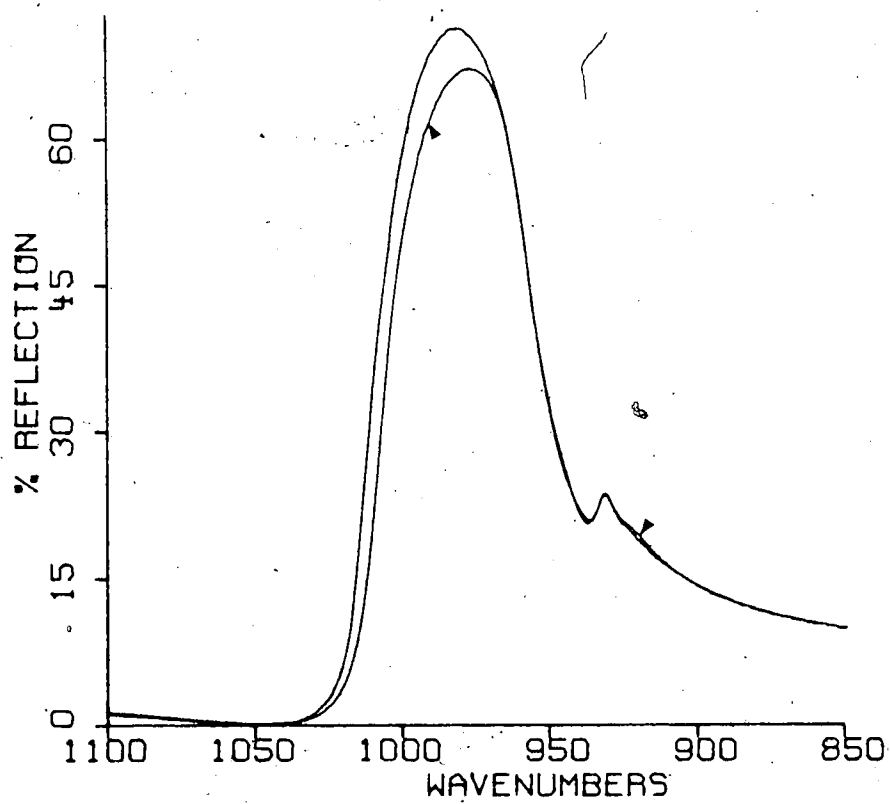
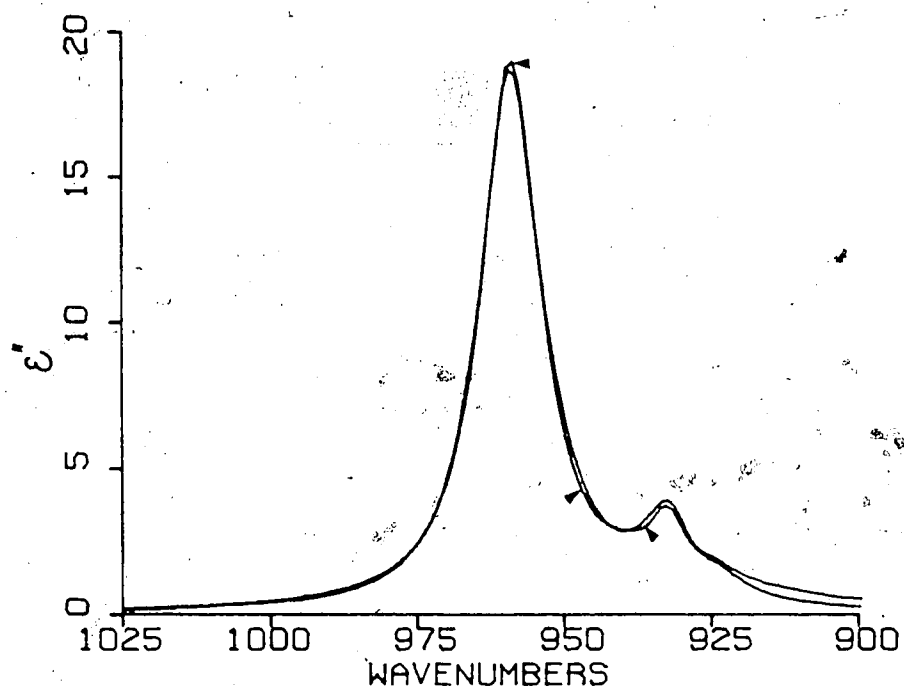


Figure 4.19a Continuation of Figure 4.19.

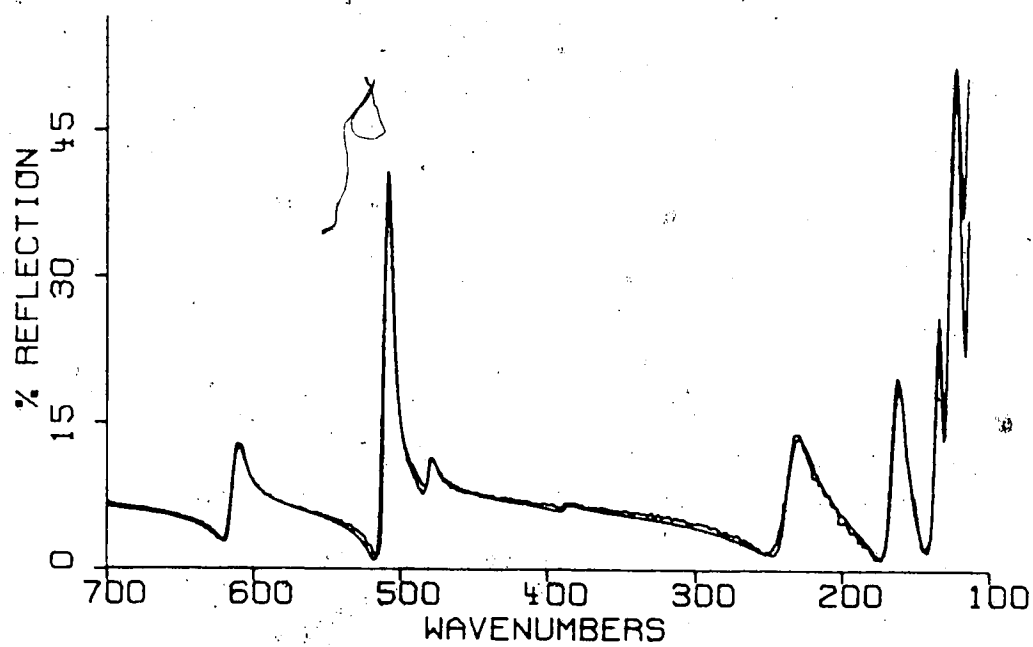
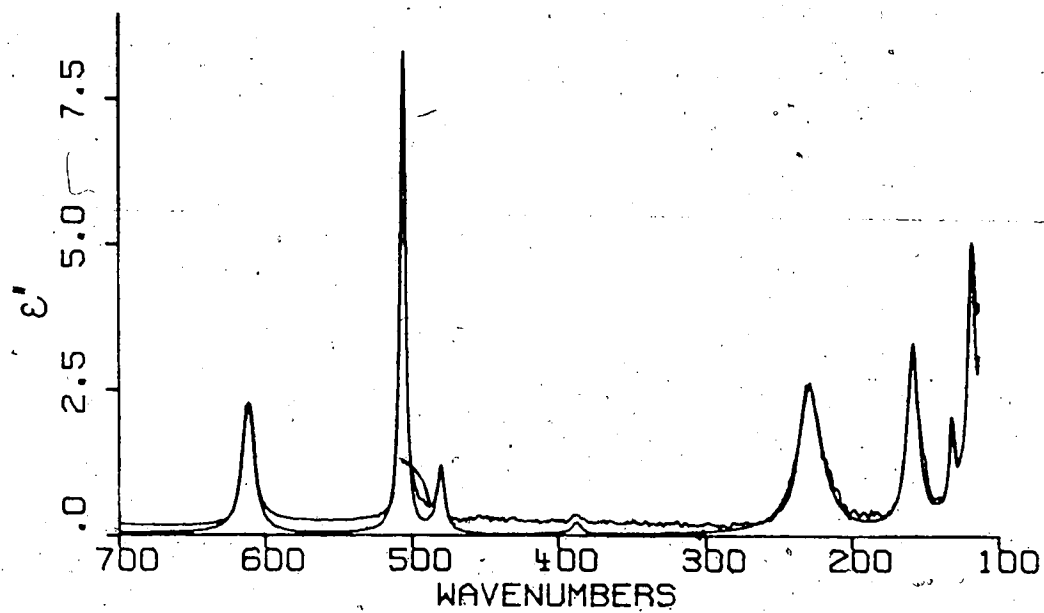


Figure 4.19b Continuation of Figure 4.19.

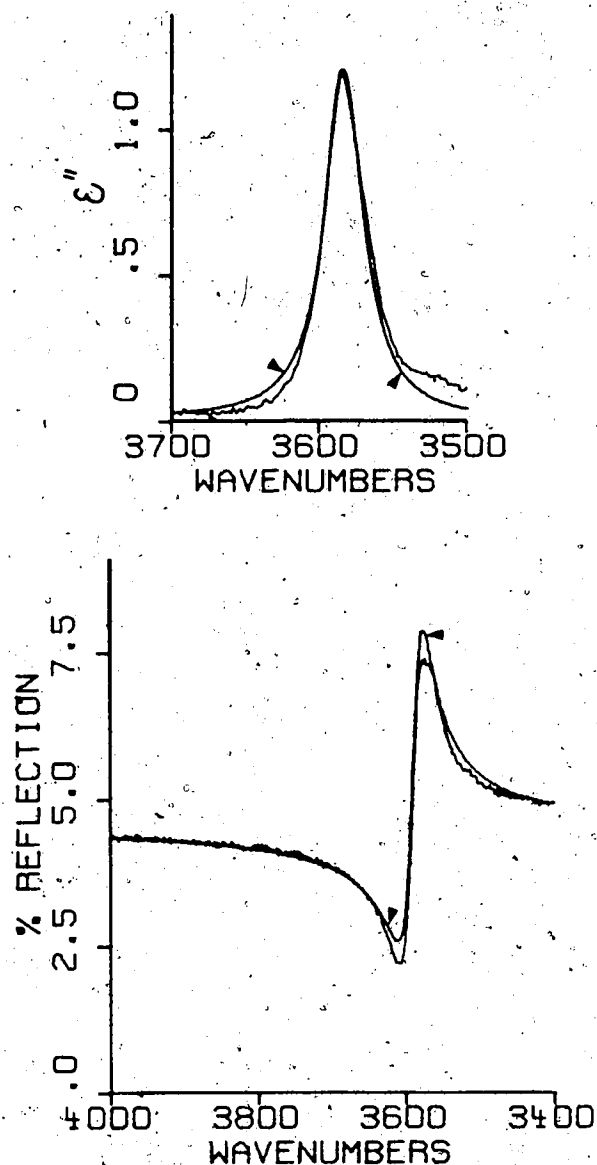


Figure 4.20 Comparison of experimental  $\alpha'$ -polarized reflectance from (001) crystal face of  $\text{Ba}(\text{ClO}_3)_2 \cdot \text{H}_2\text{O}$  and KK-derived  $\epsilon''(\nu)$  spectrum with corresponding theoretical spectra from combined Kramers-Kronig/classical dispersion fit.

Arrows indicate the theoretical curves.

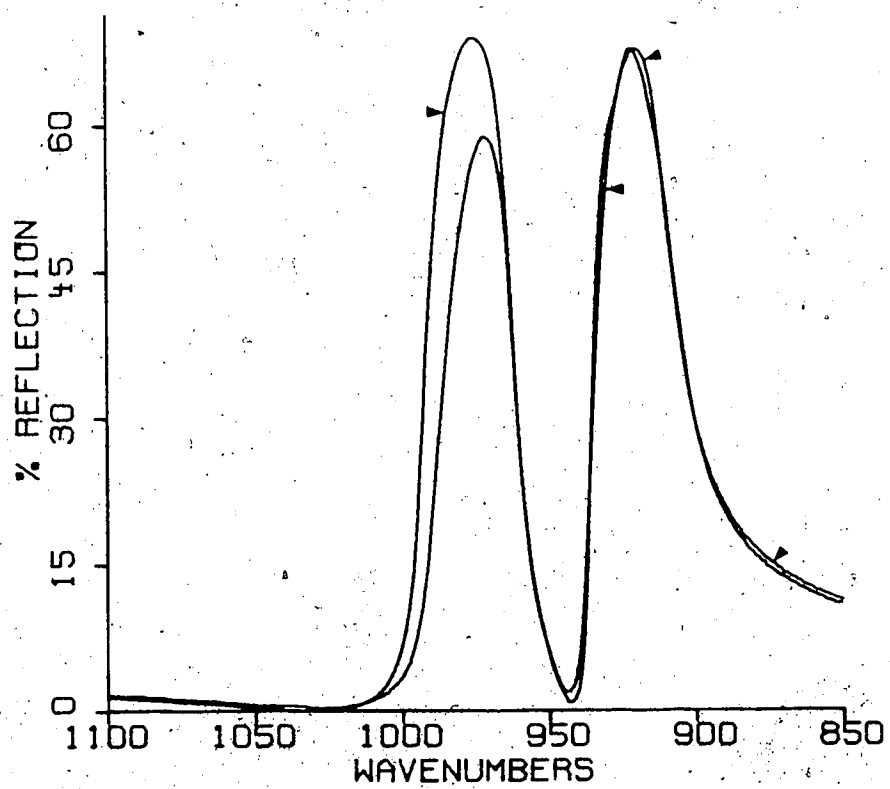
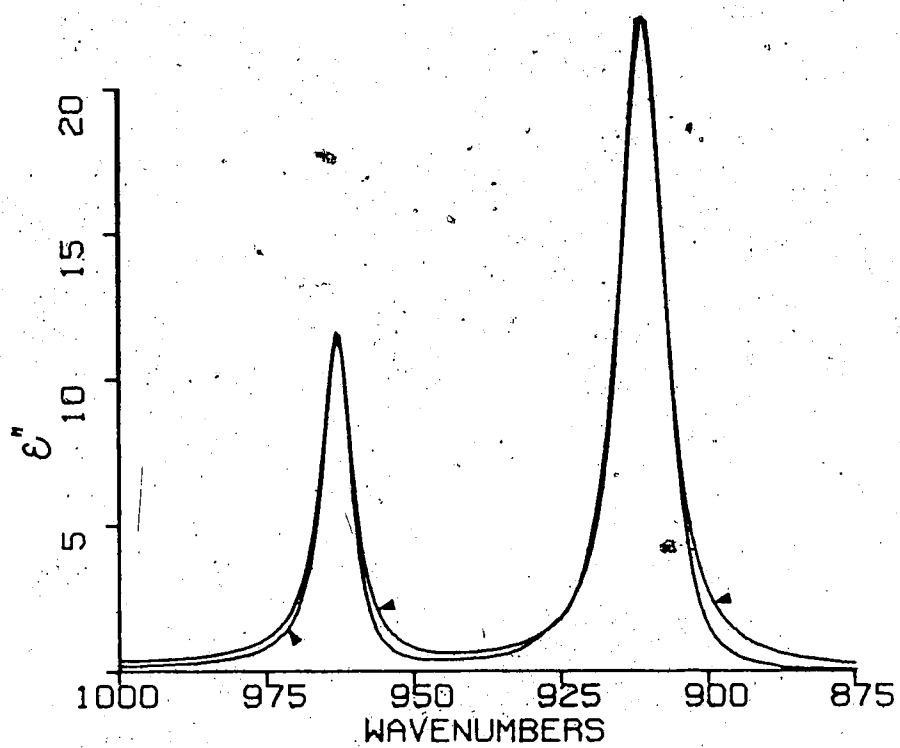


Figure 4.20a Continuation of Figure 4.20.

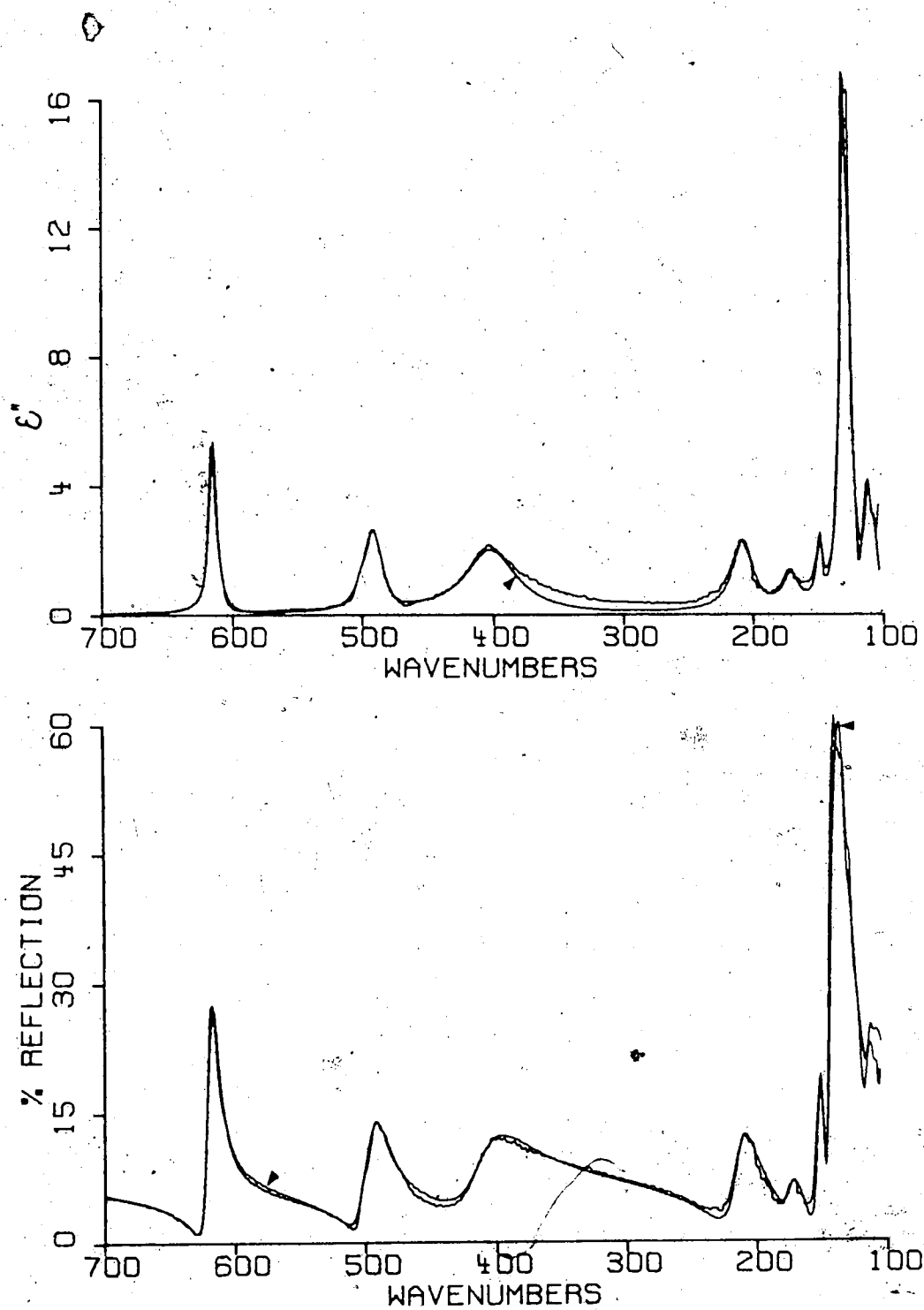


Figure 4.20b Continuation of Figure 4.20.

than the expected sodium D-line value along the  $a'$ -axis, and suggests that the measured reflectance for this polarization might be slightly low. A compilation of these oscillator parameters and their estimated accuracies is given in Tables 4.9 (b-polarized) and 4.10 ( $a'$ -polarized). The error allowances indicate to what extent a particular parameter could be adjusted before causing a measurable deterioration in the fitted result. Strong, relatively narrow bands ( $\text{FWHM} < 8 \text{ cm}^{-1}$ ) are estimated to have peak frequencies accurate to  $\pm 0.5 \text{ cm}^{-1}$ . For most other bands, except those with very large damping terms, the estimated frequency accuracy is reduced to  $\pm 1 \text{ cm}^{-1}$ . The wide variation in the errors associated with the oscillator strengths and damping values indicates the difficulty in accurately determining the parameters of weak features, particularly when they occur in the vicinity of a strong peak. However, for the majority of the fitted peaks, the estimated uncertainties in  $S_j$  and  $\gamma_j$  are less than 10%.

Except for the  $\text{ClO}_3^-$  ion stretching region ( $1350\text{--}1100 \text{ cm}^{-1}$ ), and to a lesser extent, the regions of strong water absorption, it was possible to simultaneously obtain a good fit to the measured reflectance and the KK-derived  $\epsilon''(\nu)$  spectra. This result is significant since only a few complicated reflectance spectra have been successfully modelled with a set of damped harmonic oscillators<sup>93,94,172</sup> and, to our knowledge,  $\text{Ba}(\text{ClO}_3)_2 \cdot \text{H}_2\text{O}$  represents the most complicated example to date.

Table 4.9 Final Set of Classical Oscillator Parameters for  
b-Polarized Single Crystal  $\text{Ba}(\text{ClO}_3)_2 \cdot \text{H}_2\text{O}$  Data

$j$	$\nu_j(\text{cm}^{-1})$	$\underline{E} \parallel b$	
		$S_j (\times 10^4 \text{ cm}^{-2})$	$\gamma_j (\text{cm}^{-1})$
1	$105 \pm 2$	$(2.15) \pm 3\%$	$7.2 \pm 0.3$
2	$120 \pm 0.5$	$(0.235) \pm 10\%$	$5.5 \pm 0.5$
3	$133 \pm 0.5$	$(0.082) \pm 10\%$	$4.5 \pm 0.2$
4	$160 \pm 1$	$(0.450) \pm 5\%$	$8.7 \pm 0.2$
5	$230 \pm 2$	$(1.20) \pm 5\%$	$20.0 \pm 1.0$
6	$388 \pm 1$	$(0.063) \pm 10\%$	$8.0 \pm 0.5$
7	$481 \pm 1$	$(0.349) \pm 1\%$	$6.3 \pm 0.2$
8	$507 \pm 0.5$	$(1.81) \pm 2\%$	$4.2 \pm 0.2$
9	$612 \pm 1$	$(1.34) \pm 1\%$	$9.5 \pm 0.2$
10	$925 \pm 2$	$(0.968) \pm 20\%$	$13.0 \pm 2.0$
11	$933 \pm 1$	$(1.64) \pm 7\%$	$7.5 \pm 0.3$
12	$940 \pm 1$	$(0.555) \pm 20\%$	$10.0 \pm 2.0$
13	$959 \pm 1$	$(22.5) \pm 3\%$	$12.1 \pm 0.3$
14	$1606 \pm 0.5$	$(1.91) \pm 2\%$	$7.8 \pm 0.2$
15	$3514 \pm 1$	$(9.31) \pm 3\%$	$17.5 \pm 0.5$

$$\epsilon_\infty = 2.49 \pm 0.01$$

Table 4.10 Final Set of Classical Oscillator Parameters  
for a'-Polarized Single Crystal  $\text{Ba}(\text{ClO}_3) \cdot \text{H}_2\text{O}$   
Data

$\underline{E} \parallel b$			
$j$	$\nu_j (\text{cm}^{-1})$	$S_j (x 10^4 \text{ cm}^{-2})$	$\gamma_j (\text{cm}^{-1})$
1	$92 \pm 2$	$(0.043) \pm 50\%$	$8.5 \pm 2.0$
2	$109 \pm 1$	$(0.134) \pm 10\%$	$7.0 \pm 1.0$
3	$114 \pm 0.5$	$(0.180) \pm 10\%$	$5.5 \pm 0.5$
4	$129 \pm 0.5$	$(0.415) \pm 20\%$	$5.7 \pm 0.5$
5	$131 \pm 1$	$(0.604) \pm 10\%$	$8.5 \pm 2.0$
6	$133 \pm 0.5$	$(0.667) \pm 20\%$	$4.7 \pm 0.5$
7	$151 \pm 0.5$	$(0.143) \pm 20\%$	$5.5 \pm 0.1$
8	$173 \pm 1$	$(0.263) \pm 20\%$	$15.0 \pm 3.0$
9	$210 \pm 1$	$(0.887) \pm 5\%$	$19.0 \pm 0.5$
10	$404 \pm 2$	$(3.90) \pm 15\%$	$48.0 \pm 5.0$
11	$487 \pm 1$	$(0.209) \pm 15\%$	$9.0 \pm 1$
12	$493 \pm 1$	$(1.31) \pm 2\%$	$12.5 \pm 0.5$
13	$502 \pm 1$	$(0.380) \pm 20\%$	$12.0 \pm 2.0$
14	$616 \pm 1$	$(2.38) \pm 5\%$	$7.2 \pm 0.3$
15	$909 \pm 0.5$	$(4.46) \pm 5\%$	$7.0 \pm 1.0$
16	$912 \pm 0.5$	$(12.9) \pm 4\%$	$7.7 \pm 0.2$
17	$963.3 \pm 0.5$	$(6.65) \pm 2\%$	$6.0 \pm 0.2$
18	$3584 \pm 2$	$(13.7) \pm 5\%$	$31.8 \pm 1.0$

$$\epsilon_{\infty} = 2.40 \pm 0.01$$

The fact that the  $\text{ClO}_3^-$  ion and water molecule stretching modes do not conform well to a description based on damped harmonic oscillators can best be explained by the tendency of these modes to undergo anharmonic coupling. Evidence for this perturbation is seen in the fairly large oscillator strengths and damping constants associated with these modes<sup>158</sup> (modes 10-15 in Table 4.9 and modes 15-18 in Table 4.10). To appreciate the magnitude of these quantities, it is useful to compare them with the corresponding values in a related crystal. Such a dispersion analysis has been conducted on  $\text{NaClO}_3$  crystal by Anderman and Dows.<sup>96</sup> For the  $\text{ClO}_3^-$  ion stretching modes, they obtained damping constants ranging from  $5\text{--}6\text{ cm}^{-1}$  and a maximum oscillator strength of  $16.4\text{ cm}^{-2}$  (for  $\nu_{3b}$ ); this compares with our values of  $6\text{--}13\text{ cm}^{-1}$  for the damping constant and a maximum oscillator strength of  $22.5\text{ cm}^{-2}$  (mode 13 in Table 4.9). Obviously the  $\text{ClO}_3^-$  ions in  $\text{Ba}(\text{ClO}_3)_2 \cdot \text{H}_2\text{O}$  are undergoing some additional relaxation process. The presence of hydrogen bonding in  $\text{Ba}(\text{ClO}_3)_2 \cdot \text{H}_2\text{O}$  strongly suggests that the appreciable width of these  $\epsilon''(\nu)$  bands is due to anharmonic coupling of the  $\text{ClO}_3^-$  ion stretching modes to the water molecule vibrational states, particularly overtone states of the rotational vibrations. A similar explanation was put forward by Wilkinson *et al.*<sup>189</sup> to account for the increased breadth of the  $\text{SO}_4^{2-}$  ion modes in  $\text{CaSO}_4 \cdot 2\text{H}_2\text{O}$  compared with  $\text{CaSO}_4$ .

However, strong anharmonic coupling can also occur between the symmetric ( $\nu_1$ ) and antisymmetric ( $\nu_3$ )  $\text{ClO}_3^-$  ion stretching modes since they are close in frequency, of considerable strength, and their reducible representations contain unit-cell-group symmetry species of the same type (Chapter VI). Thus, the  $\text{ClO}_3^-$  ion stretching region may be complicated by the presence of interionic coupling and interaction with water vibrational modes. The exact nature of this distortion cannot be easily predicted.

The effects of mechanical anharmonicity have been treated by several different quantum-mechanical models.<sup>190</sup> Although these various theories have fundamental differences, they have certain common features. The main consequences of cubic or higher order terms in the crystal's potential energy are: that the damping is not a constant parameter, but is frequency and temperature dependent; and that the resonance frequency is not precisely the harmonic value, but is frequency-shifted by an amount which is temperature dependent. The unusual success of the classical model is related to the fact that these deviations are usually very small compared with the resonance frequency,  $\nu_j$ , and that this model gives almost identical results to the various quantum-mechanical theories at  $\nu = \nu_j$ . The damped harmonic oscillator model then is strictly valid at the center of the dispersion region. Since the  $\epsilon''(\nu)$  bands exhibit a much narrower region of dispersion than the corresponding  $R(\nu)$  bands, the oscillator parameters derived

from a classical dispersion fit to the  $\epsilon''(\nu)$  spectra should be more reliable, thus substantiating our earlier empirical conclusion. Any effects of anharmonic coupling should be most apparent in the wings of the bands. Comparison of our fitted and KK-derived  $\epsilon''(\nu)$  spectra shows that this is indeed the region of greatest deviation.

In order to satisfactorily reproduce the peaks, dips, and shoulders in the experimental spectra (see Table 4.7), it was necessary to use several more oscillators in the fitting procedure. However, only those features believed to be due to fundamental transitions were included. Although it might be possible to simulate the numerous weak features due to overtone and combination modes by the superposition of many more oscillators, these additional dispersion parameters would have no physical significance. Recall from Section 1.1d that the damped harmonic oscillator model for dispersion in crystals was based on the selection rule for infrared activity being  $\underline{k} = 0$ , that is, the wave vector of vibration being equal to zero. However, this approximation of the general  $\underline{k} = \underline{K}$  selection rule, where  $\underline{K}$  is equal to the wave vector of radiation in the crystal, is only valid for fundamental transitions. In the case of overtone and combination modes, the selection rule  $\sum \underline{k}_i = \underline{K}$  must be used; the contribution to  $\epsilon''(\nu)$  from these modes therefore requires a summation over all values of  $\underline{k}$  in the first Brillouin zone.<sup>190</sup> Since the complete dispersion curve for  $\text{Ba}(\text{ClO}_3)_2 \cdot \text{H}_2\text{O}$  is unknown, a classical

dispersion analysis is restricted to the fundamental modes.

For the b-polarized data, weak oscillators were introduced at  $925\text{ cm}^{-1}$  and  $940\text{ cm}^{-1}$  to respectively simulate the low frequency shoulder and the dip between the two resonances at  $959$  and  $933\text{ cm}^{-1}$  (see Figure 4.19a). The observation that a sharp weak resonance occurring to low frequency of a strong reflection band is situated at a frequency of a reflectance minimum, was first made in 1961 by Spitzer and Kleinman<sup>93</sup> during their detailed dispersion analysis of the reflection spectra of quartz.

For the a'-polarized data, it was necessary to introduce several new oscillators for an adequate fit. The shoulders on the broad  $493\text{ cm}^{-1}$  peak were correctly described by two weak-resonances at  $487$  and  $502\text{ cm}^{-1}$ . The essential features of the band centered at  $130\text{ cm}^{-1}$  in the conduction spectrum (see Table 4.7) were fairly well reproduced with three closely spaced oscillators, although five definite features were noted in this region. Further oscillators might improve this fit, but the closeness of this band to the low frequency integration limit,  $105\text{ cm}^{-1}$ , precludes such a refinement. An additional peak at  $110\text{ cm}^{-1}$  reproduced quite well the shoulder on the  $114\text{ cm}^{-1}$  peak in the KK-derived  $\epsilon''(\nu)$  spectrum. Its inability to match the observed reflectance can also be attributed to its proximity to the low frequency limit of the measured data. The broad strong reflection band at  $920\text{ cm}^{-1}$  was only well described when two oscillators at  $912$  and  $909\text{ cm}^{-1}$ , in the

approximate intensity ratio 3:1, were assigned to this feature. The necessity of two oscillators was indicated by the flat top of the corresponding KK-derived  $\epsilon''(\nu)$  band; a single isolated oscillator exhibits a definite peak as can be seen from the  $963\text{ cm}^{-1}$   $\epsilon''(\nu)$  band.

In conclusion, the dispersion parameters obtained from a combined Kramers-Kronig/classical dispersion analysis were significantly improved over those derived from the peak characteristics of the conductivity spectra, thus justifying this more lengthy procedure. Secondly, the success of the classical damped harmonic oscillator model in describing most of the reflection features of  $\text{Ba}(\text{ClO}_3)_2 \cdot \text{H}_2\text{O}$  shows that this model is approximately correct. The nature and extent of the observed deviations indicate that the limited range of reflection data incurs little error in the derived optical parameters and that the major source of deviation from the predictions of the damped harmonic oscillator model is anharmonic coupling.

## CHAPTER V.

### ERROR ANALYSIS

This chapter presents a compilation of the principal errors encountered in the determination of the infrared optical constants of  $\text{Ba}(\text{ClO}_3)_2 \cdot \text{H}_2\text{O}$  by reflectance spectroscopy, at near-normal incidence, followed by a Kramers-Kronig analysis. The errors are classified as experimental or computational, with the experimental errors being further distinguished as random or systematic. Where possible, the magnitude of the various errors is estimated (Section 5.1). The sensitivity of the KK-method to errors in the measured reflectance is also studied (Section 5.2). Since many of these errors have been previously discussed, only a brief summary is given here.

#### 5.1 Experimental Errors

Experimental sources of error may be of random or systematic type. Systematic errors may be of any magnitude but tend to be approximately invariant when an experiment is repeated, whereas random errors fluctuate in sign and magnitude. In the following error analysis, the errors are identified as to type, approximate magnitude, and appropriate corrective action (if any). The majority of these errors are common to any infrared reflectance study, but a few are peculiar to our apparatus and samples.

### 5.1a Effect of Non-Normal Incidence

The dependence of reflectance of plane-polarized light upon angle of incidence was illustrated in Figure 1.2 with theoretical reflectance curves for  $n = 3$  and  $k = 1$ . It was observed that for  $\phi = 10^\circ$ , to a very good approximation,  $R = R_s = R_p$ . A similar result was obtained for mid-infrared reflectance spectra of polycrystalline  $\text{Ba}(\text{ClO}_3)_2 \cdot \text{H}_2\text{O}$  recorded under TE(s-) and TM(p-) polarization, at  $9.5^\circ$  incidence. In the high frequency region, where the background reflectance was  $\sim 0.05$ , the  $R_s$  curve was  $\sim 0.004$  units higher than the  $R_p$  curve. From a model calculation, assuming  $k = 0$  and equal amounts of s- and p-polarized radiation (Table 3.2), this difference was consistent with the  $9.5^\circ$  angle of incidence. Also, the average value of  $R_s$  and  $R_p$  was equal to the unpolarized normal incidence reflectance  $R_0$ .

To obtain a better estimate of the error associated with operating at  $9.5^\circ$  incidence, the various quantities,  $R_0$ ,  $R_s$ ,  $R_p$ , and  $R$ , where  $R = 1/2(R_s + R_p)$ , were calculated for quartz<sup>93</sup> and silicon<sup>150</sup> from their known optical constants. The relevant equations are [1.36] to [1.40]. Three different situations were considered: i) intermediate  $R$ , low  $k$ ; ii) low  $R$ , low  $k$ , and iii) intermediate  $R$ ,  $k > n$ . In all cases, the difference between  $R$  and  $R_0$ , for  $10^\circ$  incidence, was less than  $0.0001$  reflectance units. Since this systematic error is considerably smaller than the precision of the reflectance measurements (see Section 5.1j), it was ignored.

### 5.1b Apparatus Polarization

Apparatus polarization refers to the discrimination of an instrument to a particular component of radiation. This effect can give rise to both a systematic and random error. A systematic error occurs when the reflectance spectra are recorded for unpolarized conditions, at non-normal incidence, under the assumption of equal contributions from s- and p-polarized radiation. The measurement and correction for this systematic error were discussed in detail in Section 3.2b. A random error arises from an increased noise level, when the inefficient polarization is used. The degree of apparatus polarization for the Nicolet 7199 FTIR instrument is shown in Figure 3.13 for the KBr beamsplitter and Figure 5.1 for the  $\text{CaF}_2$  and 3  $\mu\text{m}$  mylar beamsplitters. It can be seen that the preference for s-polarized light is quite pronounced in the near- and far-infrared regions. In the mid-infrared, the relative amounts of s- and p-polarized light are approximately equal. Thus, to optimize the S/N ratio, the polarization experiments in all frequency regions were performed under TE(s-) polarization.

### 5.1c Polarizer Efficiency

Polarized infrared radiation was produced by a series of wire grid polarizers with different substrates:  $\text{BaF}_2$  (near-infrared), AgBr (mid-infrared), and polyethylene (far-infrared). The efficiency of a polarizer is given by its average transmittance for two orthogonal polarizations, and its degree of polarization, i.e. the purity of the po-

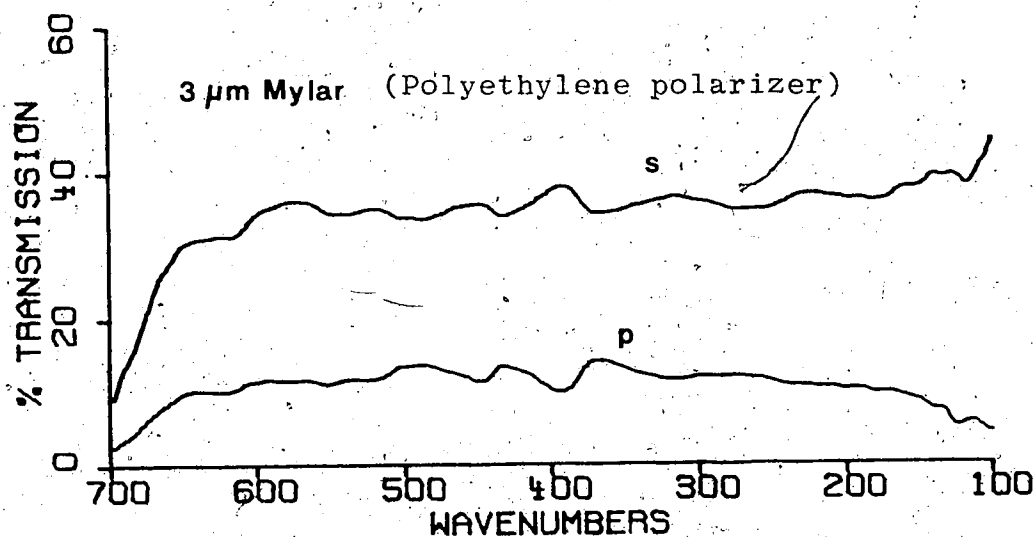
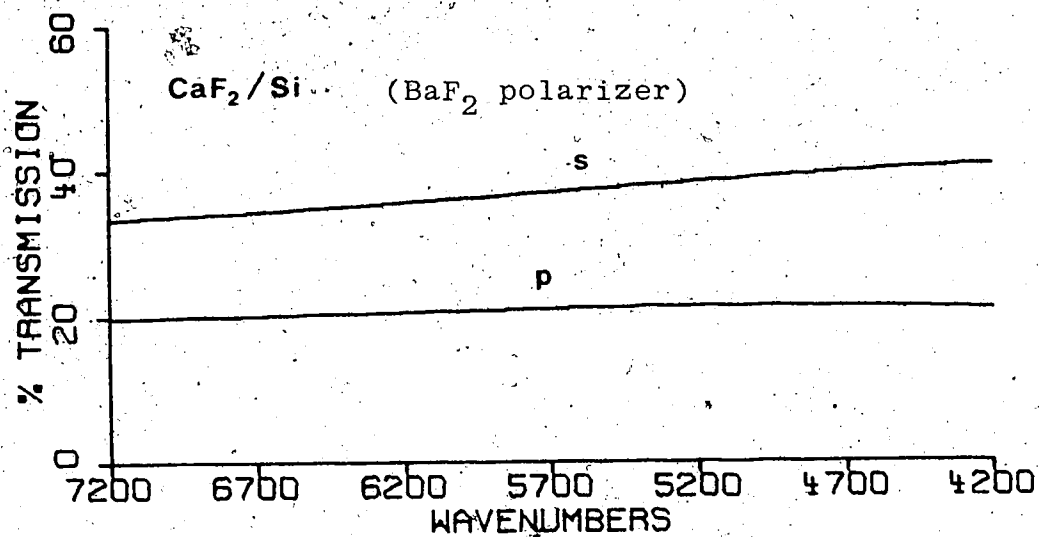


Figure 5.1 Degree of apparatus polarization for the Nicolet 7199 FTIR instrument with the CaF<sub>2</sub> and 3 μm mylar beamsplitters.

larized radiation. Poor transmission characteristics of the polarizer can increase the random error of noise while incomplete polarization can introduce a systematic error.

The mid-infrared polarizer displayed an average transmittance of 17-22% in the region  $800-4400\text{ cm}^{-1}$  (Figure 3.13). Its degree of polarization was measured to be at least 98% based on the relative intensities of the features at  $1604\text{ cm}^{-1}$  in the a'- and b-polarized reflectance spectra of the (001) crystal face of  $\text{Ba}(\text{ClO}_3)_2 \cdot \text{H}_2\text{O}$  (Figures 3.24 and 3.25).

The average transmittance of the far-infrared polarizer was 24% in the region  $100-500\text{ cm}^{-1}$ . Its degree of polarization was more difficult to estimate but was at least 95%. Comparison of Figures 3.24 and 3.25 shows that the b-polarized peak at  $123\text{ cm}^{-1}$  corresponds with the position of a reflectance minimum in the a'-polarized spectrum.

For the near-infrared polarizer, the average transmittance was 26-32% in the range  $1800-7200\text{ cm}^{-1}$ . From intensity measurements of the  $1604\text{ cm}^{-1}$  peak, the degree of polarization exceeded 98%.

In summary, polarizer efficiency may contribute a maximum systematic error of 2% of the measured reflectance value. Since the extent of this error is not accurately known, no corrective action was taken.

#### 5.1d Optical and Electronic Errors

The principal optical and electronic errors influencing the accuracy of our reflection results are instrument

instability, incorrect signal amplification, detector linearity, and incorrect phase correction.

Instrument instability manifests itself as drift and noise. Instrument drift can produce a systematic error if the background and sample spectra are always collected in the same order. This problem was found to be most severe in the near-infrared region. If the instrument was not allowed to sufficiently equilibrate after tuning, a significant deterioration in the high energy performance occurred with time. Therefore, the constancy of the energy throughput was carefully checked prior to and during data collection, by recording several background spectra.

This modified procedure was not adopted in the mid- and far-infrared regions, where instrument drift was less prominent.

Instrument noise contributes a random error and was gauged from several 100% lines run prior to each experiment. Recall that a 100% line is the ratio of two successive single-beam energy spectra, run under identical conditions, with no sample. Our 100% lines were recorded under the same experimental conditions as the background reflectance spectra for  $\text{Ba}(\text{ClO}_3)_2 \cdot \text{H}_2\text{O}$ , i.e. with the gold mirror in the Harrick reflectance accessory at  $9.5^\circ$  incidence and with and without the polarizer in the beam.

A problem peculiar to the far-infrared investigation on the Nicolet 7199 instrument was the appearance of "glitches" on the spectra, whose frequencies were reproduced.

cible for a given moving mirror velocity. This is illustrated in Figure 5.2. The two curves are 100% lines obtained for the 3  $\mu\text{m}$  mylar beamsplitter and the TGS detector with polyethylene window, at 8  $\text{cm}^{-1}$  resolution. The only difference is that the room lights were on for Curve A and off for Curve B. It can be seen that the glitches at  $\sim 330$  and  $\sim 660 \text{ cm}^{-1}$  are not present in Curve B. Consequently, all far-infrared spectra were collected with the fluorescent room lights off.

Typical 100% lines obtained for the various spectral regions on the Nicolet 7199 are shown in Figure 5.3. These spectra were all recorded at 2  $\text{cm}^{-1}$  resolution. The variable operating parameters of gain, number of scans (NSS), and polarization, are indicated; constant parameters are described in Sections 2.7b and 2.7c.

Two 100% lines are presented for the KBr on Ge beamsplitter with the liquid nitrogen cooled Hg Cd Te detector. The upper curve, recorded with no polarizer in the beam, exhibits a signal-to-noise ratio (S/N) of  $\sim 1200$  for a measurement time of 6.1 minutes (300 scans). When a polarizer is placed in the instrument, and set to transmit TE(s-) polarized radiation (lower curve), the S/N ratio is reduced to  $\sim 600$  below  $2800 \text{ cm}^{-1}$  and to  $\sim 350$  above  $2800 \text{ cm}^{-1}$ , for an increased measurement time of 15.3 minutes (750 scans). The S/N ratio improves as the square root of the measurement time; all other operating parameters being the same.

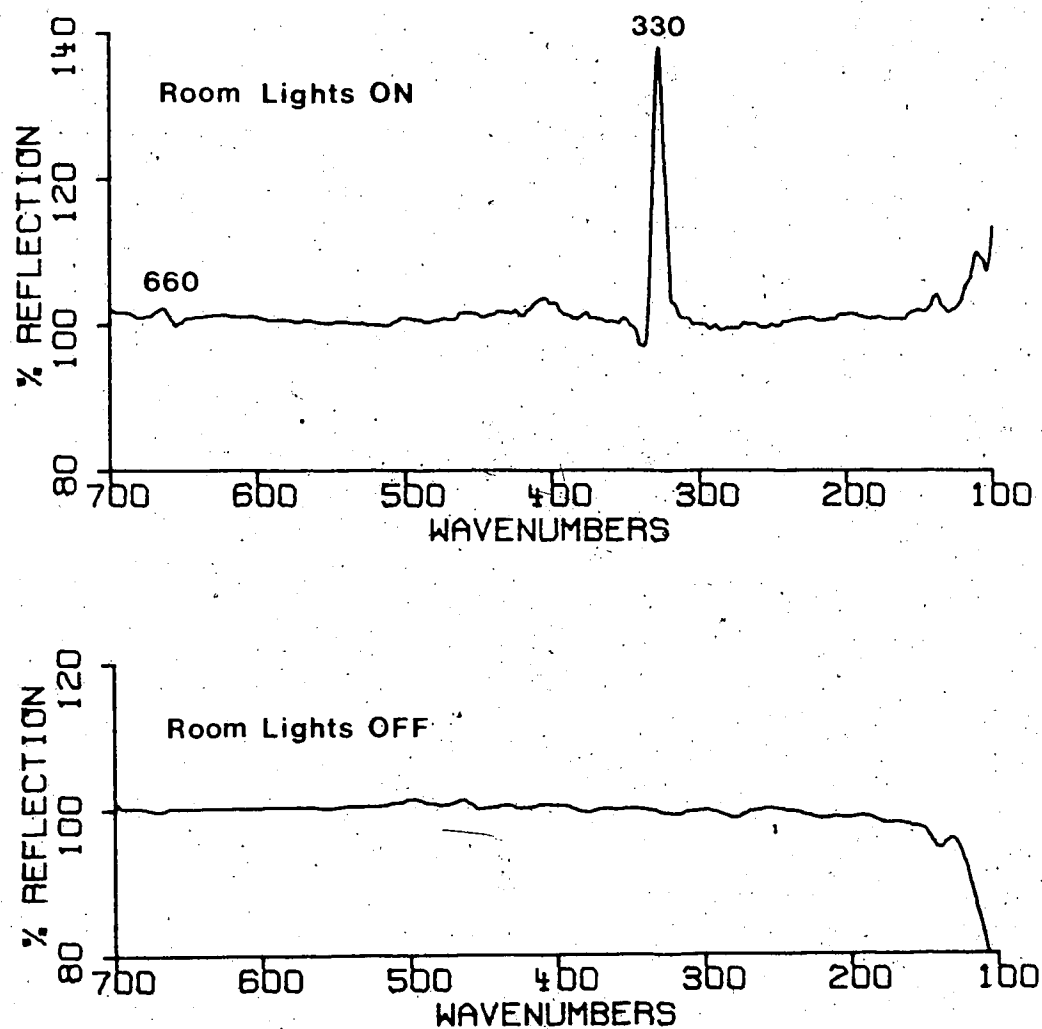


Figure 5.2 Comparison of 100% lines obtained with and without the room lights on; 3  $\mu$ m mylar beamsplitter and DTGS/polyethylene detector.

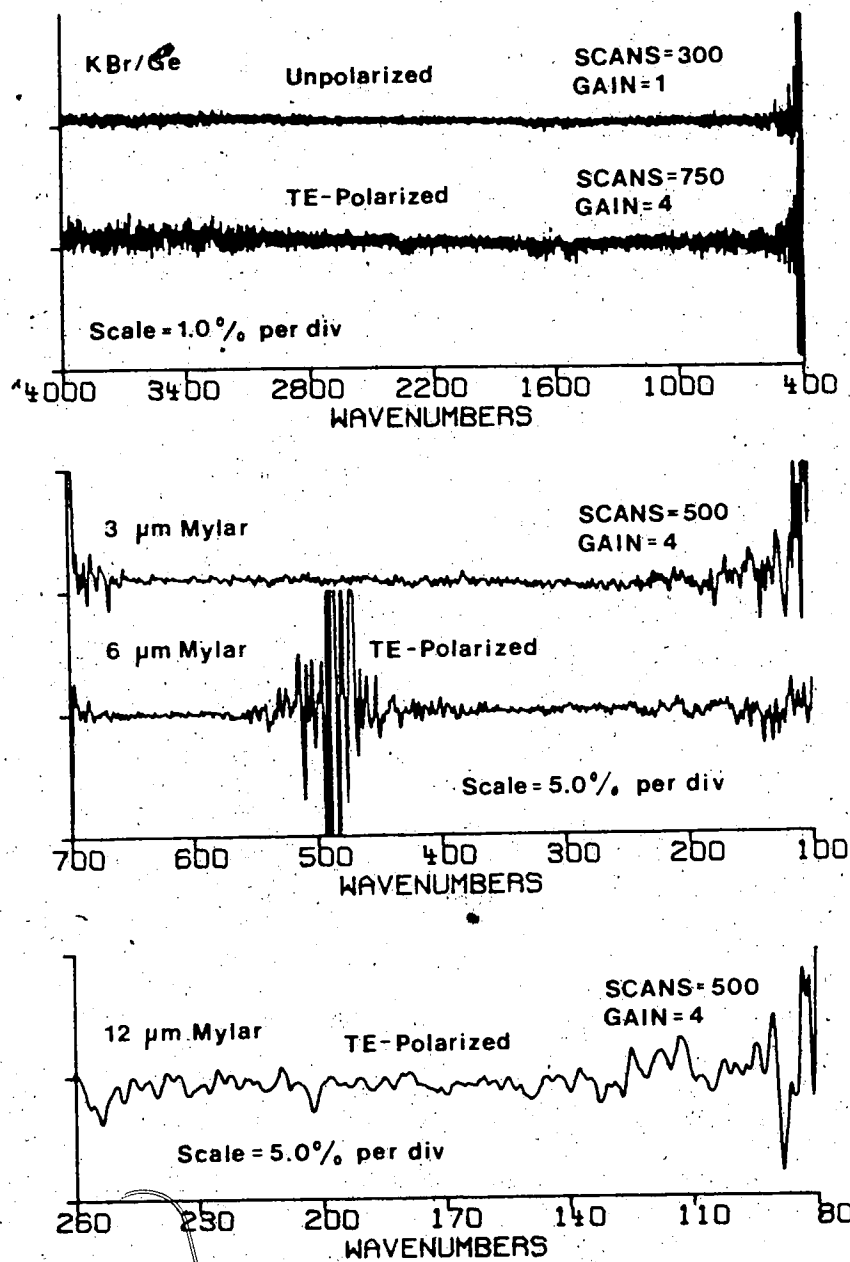


Figure 5.3 Typical 100% lines obtained for the various spectral regions on the Nicolet instrument for 2 cm<sup>-1</sup> resolution.

The 100% lines for the far-infrared region were recorded with the TGS detector, using TE-polarized light. These spectra are directly comparable since a gain setting of 4 and a measurement time of 30 minutes (500 scans) were used in all cases. It should be noted that the reflectance scale for the far-infrared spectra is 5% R per division while that of the mid-infrared spectra is only 1% R per division. The 3  $\mu\text{m}$  mylar beamsplitter displays a S/N of  $\sim 250$  in the region 200-650  $\text{cm}^{-1}$ . This performance is repeated by the 6.25  $\mu\text{m}$  mylar beamsplitter in the region of its first interference fringe, or "window", from  $\sim 150$ -420  $\text{cm}^{-1}$ . In its second "window" region of  $\sim 550$ -670  $\text{cm}^{-1}$ , its S/N is increased to  $\sim 500$ . The 12.5  $\mu\text{m}$  mylar beamsplitter exhibits a S/N of only  $\sim 100$  in the region 100-260  $\text{cm}^{-1}$ . Thus, the random error due to instrument noise appears to be less than  $\pm 1.0\%$  except in the very far-infrared region. However, many of the  $\text{Ba}(\text{ClO}_3)_2 \cdot \text{H}_2\text{O}$  sample spectra were recorded several hours after the associated background spectra, so the error due to instrument stability may be underestimated by these 100% lines.

Another possible source of instrument error occurs during the amplification and renormalization of the infrared signal. If the detector voltages are incorrectly programmed, this introduces a systematic error in the measured reflectance, whose magnitude is dependent upon the particular gain setting. Although this amplification error

is frequently neglected, it is an important consideration in the accurate determination of the reference mirror's reflectance.

To assess this error, reflectance measurements were performed on a glass slide for various gain settings, keeping all other operating parameters constant. Glass was selected because it is optically stable and a relatively weak reflector so a range of gain settings are permissible before saturation occurs. It was assumed that the spectrum obtained with a gain setting of 1 for both the sample and background collections gave the correct absolute reflectance. The measured reflectances for different sample gain settings were then compared with the accepted values at several frequencies, and the average deviation was calculated. These results are presented in Table 5.1. In order to determine the amplification error for gain settings greater than 16, it was necessary to reduce the infrared intensity by placing a polarizer in the beam. A TE-polarized reflectance spectrum of glass, recorded with a gain setting of 4 was used to compute the error in the higher gain settings. These results were then normalized to a gain setting of 1 by including the previously determined error in the GAIN=4 setting. The validity of this procedure is demonstrated by the fact that the errors calculated for a gain of 16, via the direct and indirect methods, are in very good agreement (within 0.1%). The greatest amplification error of -1.3% was observed for a gain of 2. For

Table 5.1 Determination of Electronic Amplification Errors  
for Nicolet 7199 FTIR Instrument

Frequency (cm <sup>-1</sup> )	Measured % R(v)*				
	Gain = 1	Gain = 2	Gain = 4	Gain = 8	Gain = 16
4400	7.27	7.37	7.18	7.24	7.21
3800	7.16	7.22	7.06	7.10	7.09
3200	5.24	5.30	5.18	5.23	5.20
2600	4.82	4.90	4.78	4.83	4.81
2000	2.99	3.01	2.95	2.99	2.96
1060	29.3	29.6	29.0	29.3	29.1
470	23.9	24.5	23.7	24.0	23.8
<hr/>					
Av. % Error/Gain = 1	101.3		98.9	99.9	99.3

\* Unpolarized reflectance spectra of a glass microscope slide. All operating parameters identical except for Gain setting of sample spectra.

Frequency (cm <sup>-1</sup> )	Measured % R(v) <sup>†</sup>		
	Gain = 4	Gain = 16	Gain = 32
4400	7.89	7.90	7.97
3800	7.70	7.70	7.75
3200	5.63	5.70	5.73
2600	5.27	5.28	5.34
2000	3.30	3.30	3.34
1060	31.4	31.7	32.0
470	25.8	25.7	26.0
<hr/>			
Av. % Error/Gain = 4	100.3		101.3
Est. % Error/Gain = 1	99.2		100.2

<sup>†</sup> TE-polarized reflectance spectra of a glass microscope slide.

gain settings of 8 and 32, the errors were less than 0.2%. Again, these errors were much less than the precision of the reflectance measurements and were neglected. However, careful selection of the gain settings helped to minimize this systematic error.

Nonlinearity in the response of the detector or pre-amplifier contributes another source of systematic error. This effect is observed in single-beam energy spectra as non-zero energy in regions where the intensity is known to be zero. For example, a KBr beamsplitter absorbs all radiation below  $350\text{ cm}^{-1}$ . However, on the Nicolet 7199 instrument, with the KBr beamsplitter and the liquid nitrogen cooled, type B, Hg Cd Te detector, stray radiation was measured below  $350\text{ cm}^{-1}$ . The maximum intensity of the features below  $350\text{ cm}^{-1}$  was only 0.3% of the peak amplitude at  $1800\text{ cm}^{-1}$ , suggesting that the error contributed by detector non-linearity is somewhat less than 0.5% of the measured reflectance value.

The influences of detector nonlinearity, combined with phase correction errors, are also found in transmission spectra of strongly absorbing materials as negative peaks, in regions where the samples are 100% absorbing. These effects were investigated on the Nicolet 7199 for samples of 50 and 100  $\mu\text{m}$  thick Mylar, in the mid-infrared region. From a total of 14 measurements at peak frequencies of 1025, 1115, 1265, 1415, and  $1725\text{ cm}^{-1}$ , the deviation from 0.00% transmittance was calculated to be  $0.11 \pm 0.01\%$  T, with

95% confidence.

Recently, it has been shown that the accuracy of the Mertz method of phase correction, which is used by the Nicolet, is limited by the asymmetry of the interferogram.<sup>191</sup> In the case of a perfectly symmetrical interferogram, the procedure is exact and gives the best approximation to a spectrum that can be achieved by FTIR spectroscopy.

In our reflectance study, the interferograms of the  $\text{Ba}(\text{ClO}_3)_2 \cdot \text{H}_2\text{O}$  samples were remarkably symmetrical in the mid- and far-infrared regions where the predominant absorption occurred. However, in the near-infrared, where sample absorption was broad and weak, the interferograms were considerably less symmetrical. The interferograms for the reference mirror, over all regions, were quite asymmetric. The residual error in the phase correction due to this asymmetry was partially compensated for by the calibration of the reference mirror against the silicon standard. From the available data, it is estimated that the combined effects of detector non-linearity and phase correction error yield a fractional error of  $\leq 1\%$  in the reported reflectance values.

#### 5.1e Reference Mirror Reflectance

The accurate measurement of sample reflectance requires that the reflectance of the reference mirror be known for all frequencies in the range of interest. A gold mirror was used in this study because of its very high reflectance

over the entire infrared region. However, gold is a soft material, and its reflecting properties were found to gradually deteriorate with time. It was, therefore, calibrated against a silicon standard prior to several experiments, to determine the necessary correction. This procedure is described in detail in Section 3.2b.

Typical calibration curves for the mid- and near-infrared regions are shown in Figures 3.15 and 3.16, respectively. Comparison of calibrated and averaged reflectance results for  $\text{Ba}(\text{ClO}_3)_2 \cdot \text{H}_2\text{O}$  in the mid- and far-infrared regions indicated that the calibration error was small and random; for percent reflectance values exceeding 5%, the maximum fractional error was 0.010 in the mid-infrared (Table 3.4) and 0.030 in the far-infrared. This compares with an experimental reproducibility of 3% and 7%, respectively in these regions (see Section 5.1j). Thus, the averaged far- and mid-infrared reflectance spectra were taken as the correct results, within experimental uncertainty.

Calibration was more important in the near-infrared region. Figure 3.17 illustrates the overlap of the averaged,  $a'$ -polarized mid-infrared reflectance of single crystal  $\text{Ba}(\text{ClO}_3)_2 \cdot \text{H}_2\text{O}$  with the corresponding near-infrared spectrum, before, and after calibration. It was observed that, in the frequency range of expected spectral overlap ( $\sim 1200\text{--}4800 \text{ cm}^{-1}$ ), the measured near-infrared reflectance was too high by 5% of the mid-infrared value; after cali-

bration, this deviation was reduced to less than 1% of the value.

To summarize, in the mid- and far-infrared regions, the correction due to calibration was much less than the precision of the measurement, and was ignored. In the near-infrared, where the calibration correction was of the order of 5% of the reflectance value, the necessary correction was applied.

#### 5.1f Extraneous Reflection

Another experimental error affecting the measured reflectance is background scattering. This error was estimated from reflectance measurements made without any sample in the beam. It was found that the scattering largely arose from the sample holder, and was particularly significant in the far-infrared region. Various procedures, such as sandblasting and painting with a black absorbing paint, met with limited success. Satisfactory results were finally obtained when a piece of black velvet material (polycrystalline sample holder) or black paper (single crystal sample holder) was affixed to the front surface of the holder.

In the case of the polycrystalline sample holder (Figure 2.7), the background reflectance was reduced to  $\sim 0.15\% R$  in the region  $50\text{--}250\text{ cm}^{-1}$ . This holder was only used to record the very far-infrared reflectance of polycrystalline  $\text{Ba}(\text{ClO}_3)_2 \cdot \text{H}_2\text{O}$  on the R.I.I.C. A more serious

systematic error occurred during the processing of the R.I.I.C. intensity data. Since the power spectrum was computed, the noise was always positive (Section 2.5). It is estimated that this shifted the baseline upward by a further 1.35% R. Thus, the total extraneous reflectance is ~1.5% R. This constant value was subtracted from the measured  $\text{Ba}(\text{ClO}_3)_2 \cdot \text{H}_2\text{O}$  reflectance on the R.I.I.C., before merging with the Nicolet data (see Figure 3.20).

The single crystal sample holder (Figure 2.8) was used to record all other final reflectance spectra of  $\text{Ba}(\text{ClO}_3)_2 \cdot \text{H}_2\text{O}$ . Its original design involved a  $17^\circ$  taper of the sample aperture, based on measurements of the optical path at the reflecting surface (see Figure 2.5). However, it was observed that this prototype contributed a significant amount of background reflectance, even with the black paper taped to the front surface. This is shown in Curve A of Figure 5.4. The percent reflectance due to the sample holder gradually increased from ~0.02% R at  $3400 \text{ cm}^{-1}$  to ~0.08% R at  $700 \text{ cm}^{-1}$ . When the taper of the sample aperture was increased to  $20^\circ$ , the background reflectance from the holder was reduced to a constant level of ~0.02% R in the mid-infrared (Curve B) and ~0.03% R in the far-infrared.

#### 5.1g Sample Deterioration

A problem peculiar to the infrared reflectance study of  $\text{Ba}(\text{ClO}_3)_2 \cdot \text{H}_2\text{O}$  was the sample's apparent sensitivity to prolonged instrument purging with dry nitrogen gas. Fig-

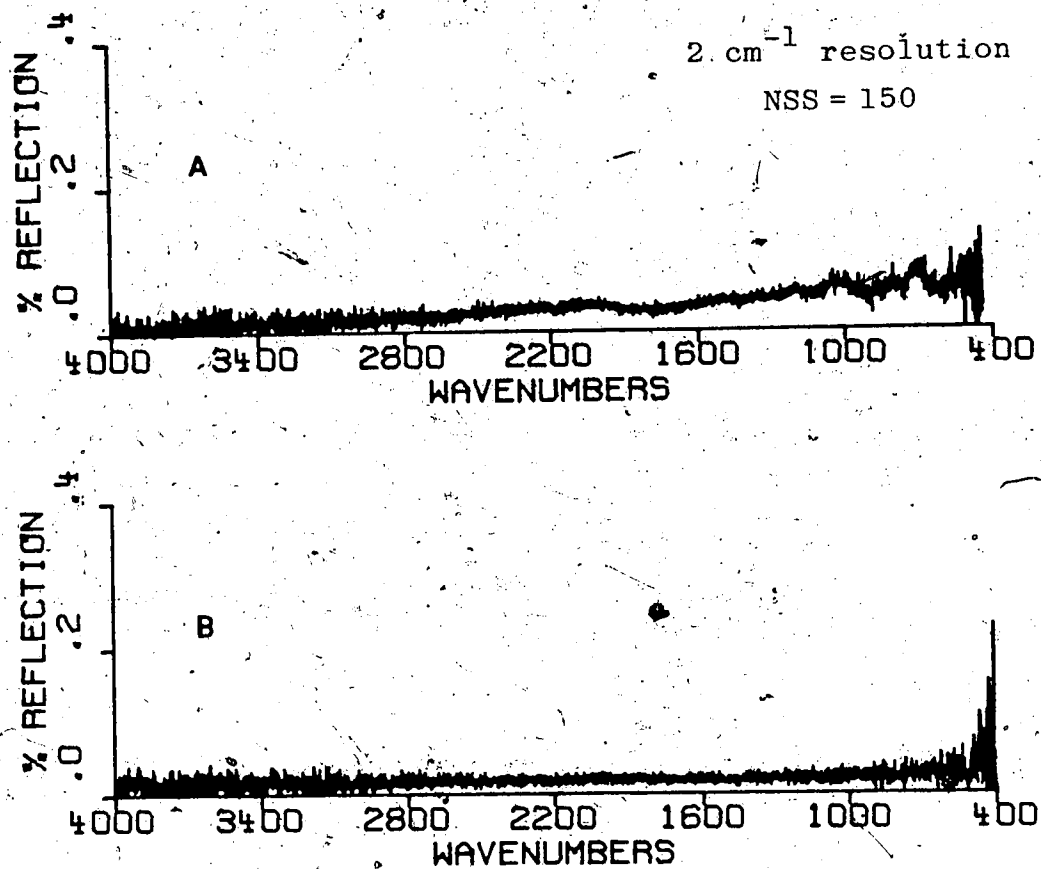


Figure 5.4 Background reflectance contributed by single crystal sample holder for different tapers of the sample aperture.

Curve A: 17° taper

Curve B: 20° taper

ures 3.11 and 3.11a illustrate the dramatic spectral changes which occurred to polycrystalline  $\text{Ba}(\text{ClO}_3)_2 \cdot \text{H}_2\text{O}$  after two hours of purging, and how the original spectrum was simply recovered by repolishing the sample with isopropanol. The changes were not constant with frequency, but more pronounced at the reflectance maxima. To minimize this effect, the spectra were recorded immediately after placing the freshly polished sample in the instrument, and for relatively short collection periods; typically 5 minutes (250 scans) for the mid- and near-infrared regions, and 15 minutes (250 scans) for the far-infrared region. It was found that the rate of spectral change, as gauged from two successive 250 scan collections, was approximately proportional to the absolute reflectance. For the mid-infrared spectra of polycrystalline  $\text{Ba}(\text{ClO}_3)_2 \cdot \text{H}_2\text{O}$ , the percent change during this 10 minute period was -0.1% at  $3576 \text{ cm}^{-1}$  ( $R = 0.065$ ), -0.3% at  $922 \text{ cm}^{-1}$  ( $R = 0.371$ ) and -0.5% at  $977 \text{ cm}^{-1}$  ( $R = 0.586$ ). In the far-infrared region, the measured reflectance changed by -2% of the value during a 30 minute period. Thus, during the individual sample collections, the maximum percent changes are expected to be -0.25% in the mid-infrared and -1% in the far-infrared. Since the magnitude of these errors is considerably less than the precision of the reflectance measurements, they were ignored.

#### 5.1h Sample Holder Positioning

In order to obtain an accurate estimate of the error involved in positioning the sample holder without the complication of other factors, silicon was chosen as the sample, and comparison was restricted to spectra recorded on the same day and for the same gold mirror. A groove cut into the reflectance accessory acted as a physical stop to the holder and improved the reproducibility in its positioning. The test was carried out by recording a series of silicon reflectance spectra, in which the holder plus sample assembly were removed, then repositioned in the instrument after each data collection. It was found that the error involved in this operation increased with increasing frequency. For example, the standard deviation at  $800\text{ cm}^{-1}$  was only 0.5% of the reflectance value, whereas at  $4000\text{ cm}^{-1}$ , it was 1%. Since incorrect positioning of the sample holder always causes the measured reflectance to be less than the actual value, the  $\text{Ba}(\text{ClO}_3)_2 \cdot \text{H}_2\text{O}$  spectra exhibiting the greatest overall reflectance were used in the merging procedure.

#### 5.1i Sample Uniformity

The error due to sample nonuniformity is difficult to estimate since several factors contribute to the observed variations in the measured reflectance. Since a poor optical finish gives systematically low reflectance values, the best quality sample spectra were judged as those dis-

playing the highest overall reflectance.

The polycrystalline nature of the  $\text{Ba}(\text{ClO}_3)_2 \cdot \text{H}_2\text{O}$  pellets was verified by polarized infrared reflectance measurements (Section 3.1b). All features observed under TM(p-) polarization were reproduced under TE(s-) polarization; the only difference was the  $R_s$  curve rose slightly above the  $R_p$  curve for all frequencies; as expected for a  $9.5^\circ$  angle of incidence. It was therefore concluded that the polycrystalline samples exhibited no preferential orientation.

The consistency of the sample preparation and polishing techniques was demonstrated by the near-identical reflectance spectra obtained for two different samples (Figures 3.4, 3.5 and 3.7).

#### 5.1j Residual Systematic and Random Errors

It is of interest to compare the residual error in the measured  $\text{Ba}(\text{ClO}_3)_2 \cdot \text{H}_2\text{O}$  reflectance values with that predicted from our foregoing discussion of experimental errors. The principal effects contributing to the reproducibility error are: instrument noise and drift, sample deterioration and nonuniformity, and placement of the sample holder. Except for instrument drift, the magnitude of these errors has been previously estimated. Since it is not known how these various errors interact, only an effective upper limit can be calculated from the sum of the individual fractional errors. Comparison with the measured deviations in the  $\text{Ba}(\text{ClO}_3)_2 \cdot \text{H}_2\text{O}$  reflectance values

should then give an estimate of the error due to instrument drift. This error analysis was carried out on the a.-polarized reflectance data for the (001) crystal face of  $\text{Ba}(\text{ClO}_3)_2 \cdot \text{H}_2\text{O}$ .

In the mid-infrared region, the reflectance was measured at 64 different frequencies from  $480\text{--}4800\text{ cm}^{-1}$ , for 6 independent 250 scan sample collections. The average standard deviation was determined to be 3.0% of the reflectance value. Typical 90% confidence limits for this data were:  $3500\text{ cm}^{-1}$ ,  $\% R = 5.27 \pm 0.10$ ;  $980\text{ cm}^{-1}$ ,  $\% R = 48.59 \pm 0.59$ ; and  $720\text{ cm}^{-1}$ ,  $\% R = 6.20 \pm 0.10$ .

Under the operating conditions of these spectra, noise contributes a constant random error of  $\pm 0.05\%$  reflection below  $2800\text{ cm}^{-1}$  and  $\pm 0.10\% R$  above  $2800\text{ cm}^{-1}$ . Thus, for a sample reflectance of 10%, the noise contributes fractional errors in the measured values of  $\pm 0.5\%$  and  $\pm 1.0\%$ , respectively. The degree of sample deterioration and uniformity may differ for the various sample collections, but it is expected that this error is less than 0.5% in the mid-infrared. Also, the average fractional error observed for the sample holder positioning was 0.5%. Of the 3.0% sample reproducibility error, 1.5–2.0% has been accounted for by instrument noise, sample deterioration and uniformity, and placement of the holder. This suggests that instrument drift contributes the remaining 1.0–1.5% error in the reflectance values.

Recently, a check of the Nicolet instrument stability in the mid-infrared region, over a period of hours, showed that this estimate was reasonable. A series of 100% lines were collected, involving a reference spectrum at time  $T_0$  and several sample spectra at later times  $T_1$ ,  $T_2$ , etc. It was found that the instrument throughput gradually diminished with time and was most pronounced at higher energies, e.g. in a 2 hour period, the downward drift in the 100% line at various frequencies was:  $2200\text{ cm}^{-1}$ : 0.5%;  $3400\text{ cm}^{-1}$ : 1.0%; and  $4000\text{ cm}^{-1}$ : 1.5%.

In the far-infrared region, the  $\text{Ba}(\text{ClO}_3)_2 \cdot \text{H}_2\text{O}$  reflectance was measured at 19 different frequencies in the range  $250\text{--}620\text{ cm}^{-1}$ , and for 8 independent 250 scan collections. The average standard deviation was determined to be 7.3% of the measured value. Typical 90% confidence limits<sup>192</sup> for this data were:  $480\text{ cm}^{-1}$ , %  $R = 9.83 \pm 0.34$ ;  $400\text{ cm}^{-1}$ , %  $R = 11.76 \pm 0.51$ ; and  $300\text{ cm}^{-1}$ , %  $R = 6.92 \pm 0.37$ . Noise is a much more serious problem in the far-infrared;

and for the conditions of the individual sample spectra, contributes a constant random error of  $\pm 0.3\text{--}0.4\%$  reflection. For a sample reflectance of 10%  $R$ , this translates to a fractional error of 3-4%. The combination of sample deterioration and uniformity are expected to produce a fractional error of 1%. It is also expected that the error due to sample holder positioning is approximately the same as in the mid-infrared region, i.e. 0.5% of the value. These sources represent a total reproducibility error

of ~4.5-5.0%. The residual error of -2.3 - 2.8% is assigned to instrument drift. Because of the much longer far-infrared sample collections, this value seems reasonable.

## 5.2 Computational Errors

The major source of error in the practical implementation of the Kramers-Kronig method is the finite range of the measured reflectance data. This truncation error has been investigated with theoretical reflection data.<sup>81,193</sup> In Section 4.1b, we also used simulated data to check the integrity of our Kramers-Kronig program. For a model sample, possessing several resonance peaks in the region 200-2000  $\text{cm}^{-1}$ , an integration range of 10-4000  $\text{cm}^{-1}$  gave imaginary dielectric constants,  $\epsilon''$  accurate to 1% below 1000  $\text{cm}^{-1}$ , and to 2-3% above 1000  $\text{cm}^{-1}$ . The largest relative errors were observed in the regions of rapidly changing slope,  $\partial\epsilon''/\partial\nu$ . Comparison of results obtained with integration ranges of 200-2000  $\text{cm}^{-1}$  and 10-2000  $\text{cm}^{-1}$  showed that neglect of the low frequency data incurred much less error than the high frequency truncation.

Since the predominant infrared absorption by  $\text{Ba}(\text{ClO}_3)_2 \cdot \text{H}_2\text{O}$  occurs below 1000  $\text{cm}^{-1}$ , with the exception of relatively weak hydrate bands at ~1600 and ~3600  $\text{cm}^{-1}$ , it is expected that little error is caused by the high frequency integration limit of 4400  $\text{cm}^{-1}$ . To verify this, the KK-analysis was repeated for the a'-polarized reflectance measurements on the (001) crystal face, including data to 6500  $\text{cm}^{-1}$  (Section 4.2b). The resultant changes in the  $\epsilon'$

and  $\epsilon''$  values were small and random in direction; the average magnitude being of the order of 0.02 units (Table 4.6).

The sensitivity of the derived optical constants to a localized reflectance error and to a small reflectance error over a wide frequency range, were investigated.

A localized reflectance error was observed for one of the  $\text{Ba}(\text{ClO}_3)_2 \cdot \text{H}_2\text{O}$  single crystals, which contained a trace impurity of  $\text{Ba}(\text{BrO}_3)_2 \cdot \text{H}_2\text{O}$  (see Figures 3.4 and 3.5). Figure 5.5 illustrates the measured deviation in the b-polarized reflectance for the pure (File C: SC-BCL·H2O-01) and impure (File A: SC-BCL·H2O-02) samples. The spectral differences are localized in the region  $500\text{--}1000\text{ cm}^{-1}$ , with a maximum absolute error of 0.4 percent reflectance. The associated errors in  $\epsilon''$  are of the largest magnitude in this same frequency region. Values of the KK-derived real and imaginary dielectric constants are compared in Table 5.2. It can be seen that the maximum absolute error in  $\epsilon''$  of 0.6 units occurs at the peak frequency of  $963\text{ cm}^{-1}$  ( $\epsilon'' = 13.2$ ). In the regions  $<500\text{ cm}^{-1}$  and  $>1000\text{ cm}^{-1}$ , the errors in  $\epsilon'$  and  $\epsilon''$  are less than 1% of the value for  $\epsilon'$  and  $\epsilon'' > 1.0$ .

A small reflectance error over a wide frequency range can occur from any of the experimental errors discussed in Sections 5.1 and 5.2. Figure 5.6 illustrates the measured discrepancy between two independent b-polarized reflectance spectra of  $\text{Ba}(\text{ClO}_3)_2 \cdot \text{H}_2\text{O}$  in the region  $1100\text{--}4400\text{ cm}^{-1}$ .

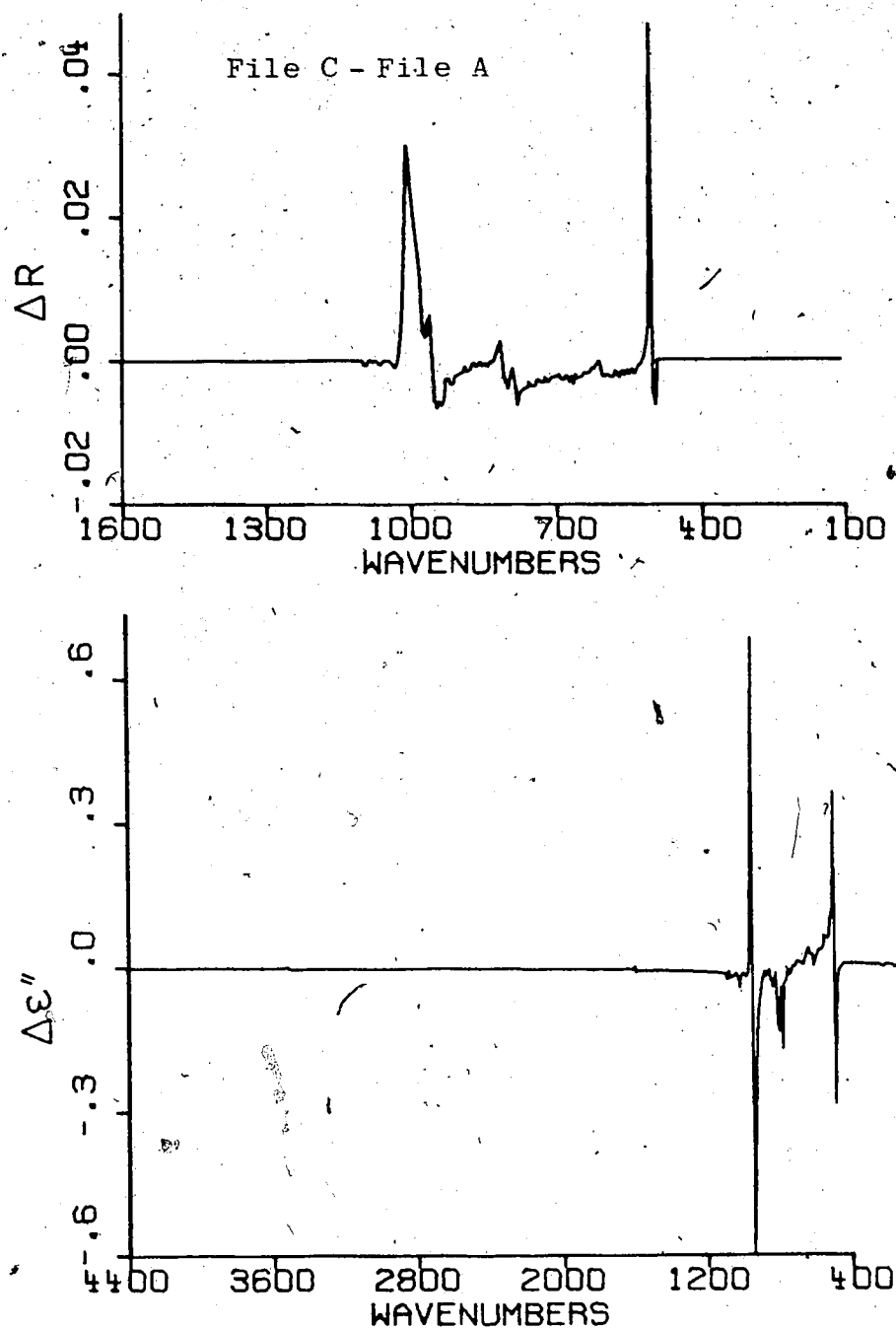


Figure 5.5 Error in KK-derived  $\epsilon''(\nu)$  values associated with a localized error in the measured reflectance.

Data are for b-polarized (001) face of  $\text{Ba}(\text{ClO}_3)_2 \cdot \text{H}_2\text{O}$ .

Table 5.2 Effect of Small Differences in Measured Reflectance Upon KK-Derived Dielectric Constants; Illustrated for b-Polarized Reflectance Data for  $\text{Ba}(\text{ClO}_3)_2 \cdot \text{H}_2\text{O}$

Frequency $\nu(\text{cm}^{-1})$	$\epsilon'(\nu)$			$\epsilon''(\nu)$		
	A*	B*	C*	A*	B*	C*
114.7	-1.280	-1.279	-1.280	3.101	3.093	3.097
120.5	-1.463	-1.466	-1.464	4.928	4.913	4.920
159.1	1.629	1.620	1.624	3.110	3.107	3.108
230.4	1.983	1.971	1.977	2.660	2.658	2.659
400.2	2.856	2.854	2.855	0.249	0.261	0.255
481.2	3.273	3.273	3.281	1.163	1.161	1.152
502.4	5.537	5.571	5.586	2.097	1.694	1.666
606.5	3.749	3.838	3.761	1.191	1.226	1.209
616.1	1.409	1.448	1.415	1.186	1.185	1.185
855.3	3.718	3.711	3.716	0.313	0.315	0.283
953.6	9.650	9.945	10.377	11.567	11.074	10.949
963.3	-6.546	-6.848	-6.850	12.488	12.687	13.172
1109.8	1.596	1.580	1.598	0.058	0.063	0.042
1300.8	2.129	2.103	2.130	0.040	0.028	0.030
1499.4	2.317	2.303	2.318	0.041	0.041	0.033
1605.4	2.457	2.444	2.468	1.498	1.544	1.492
2203.3	2.399	2.387	2.399	0.029	0.026	0.024
3175.2	2.478	2.458	2.478	0.072	0.075	0.069
3753.8	2.412	2.397	2.412	0.035	0.027	0.032

\* Spectrum C assumed correct; Spectrum A contains localized reflectance errors (see Figure 5.5); Spectrum B contains a small reflectance error over a wide frequency range (see Figure 5.6).

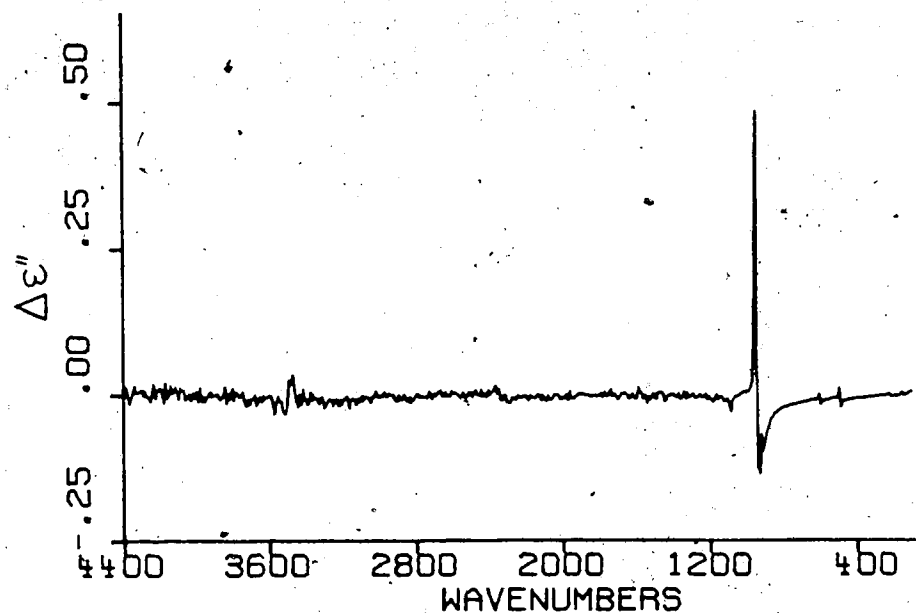
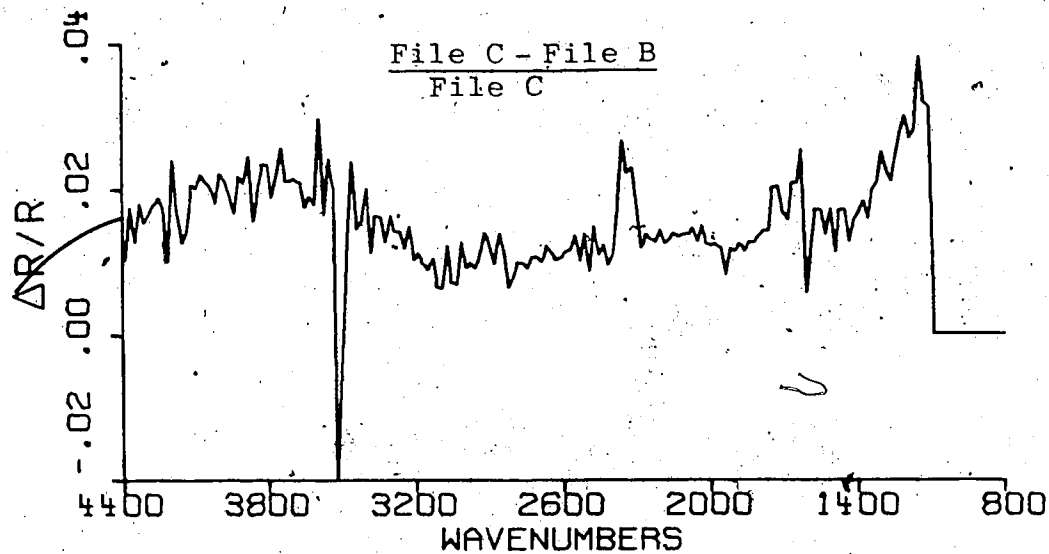


Figure 5.6 Error in KK-derived  $\epsilon''(\nu)$  values associated with an  $\pm 2\%$  error in the measured reflectance over a wide frequency range.

Data are for b-polarized (001) face of  $\text{Ba}(\text{ClO}_3)_2 \cdot \text{H}_2\text{O}$ .

File C is the composite reflectance spectrum for sample -02 (6 averaged spectra, total # scans = 1375), and File B is the corresponding spectrum for sample -01 (5 averaged spectra, total # scans = 1125). Below  $1100\text{ cm}^{-1}$ , the input reflectance data to the Kramers-Kronig program was identical for the two cases. The average fractional difference in the region  $1100\text{--}4400\text{ cm}^{-1}$  is  $\sim 2\%$ . This resulted in a fairly small error in the derived optical constants, except where  $\partial\epsilon'/\partial\nu$  or  $\partial\epsilon''/\partial\nu$  were large (Table 5.2). Below  $900\text{ cm}^{-1}$ , the fractional errors in  $\epsilon'$  and  $\epsilon''$  are  $\sim 1\text{--}2\%$ ; above  $900\text{ cm}^{-1}$ , this error increases to  $\sim 3\text{--}4\%$ . The largest absolute error in  $\epsilon'$  of 0.49 units at  $963\text{ cm}^{-1}$  is only 3.7% of the value.

In conclusion, an experimental reflectance error of  $\sim 2\%$  of the value produces a maximal fractional error in the associated optical constants of  $\sim 4\%$ , and a typical fractional error of  $\sim 2\%$ . According to Nilsson and Munkby's<sup>81</sup> model calculations, the deviation in the optical constants is approximately proportional to the deviation in the reflectance. Therefore, based upon the relative standard deviations observed in the polarized reflectance data for single crystal  $\text{Ba}(\text{ClO}_3)_2 \cdot \text{H}_2\text{O}$ , the average percentage error in the derived optical constants is  $\sim 7\%$  in the far-infrared and  $\sim 3\%$  in the mid-infrared regions.

## CHAPTER VI.

### INTERPRETATION OF OPTICAL SPECTRA FOR $\text{Ba}(\text{ClO}_3)_2 \cdot \text{H}_2\text{O}$ -

#### VIBRATIONAL ASSIGNMENT AND DIPOLE MOMENT

##### DERIVATIVE CALCULATIONS

In this chapter, the infrared reflection spectra of  $\text{Ba}(\text{ClO}_3)_2 \cdot \text{H}_2\text{O}$  are assigned (Section 6.2). The vibrational description is based on a factor group analysis (Section 6.1) and the discussion is limited to specific contributions of this work. Dipole moment derivatives with respect to crystal normal coordinates,  $\partial \mu / \partial Q$ , are calculated from the measured transition strengths. For the internal water modes, the  $\partial \mu / \partial Q$ 's are transformed to bond moment derivatives,  $\partial \mu / \partial r$  and  $\partial \mu / \partial \theta$ , and comparison is made with the corresponding values reported for water vibrations in the vapor, liquid and solid phases (Section 6.3).

#### 6.1 Factor Group Analysis

A necessary first step in the vibrational assignment of  $\text{Ba}(\text{ClO}_3)_2 \cdot \text{H}_2\text{O}$  is to perform a factor group analysis. This procedure is well described by W.G. Fateley *et al.*<sup>194</sup> and is based on the early work of Bhagavantam and Venkatarayudu,<sup>195</sup> and of Hornig<sup>196</sup> and Halford.<sup>197</sup> An underlying premise is that the  $k = 0$  selection rule is valid and, therefore, the only spectroscopically-active crystal vibrations are those in which all the unit cells are in-phase with one another. The smallest unit from which the entire crystal can be generated by translations alone is the primitive

unit cell. Consideration of the symmetry elements contained in this primitive unit cell gives the complete independent set of allowed  $k=0$  vibrational modes, and is termed a factor group analysis. The unit cell group, factor group, and point group of the crystal class are all isomorphic.

The effect of the crystal forces on the spectra of a solid can be readily appreciated from a comparison with the corresponding gas phase spectra. Many of the bands observed for the gas are split into several components in the spectra of the solid. This multiplet splitting, referred to as factor group splitting, originates from two different sources involving interaction of a given molecule or ion in the crystal with its neighbors.

The first of these is a static effect, called site splitting, which may occur when the site occupied by a molecule in the crystal is of lower symmetry than the point group of the free molecule. The site group is the group of symmetry operations which leave the site invariant, and it reflects the static crystal potential at the site in question. Thus a vibrational mode which is degenerate in the free molecule may have its degeneracy reduced under the site symmetry. Site splitting may also occur when one type of molecule occupies two non-equivalent sites in the crystal. Even if the degeneracy of the molecular mode is unaffected, the crystal's static field usually causes a frequency shift relative to the gas-phase value.

The second source of multiplet splitting in a crystal is a dynamic effect termed Davydov splitting. This occurs when there are several equivalent molecules in the unit cell. As these molecules undergo a particular vibrational motion, they may, at any instant, have different phase relationships. These various unit-cell modes resonate at slightly different frequencies and, if the intermolecular forces are sufficiently strong, will appear as distinct peaks in the spectra. Each non-degenerate molecular mode gives  $N$  Davydov components, corresponding to the number of linearly independent combinations of the  $N$  equivalent molecules per unit cell. Since the Davydov components belong to different irreducible representations under the factor group, they appear under different polarizations in the spectra of the single crystal. If, on the other hand, the intermolecular coupling is weak, so that all of the Davydov components are nearly coincident, then only one band will be observed at the common frequency, for all polarizations active under the site symmetry, but with different relative intensities depending on which particular Davydov component is being excited.

Thus, a factor group analysis which is based solely on symmetry considerations, can only predict the nature of the expected multiplet splittings. The magnitude of these splittings is determined by the crystal forces.

In an ionic or molecular crystal, it is useful to classify the vibrations as either intramolecular or inter-

molecular since the covalent forces binding the atoms in a molecule are generally much stronger than the ionic or Van der Waals forces between the molecules. The intramolecular or internal modes involve oscillation of the atoms within a molecule, while the intermolecular or external (lattice) modes involve motion of the molecules with respect to one another. The external modes can be further subdivided into rotational (librational) vibrations and translational vibrations. Three of the translational modes involve simple translation of the entire crystal in the three cartesian directions. These zero wavevector, zero frequency vibrations are termed acoustic modes and are usually excluded from the vibrational analysis. All other crystal vibrations are classified as optic modes. Thus, for a molecular crystal containing  $N$  molecules per primitive unit cell, and  $m$  atoms per molecule, there should be  $3Nm - 3$   $\underline{k} = 0$  optic modes, of which  $N(3m - 6)$  are internal,  $3N$  are rotational, and  $3N - 3$  are translational vibrations. In the case of an ionic crystal containing  $K$  discrete (non-linear) polyatomic units and  $L$  monatomic units, the preceding description of the crystal modes is slightly modified to: the number of  $\underline{k} = 0$  optic modes is

$$\sum_{k=1}^K [N_k(3m_k - 6) + 3N_k + 3N_k] + \sum_{\ell=1}^L 3N_{\ell} - 3.$$

Unfortunately, this clear distinction of the crystal vibrations is not always possible, particularly for the external

modes which can interact to give vibrations of mixed rotational-translational character.

The symmetry classification of the crystal  $k = 0$  modes is performed by a stepwise correlation of the irreducible representation for the isolated ion or molecule to a) its site group and b) the factor group. The optical activity of these unit-cell modes is determined by their symmetry species under the factor group.

For the purposes of a factor group analysis, the ionic crystal  $\text{Ba}(\text{ClO}_3)_2 \cdot \text{H}_2\text{O}$  may be regarded as an ordered arrangement of i) monatomic  $\text{Ba}^{2+}$  ions, ii) polyatomic  $\text{ClO}_3^-$  ions, and iii)  $\text{H}_2\text{O}$  molecules. Since the isolated  $\text{ClO}_3^-$  ion and  $\text{H}_2\text{O}$  molecule frequencies are well-separated, to a first approximation, their vibrations in the crystal can be assumed uncoupled. Table 6.1 describes the symmetry and relative positions of these structural units in the crystallographic unit cell (I2/c). The multiplicity, that is the number of equivalent species of each type in the body-centered cell, is also given. The primitive unit cell, which is used in the derivation of spectral activity, is one-half the size of the body-centered cell, and contains 2 molecules of  $\text{Ba}(\text{ClO}_3)_2 \cdot \text{H}_2\text{O}$ , or 24 atoms. A total of 72  $k = 0$  crystal vibrations is expected, which may be classified as follows:

Table 6.1 Equivalent Sites in  $\text{Ba}(\text{ClO}_3)_2 \cdot \text{H}_2\text{O}$ , Space Group  $C_{2h}^6$  (I2/c)

Group	Symmetry	Multiplicity	Wyckoff Notation
$\text{Ba}^{2+}$	$C_2$	4	(e)
$\text{ClO}_3^-$	$C_1$	8	(f)
$\text{H}_2\text{O}$	$C_2$	4	(e)

Wyckoff positions:

(e)  $0y \frac{1}{4}, \frac{1}{2} \frac{1}{2} -y \frac{1}{4}, \frac{1}{2} \frac{1}{2} +y \frac{3}{4}, 0 \bar{y} \frac{3}{4}$

(f)  $xyz, \bar{x}\bar{y}\bar{z}, \bar{x}y \frac{1}{2} -z, x\bar{y} \frac{1}{2} +z$

$\frac{1}{2} +x \frac{1}{2} +y \frac{1}{2} +z, \frac{1}{2} -x \frac{1}{2} -y \frac{1}{2} -z, \frac{1}{2} -x \frac{1}{2} +y \bar{z}, \frac{1}{2} +x \frac{1}{2} -y z$

Table 6.2 Character Table for Group  $C_{2h}$

$C_{2h}$	E	$C_2$	i	$\sigma_h$	Infrared Activity	Raman Activity
Ag	1	1	1	1	Rz	$\alpha_{xx}, \alpha_{yy}, \alpha_{zz}, \alpha_{yy}$
Bg	1	-1	1	-1	Rx, Ry	$\alpha_{yz}, \alpha_{zx}$
Au	1	1	-1	-1	Tz	
Bu	1	-1	-1	1	Tx, Ty	

Table 6.3 Correlation Table for Group  $C_{2h}$  and its Subgroups

$C_{2h}$	$C_1$	$C_2$	$C_s$	$C_i$
Ag	A	A	A'	Ag
Bg	A	B	A''	Ag
Au	A	A	A'	Au
Bu	A	B	A''	Au

$$\text{ClO}_3^- \text{ ion modes } \left\{ \begin{array}{ll} 4 \times (3 \times 4 - 6) = 24 & \text{internal} \\ 4 \times 3 & = 12 \text{ rotational} \\ 4 \times 3 & = 12 \text{ translational} \end{array} \right.$$

$$\text{H}_2\text{O modes } \left\{ \begin{array}{ll} 2 \times (3 \times 3 - 6) = 6 & \text{internal} \\ 2 \times 3 & = 6 \text{ rotational} \\ 2 \times 3 & = 6 \text{ translational} \end{array} \right.$$

$$\text{Ba}^{2+} \text{ ion modes } \left\{ \begin{array}{ll} 2 \times 3 = 6 & \text{translational} \end{array} \right.$$

It must be emphasized that this clear distinction of the vibrational modes is only valid if they do not interact appreciably. However, if the unperturbed vibrations are similar in frequency and belong to the same symmetry species, they can dynamically couple to give crystal modes of mixed character.

The factor group for  $\text{Ba}(\text{ClO}_3)_2 \cdot \text{H}_2\text{O}$  is  $C_{2h}$ . Its character table and spectral activity are given in Table 6.2. As a consequence of the crystal's centrosymmetry, the infrared-active vibrations are Raman-inactive, and vice versa. The correlation of  $C_{2h}$  with its sub-groups is given in Table 6.3. The site group must necessarily be a subgroup of the factor group and of the point group of the isolated molecule or ion.

In  $\text{Ba}(\text{ClO}_3)_2 \cdot \text{H}_2\text{O}$ , the water molecules are located on sites of  $C_2$  symmetry, which means that the  $C_{2v}$  molecular modes which are symmetric with respect to the  $C_2$  operation, *i.e.*  $A_1$  and  $A_2$ , correlate with the A species, while the  $C_{2v}$  water modes which are antisymmetric with respect to  $C_2$ , *i.e.*  $B_1$  and  $B_2$ , correlate with the B species. This

correlation is depicted schematically in Table 6.4. Under the factor group, the vibrations of the two equivalent water molecules in the unit cell can couple to give *gerade* and *ungerade* components. A factor group analysis thus gives the following representation and activities for the internal and external water modes described in Table 6.4:

$$\Gamma_{\text{internal}}^{\text{H}_2\text{O}} = 2\text{Ag}(\text{R}) + \text{Bg}(\text{R}) + 2\text{Au}(\text{IR}) + \text{Bu}(\text{IR})$$

$$\Gamma_{\text{external}}^{\text{H}_2\text{O}} = 2\text{Ag}(\text{R}) + 4\text{Bg}(\text{R}) + 2\text{Au}(\text{IR}) + 4\text{Bu}(\text{IR})$$

where 'R' denotes Raman-active and 'IR' denotes infrared-active.

A factor group analysis for the  $\text{ClO}_3^-$  ion modes shows that each free-ion degree of freedom yields an Ag, Au, Bg, and Bu vibration under the  $\text{C}_{2h}$  factor group (see Table 6.5). This is a result of the  $\text{C}_1$  site symmetry of the  $\text{ClO}_3^-$  ions in the lattice. A clearer physical picture of this factor group coupling may be gleaned from Figure 6.1, which shows schematically the coupling of the symmetric  $\text{ClO}_3^-$  ion stretching modes ( $\nu_1$ ) to produce unit-cell vibrations of Ag, Bg, Au and Bu symmetry. For simplicity of illustration, the unit cell is based on an orthogonal coordinate system. Since the monoclinic angle,<sup>105</sup>  $\beta$  is  $93.65^\circ$ , this approximation is reasonable. The displacements of the oxygen atoms in the various crystal vibrations are indicated by arrows. It can be seen that when the  $\nu_1$  vi-

Table 6.4 Correlation Table for the Water Molecule and Barium Ion Vibrational Modes of  $\text{Ba}(\text{ClO}_3)_2 \cdot \text{H}_2\text{O}^*$

Mode	Free $\text{H}_2\text{O}$ molecule ( $\text{C}_{2v}$ )	Site ( $\text{C}_2$ )	Unit cell ( $\text{C}_{2h}$ )	$\text{Ba}^{2+}$ ion ( $\text{C}_2$ )
$\nu_1, \nu_2, T_z$	$A_1$	A	Ag	$T_z''$
$R_z$	$A_2$		Au	
$\nu_3, T_x, R_y$	$B_1$	B	Bg	$T_x'', T_y''$
	$B_2$		Bu	

Table 6.5 Correlation Table for Internal and External Vibrational Modes of  $\text{ClO}_3^-$  Ion in  $\text{Ba}(\text{ClO}_3)_2 \cdot \text{H}_2\text{O}^*$

Mode	Free ion ( $C_{3v}$ )	Site ( $C_1$ )	Unit cell ( $C_{2h}$ )
$\nu_1, \nu_2, T_z$	$A_1$	A	$A_g$
$R_z$	$A_2$		$A_u$
$\nu_3, \nu_4, (T_x, T_y)$	E		$B_g$
$(R_x, R_y)$			$B_u$

\*The  $\text{ClO}_3^-$  ion,  $\text{H}_2\text{O}$  molecule and  $\text{Ba}^{2+}$  ion modes are distinguished by no prime, a single prime, and a double prime, respectively. The u modes are infrared active and the g modes are Raman active.

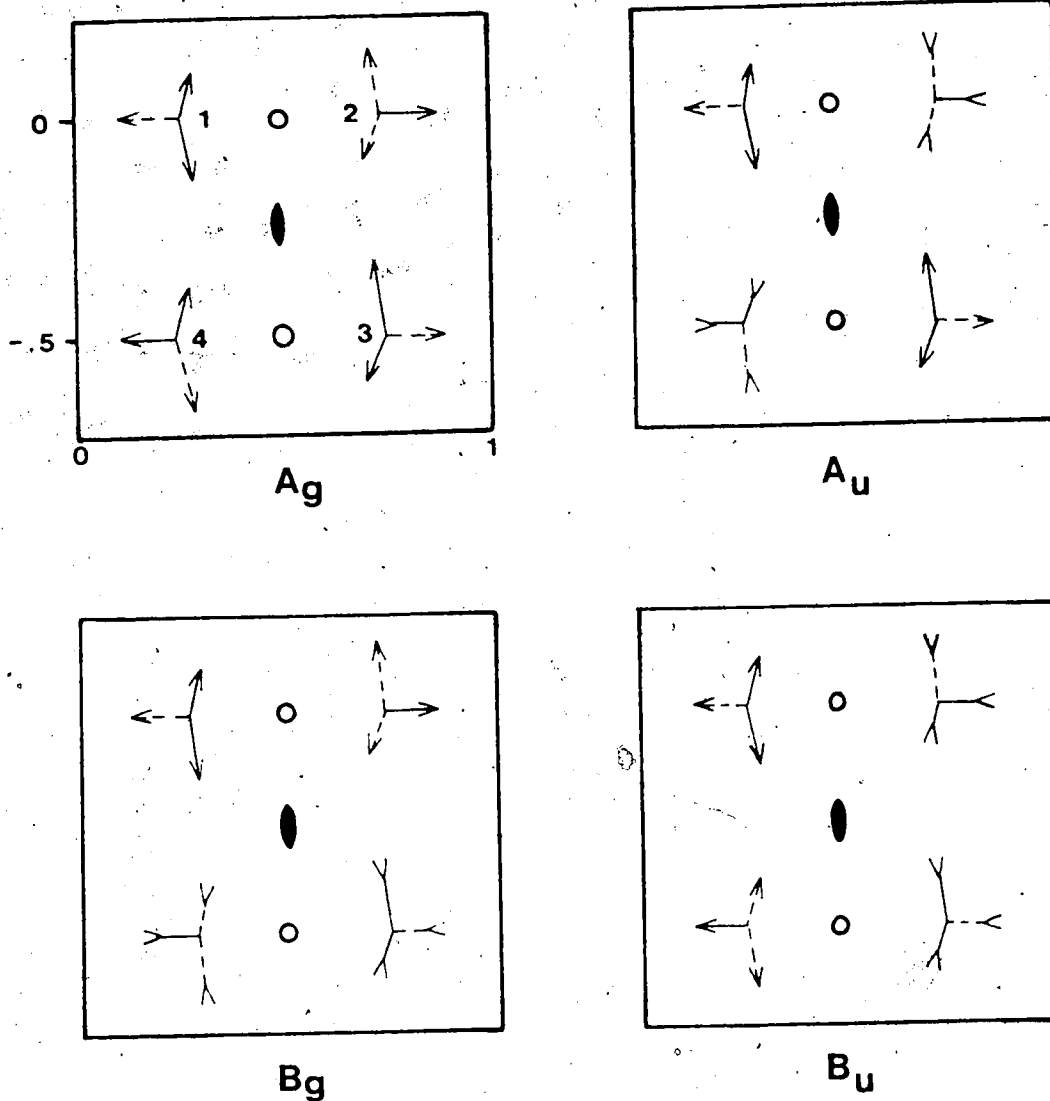


Figure 6.1 Approximate forms of the  $\text{ClO}_3^-$  ion  $v_1$  unit-cell modes in  $\text{Ba}(\text{ClO}_3)_2 \cdot \text{H}_2\text{O}$ . ( $C_{2v}$ )

The directions of the Cl-O bonds, with respect to the plane of the paper, are distinguished by solid or dashed lines. (— down; --- up); O  $\equiv$  inversion center;  $\bullet$   $\equiv$  two-fold axis, parallel to b crystal axes.

brations for ions 1-4 are in-phase, the unit-cell vibration transforms as Ag under the  $C_{2h}$  factor group (Table 6.2). If ions 1 and 2 are out-of-phase and ions 1 and 3 are in-phase, the unit-cell vibration is symmetric with respect to the two-fold rotation, but antisymmetric with respect to the inversion center; this behavior is consistent with Au symmetry (Table 6.2). The Bg and Bu unit-cell modes are derived in an analogous manner. The factor group analysis of the internal and external  $\text{ClO}_3^-$  ion modes gives the representations shown in Table 6.5, which total:

$$\Gamma_{\text{internal}}^{\text{ClO}_3^-} = 6\text{Ag}(\text{R}) + 6\text{Bg}(\text{R}) + 6\text{Au}(\text{IR}) + 6\text{Bu}(\text{IR})$$

$$\Gamma_{\text{external}}^{\text{ClO}_3^-} = 6\text{Ag}(\text{R}) + 6\text{Bg}(\text{R}) + 6\text{Au}(\text{IR}) + 6\text{Bu}(\text{IR}).$$

The  $\text{Ba}^{2+}$  ion, which can only translate off its  $C_2$  site, gives the representation:

$$\Gamma_{\text{external}}^{\text{Ba}^{2+}} = \text{Ag}(\text{R}) + 2\text{Bg}(\text{R}) + \text{Au}(\text{IR}) + 2\text{Bu}(\text{IR}),$$

which is included in Table 6.4.

Three of the 72 factor group fundamentals for  $\text{Ba}(\text{ClO}_3)_2 \cdot \text{H}_2\text{O}$  are acoustic modes; the remaining 69 are optic modes.

The irreducible representation spanned by the acoustic vibrations is readily derived from those of the  $T_x$ ,  $T_y$  and  $T_z$  motions under  $C_{2h}$ , giving:

$$\Gamma_{\text{acoustic}} = A_u + 2B_u.$$

Table 6.6 summarizes the distribution, symmetry classification, and spectral activity for the fundamental modes of  $\text{Ba}(\text{ClO}_3)_2 \cdot \text{H}_2\text{O}$ . Thus, according to the factor group analysis, the 69  $k=0$  optic modes form the representation:

$$\Gamma_{\text{internal}} = 8A_g + 7B_g + 8A_u + 7B_u$$

$$\Gamma_{\text{external}} = 9A_g + 12B_g + 8A_u + 10B_u.$$

## 6.2 Vibrational Assignments

The vibrational assignment of  $\text{Ba}(\text{ClO}_3)_2 \cdot \text{H}_2\text{O}$  is primarily based on the results of the combined Kramers-Kronig/classical dispersion analysis of the reflectance from the (001) crystal face (Section 4.3), and the group theoretical predictions of the factor group analysis (Section 6.1). The detailed assignments have been separated into three parts: i) the  $\text{H}_2\text{O}$  molecule vibrational modes (Section 6.2a), ii) the  $\text{ClO}_3^-$  ion internal modes (Section 6.2b), and iii) the lattice vibrations involving predominantly  $\text{ClO}_3^-$  and  $\text{Ba}^{2+}$  ions (Section 6.2c). Since the majority of these assignments were readily made with reference to previous infrared<sup>130,134</sup> and Raman<sup>130</sup> studies of  $\text{Ba}(\text{ClO}_3)_2 \cdot \text{H}_2\text{O}$ , the discussion has been limited to specific contributions of this work.

One of our original objectives was to compare the optical results for polycrystalline and single crystal  $\text{Ba}(\text{ClO}_3)_2 \cdot \text{H}_2\text{O}$ . This data is summarized in Table 6.7. The

Table 6.6 Irreducible Representation and Spectral Activity  
for  $\text{Ba}(\text{ClO}_3)_2 \cdot \text{H}_2\text{O}$

Vibrational mode	Crystal symmetry $C_{2h}$			
	$A_g$	$B_g$	$A_u$	$B_u$
Translational	5	7	4	5
Acoustic			1	2
Librational	4	5	4	5
Internal	8	7	8	7
Spectral activity	R	R	IR	IR
Infrared polarization			$\underline{E} \parallel b$	$\underline{E} \perp b$

Table 6.7 Comparison of Conductivity Features Observed for  
Polycrystalline  $\text{Ba}(\text{ClO}_3)_2 \cdot \text{H}_2\text{O}$  and the (001)  
Crystal Face

Polycrystalline	Single Crystal		Assignment
	Au	Bu	
3586		3584	$\nu_3'(\text{H}_2\text{O})$
3518	3514		$\nu_1'(\text{H}_2\text{O})$
1607	1606		$\nu_2'(\text{H}_2\text{O})$
1020(sh)			o/c (621+402)*
995(sh)			o/c (500+503)
959	959	963	$\nu_3(\text{ClO}_3^-)$
	940		o/c (478+481)
	933		$\nu_3(\text{ClO}_3^-)$
921	925		
		912	$\nu_1(\text{ClO}_3^-)$
		909	
617		616	$\nu_2(\text{ClO}_3^-)$
614	612		$\nu_2(\text{ClO}_3^-)$
507(sh)	507		$\nu_4(\text{ClO}_3^-)$
503		502	$\nu_4(\text{ClO}_3^-)$
		493	$\nu_4(\text{ClO}_3^-)$
490		487	o/c
481(sh)	481		$\nu_4(\text{ClO}_3^-)$
462(sh)			o/c (232+232)
458			$\nu_R'(\text{H}_2\text{O})$
451			o/c (224+232)
446			o/c (621-174)
436			o/c (232+209)
408			o/c (621-209)
		404	$\nu_R'(\text{H}_2\text{O})$
402	388		$\nu_R'(\text{H}_2\text{O})$

Table 6.7 continued

Polycrystalline	Single Crystal		Assignment
	Au	Bu	
232	230		$\nu_T^i(\text{H}_2\text{O})$
220(sh)			o/c (110+110) <sup>f</sup>
214(sh)			o/c (106+110)
209		210	$\nu_T^i(\text{H}_2\text{O})$
200(sh)			o/c (110+92)
178(sh)			o/c (70+110)
174(sh)		173	
164			
160(sh)	160		
150		151	
142			
132	133	133, 131, 129	$\nu_T(\text{cryst})^+$
122	120		$\nu_R(\text{ClO}_3^-)$
		114	
110(sh)		109	
105			
92			
83(sh)			

Frequencies in  $\text{cm}^{-1}$ . Estimated accuracy  $\pm 1 \text{ cm}^{-1}$  for peak frequencies.

\* Values in parentheses are infrared and/or Raman<sup>130</sup> frequencies, whose combination is consistent with observed frequency.

frequencies for the polycrystalline sample correspond to the peak maxima in the KK-derived conductivity spectrum,  $\nu\epsilon''$  (see Figure 4.7 and Appendix D for  $\epsilon''(\nu)$ ), whereas the single crystal frequencies were obtained from the classical dispersion fit to the reflectance and imaginary dielectric constant spectra for the (001) crystal face (see Figures 4.19 and 4.20 and Tables 4.9 and 4.10). This comparison is valid since, for bands as sharp as these, the peak frequencies are coincident in the  $\epsilon''$  and  $\nu\epsilon''$  spectra (Section 1.1d). Table 6.7 clearly shows that the majority of the polycrystalline modes appear to high frequency of the corresponding single crystal modes. This is due to the fact that a pure transverse optic mode is only observed when the incident wave vector is perpendicular to the direction of the crystal transition moment, *i.e.* one of the indicatrix axes. For reflectance measurements on the (001) crystal face of  $\text{Ba}(\text{ClO}_3)_2 \cdot \text{H}_2\text{O}$ , this condition is always satisfied for b-polarization, but only satisfied for a'-polarization, when this direction coincides with one of the indicatrix axes in the ac plane. In the case of unpolarized reflectance measurements on polycrystalline  $\text{Ba}(\text{ClO}_3)_2 \cdot \text{H}_2\text{O}$ , the indicatrix axes are oriented at arbitrary angles to the incident wave vector, which permits simultaneous excitation of the transverse optic (TO) and longitudinal optic (LO) modes. Since  $\nu_{\text{LO}} > \nu_{\text{TO}}$  at  $\underline{k} \approx 0$ , the observed frequency will increase with increasing contribution from the longitudinal optic component.

Based on the preceding considerations, the polycrystalline and single crystal results in Table 6.7 are in very good agreement, with a few notable exceptions. For example, the polycrystalline spectrum exhibited only a single broad peak at  $921\text{ cm}^{-1}$  ( $\text{FWHM} = 19\text{ cm}^{-1}$ ), whereas in the single crystal spectra, five distinct features were assigned to this region at 909, 912, 925, 933 and  $940\text{ cm}^{-1}$ . However, each of these fitted peaks has a FWHM ranging from  $7\text{--}10\text{ cm}^{-1}$ , so their superposition should give a broad continuum centered at  $\sim 920\text{ cm}^{-1}$ , as observed in the polycrystalline spectrum. Further evidence of unresolved, overlapping bands in the polycrystalline spectrum is seen in Table 6.7, where the broad peak at  $959\text{ cm}^{-1}$  ( $\text{FWHM} \approx 22\text{ cm}^{-1}$ ) corresponds to two features at  $959\text{ cm}^{-1}$  ( $\text{FWHM} = 12.1\text{ cm}^{-1}$ ) and  $963\text{ cm}^{-1}$  ( $\text{FWHM} = 6\text{ cm}^{-1}$ ) in the single crystal spectra. Similarly, the very weak Au mode at  $388\text{ cm}^{-1}$  is totally obscured in the polycrystalline spectrum by the presence of a very intense and broad band at  $404\text{ cm}^{-1}$ ; its only influence is perhaps seen in the slight frequency shift to lower wave-number at  $402\text{ cm}^{-1}$ .

Broad weak bands which were observed in the polycrystalline spectra, but only very weakly or not at all in the single crystal spectra, were assigned in Table 6.7 to 2-phonon overtone or combination (o/c) modes. The proposed transitions are not intended as definitive, but merely as possible explanations of the observed frequencies.

Some features apparent in the polycrystalline spectrum, but not in the polarized spectra of the (001) crystal face, could not be reasonably attributed to overtone or combination modes, unless a large anharmonicity was assumed. These modes appear at 458, 164, 142, 105 and 92  $\text{cm}^{-1}$ . Since single crystal data were only recorded to  $\sim 110 \text{ cm}^{-1}$ , the 105 and 92  $\text{cm}^{-1}$  bands were obviously not measured. It was of particular interest to determine if the 458  $\text{cm}^{-1}$  band corresponded to one of the water librations. As shown in Table 6.4, the water librational modes span the irreducible representation:  $A_g + 2B_g + A_u + 2B_u$ . However, in the infrared spectra of the (001) face, only one  $A_u$  and one  $B_u$  mode, at 388 and 404  $\text{cm}^{-1}$ , respectively, could be ascribed to these water vibrations (see Section 6.2a). Librational water modes can be characterized by their deuteration shift,  $\nu_{\text{H}_2\text{O}}/\nu_{\text{D}_2\text{O}}$  of  $\sim \sqrt{2}$ . Thus, if the 458  $\text{cm}^{-1}$  band is active under c-polarization, and shifts to  $\sim 320 \text{ cm}^{-1}$ , upon deuterium substitution, this would provide strong evidence that it is the missing  $B_u$  water rotation. This was one of the questions addressed by a polarized mid-infrared reflectance study of the natural (110) crystal faces of  $\text{Ba}(\text{ClO}_3)_2 \cdot \text{H}_2\text{O}$  and  $\text{Ba}(\text{ClO}_3)_2 \cdot \text{D}_2\text{O}$ .

However, the primary objective of this supplementary study was to determine if any of the bands observed in the region of the internal  $\text{ClO}_3^-$  ion modes ( $\sim 450\text{--}1100 \text{ cm}^{-1}$ ) were overtone/combinations involving water rotational motion. The factor group analysis (Section 6.1) predicts

6Au and 6Bu infrared-active  $\text{ClO}_3^-$  ion internal modes, whereas we noted 7Au and 7Bu features in this region. A significant frequency shift upon deuteration should identify which bands are not due to  $\text{ClO}_3^-$  ion fundamentals, but arise from water combinations.

In order to strictly compare the hydrate and deuterate spectra, they must be collected for the same crystal face and with the same experimental geometry. To provide rapid, qualitative data, the natural, unpolished (110) crystal faces were used. Figure 3.2 shows that the longest edge of this (110) face is parallel to the c-axis. If the incident electric vector is oriented in this direction, it will excite Bu modes which have a significant component along c. This experiment should indicate whether the  $458\text{ cm}^{-1}$  band in the polycrystalline spectrum is c-polarized. On the other hand, if the incident electric vector is oriented perpendicular to this direction, but in the (110) plane, it will excite ab-polarized crystal modes, i.e. Au modes polarized along b and Bu modes polarized predominantly along a. This should reveal all modes observed in the spectra of the polarized (001) crystal face.

Table 6.8 lists the peak frequencies and reflectance values for the c- and ab-polarized spectra of the (110) crystal faces of  $\text{Ba}(\text{ClO}_3)_2 \cdot \text{H}_2\text{O}$  and  $\text{Ba}(\text{ClO}_3)_2 \cdot \text{D}_2\text{O}$ . The frequency accuracy was estimated from the breadth of the reflectance bands. The reflectance values, although not definitive, give a qualitative indication of the relative

Table 6.8 Comparison of Peak Reflectance Values for c- and ab- Polarized Spectra of the (110) Face of  $\text{Ba}(\text{ClO}_3)_2 \cdot \text{H}_2\text{O}$  and  $\text{Ba}(\text{ClO}_3)_2 \cdot \text{D}_2\text{O}$

$\underline{E} \parallel c$			
$\text{Ba}(\text{ClO}_3)_2 \cdot \text{H}_2\text{O}$		$\text{Ba}(\text{ClO}_3)_2 \cdot \text{D}_2\text{O}$	
$\nu_{\text{max}} (\text{cm}^{-1})$	$R_{\text{max}}$	$\nu_{\text{max}} (\text{cm}^{-1})$	$R_{\text{max}}$
457(3)	0.063		
477, sh	0.073	467, sh	0.065
489(2)	0.118	480(2)	0.137
505(1)	0.181	504(1)	0.185
620(2)	0.060	619(2)	0.095
951(3)	0.428	947(3)	0.368
980(3)	0.486	980(3)	0.467
997, sh	0.442	993, sh	0.442
1013, sh	0.413	1012, sh	0.397
3376(4)	0.046	2663(3)	0.034
$\underline{E} \parallel ab$			
480(2)	0.112	470, sh	0.077
489(2)	0.116	480(2)	0.139
493(2)	0.111		
503(1)	0.158	504(1)	0.110
510(1)	0.116	510(1)	0.163
613(2)	0.150	613(2)	0.106
620(1)	0.131	620(1)	0.094
923(2)	0.586	921(2)	0.482
929, sh	0.557	929, sh	0.433
975(3)	0.528	973(3)	0.451
1007(2)	0.181	1005(2)	0.145
1604(2)	0.058	1183(2)	0.034
3514(4)	0.066	2571(2)	0.043
3577(5)	0.052	2612(3)	0.035
		2666(2)	0.045

Estimated frequency accuracy is given in parentheses.

intensity of the features. It can be seen that the peak at  $457\text{ cm}^{-1}$  in the c-polarized spectrum of the hydrate is absent in the corresponding spectrum of the deuterate. This data was not recorded below  $400\text{ cm}^{-1}$ , so it is not known whether this band shifts to  $\sim 320\text{ cm}^{-1}$ . This information was however available from previous ac-polarized transmission measurements<sup>130</sup> on single crystal  $\text{Ba}(\text{ClO}_3)_2 \cdot \text{H}_2\text{O}$ , which showed a band at  $454\text{ cm}^{-1}$  shifting to  $360\text{ cm}^{-1}$  upon deuterium substitution. The evidence strongly suggests that the reflectance band at  $457\text{ cm}^{-1}$  is c-polarized and corresponds to a  $\text{H}_2\text{O}$  rotational mode. Since the data for the (110) crystal face was not Kramers-Kronig transformed, the associated resonance frequency can only be reasonably obtained from the conductivity peak maximum in the polycrystalline spectrum, which occurs at  $458\text{ cm}^{-1}$ .

The reflectance peak frequencies for the (110) face of the hydrate and deuterate crystals are compared with our previous polarized-reflectance peak frequencies for the (001) crystal face of  $\text{Ba}(\text{ClO}_3)_2 \cdot \text{H}_2\text{O}$ , in Table 6.9. As expected, the features in the E(ab) spectrum comprise the sum of the bands observed in the E(b) and E(a) spectra, with the exception of the  $1007\text{ cm}^{-1}$  band in the E(ab) spectrum, which has no counterpart in the E(b) or E(a) spectra. The broad band at  $975\text{ cm}^{-1}$  in the E(ab) spectrum can be rationalized as the unresolved intensity-overlap of the peaks at  $971\text{ cm}^{-1}$ , E(a) and  $980\text{ cm}^{-1}$ , E(b).

Table 6.9 Comparison of Observed Frequencies for  
 $\text{Ba}(\text{ClO}_3)_2 \cdot \text{H}_2\text{O}$  and  $\text{Ba}(\text{ClO}_3)_2 \cdot \text{D}_2\text{O}$  Reflectance  
 Maxima

$\text{Ba}(\text{ClO}_3)_2 \cdot \text{H}_2\text{O}$				$\text{Ba}(\text{ClO}_3)_2 \cdot \text{D}_2\text{O}$	
(001) Face		(110) Face		(110) Face	
E(b)*	E(a)	E(c)	E(ab)	E(c)	E(ab)
		457			
479		477(sh)	480	467(sh)	470(sh)
	492	489	493, 489	480	480
	503	505	503	504	504
509			510		510
609			613		613
	618	620	620	619	620
	922		923		922
931			929(sh)		929(sh)
		951		947	
	971		975		973
980		980		980	
		997(sh)		993(sh)	
			1007		1005
		1013(sh)		1013	
1604			1604		1183
3510			3514		2571
					2612
	3572	3576	3577	2663	2666

Frequencies in  $\text{cm}^{-1}$  units.

\*The electric vector is polarized in the crystal axis direction given in parentheses.

It is obvious from Table 6.9 that none of the reflectance features in the region  $450\text{--}1100\text{ cm}^{-1}$  shift significantly in going from the hydrate to the deuterate crystal. Thus none of the extra Au or Bu species modes can be reasonably accounted for as combination/overtone of water rotational modes. In most cases, the frequency shift is within the estimated experimental uncertainty. However, the bands at  $477$  and  $489\text{ cm}^{-1}$  in the e-polarized spectrum of the hydrate which shift to  $467$  and  $480\text{ cm}^{-1}$  in the spectrum of the deuterate, appear to involve a small amount of coupling with the water modes. The same can be said for the bands at  $480$  and  $491\text{ cm}^{-1}$  in the ab-polarized spectra of the hydrate which shift to  $470$  and  $480\text{ cm}^{-1}$  in the corresponding deuterate spectrum. To further complicate the vibrational assignment of the  $\text{ClO}_3^-$  ion internal modes, additional Bu vibrations were observed in the c-polarized (110) reflectance spectra at  $951$ ,  $980$ ,  $997$  and  $1013\text{ cm}^{-1}$ . This result will be discussed in Section 6.2b.

The approximate orientation of the transition moment for the Bu crystal modes was supplied by a comparison of the a'-polarized (001) and c-polarized (110) reflectance spectra (Table 6.9). Recall that for a monoclinic crystal, only the indicatrix axis parallel to b is fixed by symmetry; the remaining two axes lie in the ac plane, but their position is frequency-dependent. Since the bands at  $490$ ,  $504$ ,  $619$ , and  $3574\text{ cm}^{-1}$  were observed under both a'- and c-polarization, their transition moments must lie at an

intermediate position between the a- and c-axes. On the other hand, bands at 922 and 971  $\text{cm}^{-1}$ , only observed under a'-polarization and bands at 457, 477, 951, 980, 997, and 1013  $\text{cm}^{-1}$ , only observed under c-polarization, must have their transition moments primarily aligned along the a- and c-axes, respectively.

The detailed assignment of the crystal vibrations in  $\text{Ba}(\text{ClO}_3)_2 \cdot \text{H}_2\text{O}$  will now be discussed with reference to the factor group analysis.

#### 6.2a Vibrations of Water Molecules

In  $\text{Ba}(\text{ClO}_3)_2 \cdot \text{H}_2\text{O}$ , there are two equivalent water molecules in the primitive unit cell located on sites of  $C_2$  symmetry. The factor group analysis predicts three infrared-active internal water modes of species  $A_u(\nu_1)$ ,  $A_u(\nu_2)$ , and  $B_u(\nu_3)$ . The polarized conductivity data for the (001) crystal face (Table 6.7), clearly show  $A_u$  (b-polarized) modes at 3514 and 1606  $\text{cm}^{-1}$  and a  $B_u$  (a'-polarized) mode at 3584  $\text{cm}^{-1}$ . These frequencies and symmetry species are in excellent agreement with the polarized infrared transmission measurements of Bertie *et al.*<sup>130</sup> on single crystal  $\text{Ba}(\text{ClO}_3)_2 \cdot \text{H}_2\text{O}$  at 298°K; they reported the symmetric OH stretch and bend at 3516 and 1609  $\text{cm}^{-1}$ , respectively, and the antisymmetric OH stretch at 3584  $\text{cm}^{-1}$ . Our KK-derived conductivity data confirm these earlier assignments. The small frequency discrepancies are undoubtedly due to reflection effects distorting the transmission bands.

The librational modes of the water molecules span the irreducible representation  $A_u + A_g + 2B_u + 2B_g$  under the  $C_{2h}$  factor group and, to a first approximation, can be described as vibrations about the principal inertial axes. With reference to Figure 1.8, the in-plane rock ( $R_x$ ) and the out-of-plane wag ( $R_y$ ) and twist ( $R_z$ ) transform as  $B_u$ ,  $B_u$ , and  $A_u$ , respectively. As previously noted in the introductory chapter (see Table 1.6), considerable controversy has surrounded the assignment of the librational modes in  $Ba(ClO_3)_2 \cdot H_2O$ . The ordering of these frequencies or their relative intensities cannot be easily predicted without a detailed knowledge of the force field about the water molecule.

In crystal hydrates, it is generally expected that the rock appears to high frequency of the twist or wag.<sup>198</sup> This is rationalized by the greater interaction of the water molecules with atoms in the molecular H-O-H plane than with atoms out of this plane. For  $Ba(ClO_3)_2 \cdot H_2O$ , this empirical prediction was confirmed by the single crystal inelastic neutron scattering experiment of Thaper *et al.*<sup>115</sup> However, their reported frequencies of  $477 \text{ cm}^{-1}$  (rock) and 457 and  $395 \text{ cm}^{-1}$  (twist and wag) cannot be strictly compared with the values obtained from related infrared and Raman studies, since different selection rules apply in the two cases: Optical measurements give  $k = 0$  values which are determined by the symmetry selection rules of the factor group, whereas neutron measurements probe all values of  $k$  in the first

Brillouin zone.<sup>199</sup>

On the basis of deuteration shifts  $\nu_{\text{H}_2\text{O}}/\nu_{\text{D}_2\text{O}}$  of 1.3-1.4, Bertie *et al.*<sup>130</sup> assigned transmission peaks at 454 and 395  $\text{cm}^{-1}$  to the water librations. The 454  $\text{cm}^{-1}$  band was only observed under ac-polarization, and the 395  $\text{cm}^{-1}$  band appeared under both ac- and b-polarization. They stated that their polarization data was confused below 400  $\text{cm}^{-1}$ , so the polarization of the 395  $\text{cm}^{-1}$  band was uncertain. Assignment of these librations was assisted by the earlier literature; in particular, the dmr study of  $\text{Ba}(\text{ClO}_3)_2 \cdot \text{D}_2\text{O}$  by Chiba.<sup>110</sup> From the temperature dependence of the deuteron quadrupole coupling, Chiba calculated the rock to high frequency of the twist and wag, which are nearly degenerate. Thus, Bertie *et al.*<sup>130</sup> assigned the Bu mode at 454  $\text{cm}^{-1}$  to the rock and the band at 395  $\text{cm}^{-1}$ , of indeterminate polarization, to the degenerate pair of twist and wag.

In 1978, Eriksson and Lindgren<sup>134</sup> reassigned the water librations to 467  $\text{cm}^{-1}$  (rock), 457  $\text{cm}^{-1}$  (twist), and 396  $\text{cm}^{-1}$  (wag), on the basis of infrared transmission measurements on polycrystalline  $\text{Ba}(\text{ClO}_3)_2 \cdot \text{H}_2\text{O}$  at 100°K. Their corresponding room-temperature frequencies were 451 and 390  $\text{cm}^{-1}$ . Since they did not determine the symmetry species of these vibrations, their main justification for assigning the band at 457  $\text{cm}^{-1}$  to the twist was its low observed intensity. Since the twisting mode involves no change in the permanent dipole moment, it is expected to

absorb much more weakly than the rocking and wagging modes, for which the permanent dipole moment oscillates. Eriksson *et al.*<sup>135</sup> also performed a normal coordinate analysis of the nine infrared-active water modes in  $\text{Ba}(\text{ClO}_3)_2 \cdot \text{H}_2\text{O}$ , and found reasonable agreement between their calculated and observed frequencies. It was noted that the librational frequencies exhibited the largest relative error of  $\sim 2.5\%$ , compared with  $\sim 0.5\%$  for the other modes.

The results of our polarized infrared reflectance measurements support, however, the earlier assignments of Bertie *et al.*<sup>130</sup> The strong and broad absorption they reported at  $395 \text{ cm}^{-1}$  has now been resolved into an Au mode at  $388 \text{ cm}^{-1}$  and a Bu (a'-polarized) mode at  $404 \text{ cm}^{-1}$ . This strongly suggests that the  $388 \text{ cm}^{-1}$  band is due to the twist and the  $404 \text{ cm}^{-1}$  band arises from the wag. The very low intensity of the  $388 \text{ cm}^{-1}$  band is consistent with this assignment. The c-polarized band at  $458 \text{ cm}^{-1}$ , observed for the (110) crystal face and for the polycrystalline sample (Tables 6.7 and 6.9), is assigned to the Bu rocking mode. Its slight deviation from Bertie's *et al.* reported value of  $454 \text{ cm}^{-1}$ , can be explained by the fact that our observed resonance frequency includes a contribution from the associated longitudinal optic mode.

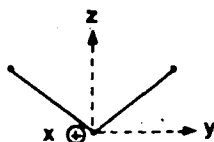
Further evidence supporting these librational assignments can be found in a model set of normal coordinate calculations by Eriksson and Lindgren<sup>200</sup> for tetrahedrally- and trigonally-coordinated water molecules. They considered

only one water molecule and assumed central forces between the water molecule and its three or four nearest-neighbor atoms; the interaction with more distant atoms was assumed to be much weaker. The results of these calculations should therefore be of general applicability, if the preceding limitations are valid. It is noteworthy that Eriksson and Lindgren<sup>200</sup> predicted that, in a tetrahedral environment, the rock should appear to low frequency of the twist and wag, which is contrary to the usual expectation.<sup>198</sup>

Figure 1.7 shows that the water molecules in  $\text{Ba}(\text{ClO}_3)_2 \cdot \text{H}_2\text{O}$  reside in a nearly trigonal planar environment. The  $\text{Ba}^{2+}$  ion is situated on the water molecule's two-fold rotation axis ( $\text{Ba} \cdots \text{O}_w = 2.60 \text{ \AA}$ ), and the hydrogen atoms form weak bonds with the nearest-neighbor oxygen atoms O(2) of the  $\text{ClO}_3^-$  ion ( $\text{O}_w \cdots \text{O}(2) = 2.891 \pm 0.005 \text{ \AA}$ ).<sup>105</sup> The water molecule and its immediate environment in the (010) plane are shown in Figure 6.2. Intermolecular coupling between the two water molecules in the primitive unit cell is expected to be weak since the distance of closest approach<sup>105</sup> is  $4.73 \text{ \AA}$ . Thus, the conditions of Eriksson and Lindgren's<sup>200</sup> calculations are well-satisfied. Table 6.10 gives their predicted frequencies and polarization behavior for a representative trigonally-coordinated water molecule on a site of  $C_{2v}$  symmetry, and compares them with our observed values for  $\text{Ba}(\text{ClO}_3)_2 \cdot \text{H}_2\text{O}$ . Because of the manner in which Eriksson and Lindgren defined their force field, their results do not distinguish between the cases of  $C_{2v}$ ,  $C_2$ , and

Table 6.10 Comparison of Observed Frequencies and Polarization of Water Vibrational Modes in  $\text{Ba}(\text{ClO}_3)_2 \cdot \text{H}_2\text{O}$  with those Predicted for a Water Molecule in a Trigonal Environment

Coordinate system:



+ coming out of page  
- going into page

<u>Observed</u>	<u>Predicted*</u>		
<u>Frequency</u> <u>(Symmetry)<sup>†</sup></u>	<u>Frequency</u> <u>(Symmetry)</u>	<u>Approximate</u> <u>Normal Mode<sup>‡</sup></u>	<u>Description</u>
	103( $B_2$ )		( $T_x$ )
210(Bu)	242( $B_1$ )		( $T_y$ )
230(Au)	305( $A_1$ )		( $T_z$ )
404(Bu)	412( $B_2$ )		wag( $R_y$ )
388(Au)	412( $A_2$ )		twist( $R_z$ )
458(Bu)	526( $B_1$ )		rock( $R_x$ )
1606(Au)	1669( $A_1$ )		bend( $\nu_2$ )
3514(Au)	3515( $A_1$ )		symmetric stretch( $\nu_1$ )
3584(Bu)	3564( $B_1$ )		asymmetric stretch( $\nu_3$ )

\*Reference 200. Site symmetry is  $C_{2v}$ .

<sup>†</sup>Site symmetry is  $C_2$ .

<sup>‡</sup>Only one water molecule in the unit cell is shown. For the Au and Bu unit-cell modes, the atom displacements in the second water molecule are opposite in sense to those of the first water molecule.

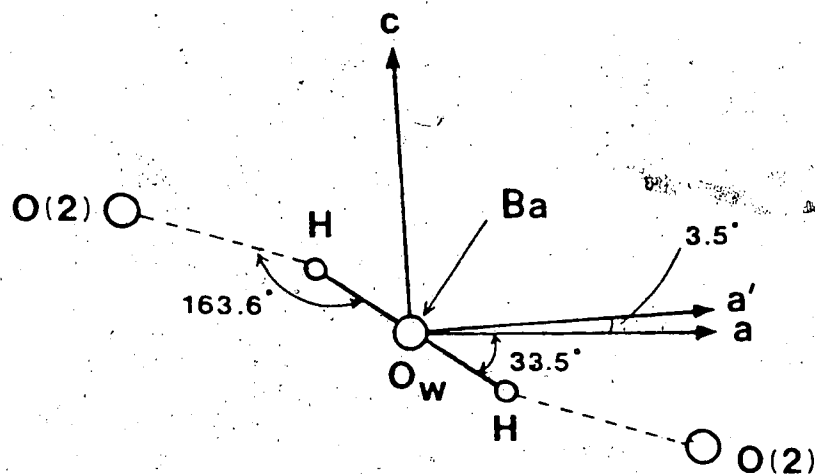


Figure 6.2 Trigonal environment of  $\text{H}_2\text{O}$  molecules in  $\text{Ba}(\text{ClO}_3)_2 \cdot \text{H}_2\text{O}$ .

The projection on the  $(010)$  plane is shown. The  $\text{O}_w\text{-O}(2)$  vector is directed into the page.

Table 6.11 Intensity Ratios for  $a'$ - and  $c$ - Polarized Components of Water Rocking and Wagging Vibrations, Calculated Under Oriented Gas Model

Mode	Direction of $\partial\mu/\partial Q$	Direction cosines		$\frac{I_{a'}}{I_c}$
		$a'$ -axis	$c$ -axis	
$\nu_{\text{rock}}$	along H-H	0.80	0.60	1.8
$\nu_{\text{wag}}$	$\perp$ to H-O-H	0.60	0.80	0.6

$C_s(\sigma_{xz})$  site symmetry. Thus, their  $A_1$  and  $A_2$  modes should correspond with our  $A_u$  modes, and their  $B_1$  and  $B_2$  modes with our  $B_u$  modes. The approximate motion of one of the water molecules in the unit cell is also shown schematically in Table 6.10, assuming negligible vibrational coupling.

A significant result of Eriksson and Lindgren's model calculations is that the rock is predicted to high frequency of the twist and wag, which are degenerate. This is consistent with our findings and those of Bertie *et al.*<sup>130</sup> and Chiba,<sup>110</sup> but inconsistent with Eriksson and Lindgren's<sup>134</sup> own water librational assignments for  $Ba(ClO_3)_2 \cdot H_2O$ ; no comment was made regarding this apparent contradiction. In conclusion, the majority of the available data on  $Ba(ClO_3)_2 \cdot H_2O$  supports the assignment of the rock, wag, and twist to frequencies at 454, 404, and  $388\text{ cm}^{-1}$ , respectively.

Our polarized reflection study indicates, however, that the rocking and wagging motions may be mixed in the two  $B_u$  rotational vibrations. This dynamical coupling can occur because these water modes have the same symmetry under the  $C_{2h}$  factor group, and are close in frequency. Evidence for this mixing can be found in the observed polarization behavior of these modes, according to the following argument.

In the absence of mixing, the oriented gas model<sup>201</sup> should give a reasonable description of the relative intensities and direction of polarization for the wagging and

rocking modes. This model predicts the transition moment for the rock along the H-H line, and that for the wag, perpendicular to the H-O-H plane. Table 6.11 gives the cosine of the angle between these molecular transition moment vectors and the  $a'$ - and  $c$ -axes, which are referred to as direction cosines. The relative intensities of the  $a'$ - and  $c$ -polarized components of these vibrations are given by the ratio of the squares of the associated direction cosines. Although  $\text{Ba}(\text{ClO}_3)_2 \cdot \text{H}_2\text{O}$  has two molecules per unit cell, their individual transition moments are related by a simple permutation of sign, so the above procedure is valid.

It can be seen that the rock should display maximum intensity along  $a'$ , while the wag should absorb most strongly along  $c$ . This is inconsistent with our reflectance spectra for these modes. The rock only appeared under  $c$ -polarization, and the wag only under  $a'$ -polarization. These findings suggest that these crystal vibrations are not pure wagging or rocking motions, but are mutually orthogonal linear combinations of both motions. Figure 6.2 shows that hydrogen bonding to the chlorate ion oxygen O(2) can impart a component of rock or wag during the wagging and rocking vibrations, respectively.

The translational vibrations of the water molecules in  $\text{Ba}(\text{ClO}_3)_2 \cdot \text{H}_2\text{O}$  form the representation:  $\text{Ag} + \text{Au} + 2\text{Bg} + 2\text{Bu}$  (Table 6.4). To a first approximation, these translations can be described as motions along the principal inertial axes. The infrared-active translation along the 2-fold

axis,  $T_z$ , transforms as  $A_u$ , and the infrared-active translations perpendicular to the 2-fold,  $T_x$  and  $T_y$ , transform as  $B_u$ . However, it should be noted that these vibrations can mix with the rotational and translational motions of the  $\text{ClO}_3^-$  ions, since they occur in the same frequency region.

The water translational modes in crystal hydrates are characterized by a deuterium shift of -1.04. On this basis, Bertie *et al.*<sup>130</sup> assigned bands at 234 and 207  $\text{cm}^{-1}$ , in the infrared transmission spectra of single crystal  $\text{Ba}(\text{ClO}_3)_2 \cdot \text{H}_2\text{O}$  at 300°K, to water translations, but were unable to determine their corresponding polarization behaviour. Eriksson and Lindgren<sup>134</sup> also used the isotope effect to assign transmission bands at 235, 208 and 75  $\text{cm}^{-1}$  in polycrystalline  $\text{Ba}(\text{ClO}_3)_2 \cdot \text{H}_2\text{O}$  at 298°K to water translations. These previously reported values compare well with our observed conductivity peaks for the (001) crystal face, at 230  $\text{cm}^{-1}$  (b-polarized) and 210  $\text{cm}^{-1}$  (a'-polarized). In order to assign these modes to specific water translations, reference was again made to the model calculations of Eriksson and Lindgren,<sup>200</sup> which are summarized in Table 6.10. It can be seen that the  $T_z$  mode is predicted to be the highest frequency translation, that the in-plane  $T_y$  mode should appear at a similar, but lower frequency, and that the out-of-plane  $T_x$  mode, which in the first approximation involves no change in nearest neighbor distances, should appear at a much lower frequency. The absolute fre-

quencies calculated by Eriksson and Lindgren<sup>200</sup> cannot be strictly compared with our values; however, their relative magnitudes should reasonably describe the situation in  $\text{Ba}(\text{ClO}_3)_2 \cdot \text{H}_2\text{O}$ , as long as the assumptions of their model calculations are valid.

The present study shows that the  $A_u$  translation occurs to high frequency of the  $B_u$  translational mode, in agreement with Eriksson and Lindgren's prediction.<sup>200</sup> Thus, the  $A_u$  mode at  $230 \text{ cm}^{-1}$  is assigned to the water translation along the dipolar axis, and the  $B_u$  mode at  $210 \text{ cm}^{-1}$  is assigned to the water translation in the H-O-H plane, and perpendicular to the  $C_2$ -axis. The out-of-plane water translation is presumed to occur below  $80 \text{ cm}^{-1}$ , which was the effective lower frequency limit of Bertie's *et al.*<sup>130</sup> infrared transmission measurements. As previously indicated, Eriksson and Lindgren<sup>134</sup> assigned this vibration to a band at  $75 \text{ cm}^{-1}$ . Their observed  $1 \text{ cm}^{-1}$  shift upon deuteration, with a purported frequency resolution of  $3 \text{ cm}^{-1}$ , is weak evidence for this assignment, but must be accepted until more definitive polarization results are obtained.

The vibrational assignment of the water modes in  $\text{Ba}(\text{ClO}_3)_2 \cdot \text{H}_2\text{O}$  is summarized in Table 6.12. The gerade frequencies were obtained from Bertie's *et al.*<sup>130</sup> single crystal Raman measurements at  $298^\circ\text{K}$ , unless otherwise indicated. To appreciate the origin of the observed crystal frequencies and their factor group splittings, the correlation with the isolated water molecule modes is also given.

Table 6.12 Site and Davydov Splitting of the Water Modes  
in  $\text{Ba}(\text{ClO}_3)_2 \cdot \text{H}_2\text{O}$ . Frequencies in  $\text{cm}^{-1}$ .

<u>Internal Modes</u>		
Molecular Mode* ( $\text{C}_{2v}$ )	Site State† ( $\text{C}_2$ )	Factor Group state* ( $\text{C}_{2h}$ )
$\nu_1 (A_1)$ 3657	3514(A)	3514(Ag) 3514(Au)
$\nu_2 (A_1)$ 1595	1606(A)	? (Ag) 1606(Au)
$\nu_3 (B_1)$ 3756	3583(B)	3584(Bu) 3582(Bg) at 90°K
<u>Rotational Modes</u>		
$R_z (A_2)$	388(A)	? (Ag) 388(Au)
$R_x (B_1)$	468(B)	478(Bg) 458(Bu)
$R_y (B_2)$	404(B)	? (Bg) 404(Bu)
<u>Translational Modes</u>		
$T_z (A_1)$	231(A)	232(Ag) 230(Au)
$T_y (B_1)$	205.5(B)	210(Bu) 201(Bg)
$T_x (B_2)$	72.5(B)	75 <sup>§</sup> (Bu) 70(Bg)

\* Reference 202.

† Raman frequencies at 300°K from Reference 130.

‡ Site state frequencies were obtained by averaging the factor group frequencies originating from a common site.

§ Reference 134.

Factor group states denoted with a ? were not observed, probably because of low intensity; their frequencies were estimated from associated gerade or ungerade mode. Underlined symmetry species are predicted values.

U

### 6.2b Internal Vibrations of the $\text{ClO}_3^-$ Ion Modes

The four  $\text{ClO}_3^-$  ions in the primitive unit cell of  $\text{Ba}(\text{ClO}_3)_2 \cdot \text{H}_2\text{O}$  are located on general positions ( $C_1$  sites). According to the factor group analysis (Table 6.5), the symmetric stretching and bending vibrations of the free  $\text{ClO}_3^-$  ion,  $\nu_1$  and  $\nu_2$ , each give  $A_g + A_u + B_g + B_u$  Davydov components under the  $C_{2h}$  factor group, while the anti-symmetric stretching and bending vibrations,  $\nu_3$  and  $\nu_4$ , each transform as  $2A_g + 2A_u + 2B_g + 2B_u$ . Since symmetry permits these molecular displacements to contribute to the same crystal vibrations, a strict assignment of the observed modes to components of  $\nu_1$ ,  $\nu_2$ , etc. may not be correct; however, this procedure is useful as a first approximation.

The infrared and Raman spectra of  $\text{ClO}_3^-$  ion in aqueous solution have been reported by Gardiner *et al.*<sup>203</sup> On the basis of measured depolarization ratios and a normal coordinate analysis, they assigned Raman bands at 933, 608, 977, and 477  $\text{cm}^{-1}$ , respectively to the  $\nu_1(A)$ ,  $\nu_2(A)$ ,  $\nu_3(E)$ , and  $\nu_4(E)$   $\text{ClO}_3^-$  ion vibrations. These values are assumed to be close to the unperturbed  $\text{ClO}_3^-$  ion frequencies. Measured differences with the associated  $\text{ClO}_3^-$  ion frequencies in  $\text{Ba}(\text{ClO}_3)_2 \cdot \text{H}_2\text{O}$  should reflect the influence of the static and dynamical crystal forces.

The  $\text{ClO}_3^-$  ion internal mode region of solid  $\text{Ba}(\text{ClO}_3)_2 \cdot \text{H}_2\text{O}$  has been previously studied. The first extensive infrared transmission and Raman measurements on single crys-

tal and polycrystalline  $\text{Ba}(\text{ClO}_3)_2 \cdot \text{H}_2\text{O}$  were performed by Bertie *et al.*<sup>130</sup> in 1973. Although their Raman spectra displayed relatively sharp bands with unambiguous polarization behavior, their infrared study was severely hampered by broad, strong absorption of indeterminate polarization in the region  $900\text{--}1000\text{ cm}^{-1}$ ; this prevented them from making a definite assignment of the *ungerade* components of  $\nu_1$  and  $\nu_3$ . The infrared and Raman frequencies and symmetries reported by Bertie *et al.*<sup>130</sup> and their proposed assignments are given in Table 6.13.

In 1975, Lutz and Klüppel<sup>204</sup> remeasured the polycrystalline infrared transmission and single crystal Raman spectra of  $\text{Ba}(\text{ClO}_3)_2 \cdot \text{H}_2\text{O}$  in the region  $30\text{--}4000\text{ cm}^{-1}$ . This work constituted part of a systematic investigation of the alkaline-earth halogenate monohydrates. Apparently, these workers were unaware of the earlier work by Bertie *et al.*<sup>130</sup>. They also reported the infrared reflectance spectra of the polycrystalline and single crystal samples, but gave no indication of the intensity scale. Their observed infrared and Raman frequencies, symmetries, and proposed assignments are summarized in Table 6.13.

Comparison of the results for Bertie *et al.*<sup>130</sup> and Lutz and Klüppel<sup>204</sup> shows some significant discrepancies in frequencies and assignments. In the following discussion of our polarized infrared reflection and KK-derived conductivity data, these ambiguities will be addressed and, hopefully, clarified.

Table 6.13 Previous Assignments of  $\text{ClO}_3^-$  Ion Internal Modes in  $\text{Ba}(\text{ClO}_3)_2 \cdot \text{H}_2\text{O}$ 

Reference 130		Reference 204	
IR*	Raman	IR†	Raman
1005	$\left. \begin{array}{l} \nu_1 \text{ and } \nu_3 \\ \nu_3 \end{array} \right\}$	1008†(Bu)	985(Ag)
980		970	965(Bg)
960		950	
920		915	935(Bg)
912			916(Ag)
620(Bu)	$\left. \begin{array}{l} \nu_2 \\ \nu_2 \end{array} \right\}$	615	610
615(Au)			
508(Au)	$\left. \begin{array}{l} \nu_4 \\ \nu_4 \end{array} \right\}$	506	501(Bg)
504(Bu)		501	485(Ag)
485(Au, Bu)		480	

\* polarized infrared transmission measurements on single crystal  $\text{Ba}(\text{ClO}_3)_2 \cdot \text{H}_2\text{O}$ .† Infrared transmission measurements on polycrystalline  $\text{Ba}(\text{ClO}_3)_2 \cdot \text{H}_2\text{O}$ .

‡ Reflectance peak maximum in c-polarized spectrum.

Our observed conductivity peak frequencies and symmetries for single crystal  $\text{Ba}(\text{ClO}_3)_2 \cdot \text{H}_2\text{O}$ , in the  $\text{ClO}_3^-$  ion internal mode region, are presented in Table 6.14. The relative intensities of these spectral features, as determined by a damped harmonic oscillator fit (Tables 4.9 and 4.10), are also given. This data is compared with the associated *gerade* mode frequencies, symmetries and relative intensities, as reported by Bertie *et al.*<sup>130</sup> In the infrared, we obtained 6 Bu + 4 Au modes in the  $\nu_1 - \nu_3$  region, and 4 Bu + 3 Au modes in the  $\nu_2 - \nu_4$  region; this compares with an expected 3 Au + 3 Bu modes, in each of these regions.

In order to explain these additional features, account was taken of their observed intensities and band shapes, since fundamental vibrations are typically much stronger and sharper than combination or overtone modes. On this basis, the very broad, weak Bu modes at 995 and 1020  $\text{cm}^{-1}$  are assigned to the first overtone of  $\nu_4$ . The irreducible representation spanned by  $2\nu_4$  for the free  $\text{ClO}_3^-$  ion is  $\Gamma = A_1 + E$ , so under the  $C_{2h}$  factor group this correlates with a very large number of crystal states (3Au + 3Ag + 3Bu + 3Bg). The average value of the Davydov components for  $\nu_4$  is 494  $\text{cm}^{-1}$  (see Table 6.17), which predicts that the  $2\nu_4$  modes should occur in the vicinity of 990  $\text{cm}^{-1}$ ; this is what we observed.

The medium strength Bu mode at 963  $\text{cm}^{-1}$  and the very strong Au mode at 959  $\text{cm}^{-1}$  are assigned to  $\nu_3$ , which is consistent with Bertie *et al.*'s<sup>130</sup> assignment of Raman

Table 6.14 Relative Intensity of Features in Conductivity  
and Raman Spectra of Single Crystal  
 $\text{Ba}(\text{ClO}_3)_2 \cdot \text{H}_2\text{O}$  in the  $\text{ClO}_3^-$  Ion Internal Mode  
Region

Conductivity			Raman <sup>130</sup>		
$\nu$	Symmetry	Intensity*	$\nu$	Symmetry	Intensity
1020	Bu	w, vb <sup>†</sup>	986	Ag	vw
995	Bu	w, vb <sup>†</sup>	986	Bg	w
963	Bu	ms	965	Ag	ms
959	Au	vs, b	959	Bg	w
950	Bu	m <sup>†</sup>			
940	Au	vw, b			
933	Au	w	934	Ag	vs
925	Au	w, b	931	Bg	s
912	Bu	s	918	Ag	ms
909	Bu	m	915	Bg	ms
616	Bu	m	621	Bg	m
612	Au	w	611	Ag	w
507	Au	m	500	Ag	s
502	Bu	vw, b	500	Bg	ms
493	Bu	w, b	486	Ag	ms
487	Bu	vw	484	Bg	w
481	Au	vw			

\* Conductivity peak intensities from fitted oscillator strength values in Tables 4.9 and 4.10, according to:  
 $S_j (\times 10^4 \text{ cm}^{-2})$ : vw < 1; w 1-2; m 2-5; ms 5-10; s 10-20; vs > 20  
 'b' and 'vb' designations are given to bands with  
 FWHM = 10-20  $\text{cm}^{-1}$  and > 20  $\text{cm}^{-1}$ , respectively.

† Approximate intensities from conductivity spectrum of polycrystalline  $\text{Ba}(\text{ClO}_3)_2 \cdot \text{H}_2\text{O}$ .

‡ Intensity estimated from c-polarized reflectance spectrum of (110) face.

bands at  $965\text{ cm}^{-1}$  (Ag) and  $959\text{ cm}^{-1}$  (Bg) to  $\nu_3$ . The proximity of these  $\nu_3$  fundamental modes to the components of  $2\nu_4$  may cause some mixing of these crystal vibrations, via Fermi resonance. A medium intensity band, observed at  $950\text{ cm}^{-1}$  in the c-polarized reflection spectrum of the (110) crystal face (Table 6.9), is assigned to the second Bu component of  $\nu_3$ . However, this reflectance peak frequency is only a crude estimate of the true resonance frequency. Further work is required for a more accurate value of this  $\nu_3$  mode.

The extra Au mode in the  $\nu_1 - \nu_3$  region is believed to be the very weak, broad feature at  $940\text{ cm}^{-1}$ . Table 6.9 shows that the corresponding reflectance peak only shifted by  $2\text{ cm}^{-1}$  in going from the hydrate to the deuterate crystal. This suggests that this vibration involves negligible water motion and is more likely due to  $2\nu_4$  or to some higher order overtone or combination transition. The second Au component of  $\nu_3$  is assigned to the weak conductivity peak at  $933\text{ cm}^{-1}$ . The weak Au mode at  $925\text{ cm}^{-1}$  and the strong Bu mode at  $912\text{ cm}^{-1}$  are assigned to  $\nu_1$ . The origin of the medium intensity Bu mode at  $909\text{ cm}^{-1}$  is discussed below.

A factor group analysis, as performed in Section 6.1, is only strictly valid for an ordered crystal. However,  $\text{Ba}(\text{ClO}_3)_2 \cdot \text{H}_2\text{O}$  contains  $^{37}\text{Cl}$  and  $^{35}\text{Cl}$  in the natural abundance of 1:3. Thus, on average, the primitive unit cell of  $\text{Ba}(\text{ClO}_3)_2 \cdot \text{H}_2\text{O}$  contains one  $^{37}\text{ClO}_3^-$  ion and three

$^{35}\text{ClO}_3^-$  ions. Since the observed infrared conductivity and Raman peaks are relatively sharp, and exhibit a clear polarization dependence, this indicates that the perturbation by the  $^{37}\text{ClO}_3^-$  ions is small, and the so-called virtual crystal limit<sup>205</sup> applies, i.e. the factor group selection rules derived for the pure crystal are retained.

The effect of an isotopic impurity on the crystal vibrations is succinctly described by Rayleigh's Principle,<sup>206</sup> which states that the increase (decrease) of mass of any atom will lead to a new set of frequencies which are unchanged or decreased (increased) by an amount which is no greater than the interval to the next unperturbed frequency.

There exist two types of mixed crystal systems. When the phonon frequencies are slightly shifted with respect to the pure crystal frequencies, and this shift is dependent on the impurity concentration, the crystal is referred to as within the amalgamation limit. The other extreme is a persistence type crystal in which the two constituents yield distinct absorption bands, whose frequencies are essentially independent of composition. These two mixed crystal types are schematically represented in Figure 6.3.

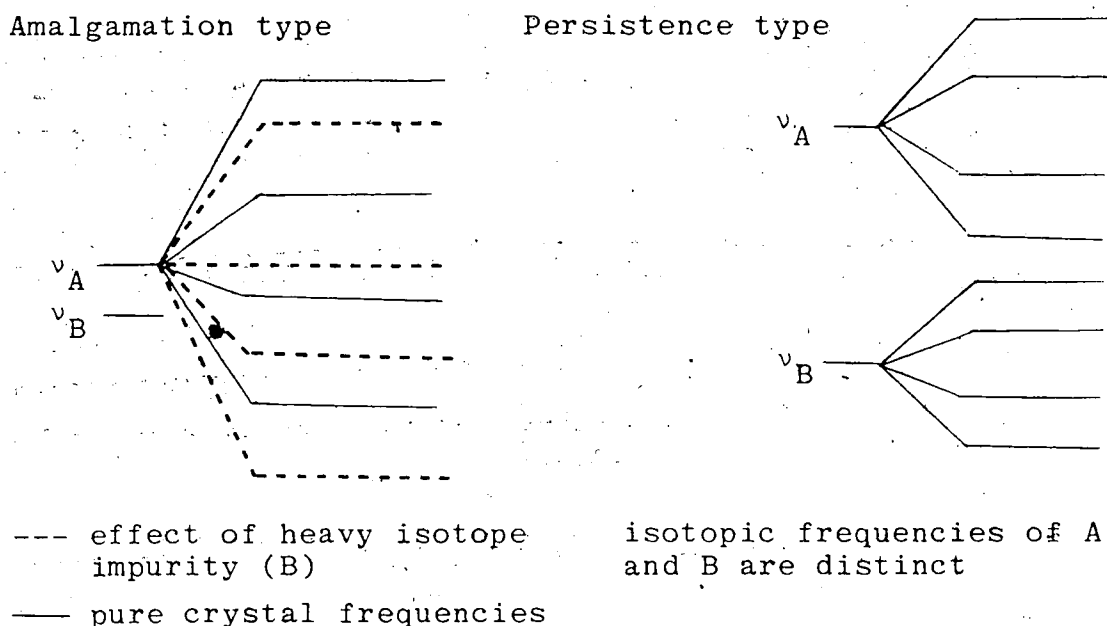


Figure 6.3 Spectral behavior of amalgamation- and persistence-type mixed crystals.

Model calculations by Onodera and Toyozawa<sup>207</sup> have shown that the most important parameter determining whether a mixed crystal belongs to the amalgamation or persistence type is the ratio of the frequency difference between the two constituents ( $\Delta$ ) and the width of the energy band spanned by the Davydov components ( $T$ ). Figure 6.4 shows the boundary between these two crystal systems as a function of composition. For  $\Delta/T$  values above the dashed line, two separate energy bands are predicted, whereas below this line, the two bands unite to give a single band. Since this calculated curve assumes a random distribution of impurity atoms and an interaction energy which is only depen-

Table 6.15 Comparison of Calculated\*  $^{37}\text{Cl}/^{35}\text{Cl}$  Splittings of  $\text{ClO}_3^-$  Ion Internal Modes in  $\text{KClO}_3$  ( $\Delta$ ) and Observed Frequency Range for these Vibrations in  $\text{Ba}(\text{ClO}_3)_2 \cdot \text{H}_2\text{O}$  (T).

Mode	$\Delta(\text{cm}^{-1})$	T( $\text{cm}^{-1}$ )	$\Delta/T$
$\nu_1$	7.6	16	0.48
$\nu_2$	4.8	10	0.48
$\nu_3$	11.3	34	0.33
$\nu_4$	1.2	26	0.05

\* Reference 208

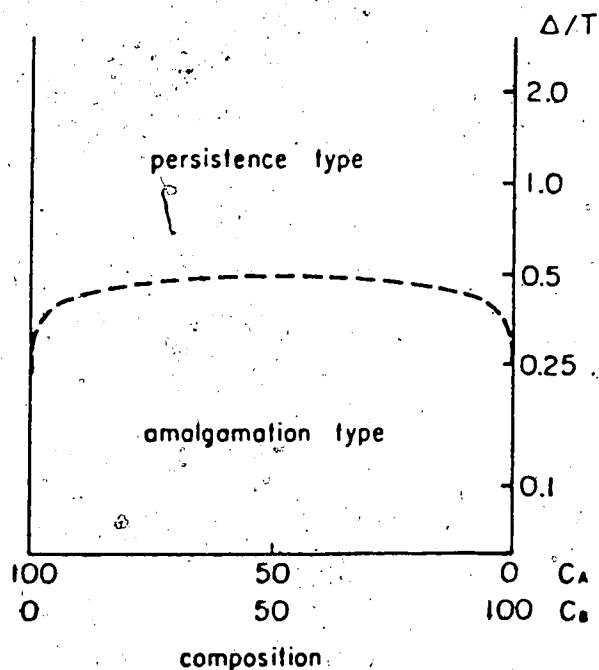


Figure 6.4 Boundary of the amalgamation and persistence type systems. Redrawn from Reference 207.

Note that the  $\Delta/T$  is plotted on a logarithmic scale.

dent on the relative position of the atoms, it should be generally applicable.

In Table 6.15, the  $\Delta/T$  ratio is presented for the various  $\text{ClO}_3^-$  ion internal modes of  $\text{Ba}(\text{ClO}_3)_2 \cdot \text{H}_2\text{O}$ . The isotopic  $^{35}\text{Cl}/^{37}\text{Cl}$  splittings were obtained from Bates and Stidham's<sup>208</sup> normal coordinate calculations for  $\text{KClO}_3$ , and the width of the energy bands was taken from our internal  $\text{ClO}_3^-$  ion vibrational assignments, summarized in Table 6.17.

For a 25:75 percent composition of  $^{37}\text{Cl}/^{35}\text{Cl}$ , the  $\nu_3$  and  $\nu_4$  crystal vibrations clearly lie within the amalgamation limit, while the  $\nu_1$  and  $\nu_2$  vibrations are of intermediate amalgamation-persistence character. Figure 6.5 shows the behaviour that might be expected for the  $\nu_1$  and  $\nu_2$  vibrations: a band of frequencies slightly shifted to lower values with respect to the isotopically pure  $^{35}\text{Cl}$  lattice, and one or more frequencies displaced out of this band. These discrete frequencies are referred to as localized modes<sup>209</sup> and predominantly involve vibration of the  $^{37}\text{ClO}_3^-$  ion. It can be seen that the lowest frequency vibration of

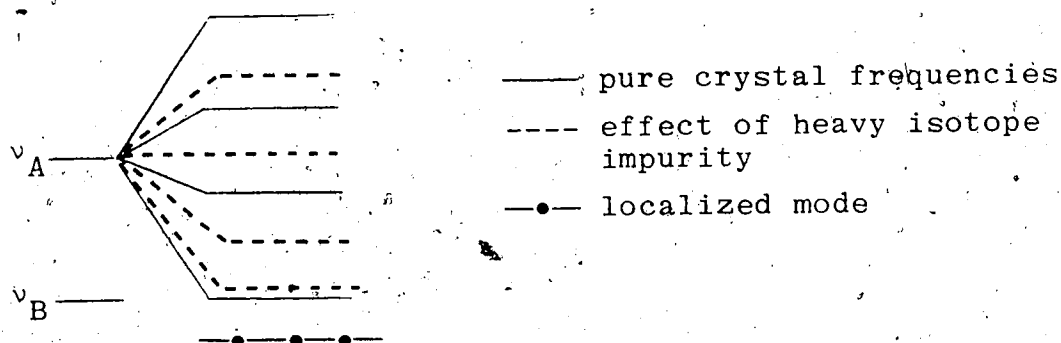


Figure 6.5. Expected behavior for a crystal of intermediate amalgamation-persistence character.

the energy band is shifted upward. This is due to the greater interaction of the impurity levels with the bottom of the main band;<sup>207</sup> the isolated mode may, therefore, exhibit the same symmetry species as the lowest frequency Davydov component.

In  $\text{Ba}(\text{ClO}_3)_2 \cdot \text{H}_2\text{O}$ , the lowest frequency component of the  $\nu_1$   $^{35}\text{ClO}_3^-$  multiplet is the  $912\text{ cm}^{-1}$  band of Bu symmetry (Table 6.17). Based on the preceding discussion, the Bu mode at  $909\text{ cm}^{-1}$  is assigned to a  $\nu_1$  localized mode of  $^{37}\text{ClO}_3^-$  ion. The observed intensity ratio of the bands at  $912$  and  $909\text{ cm}^{-1}$  is 2.9:1 (Table 4.10); this compares with a 3:1 distribution of the  $^{35}\text{ClO}_3^-$  and  $^{37}\text{ClO}_3^-$  ions in the lattice.

According to Bertie *et al.*,<sup>130</sup> the  $\nu_2$   $\text{ClO}_3^-$  ion vibration also exhibited a resolvable isotope dependence; an Ag mode at  $612\text{ cm}^{-1}$  in the Raman spectra of  $\text{Ba}(\text{ClO}_3)_2 \cdot \text{D}_2\text{O}$  was assigned to  $\nu_2$  of  $^{37}\text{ClO}_3^-$ . From Table 6.17, it can be seen that the Ag mode is the lowest frequency vibration of the  $\nu_2$  multiplet, which is consistent with the assignment of the stretching modes.

This set of assignments for the *ungerade* modes of  $\nu_1$  and  $\nu_3$  clearly disagree with the previous assignments of the associated *gerade* species (see Table 6.13). An alternative explanation of the observed Raman bands is suggested below, which more reasonably accounts for the observed intensities, and which does not require an unusually large isotopic splitting for the  $\nu_1$  vibration.

It is proposed that the very weak Ag and Bg modes observed by Bertie *et al.*<sup>130</sup> at  $986\text{ cm}^{-1}$  are not  $\nu_3$  fundamental modes, but are due to  $2\nu_4$ . This suggests that the very strong Ag and Bg modes at  $934$  and  $931\text{ cm}^{-1}$  arise from  $\nu_3$ . The Raman band at  $934\text{ cm}^{-1}$  was assigned by Bertie *et al.*<sup>130</sup> to the Ag component of  $\nu_1$  because it was the most intense feature in the spectrum. This type of empirical selection rule is frequently used. However, Scheuermann and Schutte<sup>210</sup> have cautioned that the Ag mode of  $\nu_1$  can only be definitely assigned if it is both the most intense and narrowest band in the Raman spectrum. In the case of  $\text{Ba}(\text{ClO}_3)_2 \cdot \text{H}_2\text{O}$ , the Ag mode at  $934\text{ cm}^{-1}$  is the strongest Raman band, but the medium strength Ag mode at  $918\text{ cm}^{-1}$  is sharper. Thus, an assignment of the Ag and Bg modes at  $918$  and  $915\text{ cm}^{-1}$ , respectively, to the symmetric Cl-O stretching vibration,  $\nu_1$ , is reasonable. The particular merit of this revised assignment is that it does not require an isotopic shift of  $-15\text{ cm}^{-1}$  for  $\nu_1$ , when the calculated shift<sup>208</sup> is only  $7.6\text{ cm}^{-1}$  (Table 6.15).

The assignment of the  $\text{ClO}_3^-$  ion stretching modes in  $\text{Ba}(\text{ClO}_3)_2 \cdot \text{H}_2\text{O}$  is summarized in Table 6.16, along with a suggested correspondence to previous infrared and Raman results. It should be noted when comparing these infrared frequencies that our values correspond to the conductivity peak maxima, whereas those reported by Bertie *et al.*<sup>130</sup> and Lutz and Klüppel<sup>204</sup> correspond to the transmission peak minima. For example, the very strong conductivity

Table 6.16 Assignment of  $\text{ClO}_3^-$  Ion Stretching Modes in  $\text{Ba}(\text{ClO}_3)_2 \cdot \text{H}_2\text{O}$  and Suggested Correspondence with Previous Results

Present* Study		Reference 130		Reference 204		Assignment
Au	Bu	IR	Raman	IR	Raman	
			Ag Bg		Ag Bg	
	1020 <sup>†</sup>		<u>986</u>		<u>985</u>	o/c
	995 <sup>†</sup>	<u>1005</u>	<u>986</u>	1008		
	963	<u>980</u>	965	970		} $\nu_3$
959			959		965	
	950 <sup>†</sup>	<u>960</u>	<u>934</u>	950		
933			<u>931</u>		<u>935</u>	
925		<u>920</u>	<u>918</u>		916	
	912	<u>912</u>	<u>915</u>	915		} $\nu_1$
	909					
						$\nu_1(^{37}\text{Cl})$

Frequencies in  $\text{cm}^{-1}$ . Underlined frequencies correspond to modes whose previous assignment (see Table 6.13) has been revised or made more definitive.

\*Frequencies derived from combined KK/classical dispersion fit to single crystal  $R(\nu)$  and  $\epsilon''(\nu)$  spectra.

<sup>†</sup>Conductivity peak frequencies for polycrystalline  $\text{Ba}(\text{ClO}_3)_2 \cdot \text{H}_2\text{O}$ .

<sup>‡</sup>c-polarized reflectance peak frequency for (110) crystal face.

peaks at 963 and 959  $\text{cm}^{-1}$  appear to be at 980  $\text{cm}^{-1}$  in the transmission spectra, whereas, the associated reflectance maxima occur at 971 and 980  $\text{cm}^{-1}$ , respectively (Table 6.9).

In the  $\nu_2$ - $\nu_4$  region, 4Bu + 3Au modes were observed in the conductivity spectra (Figure 4.13 and Table 6.14); this compares with 3Bu + 3Au modes predicted by the factor group analysis. Bertie *et al.*<sup>130</sup> assigned infrared transmission peaks at 615  $\text{cm}^{-1}$  (b-polarized) and 620  $\text{cm}^{-1}$  (ac-polarized) to the Au and Bu components respectively, of the symmetric  $\text{ClO}_3^-$  ion deformation,  $\nu_2$ . These values are in very good agreement with our observed conductivity peaks at 612  $\text{cm}^{-1}$  (b-polarized) and 616  $\text{cm}^{-1}$  (a'-polarized), thus confirming their earlier assignments. Bertie *et al.*<sup>130</sup> also ascribed Au modes at 508 and 485  $\text{cm}^{-1}$  and Bu modes at 504 and 485  $\text{cm}^{-1}$  to the Davydov components of  $\nu_4$ . In this region, we observed Au modes at 507 and 481  $\text{cm}^{-1}$  and Bu modes at 502, 493 and 487  $\text{cm}^{-1}$ . The assignment of the Bu modes is not obvious. Since the 493  $\text{cm}^{-1}$  band is the most intense of the three Bu vibrations, it is assigned to a factor group component of  $\nu_4$ . The 502  $\text{cm}^{-1}$  band is in closest agreement with Bertie *et al.*'s<sup>130</sup> reported frequency of 504  $\text{cm}^{-1}$  and is, therefore, also assigned to  $\nu_4$ . The remaining Bu mode at 487  $\text{cm}^{-1}$  is most likely an overtone or combination band. In view of the deuteration shifts observed in this frequency range (see Table 6.9), the 487  $\text{cm}^{-1}$  band may arise from a combination of a water rotation and an acoustic vibration. Such a transition should occur in the vicinity of 490  $\text{cm}^{-1}$ .

Although acoustic modes have zero frequency under the factor group approximation, they possess non-zero frequencies at the Brillouin zone boundary and may, therefore, participate in combination modes.<sup>211</sup>

The vibrational assignment of the  $\text{ClO}_3^-$  ion internal modes is summarized in Table 6.17. The *gerade* frequencies were obtained from the single crystal Raman measurements of Bertie *et al.*,<sup>130</sup> but their assignments have been revised according to Table 6.16. The origin of the factor group splitting is also shown schematically.

In Table 6.18, the site frequencies for the internal  $\text{ClO}_3^-$  ion modes in  $\text{Ba}(\text{ClO}_3)_2 \cdot \text{H}_2\text{O}$  are compared with the corresponding values in aqueous solution and in crystalline  $\text{NaClO}_3$  and  $\text{KClO}_3$ . The site frequencies were deduced from the average value of the observed Davydov components, although this procedure may not be valid if there is significant interaction between equivalent molecules in neighboring unit cells. It can be seen that for  $\text{NaClO}_3$  and  $\text{KClO}_3$ , all four of the  $\text{ClO}_3^-$  ion modes resonate at higher frequency than in solution; whereas for  $\text{Ba}(\text{ClO}_3)_2 \cdot \text{H}_2\text{O}$ , the deformation modes,  $\nu_2$  and  $\nu_4$ , occur at higher frequencies and the stretching modes,  $\nu_1$  and  $\nu_3$ , appear at lower frequencies. This difference in behaviour is most reasonably attributed to the presence of weak hydrogen bonding in  $\text{Ba}(\text{ClO}_3)_2 \cdot \text{H}_2\text{O}$ .

Table 6.17 Site and Correlation Splitting of the Internal Chlorate Ion Modes in  $\text{Ba}(\text{ClO}_3)_2 \cdot \text{H}_2\text{O}$ . Frequencies in  $\text{cm}^{-1}$ .

Free ion mode* ( $\text{C}_{2v}$ )	Site state† ( $\text{C}_1$ )	Factor group state ( $\text{C}_{2h}$ )
$\nu_1(\text{A}_1)$ 933	917(A)	925(Au) 918(Ag) 915(Bg) 912(Bu) $\nu_1$ (35 Cl) 909(Bu) $\nu_1$ (37 Cl)
$\nu_2(\text{A}_2)$ 608	615(A)	621(Bg) 616(Bu) 612(Au) 611(Ag)
$\nu_3(\text{E})$ 977	949(A)	965(Ag) 963(Bu) 959(Au) 959(Bg) ..... 950†(Bu) 934(Ag) 933(Au) 931(Bg)
$\nu_4(\text{E})$ 477	494(A)	507(Au) 502(Bu) 500(Ag) 500(Bg) 493(Bu) 486(Ag) 484(Bg) 481(Au)

\* Free  $\text{ClO}_3^-$  ion frequencies are aqueous solution values from Reference 203.

† Site frequencies are the average value of the frequencies originating from a common site; in the case of the E modes, the site splitting is not shown since there is no evidence for its magnitude.

‡ Reflectance peak frequency in c-polarized spectrum of (110) crystal face.

Table 6.18 Comparison of Chlorate Ion Vibrational Frequencies in Aqueous Solution and in Solid  $\text{NaClO}_3$ ,  $\text{KClO}_3$ , and  $\text{Ba}(\text{ClO}_3)_2 \cdot \text{H}_2\text{O}$

Mode	Solution*	$\text{NaClO}_3^\dagger$	$\text{KClO}_3^\ddagger$	$\text{Ba}(\text{ClO}_3)_2 \cdot \text{H}_2\text{O}$
$\nu_1$	933(A <sub>1</sub> )	936(A)	940(A')	917(A)
$\nu_2$	608(A <sub>2</sub> )	621(A)	620(A')	615(A)
$\nu_3$	977(E)	972(E)	990(A') 987(A'')	949(A)
$\nu_4$	477(E)	484(E)	490(A') 485(A'')	494(A)

\*Reference 203.

†References 96 and 97.

‡Reference 99.

### 6.2c Lattice Vibrations Involving $\text{Ba}^{2+}$ and $\text{ClO}_3^-$ Ions

The external  $k = 0$  optic modes of  $\text{Ba}(\text{ClO}_3)_2 \cdot \text{H}_2\text{O}$  involving the  $\text{Ba}^{2+}$  and  $\text{ClO}_3^-$  ions form the representation  $7\text{Ag} + 6\text{Au} + 8\text{Bg} + 6\text{Bu}$  (Tables 6.4 and 6.5). Since symmetry permits these translational and rotational motions to contribute to the same vibration, the observed crystal modes cannot be described as pure translations or rotations. However, as a first approximation, they can be assigned as primarily of translational or rotational character.

The lattice vibrations of  $\text{Ba}(\text{ClO}_3)_2 \cdot \text{H}_2\text{O}$  have been previously assigned by Bertie *et al.*<sup>130</sup> Because they were unable to determine the polarization behavior of the far-infrared or Raman bands, their assignments were largely based on the empirical prediction that the predominantly translational modes should be strong in the infrared and weak in the Raman, whereas the rotational vibrations should be strong in both. However, a vibration involving a large component of rotation about the  $\text{ClO}_3^-$  ion axis, which is only active through distortion of the ion from  $C_{3v}$  symmetry, was expected to be weak in both types of spectra. Assignment of the predominantly  $\text{ClO}_3^-$  ion rotational modes was made by comparison with the reported spectra of  $\text{NaClO}_3$ <sup>97</sup> and  $\text{KClO}_3$ .<sup>99</sup> This type of comparison is valid if the crystal forces are similar. Under this condition, the rotational vibrations of the  $\text{ClO}_3^-$  ions should appear at nearly the same frequencies since they depend on the moments of inertia which are only weakly influenced by the nature of

the cation; whereas the translational modes, whose inertial mass is the molecular mass, should exhibit strongly cation-dependent frequencies. The lattice mode frequencies and assignments for  $\text{NaClO}_3$ ,  $\text{KClO}_3$ , and  $\text{Ba}(\text{ClO}_3)_2 \cdot \text{H}_2\text{O}$  are summarized in Table 6.19.

In 1978, Eriksson and Lindgren<sup>134</sup> repeated the far-infrared transmission measurements on polycrystalline  $\text{Ba}(\text{ClO}_3)_2 \cdot \text{H}_2\text{O}$  at 298°K and 100°K. Their results are compared with Bertie *et al.*'s<sup>130</sup> reported frequencies in Table 6.20, and confirm these earlier values to be accurate to within  $2 \text{ cm}^{-1}$ . However, Eriksson and Lindgren observed an additional band at  $75 \text{ cm}^{-1}$  which was discussed in Section 6.2a, but did not find features corresponding to Bertie *et al.*'s<sup>130</sup> strong bands at 102 and  $100 \text{ cm}^{-1}$  for a sample at 300°K. They tacitly accepted the lattice mode assignments of Bertie *et al.*;<sup>130</sup> their only comment was that the  $97 \text{ cm}^{-1}$  band exhibited a  $1 \text{ cm}^{-1}$  shift for both  $\text{D}_2\text{O}$  and  $\text{H}_2^{18}\text{O}$  substitution, from which they concluded that some water motion was involved in the vibration.

Table 6.20 also lists the far-infrared transmission frequencies reported by Lutz and Klüppel<sup>204</sup> for a polycrystalline sample of  $\text{Ba}(\text{ClO}_3)_2 \cdot \text{H}_2\text{O}$  at 298°K and 110°K. It can be seen that there are significant discrepancies with the results of Bertie *et al.*<sup>130</sup> and Eriksson and Lindgren.<sup>134</sup> Their c-polarized reflectance peak frequencies, measured for a single crystal sample at 298°K, are included in Table 6.20. These authors did not attempt to assign the observed

Table 6.19 Previous Lattice Mode Assignments for  $\text{NaClO}_3$ ,  
 $\text{KClO}_3$ , and  $\text{Ba}(\text{ClO}_3)_2 \cdot \text{H}_2\text{O}$

$\text{NaClO}_3^*$	$\text{KClO}_3^*$	$\text{Ba}(\text{ClO}_3)_2 \cdot \text{H}_2\text{O}^\dagger$		
		IR	Raman	
183	}	184	-	$\nu_T$
180		-	-	
176		171	175 } 173 }	$\nu_R$
-	161		163	$\nu_R$
		152	151	$\nu_T$
142	144	141	141	
134	}	136	137 } 128 }	$\nu_R$
	132			
131		130		
124		-		
			117 } 115 }	$\nu_R$
	109	110	-	
		108	107 } 105 }	$\nu_T$
		105	-	
95	}	95	-	
86		-	-	
	87		82	$\nu_R$
	83		72	
72	}	-	-	
65		-	50	
	57			

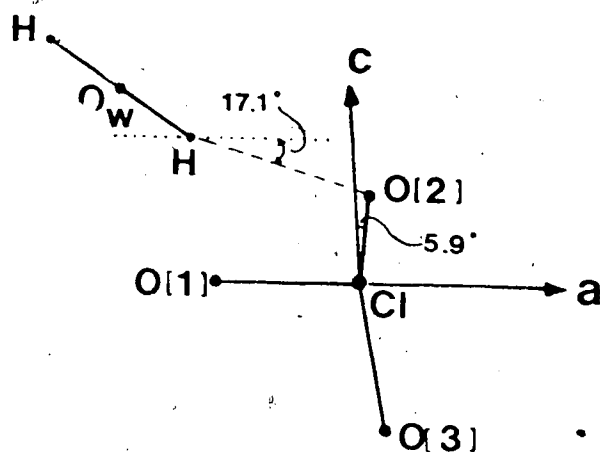
\* Assignments from Reference 99; measured frequencies at 298°K for  $\text{NaClO}_3$  and 77°K for  $\text{KClO}_3$ .

† Reference 130; measured frequencies at 90°K.

Table 6.20 Comparison of Infrared Lattice Mode Frequencies Previously Reported for  $\text{Ba}(\text{ClO}_3)_2 \cdot \text{H}_2\text{O}$

Reference 130		Reference 134		Reference 204	
300°K	90°K	298°K	100°K	298°K	110°K
175	184	176	184	170(165)*	179
165	171	165	172	160(151)	168
148	152	149	153	(143)	
138	141	139	143		
134	136	134	136	131(132)*	
126	130	126	130	121(123)	124
106	110	107	109		
102	108				
100	105			100(100)	106
96	95	95	97.1	89	91
		75	77.6		

\*Frequencies in parentheses were obtained from c-polarized reflectance spectrum of single crystal  $\text{Ba}(\text{ClO}_3)_2 \cdot \text{H}_2\text{O}$ ; the association with transmission peak frequencies is that of Reference 204.



$$\text{H} \cdots \text{O}(2) = 1.991 \pm 0.010 \text{ \AA}$$

Figure 6.6 Equilibrium  $\text{ClO}_3^-$  ion geometry<sup>105</sup> in  $\text{Ba}(\text{ClO}_3)_2 \cdot \text{H}_2\text{O}$ . The projection on the (010) plane is shown.

frequencies to specific lattice modes.

Our conductivity peak frequencies, symmetries, and relative intensities for the (001) crystal face of  $\text{Ba}(\text{ClO}_3)_2 \cdot \text{H}_2\text{O}$  in the region below  $200 \text{ cm}^{-1}$  are given in Table 6.21, and compared with the Raman frequencies of Bertie *et al.*<sup>130</sup> A correspondence between the *gerade* and *ungerade* modes is also suggested. Although we accept the majority of the lattice mode assignments proposed by Bertie *et al.*,<sup>130</sup> there are a few exceptions. The basis of these revised assignments is discussed below.

In the region below  $200 \text{ cm}^{-1}$ , we observed 4Au + 9Bu modes plus two bands of indeterminate polarization (Table 6.21); this compares with an expected 6Au + 6Bu infrared-active lattice modes. Overtone or combination transitions are the most likely origin of the extra Bu modes. The fact that too few Au modes were observed can be ascribed either to accidental degeneracy, low intensity, or to these modes occurring below  $105 \text{ cm}^{-1}$ , the lower frequency limit of our polarized single crystal data.

According to the intensity predictions of Bertie *et al.*,<sup>130</sup> the translational and rotational vibrations should both absorb strongly in the infrared, with the exception of the  $R_z$  motion of the  $\text{ClO}_3^-$  ion. For the free  $\text{ClO}_3^-$  ion, the  $R_z$  mode is inactive in both the infrared and Raman but in  $\text{Ba}(\text{ClO}_3)_2 \cdot \text{H}_2\text{O}$ , the  $C_1$  site symmetry permits this mode to gain intensity from mixing with other lattice vibrations. The influence of the crystal forces is apparent

Table 6.21 Assignment of Lattice Modes in  $\text{Ba}(\text{ClO}_3)_2 \cdot \text{H}_2\text{O}$   
and Suggested Correspondence with Raman Results

Present Study*		Raman†		Assignment
Au	Bu	300°K	90°K	
			175 w	
	173 m, vb	~165 sh	173 w	} $R_x, R_y$
160 m, b	164†w	158	163 s	
	151 w		151 w	} o/c (105+52)
	142†vw		141 sh	
133 w	133 ms		137 ms	} R
	131 ms	133	136	
	129 m	124	128 ms	
120 m			117 w	} T
	114 m		115 w	
105†ms	109 m	106	107 w	
	92†vs		82 vw	} $R_z$
	83†sh	70	72 w	
		52	50 mw	

\*Frequencies obtained from combined KK/classical dispersion fit to  $R(\nu)$  and  $\epsilon''(\nu)$  data for (001) crystal face of  $\text{Ba}(\text{ClO}_3)_2 \cdot \text{H}_2\text{O}$ .

†Reference 130.

‡Conductivity peak frequencies for polycrystalline  $\text{Ba}(\text{ClO}_3)_2 \cdot \text{H}_2\text{O}$ .

Values in parentheses are combinations of fundamental modes consistent with observed frequency. Underlined frequencies correspond to modes whose previous assignment (Table 6.19) has been revised.

from the equilibrium geometry<sup>105</sup> shown in Figure 6.7:  
 $r_{\text{Cl-O}} = 1.480, 1.483, \text{ and } 1.493 \text{ \AA} (\pm 0.004 \text{ \AA})$  and  $\angle \text{OClO} = 106.6, 105.1 \text{ and } 107.1^\circ (\pm 0.2^\circ)$ . Since the perturbation from  $C_{3v}$  symmetry is only slight, the vibrational coupling should be weak and the intensities should follow the predictions of Bertie *et al.*<sup>130</sup> From the lattice mode assignments of  $\text{NaClO}_3$  and  $\text{KClO}_3$  in Table 6.19, the  $R_z$  mode in  $\text{Ba}(\text{ClO}_3)_2 \cdot \text{H}_2\text{O}$  is expected in the vicinity of  $80\text{--}90 \text{ cm}^{-1}$ . Thus, very weak infrared features below  $200 \text{ cm}^{-1}$ , but not in the range  $80\text{--}90 \text{ cm}^{-1}$ , can be reasonably attributed to overtone or combination (o/c) modes. On this basis, the very weak Bu transition at  $142 \text{ cm}^{-1}$ , and the weak bands at  $151 \text{ cm}^{-1}$  in both the infrared (Bu) and Raman<sup>130</sup> spectra, are assigned to o/c transitions. Tentative explanations of these observed frequencies are presented in Table 6.21; a more definitive assignment requires a temperature-dependent study of the infrared intensities.

Weak Raman bands at  $117$  and  $115 \text{ cm}^{-1}$  were assigned by Bertie *et al.*<sup>130</sup> to rotational vibrations, since no associated infrared features were observed. However, we found medium intensity conductivity peaks at  $120 \text{ cm}^{-1}$  (Au) and  $114 \text{ cm}^{-1}$  (Bu). It is our present belief that these modes are more likely due to translational vibrations. Table 6.19 shows that none of the assigned rotational bands of  $\text{NaClO}_3$  and  $\text{KClO}_3$  are in close correspondence ( $< 5 \text{ cm}^{-1}$ ) with these peak frequencies for  $\text{Ba}(\text{ClO}_3)_2 \cdot \text{H}_2\text{O}$ . Furthermore, if the motions involved in the translations are primarily a

diatomic type oscillation of the cation and the  $\text{ClO}_3^-$  ion and the intermolecular forces are similar in these chlorate crystals, then the relative order of the translational frequencies is approximately given by the ratio of their reduced masses, *i.e.*  $1.44(\text{Na}\cdots\text{ClO}_3): 1.34(\text{K}\cdots\text{ClO}_3): 1.00(\text{Ba}\cdots\text{ClO}_3)$ . The highest frequency translational modes reported<sup>99</sup> for  $\text{NaClO}_3$  and  $\text{KClO}_3$  are  $183$  and  $161\text{ cm}^{-1}$ , respectively, which predicts that the associated mode for  $\text{Ba}(\text{ClO}_3)_2\cdot\text{H}_2\text{O}$  should appear at  $\sim 120\text{ cm}^{-1}$ , which is consistent with our revised assignments.

It is also proposed that the Bu mode at  $173\text{ cm}^{-1}$  and the Au mode at  $160\text{ cm}^{-1}$  (Table 6.21) are predominantly  $R_x$  and  $R_y$  vibrations, and the shoulder at  $83\text{ cm}^{-1}$  in the polycrystalline spectrum involves  $R_z$  motion. These assignments are based on the observed intensities, breadth, and temperature-dependent frequency shifts of these vibrations, as well as the equilibrium geometry of the  $\text{ClO}_3^-$  ion in the  $\text{Ba}(\text{ClO}_3)_2\cdot\text{H}_2\text{O}$  lattice.

The relationship of the  $\text{ClO}_3^-$  ion to the water molecule in the unit cell is shown in Figure 6.6. It can be seen that the hydrogen atom of the water molecule is only  $1.99\text{ \AA}$  from the oxygen atom O(2) of the chlorate ion.<sup>105</sup> Thus, rotational motion of the  $\text{ClO}_3^-$  ion will necessarily involve some component of O(2) $\cdots$ H stretching. Since the hydrogen bond is anharmonic, the chlorate rotational bands are expected to be broad and to display appreciable temperature-dependent frequency shifts. Table 6.20 shows that

infrared transmission bands at 175 and 165  $\text{cm}^{-1}$  underwent the greatest temperature shift,  $\Delta\nu/\nu$ , in going from 300 to 90°K (0.05 and 0.036, respectively). Tables 4.9 and 4.10 show that in the lattice mode region below 200  $\text{cm}^{-1}$ , the medium intensity conductivity peaks at 173 and 160  $\text{cm}^{-1}$  have the largest band widths (FWHM = 15 and 8.7  $\text{cm}^{-1}$ , respectively). This data supports an assignment of the Bu mode at 173  $\text{cm}^{-1}$  and the Au mode at 160  $\text{cm}^{-1}$  to  $R_x$  and  $R_y$  motions of the  $\text{ClO}_3^-$  ion. The shoulder observed at 83  $\text{cm}^{-1}$  in the conductivity spectrum of polycrystalline  $\text{Ba}(\text{ClO}_3)_2 \cdot \text{H}_2\text{O}$ , and the very weak Raman band at 82  $\text{cm}^{-1}$  reported by Bertie *et al.*<sup>130</sup> for a sample at 90°K, are ascribed to predominantly  $R_z$  motion. It must be emphasized that these assignments are still tentative. Further work, in particular temperature-dependence and isotopic substitution studies, are required for unambiguous assignments. Our major contribution to the lattice mode assignment of  $\text{Ba}(\text{ClO}_3)_2 \cdot \text{H}_2\text{O}$  has been to determine the symmetry of these vibrations; this had not been previously possible by single crystal infrared transmission measurements.<sup>130</sup>

### 6.3 Dipole Moment Derivative Calculations

Two of the principle reasons for studying infrared intensities are to compare the optical characteristics of molecules in different states and media and to obtain information about intermolecular forces. In order to achieve meaningful results, the observed absorption intensities must be corrected for the change in the macroscopic electric

field strength as it enters the dielectric material, and for the local electrostatic inductive effect of surrounding molecules.<sup>212,213</sup> In the case of infrared intensities derived from imaginary dielectric constant spectra, only the local field correction is required, since the change in field strength has already been accounted for.

To correct for these effects, a microscopic model for the absorption process must be assumed. It is common to use a damped harmonic oscillator model for the shape of the absorption band and a Lorentz local field (equation [1.55]) for the internal field correction.<sup>213</sup> As indicated in Section 1.1d, the Lorentz local field is only strictly applicable to molecules located on sites of tetrahedral or higher symmetry. For molecules on crystal sites of lower symmetry, the local field must be evaluated from the lattice sums and atomic polarizabilities.<sup>30</sup> This type of calculation is a major undertaking for a complex monoclinic crystal such as  $\text{Ba}(\text{ClO}_3)_2 \cdot \text{H}_2\text{O}$  and, therefore, the Lorentz local field approximation was used. Once these models are chosen, the band features (shape, position, and intensity) only depend on the dipole moment derivative,  $\partial \mu / \partial Q_i$ , the resonance frequency,  $\nu_i$ , and the lifetime of the state,  $\gamma^{-1}$ , which are the parameters used to interpret gas-phase spectra.<sup>213</sup> However, it should be emphasized that the optical parameters derived for condensed phases are model-dependent.

In Section 4.3, the oscillator strengths  $S_j$  for the fundamental vibrations of  $\text{Ba}(\text{ClO}_3)_2 \cdot \text{H}_2\text{O}$  were determined from  $\epsilon''(\nu)$  by a classical damped oscillator model. The values of the associated dipole derivatives with respect to the crystal normal coordinates,  $\partial \mu / \partial Q_j$ , are calculated by rearrangement of equation [1.56]:

$$\left( \frac{\partial \mu}{\partial Q_j} \right)^2 = S_j \frac{\pi c^2}{N F_j^2} \quad [6.1]$$

where  $N$  = number of primitive unit cells/cm<sup>3</sup>

$c$  = speed of light in vacuum

$F_j$  = Lorentz local field,  $(\epsilon_b + 2)/3$ .

For brevity,  $\partial \mu / \partial Q_j$  is termed the crystal dipole derivative. Similarly, the dipole moment derivatives with respect to the molecular normal coordinates are referred to as molecular dipole derivatives.

Although  $\epsilon_b$  is frequently set equal to the sodium D-line value of  $\epsilon'(\nu)$ , strictly speaking, it is the real dielectric constant due to all vibrations, excluding the one of interest. In this study,  $\epsilon_b$  was obtained from the background level of  $\epsilon'(\nu)$ , to high frequency of the given band. The accuracy of  $\epsilon_b$  is estimated to be  $\pm 0.05$  which, for  $\epsilon_b = 2.5$ , results in an uncertainty of  $\sim 1\%$  in the computed  $\partial \mu / \partial Q$  value. Crystal data relevant to the dipole moment derivative calculations for  $\text{Ba}(\text{ClO}_3)_2 \cdot \text{H}_2\text{O}$  are given in Table 6.22. The number of primitive unit cells per cm<sup>3</sup>,  $N$ , is  $3.045 \times 10^{21}$ . Table 6.23 lists the resonance frequen-

Table 6.22 Crystal Data<sup>105</sup> Used in Dipole Moment Derivative Calculations for  $\text{Ba}(\text{ClO}_3)_2 \cdot \text{H}_2\text{O}$

Temperature = 298°K

$\angle \text{HOH} = 110.7^\circ$

$r(\text{O-H}) = 0.958 \text{ \AA}$

Body-centered cell

$a = 8.916 \text{ \AA}$     $b = 7.832 \text{ \AA}$     $c = 9.425 \text{ \AA}$     $\beta = 93.65^\circ$

$V = 656.8 \times 10^{-24} \text{ cm}^3$

Primitive cell

$Z = 2$

$N = 3.045 \times 10^{21} \text{ unit cells/cm}^3$

Table 6.23 Crystal Dipole Moment Derivatives of the Internal Water Modes in  $\text{Ba}(\text{ClO}_3)_2 \cdot \text{H}_2\text{O}$  ( $\text{D \AA}^{-1} \text{ amu}^{-\frac{1}{2}}$ )

Molecular Mode	Crystal Mode	$\nu$ ( $\text{cm}^{-1}$ )	S ( $\times 10^4 \text{ cm}^{-2}$ )	$\epsilon_b^\dagger$	$ \partial \mu / \partial Q ^\ddagger$
$\nu_1$	Au	3514	9.31	2.40	2.58
$\nu_2$	Au	1606	1.91	2.45	1.16
$\nu_3$	Bu	3584	13.7*	2.40	3.13

\*component along a'-axis

$^\dagger \epsilon_b$  estimated to be accurate to  $\pm 0.05$

$^\ddagger 1 \text{ D \AA}^{-1} \text{ amu}^{-\frac{1}{2}} = 1.2886 \times 10^{-2} \text{ cm}^{3/2} \text{ s}^{-1}$

cies; oscillator strengths, background dielectric constants, and crystal dipole derivatives of the internal water modes. The values of  $\partial \mu / \partial Q_j$  are reported in units of  $D \text{ \AA}^{-1} \text{ amu}^{-\frac{1}{2}}$  where one Debye, 1 D, equals  $10^{-18}$  esu-cm. Since the measured intensity is proportional to  $(\partial \mu / \partial Q)^2$ , only the magnitude of  $\partial \mu / \partial Q$  could be determined.

The molecular normal coordinates  $q_k$  are related to the crystal normal coordinates  $Q_j$  by

$$q = L^c Q \quad [6.2]$$

where the crystal eigenvector matrix  $L^c$  is obtained from a lattice dynamics calculation. The transformation of variables from  $\partial \mu / \partial Q$  to  $\partial \mu / \partial q$  is performed via:

$$\frac{\partial \mu}{\partial Q_j} = \sum_k \sum_i \frac{\partial \mu}{\partial q_{ik}} \cdot \frac{\partial q_{ik}}{\partial Q_j} = \sum_k \sum_i \frac{\partial \mu}{\partial q_{ik}} \cdot l_{ijk}^c \quad [6.3]$$

where the vector sums extend over all the  $i$  equivalent sites in the crystal and the  $k$  molecular modes. In favorable cases, a crystal normal coordinate only involves one type of molecular motion, and equation [6.3] simplifies to:

$$\frac{\partial \mu}{\partial Q_j} = \sum_i \frac{\partial \mu}{\partial q_{ik}} \cdot l_{ijk}^c, \quad [6.4]$$

which implies that the crystal normal coordinates are symmetrized unit-cell coordinates. This approximation is referred to as the Oriented Gas Model<sup>214</sup> and is frequently

employed in the interpretation of infrared and Raman intensity data. The eigenvector elements  $\epsilon_{ijk}^C$  are then simply obtained by standard projection operator methods.

The crystal eigenvector matrix  $L^C$  is not known for  $\text{Ba}(\text{ClO}_3)_2 \cdot \text{H}_2\text{O}$ , so the transformation to  $\partial \mu / \partial q$  values is restricted to crystal modes involving predominantly one type of molecular motion. This condition is approximately satisfied by the  $\nu_1(\text{Au})$ ,  $\nu_2(\text{Au})$  and  $\nu_3(\text{Bu})$  modes of  $\text{H}_2\text{O}$  and the  $\nu_2(\text{Au})$  mode of  $\text{ClO}_3^-$  ion.

Intramolecular mode mixing is not expected for the internal water vibrations of  $\text{Ba}(\text{ClO}_3)_2 \cdot \text{H}_2\text{O}$  which are either well-separated in frequency, or of different symmetry type. Figure 1.7 shows that the H-O-H planes of the water molecules in the unit cell are parallel and, under the oriented gas model, the crystal dipole moment derivative of the internal water modes is predicted to be either parallel to the  $C_2$ -axis (Au) or perpendicular to it (Bu). The crystal normal coordinates  $Q_j^{(k)}$  constructed from the molecular normal coordinates  $q_{ik}$  are:

$$Q_{\text{Au}}^{(1)} = \frac{1}{\sqrt{2}} (q_{11} - q_{21})$$

$$Q_{\text{Au}}^{(2)} = \frac{1}{\sqrt{2}} (q_{12} - q_{22}) \quad [6.5]$$

$$Q_{\text{Bu}}^{(3)} = \frac{1}{\sqrt{2}} (q_{13} - q_{23})$$

where the interchange group is  $C_1$ . This gives the simple result that  $\partial \mu / \partial q_j = 1/\sqrt{2} \partial \mu / \partial Q_j$ .

Since the molecular dipole derivatives depend upon the particular isotopic species, it has been common practice to convert these values to dipole derivatives with respect to the internal coordinates  $R_i$ . Under the Born Oppenheimer approximation, the  $\partial \underline{\mu} / \partial R_i$  are isotopically invariant.<sup>215</sup> An intermediate step in this conversion process is the calculation of dipole moment derivatives with respect to symmetry coordinates,  $\partial \underline{\mu} / \partial S_i$ . The  $S_i$  are constructed from sets of equivalent internal coordinates by the use of projection operators. The transformation to bond parameters requires knowledge of the molecular eigenvector matrix  $L$  for the normal vibrations and a model for the molecular dipole. The eigenvectors  $\ell_{ik}$  relate the symmetry coordinates  $S_i$  to the molecular normal coordinates  $q_k$ , via the matrix equation<sup>216</sup>

$$\underline{S} = \underline{L} \underline{q}, \quad [6.6]$$

and are available from a normal coordinate analysis. A frequently used model for the molecular dipole is the bond moment approximation.<sup>212,217</sup> This assumes that the total dipole moment change during a molecular vibration is the vector sum of the dipole derivatives with respect to the internal displacement coordinates  $R_j$ . A mathematical formulation of the bond moment model is:

$$\frac{\partial \underline{\mu}}{\partial q_k} = \sum_i \frac{\partial \underline{\mu}}{\partial S_i} \cdot \ell_{ik} = \sum_i \ell_{ik} \sum_j \frac{\partial \underline{\mu}}{\partial R_j} \frac{\partial R_j}{\partial S_i} \quad [6.7]$$

The general procedure for transforming crystal dipole derivatives to symmetry coordinate dipole derivatives is schematically outlined in Table 6.24; at each stage, it is illustrated for the internal water modes of  $\text{Ba}(\text{ClO}_3)_2 \cdot \text{H}_2\text{O}$ .

The L matrix was obtained from the force constant calculations of Bertie *et al.*<sup>130</sup>

The ambiguity in sign of  $\partial \mu / \partial q_k$ , results in  $2^n$  different solutions for  $\partial \mu / \partial S_i$ , where  $n$  is the number of normal coordinates  $q_k$  which belong to the same irreducible representation as  $S_i$ . Thus, a wide range of  $\partial \mu / \partial S_i$  values are possible unless  $n$  is a very small number or the normal coordinate is dominated by one term (e.g. in hydrogen vibrations). In Table 6.25, the various sign combinations of  $\partial \mu / \partial q_k$  and the corresponding  $\partial \mu / \partial S_i$  values are tabulated for the internal water modes of  $\text{Ba}(\text{ClO}_3)_2 \cdot \text{H}_2\text{O}$ . For  $\partial \mu / \partial q_3$ ,  $n = 1$ , and the magnitude of  $\partial \mu / \partial S_3$  is unambiguously determined as  $2.13 \text{ D } \text{\AA}^{-1}$ . However, this only represents the component of  $\partial \mu / \partial S_3$  along the  $a'$ -axis. Further polarized infrared reflectance work is required on a crystal face containing the  $c$ -axis in order to completely determine the orientation and magnitude of  $\partial \mu / \partial S_3$ . On the other hand, the complete vector properties of  $\partial \mu / \partial S_1$  and  $\partial \mu / \partial S_2$  are given by the b-polarized reflectance measurements.

The symmetry coordinates for the water vibrations of  $\text{Ba}(\text{ClO}_3)_2 \cdot \text{H}_2\text{O}$  are defined in Table 6.24. The bond moment approximation gives the following relationship between the

Table 6.24 Transformation of Dipole Moment Derivatives from Crystal Normal Coordinates to Internal Symmetry Coordinates and Application to the Water Modes of  $\text{Ba}(\text{ClO}_3)_2 \cdot \text{H}_2\text{O}$

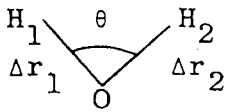
Procedure	Applied to $\text{Ba}(\text{ClO}_3)_2 \cdot \text{H}_2\text{O}$
$\pm  \partial \mu / \partial Q_k $	$\pm  \partial \mu / \partial Q_k $ in Table 6.23
oriented gas model	
$\pm  \partial \mu / \partial q_k $	$\left  \frac{\partial \mu}{\partial q_k} \right  = \frac{1}{\sqrt{2}} \left  \frac{\partial \mu}{\partial Q_k} \right $
Define internal coordinates	 $\begin{aligned} R_1 &= \Delta r_1 \\ R_2 &= \Delta r_2 \\ R_3 &= \Delta \theta \end{aligned}$
Define symmetry coordinates	$r = r_1 = r_2$
Obtain eigenvector matrix L from normal coordinate calculations, where $\tilde{S} = \tilde{L} \tilde{q}$	$S_1 = \frac{1}{\sqrt{2}} (\Delta r_1 + \Delta r_2)$ $S_2 = r \Delta \theta$ $S_3 = \frac{1}{\sqrt{2}} (\Delta r_1 - \Delta r_2)$
$\left( \frac{\partial \mu}{\partial q_k} \right) = \sum_i \left( \frac{\partial \mu}{\partial S_k} \right) l_{ik}$	$\tilde{L} = (\text{a.m.u.})^{-1/2} = \begin{matrix} & \begin{matrix} q_1 & q_2 & q_3 \end{matrix} \\ \begin{matrix} S_1 \\ S_2 \\ S_3 \end{matrix} & \begin{bmatrix} 1.016 & 0.038 & 0 \\ -0.142 & 1.525 & 0 \\ 0 & 0 & 1.038 \end{bmatrix} \end{matrix}$ $\left( \frac{\partial \mu}{\partial q_1} \right) = 1.016 \left( \frac{\partial \mu}{\partial S_1} \right) - 0.142 \left( \frac{\partial \mu}{\partial S_2} \right)$ $\left( \frac{\partial \mu}{\partial q_2} \right) = 0.038 \left( \frac{\partial \mu}{\partial S_1} \right) + 1.525 \left( \frac{\partial \mu}{\partial S_2} \right)$ $\left( \frac{\partial \mu}{\partial q_3} \right) = 1.038 \left( \frac{\partial \mu}{\partial S_3} \right)$

Table 6.25 Dipole Moment Derivatives with Respect to Symmetry Coordinates for the Internal Water Modes of  $\text{Ba}(\text{ClO}_3)_2 \cdot \text{H}_2\text{O}$  (in  $\text{D}\text{\AA}^{-1}$ )

Solution No.	Signs of $\partial \mu / \partial q_i$	$\partial \mu / \partial S_1$	$\partial \mu / \partial S_2$	$\partial \mu / \partial S_3^*$
1	+ + ±	1.87	0.490	±2.13
2	+ - ±	1.72	-0.579	±2.13
3	- + ±	-1.72	0.579	±2.13
4	- - ±	-1.87	-0.490	±2.13

\* component along  $a'$ -axis.

Table 6.26 Calculated Values of  $\partial \mu / \partial r$  and  $\partial \mu / \partial \theta$  for Internal Water Modes in  $\text{Ba}(\text{ClO}_3)_2 \cdot \text{H}_2\text{O}$

Solution No.	$\frac{\partial \mu}{\partial r} (\text{D}\text{\AA}^{-1})$	$\frac{\partial \mu}{\partial \theta} (\text{D})$
1	+2.33	+0.47
2	+2.14	-0.55
3	-2.33	+0.55
4	-2.14	-0.47
average magnitude	$2.23 \pm 0.10$	$0.51 \pm 0.04$

symmetry coordinate dipole derivatives and the bond moment derivatives  $\partial \underline{\mu} / \partial r$  and  $\partial \underline{\mu} / \partial \theta$ :

$$\left| \frac{\partial \underline{\mu}}{\partial S_1} \right| = \sqrt{2} \left| \frac{\partial \underline{\mu}}{\partial r} \right| \cos \frac{\theta}{2}$$

$$\left| \frac{\partial \underline{\mu}}{\partial S_2} \right| = \frac{1}{r} \left| \frac{\partial \underline{\mu}}{\partial \theta} \right|$$

$$\left| \frac{\partial \underline{\mu}}{\partial S_3} \right| = \sqrt{2} \left| \frac{\partial \underline{\mu}}{\partial r} \right| \sin \frac{\theta}{2} \quad [6.8]$$

where  $r$  is the equilibrium OH distance and  $\theta$  is the equilibrium HOH angle (from Table 6.22). Four different values of  $\partial \underline{\mu} / \partial r$  and  $\partial \underline{\mu} / \partial \theta$  were computed for  $\text{Ba}(\text{ClO}_3)_2 \cdot \text{H}_2\text{O}$ , corresponding to the different solutions for  $\partial \underline{\mu} / \partial S_1$  and  $\partial \underline{\mu} / \partial S_2$  in Table 6.25; the average magnitudes are  $2.23 \pm 0.10 \text{ D } \text{\AA}^{-1}$  and  $0.51 \pm 0.04 \text{ D}$ , respectively.

In the preceding calculations, we have used a zero-order bond moment approximation,<sup>212</sup> i.e. that the dipole moment of a given bond is not affected by changes in other bonds or bond angles during the molecular vibration. This requires that the bond moment derivatives be the same for vibrations of different symmetry type. For some compounds, e.g.  $\text{H}_2\text{O}$  vapor and benzene, this level of approximation has been shown to be inadequate.<sup>212,217</sup> Therefore, it is necessary to check the validity of this model in describing the internal water modes of  $\text{Ba}(\text{ClO}_3)_2 \cdot \text{H}_2\text{O}$  before discussing the significance of the results.

The polarized infrared reflection measurements on the (001) crystal face gave us the projection of the  $\nu_3(\text{Bu})$  mode along the  $a'$ -axis. If the angle between  $a'$  and the  $\nu_3$  transition moment is denoted  $A$ , then the observed symmetry coordinate dipole derivative,  $(\partial\mu/\partial S_3)_{\text{obs}} = (\partial\mu/\partial S_3)_{\text{cal}} \cos A$ , where  $(\partial\mu/\partial S_3)_{\text{cal}}$  is given by equation [6.8]. Under the assumption that  $\partial\mu/\partial r$  is the same for  $\nu_1(\text{Au})$  and  $\nu_3(\text{Bu})$ ,  $(\partial\mu/\partial S_3)_{\text{cal}} = 2.60 \pm 0.12 \text{ D } \text{\AA}^{-1}$  and  $A = 35 \pm 4^\circ$ . This agrees with the value of  $37^\circ$  expected for  $\partial\mu/\partial S_3$  oriented along the HOH plane (see Figure 6.2), and supports the validity of the bond moment model.

It is of interest to compare our bond moment derivatives with those obtained for water vibrations in the vapor,<sup>215</sup> liquid,<sup>218</sup> and ice<sup>219</sup> phases. Literature values of the integrated absorption intensities for these modes in the various phases are reported in Table 6.27, where  $A_i$  corresponds to:<sup>212</sup>

$$A_i = \frac{1}{C\ell} \int_{\text{band } i} \ln \left( \frac{I_0}{I} \right) d\nu \quad [6.9]$$

and  $C$  = concentration in moles/cm<sup>3</sup>

$\ell$  = path length in cm

$I_0$  = incident intensity

$I$  = transmitted intensity.

This can also be expressed in terms of the absorption coefficient,  $\alpha(\nu)$ , given in equation [1.17], as:

Table 6.27 Literature Values of Integrated Absorption Intensities for  $\text{H}_2\text{O}$  Vibrations in the Gas, Liquid and Solid Phases (in  $10^3$  cm/mole)

Ref.	Phase	A (observed)			A* (corrected)		
		$\nu_1$	$\nu_3$	$\nu_2$	$\nu_1$	$\nu_3$	$\nu_2$
215	Vapor	0.22	4.81	6.38	0.22	4.81	6.38
218	Liquid		89.9	5.91		75.8	4.98
219	Ice		140	-		118	-

\* Corrected integrated absorbance given by equation [6.13], where  $n = 1.33$ .

Table 6.28 Calculated Molecular Dipole Derivatives for  $\text{H}_2\text{O}$  Vapor and Comparison with Stark Measured Values

Mode	I.R. absorption			Stark effect†	
	$\omega^*(\text{cm}^{-1})$	$\nu^+(\text{cm}^{-1})$	$\partial\mu/\partial q$ ( $\text{D}\text{\AA}^{-1}\text{amu}^{-1/2}$ )	(D)	( $\text{D}\text{\AA}^{-1}\text{amu}^{-1/2}$ )
1	3833.5	3656.7	$\pm 0.23$	-0.0217	-0.23
2	1648.6	1594.6	$\pm 1.25$	+0.162	+1.13
3	3941.6	3755.8	$\pm 1.09$	+0.0971	+1.05

\* Reference 223.

† Reference 202.

‡ References 224 and 225. Reported  $\partial\mu/\partial q$  values for dimensionless normal coordinates; multiplicative conversion factor from Debye units to  $\text{D}\text{\AA}^{-1}\text{amu}^{-1/2}$  is  $2\pi\sqrt{c\omega/h}$ .

$$A_i = \frac{1}{C} \int_{\text{band } i} \alpha(\nu) d\nu. \quad [6.10]$$

Table 6.27 shows that the infrared intensity of the O-H stretching vibration increases many times in going from the gas to liquid to ice, while the intensity of the bending vibration decreases slightly from gas to liquid. This enhancement in the infrared intensity of an A-H stretching mode, upon condensation, is a characteristic feature of hydrogen-bonded systems.<sup>219</sup>

The relationship between the integrated intensity of a fundamental absorption band and the molecular dipole moment derivative in an isotropic medium is:<sup>212</sup>

$$A_i = \frac{1}{n_i} F_i^2 g_i \left( \frac{\nu_i}{\omega_i} \right) \frac{N_A \pi}{3c^2} \left( \frac{\partial \mu}{\partial q_i} \right)^2 \quad [6.11]$$

where  $n_i$  = refractive index at frequency  $\nu_i$

$F_i$  = local field correction factor

$g_i$  = degeneracy of the transition

$\nu_i$  = absorption frequency

$\omega_i$  = harmonic frequency

$N_A$  = Avogadro's number

$c$  = speed of light in vacuum.

This equation is applicable to molecules in any phase. If the Lorentz local field is assumed and the solution is dilute, this reduces to

$$A_i = \frac{1}{n} \left( \frac{n^2+2}{3} \right)^2 g_i \left( \frac{\nu_i}{\omega_i} \right) \frac{N_A \pi}{3c^2} \left( \frac{\partial \mu}{\partial q_i} \right)^2 \quad [6.12]$$

where  $n$  = refractive index of the solvent or host medium.

The term  $(n^2+2)^2/9n$  in Equation [6.12] is referred to as the Polo-Wilson correction,<sup>220</sup> and simultaneously accounts for the local field effect and the change in macroscopic field strength. Since our oscillator strengths were derived from the area under the conductivity peaks ( $\sigma = nk\nu$ ), the correction for field strength has already been implicitly made.

In Table 6.27, the corrected absorption intensities for the internal water modes in the liquid and ice phases are also listed where

$$A_i^{\text{corr}} = A_i^{\text{obs}} \frac{9n}{(n^2+2)^2} = g_i \left( \frac{\nu_i}{\omega_i} \right) \frac{N_A \pi}{3c^2} \left( \frac{\partial \mu}{\partial q_i} \right)^2 \quad [6.13]$$

and  $n$  was taken as 1.33. The degeneracy,  $g_i$ , in this case, is unity. Many authors<sup>221,222</sup> have equated  $\omega_i$  to  $\nu_i$ , but for the highly anharmonic water vibrations, the correct expression [6.13] should be used. Table 6.28 presents the literature values<sup>223,202</sup> of  $\omega$  and  $\nu$  for  $H_2O$  vapor, and the corresponding molecular dipole moment derivatives, calculated from the absorption intensities via equation [6.13]. For comparison, the values obtained from Stark effect measurements are also given.<sup>224,225</sup> These were reported for dimensionless normal coordinates, in Debye units, so it

was necessary to multiply these values by  $2\pi\sqrt{c\omega/h}$ , where  $h$  = Planck's constant, to convert them to the more usual  $D \text{ \AA}^{-1} \text{ amu}^{-\frac{1}{2}}$  units.<sup>226</sup> It can be seen that the two sets of experimental results are in very close agreement, with the largest discrepancy occurring for the  $\nu_2$  mode. If the anharmonic correction,  $\nu_i/\omega_i$  is assumed to be the same for the vapor, liquid and solid phases, then the magnitude of  $\partial\mu/\partial q_i$  in phase  $\alpha$  is simply given by:

$$\left| \frac{\partial\mu}{\partial q_i} \right|_{\alpha} = \left( \frac{A_{i(\alpha)}^{\text{corr.}}}{A_{i(\text{gas})}^{\text{corr.}}} \right)^{\frac{1}{2}} \left| \frac{\partial\mu}{\partial q_i} \right|_{\text{gas}} \quad [6.14]$$

The signs of  $\partial\mu/\partial q_i$  were chosen to correspond with the Stark results of Clough *et al.*<sup>225</sup> and Flaud and Camy-Peyret.<sup>224</sup>

Strong overlap of the  $\nu_1$  and  $\nu_3$  modes in both liquid water and ice prevented resolution of their separate band intensities. Thus, only the sum of the squares of  $\partial\mu/\partial q_1$  and  $\partial\mu/\partial q_3$  could be determined. These molecular dipole derivatives are reported in Table 6.29. The bond moment derivatives,  $\partial\mu/\partial r$  and  $\partial\mu/\partial \theta$ , calculated under the zero-order bond moment approximation, are also given. The eigenvector matrix  $L$  used in this conversion was taken from the normal coordinate analysis of water vapor by I. Mills.<sup>223</sup> Comparison with our results for the internal water modes of  $\text{Ba}(\text{ClO}_3)_2 \cdot \text{H}_2\text{O}$  shows that the magnitude of  $\partial\mu/\partial r$  is in closest correspondence with the value for liquid water.

Table 6.29 Comparison of Molecular Dipole and Bond Moment Derivatives of  $\text{H}_2\text{O}$  Internal Modes in Different Substances

$\text{H}_2\text{O}$ Phase (mode(s))	$\partial\mu/\partial q$ ( $\text{D}\text{\AA}^{-1}\text{amu}^{-1/2}$ )	$ \partial\mu/\partial r $ ( $\text{D}\text{\AA}^{-1}$ )	$ \partial\mu/\partial\theta $ (D)
vapor ( $\nu_1+\nu_3$ ) ( $\nu_2$ )	1.11 1.25	0.77	$0.82\pm0.03$
liquid ( $\nu_1+\nu_3$ ) ( $\nu_2$ )	4.31 1.10	3.0	$0.72\pm0.11$
ice ( $\nu_1+\nu_3$ )	5.37	3.7	-
$\text{Ba}(\text{ClO}_3)_2\cdot\text{H}_2\text{O}$ ( $\nu_1$ ) ( $\nu_2$ )	$\pm 1.82$ $\pm 0.82$	$2.23\pm0.10$	$0.51\pm0.04$

\* Quoted errors reflect uncertainty in sign of  $\partial\mu/\partial r$ .

Table 6.30 Crystal Dipole Moment Derivatives of the External Water Modes in  $\text{Ba}(\text{ClO}_3)_2\cdot\text{H}_2\text{O}$  ( $\text{D}\text{\AA}^{-1}\text{amu}^{-1/2}$ )

Molecular Mode	Crystal Mode	$\nu$ ( $\text{cm}^{-1}$ )	S ( $\times 10^4\text{cm}^{-2}$ )	$\epsilon_b^\dagger$	$ \partial\mu/\partial Q $
$R_x$	Bu	487	$0.209^*$	2.50	$0.38^*$
$R_y$	Bu	404	$3.90^*$	2.50	$1.64^*$
$R_z$	Au	388	0.063	2.90	0.19
$T_z$	Au	230	1.20	2.90	0.83
$T_y$	Bu	210	$0.887^*$	2.50	$0.78^*$

\* Component along  $a'$ -axis.

$^\dagger \epsilon_b$  estimated to be accurate to  $\pm 0.05$ .

The dipole moment derivatives with respect to the crystal normal coordinates have also been computed for the external water modes of  $\text{Ba}(\text{ClO}_3)_2 \cdot \text{H}_2\text{O}$ . These values are listed in Table 6.30, along with the measured transition strengths (Tables 4.9 and 4.10), and estimated background dielectric constants (from Figures 4.9 and 4.12). Further data reduction to molecular coordinates is not possible without the crystal eigenvector matrix. It was previously shown in Section 6.2a that the oriented gas model failed to describe the observed intensity and polarization behavior of the rocking and wagging motions. Since the lattice modes are close in frequency, they are undoubtedly of mixed character.

The crystal dipole moment derivatives were also calculated for the internal chlorate ion modes of  $\text{Ba}(\text{ClO}_3)_2 \cdot \text{H}_2\text{O}$ . These results, as well as the experimental  $S_j$  and  $\epsilon_b$  values, are presented in Table 6.31. Again, transformation of the  $\partial \mu / \partial Q$ 's to bond moment derivatives is not feasible until the Bu crystal modes are fully determined and the crystal and molecular eigenvector matrices are obtained from a normal coordinate analysis. However, it is expected that the crystal modes at  $612 \text{ cm}^{-1}$  (Au) and  $616 \text{ cm}^{-1}$  (Bu), which are well-separated ( $>100 \text{ cm}^{-1}$ ) from the other bands, approximately correspond with the symmetrized unit-cell modes involving  $v_2$  molecular motion. The crystal normal coordinates are then given by:

Table 6.31 Crystal Dipole Moment Derivatives of the  
Internal Chlorate Ion Modes in  $\text{Ba}(\text{ClO}_3)_2 \cdot \text{H}_2\text{O}$

Molecular Mode	Crystal Mode	$\nu$ ( $\text{cm}^{-1}$ )	$S$ ( $\times 10^4 \text{ cm}^{-2}$ )	$\epsilon_b^+$	$ \partial \mu / \partial Q ^\dagger$
$\nu_3$	Bu	963	6.65*	2.40	169 (2.17)*
	Au	959	22.5	2.50	304 (3.92)
	Au'	933	1.64	2.75	77.9(1.00)
$\nu_1$	Au	925	0.968	2.75	59.8(0.77)
	Bu	912	12.9*	2.45	233 (3.00)*
	Bu	909	4.46*	2.50	136 (1.75)*
$\nu_2$	Bu	616	2.38*	2.50	99.0(1.28)*
	Au	612	1.34	2.80	69.7(0.90)
$\nu_4$	Au	507	1.81	2.85	80.1(1.03)
	Bu	502	0.380*	2.50	39.6(0.51)*
	Bu	493	1.31*	2.50	73.5(0.95)*
	Au	481	0.349	2.90	34.8(0.45)

\* Component along  $a'$ -axis.

$^\dagger \epsilon_b$  estimated to be accurate to  $\pm 0.05$ .

$^\ddagger$  Values of  $\partial \mu / \partial Q$  reported in  $\text{cm}^{3/2} \text{ s}^{-1}$  and (in parentheses)

$\text{D } \text{\AA}^{-1} \text{ amu}^{-1/2}$ .

$$Q_{Au}^{(2)} = \frac{1}{2} (q_{12} - q_{22} + q_{32} - q_{42}) \quad [6.15]$$

$$Q_{Bu}^{(2)} = \frac{1}{2} (q_{12} - q_{22} - q_{32} + q_{42})$$

Figure 6.1 defines the relationship between the  $\text{ClO}_3^-$  ion sites in the unit cell and the crystal symmetry elements.

Under the oriented gas model, the crystal dipole moment derivative is:

$$\frac{\partial \mu}{\partial Q} = 2 \frac{\partial \mu}{\partial q} \cos \theta \quad [6.16]$$

where  $\theta$  is the angle between the molecular transition moment and the crystal axis direction along which the incident radiation is polarized. For the  $\nu_2$   $\text{ClO}_3^-$  ion vibration, the transition moment lies along the bisector of the  $\text{ClO}_3$  pyramid. From the  $\text{Ba}(\text{ClO}_3)_2 \cdot \text{H}_2\text{O}$  crystal structure,<sup>105</sup> the direction cosines of this vector, denoted  $l$ ,  $m$ , and  $n$ , with reference to the  $a'$ ,  $b$ , and  $c$  crystal axes, respectively are:

$$l = 0.726 \quad m = 0.672 \quad n = 0.145 \quad [6.17]$$

Thus, the bisector of the  $\text{ClO}_3^-$  ion pyramid makes an angle of  $\theta = \cos^{-1}(0.726) = 43.4^\circ$  with the  $a'$ -axis and

$\theta = \cos^{-1}(0.672) = 47.8^\circ$  with the  $b$ -axis. Substitution of

these direction cosines into equation [6.16], along with the associated crystal dipole derivatives from Table 6.31, gives:

$$\left| \frac{\partial \mu}{\partial Q} \right| = 2 \left| \frac{\partial \mu}{\partial q} \right| \cos(43.4^\circ) = 99.0 \text{ cm}^{3/2} \text{ s}^{-1} \quad [6.18]$$

$$\left| \frac{\partial \mu}{\partial Q} \right| = 2 \left| \frac{\partial \mu}{\partial q} \right| \cos(47.8^\circ) = 69.7 \text{ cm}^{3/2} \text{ s}^{-1} \quad [6.19]$$

Solution of equation [6.18] gives a  $|\partial \mu / \partial q|$  of

68.1  $\text{cm}^{3/2} \text{s}^{-1}$ , whereas equation [6.19] gives a value of 51.9  $\text{cm}^{3/2} \text{s}^{-1}$ . According to the oriented gas model,  $|\partial \underline{\mu} / \partial q|$  should be the same for the Au and Bu factor group components of  $\nu_2$ . The failure of this prediction suggests that the neglected intermolecular interactions are important. A more accurate description of the observed multiplet intensity for the  $\nu_2 \text{ClO}_3^-$  ion mode requires the crystal eigenvector matrix. However, the oriented gas approximation gives a reasonable estimate of  $\partial \underline{\mu} / \partial q_2$  as  $60 \pm 8 \text{ cm}^{3/2} \text{s}^{-1}$  ( $0.77 \pm 0.10 \text{ D \AA}^{-1} \text{amu}^{-1/2}$ ).

It is of interest to compare this result with those previously obtained from infrared intensity studies on  $\text{ClO}_3^-$  ion. In Table 6.32, the chlorate ion dipole derivatives are reported for  $\text{NaClO}_3$ ,<sup>96,97,227</sup>  $\text{RbClO}_3$ ,<sup>227</sup> and  $\text{ClO}_3^-$  in KBr pellets.<sup>222,228</sup> To illustrate the self-consistency of a particular method, two independent sets of  $\partial \underline{\mu} / \partial q$  values are quoted for both  $\text{NaClO}_3$  and  $\text{ClO}_3^-$  in KBr.

The first set of  $\partial \underline{\mu} / \partial q$  values are from the normal incidence infrared reflectance measurements on single crystal  $\text{NaClO}_3$  by Andermann and Dows.<sup>96</sup> The transition strengths were computed from the KK-derived optical constants, via

$$S_i = \frac{2}{\pi} \int_{\text{band } i} \epsilon'' \nu d\nu. \quad [1.87]$$

As discussed in Section 1.4, these authors report erroneous values of  $\partial \underline{\mu} / \partial q$  because of an incorrect evaluation of the lattice sums. The correct procedure for calcula-

Table 6.32 Comparison of Chlorate Ion Dipole Derivatives  
 Calculated for  $\text{NaClO}_3$ ,  $\text{RbClO}_3$  and  $\text{ClO}_3^-$  in KBr  
 ( $\text{cm}^{3/2} \text{s}^{-1}$ )

Mode	$\nu(\text{cm}^{-1})^*$	$\text{NaClO}_3^+$		$\text{NaClO}_3^\dagger \quad \text{RbClO}_3^\dagger$		$\text{ClO}_3^-$ in KBr <sup>§</sup>	
		Ref. 96	Ref. 97	Ref. 227		Ref. 222	Ref. 228
$\nu_1$	938	120	99.4	95	76	52.4	66.8
$\nu_2$	615	70.5	74.4			44.0	48.4
$\nu_{3a}$	991	175	181	161	193	177	122
$\nu_{3b}$	966						
$\nu_4$	489	41.9	35.9			37.1	36.7

\* Frequencies are from Reference 228.

<sup>†</sup> Calculated from infrared reflectance measured values of  $S_i$  via equations [6.1] and [6.16]; see text.

<sup>‡</sup> Calculated from dipolar lattice theory and measured Raman spectra.

<sup>§</sup> Calculated from infrared absorbance via equation [6.12] and  $n(\text{KBr}) = 1.559$ .

ting the molecular dipole moment derivatives of  $\text{NaClO}_3$  from the measured  $S_i$  is described by Decius and Hexter,<sup>161</sup> and basically follows equations [6.1] and [6.16] of this thesis. Equation [6.16] is appropriate under the oriented gas approximation since  $\text{NaClO}_3$  contains 4 equivalent molecules in the unit cell.<sup>97</sup> Other data relevant to the calculation of  $\partial \mu / \partial q_i$  for  $\text{NaClO}_3$  are: i) the  $\text{ClO}_3^-$  ions are located on sites of  $C_3$  symmetry,<sup>97</sup> ii) the unit cell edge<sup>229</sup> is 6.5756 Å, iii) the Na-D line value<sup>96</sup> of  $n$  is 1.5, and iv) the Lorentz local field was used.

Hartwig, Rousseau, and Porto<sup>97</sup> also recorded the reflectance spectrum of  $\text{NaClO}_3$ , but determined the transition strengths via a classical dispersion analysis (equation [1.91]). This  $S_i$  data was converted to molecular dipole moment derivatives in the manner outlined above. The derived  $\partial \mu / \partial q$  values are listed in Table 6.32 and exhibit fairly good agreement with the results of Andermann and Dows.<sup>96</sup> The values of  $\partial \mu / \partial q$  obtained from a dipolar coupling model<sup>227</sup> for the  $\nu_1$  and  $\nu_3$  modes of  $\text{NaClO}_3$  and  $\text{RbClO}_3$  single crystal have also been included in Table 6.32. These quantities were recently calculated by R. Frech<sup>227</sup> from the observed vibrational multiplet structure in the Raman spectra, and the local field correction was rigorously determined from the lattice sums and atomic polarizabilities. Thus, the agreement with the infrared reflectance

results is significant and indicates that the Lorentz local field is a reasonable approximation and that dipole-dipole interaction is the primary source of the  $\nu_1$ - $\nu_3$  factor group splittings in  $\text{NaClO}_3$ .

In the last two columns of Table 6.32, chlorate ion dipole derivatives are reported for infrared absorption intensity measurements on pressed pellets of freeze-dried  $\text{KClO}_3$  in KBr. This method was adopted both by Krynauw and Schutte<sup>222</sup> and Hart and Hollenberg.<sup>228</sup> The observed integrated intensities were converted to molecular dipole derivatives via equation [6.12], using  $n$  of KBr<sup>230</sup> equal to 1.559, and setting  $\nu_i/\omega_i$  equal to unity. This technique produced fairly reproducible results, except for  $\nu_3$  where the discrepancy is of the order of 40%. Comparison with the corresponding  $\partial\mu/\partial q$  values for  $\text{NaClO}_3$  and  $\text{RbClO}_3$  shows substantial disagreement, perhaps indicating that the local field experienced in single crystal  $\text{NaClO}_3$  and  $\text{RbClO}_3$  is different from that in powdered  $\text{KClO}_3$ .

Our value of  $\partial\mu/\partial q_2 = 60 \pm 8 \text{ cm}^{3/2} \text{ s}^{-1}$  for  $\text{Ba}(\text{ClO}_3)_2 \cdot \text{H}_2\text{O}$  is in fair agreement with the range of values reported for  $\text{NaClO}_3$  (70-74  $\text{cm}^{3/2} \text{ s}^{-1}$ ). This experimental result supports the oriented gas model as a useful first approximation for obtaining molecular parameters. A more definitive evaluation of these fundamental quantities awaits a complicated normal coordinate analysis.

## CHAPTER VII.

### CONCLUSION

To summarize, the frequencies and symmetries of the fundamental vibrations of crystalline  $\text{Ba}(\text{ClO}_3)_2 \cdot \text{H}_2\text{O}$  have been determined (Section 6.2) from polarized infrared reflectance measurements, at near-normal incidence (Section 3.3). The optical and dielectric constants for this region (Section 4.2) were obtained from a Kramers-Kronig analysis of the reflectance data (Section 4.1).

The experimental errors influencing the measured reflectance were studied in detail and, where possible, were minimized and/or corrected for (Section 5.1). This procedure gave excellent reproducibility and accuracy. In the mid-infrared region, the overall reproducibility of the  $\text{Ba}(\text{ClO}_3)_2 \cdot \text{H}_2\text{O}$  reflectance was 3% of the value, resulting in a similar error in the derived dielectric constants (Section 5.2).

The polarization results largely confirm earlier vibrational assignments of  $\text{Ba}(\text{ClO}_3)_2 \cdot \text{H}_2\text{O}$ . In the case of the water librations, the observation of a weak Au mode at  $388 \text{ cm}^{-1}$ , previously unreported, enabled the rocking, twisting, and wagging motions to be assigned to infrared bands at  $454(\text{Bu})$ ,  $388(\text{Au})$ , and  $404(\text{Bu}) \text{ cm}^{-1}$ , respectively (Section 6.2a). The near-degeneracy of the wagging and twisting frequencies is in agreement with the deuteron magnetic resonance data of Chiba<sup>110</sup> and with the model calculations of

Eriksson and Lindgren<sup>200</sup> for a water molecule in a trigonal environment. The relative intensities and polarization behavior of these vibrations suggest that the rocking and wagging motions are mixed.

The number and symmetry species of the crystal modes in the  $\text{ClO}_3^-$  stretching region ( $\sim 900\text{--}1000\text{ cm}^{-1}$ ) and in the lattice mode region ( $\sim 100\text{--}400\text{ cm}^{-1}$ ), have also been determined (Sections 6.2b and 6.2c). This information was not available from an infrared transmission study of single crystal  $\text{Ba}(\text{ClO}_3)_2 \cdot \text{H}_2\text{O}$  by Bertie *et al.*,<sup>130</sup> because accompanying high reflectivity caused severe band distortion and confused the assignments. On the basis of our infrared polarization results, a reassignment of the *gerade* components of the  $\nu_1$  and  $\nu_3$  vibrations of  $\text{ClO}_3^-$  is proposed which, unlike previous work,<sup>130</sup> does not invoke an unusually large isotopic shift of  $\sim 15\text{ cm}^{-1}$  for the  $\nu_1$  modes of  $^{35}\text{ClO}_3^-$  and  $^{37}\text{ClO}_3^-$ , when the calculated shift is only  $\sim 8\text{ cm}^{-1}$  (Section 6.2b).

The observed reflectance and Kramers-Kronig derived dielectric loss spectra were both successfully modelled with a set of damped harmonic oscillators, indicating that this classical dispersion model is a reasonable description of the infrared absorption process in  $\text{Ba}(\text{ClO}_3)_2 \cdot \text{H}_2\text{O}$  (Section 4.3). The advantages of this combined Kramers-Kronig/Classical Dispersion method for obtaining reliable values of the dispersion parameters are clearly demonstrated, particularly for overlapping bands. From the measured

transition strengths the associated dipole moment derivatives, with respect to the crystal normal coordinates, were evaluated under the assumption of a Lorentz local field (Section 6.3). Under the further assumption of the oriented gas model, the molecular dipole moment derivative for the  $\nu_2$  vibration of  $\text{ClO}_3^-$  was estimated to be  $60 \pm 8 \text{ cm}^{3/2} \text{ s}^{-1}$ .

The transformation from crystal dipole moment derivatives to bond moment derivatives was performed for the internal water modes, under a zero-order bond moment approximation (Section 6.3), using the results of an intramolecular force field calculation by Bertie *et al.*<sup>130</sup> This gave bond moment derivatives of  $\partial \mu / \partial r = 2.23 \pm 0.10 \text{ D } \text{\AA}^{-1}$  and  $\partial \mu / \partial \theta = 0.51 \pm 0.04 \text{ D}$ , where  $r$  is the equilibrium O-H distance and  $\theta$  is the equilibrium H-O-H angle. The fact that independent calculations of  $\partial \mu / \partial r$  from the  $\nu_1(\text{Au})$  and  $\nu_2(\text{Bu})$  stretching vibrations were in good agreement, strongly supports the validity of the bond moment model for these particular O-H vibrations.

Further polarized infrared reflectance measurements on a crystal face of  $\text{Ba}(\text{ClO}_3)_2 \cdot \text{H}_2\text{O}$  containing the c-axis, are required to completely determine the orientation and magnitude of the transition moments for the Bu fundamental modes. A more rigorous evaluation of the bond moment derivatives awaits a full normal coordinate analysis, including a local field correction based on the lattice dipole sums and atomic

polarizabilities. Finally, a study of the temperature dependence of the infrared spectra will enable a more definitive assignment of the overtone and combination transitions.

---

REFERENCES

1. E.E. Bell, in "Handbuch der Physik", Vol. XXV/2a, edited by L. Genzel (Springer-Verlag, Berlin, 1967), p. 1.
2. F. Wooten, "Optical Properties of Solids" (Academic Press, New York, 1972), pp. 15-38.
3. A.R. Von Hippel, "Dielectrics and Waves" (The M.I.T. Press, Cambridge, 1954), pp. 1-8.
4. F. Stern, in "Solid State Physics", Vol. 15, edited by F. Seitz and D. Turnbull (Academic Press, New York, 1963), p. 299.
5. G.R. Fowles, "Introduction to Modern Optics" (Holt, Rinehart, and Winston, Inc., New York, 1975), p. 152.
6. G. Turrell, "Infrared and Raman Spectra of Crystals" (Academic Press, London, 1972), p. 141.
7. Reference 5, pp. 153-154.
8. Reference 1, pp. 4-5.
9. Reference 6, p. 139.
10. J.B. Hasted, in "Methods of Experimental Physics", Vol. 13, Part B, edited by D. Williams (Academic Press, New York, 1976), p. 135.
11. J. Hiraishi, N. Taniguchi, and H. Takahashi, J. Chem. Phys., 65, 3821 (1976).
12. Reference 1, p. 9.
13. Reference 1, p. 16.
14. D.L. Greenaway and G. Harbeke, "Optical Properties and Band Structure of Semiconductors" (Pergamon Press, London, 1968), p. 6.
15. N.H. Hartshorne and A. Stuart, "Practical Optical Crystallography" (American Elsevier Publishing Co. Inc., New York, 1969), p. 47.
16. Reference 5, p. 177.
17. Reference 15, p. 91.

18. P. Gay, "An Introduction to Crystal Optics" (Longmans, Green, and Co. Ltd., London, 1967), p. 36.
19. J.C. Decius and R.M. Hexter, "Molecular Vibrations in Crystals" (McGraw-Hill Inc., New York, 1977), p. 180.
20. E.E. Koch, A. Otto, and K.L. Kliewer, Chem. Phys., 3, 362 (1974).
21. P. Dub, Phys. Status Solidi B, 104, 109 (1981).
22. Reference 6, p. 80.
23. P.W. Atkins, "Physical Chemistry" (W.H. Freeman and Co., San Francisco, 1978), p. 755.
24. Reference 2, pp. 42-52.
25. D.A. Dows, in "Physics and Chemistry of the Organic Solid State", Vol. 1, edited by D. Fox, M.M. Labes, and A. Weissberger (John Wiley & Sons, New York, 1963), p. 672.
26. Reference 19, pp. 190-193.
27. M. Gottlieb, J. Opt. Soc., 50, 343 (1960).
28. D.L. Mills and E. Burnstein, Rep. Prog. Phys., 37, 817 (1974).
29. Reference 6, pp. 148-149.
30. Reference 19, pp. 214-217.
31. J. Fahrenfort, in "Infrared Spectroscopy and Molecular Structure", edited by M. Davies (Elsevier Publishing Co., Amsterdam, 1963), pp. 380-381.
32. H.O. McMahon, J. Opt. Soc. Am., 40, 376 (1950).
33. P.O. Nilsson, Appl. Opt., 7, 435 (1968).
34. J. Casset, J. Opt. Soc. Am., 69, 725 (1979).
35. T.A. McMath, R.A.D. Hewko, O. Singh, A.E. Curzon, and J.C. Irwin, J. Opt. Soc. Am., 67, 630 (1977).
36. C.M. Randall and R.D. Rawcliffe, Appl. Opt., 6, 1889 (1967).
37. E.D. McAlister, J.J. Villa, and C.D. Salzberg, J. Opt. Soc. Am., 46, 485 (1956).

38. C.D. Salzberg and J.J. Villa, J. Opt. Soc. Am., 47, 244 (1957).
39. S. Jyomura, I. Matsuyama, and G. Toda, J. Appl. Phys., 51, 5838 (1980).
40. A.P. Marchetti, C.D. Salzberg, and E.I.P. Walker, J. Chem. Phys., 64, 4693 (1976).
41. J.E. Bertie and E. Whalley, J. Chem. Phys., 46, 1271 (1967).
42. I. Simon, J. Opt. Soc. Am., 41, 336 (1951).
43. D.M. Roessler, Brit. J. Appl. Phys., 16, 1359 (1965).
44. R.E. Lindquist and A.W. Ewald, J. Opt. Soc. Am., 53, 247 (1963).
45. W.R. Hunter, J. Opt. Soc. Am., 55, 1197 (1965).
46. Reference 1, p. 41.
47. O. Hunderi, Appl. Opt., 11, 1572 (1972).
48. Reference 14, p. 25.
49. S.N. Jasperson and S.E. Schnatterly, Rev. Sci. Instrum., 40, 761 (1969).
50. R.M.A. Azzam, Optik, 58, 251 (1981).
51. D.G. Avery, Proc. Phys. Soc. (London), B65, 425 (1952).
52. G.R. Field and E. Murphy, Appl. Opt., 10, 1402 (1971).
53. D.W. Juenker, J. Opt. Soc. Am., 55, 295 (1965).
54. J. Fahrenfort, Spectrochim. Acta, 17, 698 (1961).
55. K. Tsuji and H. Yamada, J. Phys. Chem., 76, 260 (1972).
56. H. Yamada and K. Suzuki, Spectrochim. Acta, 23A, 1735 (1967).
57. J.P. Devlin, G. Pollard, and R. Frech, J. Chem. Phys., 53, 4147 (1970).
58. Reference 1, pp. 51-53.
59. K.D. Cummings and D.B. Tanner, J. Opt. Soc. Am., 70, 123 (1980).

60. E.V. Loewenstein and D.R. Smith, Appl. Opt., 10, 577 (1971).
61. W.T. Beauchamp and J.D. Rancourt, Appl. Opt., 19, 3239 (1980).
62. S.S. Mitra, in "Optical Properties of Solids", edited by S. Nudelman and S.S. Mitra (Plenum Press, New York, 1969), p. 371.
63. M. Cardona, *ibid.*, p. 137.
64. J.S. Toll, Phys. Rev., 104, 1760 (1956).
65. R. de L. Kronig, J. Opt. Soc. Am., 12, 547 (1926).
66. Reference 2, p. 181.
67. T.S. Moss, "Optical Properties of Semi-Conductors" (Butterworths Scientific Publications, London, 1959), p. 24.
68. T.G. Goplen, D.G. Cameron, and R.N. Jones, Appl. Spectrosc., 34, 657 (1980).
69. C.W. Robertson, H.D. Downing, B. Curnutte, and D. Williams, J. Opt. Soc. Am., 65, 432 (1975).
70. J.E. Bertie, H.J. Labbé, and E. Whalley, J. Chem. Phys., 50, 4501 (1969).
71. T.S. Robinson and W.C. Price, Proc. Phys. Soc. (London), 66B, 969 (1953).
72. G. Andermann, A. Caron, and D.A. Dows, J. Opt. Soc. Am., 55, 1210 (1965).
73. Reference 1, p. 42.
74. Reference 4, pp. 338-340.
75. G. Leveque, J. Phys. C, 10, 4877 (1977).
76. R.A. MacRae, E.T. Arakawa, and M.W. Williams, Phys. Rev., 162, 615 (1967).
77. V.K. Miloslavskii, Opt. Spectrosc. (USSR), 21, 193 (1966).
78. D.M. Roessler, Brit. J. Appl. Phys., 17, 1313 (1966).
79. V.K. Zaitsev and M.I. Fedorov, Opt. Spectrosc. (USSR), 44, 691 (1978).

80. F.C. Jahoda, Phys. Rev., 107, 1261 (1957).
81. P.O. Nilsson and L. Munkby, Phys. Kondens. Mater., 10, 290 (1969).
82. D.W. Berreman, Appl. Opt., 6, 1519 (1967).
83. M.R. Querry and W.E. Holland, Appl. Opt., 13, 595 (1974).
84. G.M. Hale, W.E. Holland, and M.R. Querry, Appl. Opt., 12, 48 (1973).
85. J.D. Neufeld and G. Andermann, J. Opt. Soc. Am., 62, 1156 (1972).
86. O.S. Heavens, "Optical Properties of Thin Solid Films" (Butterworths Scientific Publications, London, 1955), p. 92.
87. F.W. King, J. Opt. Soc. Am., 68, 994 (1978).
88. R.K. Ahrenkiel, J. Opt. Soc. Am., 61, 1651 (1971).
89. R.K. Ahrenkiel, J. Opt. Soc. Am., 62, 1009 (1972).
90. R.Z. Bachrach and F.C. Brown, Phys. Rev. B, 1, 818 (1970).
91. L.W. Pinkley, P.P. Sethna, and D. Williams, J. Phys. Chem., 82, 1532 (1978) and references cited therein.
92. H.W. Verleur, J. Opt. Soc. Am., 58, 1356 (1968).
93. W.G. Spitzer and D.A. Kleinman, Phys. Rev., 121, 1324 (1961).
94. V.K. Nangia, H.H. Soonpaa, and B.S. Rao, J. Opt. Soc. Am., 72, 232 (1982).
95. Y. Iyechika, K. Yakushi, and H. Kuroda, Bull. Chem. Soc. Jpn., 53, 603 (1980).
96. G. Andermann and D.A. Dows, J. Phys. Chem. Solids, 28, 1307 (1967).
97. C.M. Hartwig, D.L. Rousseau, and S.P.S. Porto, Phys. Rev., 188, 1328 (1969).
98. M. Pagannone, B. Fornari, G. Mattei, and L. Mattioli, Gazz. Chim. Ital., 109, 511 (1979).
99. J.B. Bates, J. Chem. Phys., 55, 494 (1971).

100. "Gmelins Handbuch der Anorganischen Chemie" (Verlag Chemie, Berlin, 1932), System No. 30, p. 214.
101. W.F. Linke, "Solubilities of Inorganic and Metal-Organic Compounds", Vol. 1 (American Chemical Society, Washington, D.C., 1958), p. 354.
102. "International Critical Tables", Vol. III, edited by E.W. Washburn (McGraw-Hill Book Co. Inc., New York, 1928), p. 105.
103. M.W. Porter and R.C. Spiller, "The Barker Index of Crystals", Vol. II, Pt. 2 (W. Heffer & Sons Ltd., Cambridge, 1956), M. 347.
104. G. Kartha, Proc. Indian Acad. Sci., 36A, 501 (1952).
105. S.K. Sikka, S.N. Momin, H. Rajagopal, and C. Chidambaram, J. Chem. Phys., 48, 1883 (1968).
106. A.A. Silvidi and J.W. McGrath, J. Chem. Phys., 33, 1789 (1960).
107. R.D. Spence, J. Chem. Phys., 23, 1166 (1965).
108. M. Falk and O. Knop, in "Water. A Comprehensive Treatise", Vol. 2, edited by F. Franks (Plenum Press, New York, 1973), pp. 84-86.
109. A.A. Silvidi, J.W. McGrath, and D.F. Holcomb, J. Chem. Phys., 41, 105 (1964).
110. T. Chiba, J. Chem. Phys., 39, 947 (1963).
111. T. Chiba and Y. Kakiuchi, Bull. Chem. Soc. Jpn., 41, 828 (1968).
112. B. Berglund, A. Eriksson, J. Lindgren and J. Tegenfeldt, J. Mol. Struct., 52, 113 (1979).
113. M. Shporer and A.M. Achlama, J. Chem. Phys., 65, 3657 (1976).
114. H.J. Prask and H. Boutin, J. Chem. Phys., 45, 699 (1966).
115. C.L. Thaper, B.A. Dasannacharya, A. Sequeira, and P.K. Iyengar, Solid State Commun., 8, 497 (1970).
116. C.L. Thaper, A. Sequeira, B.A. Dasannacharya, and P.K. Iyengar, Phys. Status Solidi, 34, 279 (1969).
117. S. Kojima, K. Kato, and S. Annaka, J. Phys. Soc. Jpn., 11, 805 (1956).

118. S. Nakamura and H. Enokiya, J. Phys. Soc. Jpn., 18, 183 (1963).
119. C.V. Ramamohan and J. Sobhanadri, J. Phys. Soc. Jpn., 31, 309 (1971).
120. H. Vargas, J. Pelzl, J. Laugier, D. Dautreeppe, and J.P. Mattieu, J. Mag. Res., 20, 269 (1975).
121. J. Pietrzak and J. Kasprzak, Phys. Status Solidi A, 41, K25 (1977).
122. R.K. Khanna and J. Sobhanadri, Phys. Status Solidi A, 17, 65 (1973).
123. L.S.G. Cancelli, G.M. Gualberto, C.A.S. Lima, H. Vargas and J. Pelzl, J. Chem. Phys., 68, 2844 (1978).
124. G.G.T. Guarini, R. Spinicci, and L. Virgili, J. Therm. Anal., 13, 263 (1978).
125. J. Laugier, H. Vargas, A. Baudry, and J. Pelzl, Phys. Status Solidi A, 24, K67 (1974).
126. F.A. Miller and C.H. Wilkins, Anal. Chem., 24, 1253 (1952).
127. F.A. Miller, G.L. Carlson, F.F. Bentley, and W.H. Jones, Spectrochim. Acta, 16, 135 (1960).
128. C. Rocchiccioli, C.R. Acad. Sci., Ser. B, 242, 2922 (1956).
129. K. Fukushima and T. Yanagida, Bull. Chem. Soc. Jpn., 45, 2285 (1972).
130. J.E. Bertie, A.M. Heyns, and O. Oehler, Can. J. Chem., 51, 2275 (1973).
131. G. Brink, Appl. Spectrosc., 30, 630 (1976).
132. B. Berglund, J. Lindgren, and J. Tegenfeldt, J. Mol. Struct., 43, 169 (1978).
133. B. Berglund, J. Lindgren, and J. Tegenfeldt, J. Mol. Struct., 43, 179 (1978).
134. A. Eriksson and J. Lindgren, Acta Chem. Scand., A32, 737 (1978).
135. A. Eriksson, M.A. Hussein, B. Berglund, J. Tegenfeldt, and J. Lindgren, J. Mol. Struct., 52, 95 (1979).

136. A. Eriksson, B. Berglund, J. Tegenfeldt, and J. Lindgren, *J. Mol. Struct.*, 52, 107 (1979).
137. N.B. Abbott and A. Elliott, *Proc. R. Soc. London*, A234, 247 (1956).
138. M. Hass and G.B.B.M. Sutherland, *Proc. R. Soc. London*, A236, 427 (1956).
139. J.R. Jasperse, A. Kahan, J.N. Plendl, and S.S. Mitra, *Phys. Rev.*, 146, 526 (1966).
140. C.K. Wu and G. Andermann, *J. Opt. Soc. Am.*, 58, 519 (1968).
141. A. Kachare, M.P. Soriaga, and G. Andermann, *J. Opt. Soc. Am.*, 64, 1450 (1974).
142. I. Nakagawa, *Bull. Chem. Soc. Jpn.*, 44, 3014 (1971).
143. M. Hass, *Phys. Rev.*, 117, 1497 (1960).
144. A. Hadni, J. Claudel, D. Chanal, P. Strimer, and P. Vergnat, *Phys. Rev.*, 163, 836 (1967).
145. Reference 62, pp. 354-356.
146. D.L. Wood and S.S. Mitra, *J. Opt. Soc. Am.*, 48, 537 (1958).
147. B. Szigeti, *Proc. R. Soc. London*, A204, 51 (1950).
148. H.E. Bennett, M. Silver, and E.J. Ashley, *J. Opt. Soc. Am.*, 53, 1089 (1963).
149. I. Schultz, *J. Opt. Soc. Am.*, 44, 357 (1954).
150. D. Edwards and E. Ochoa, *Appl. Opt.*, 19, 4130 (1980).
151. H.R. Philipp and H. Ehrenreich, *Phys. Rev.*, 129, 1550 (1963).
152. W.G. Spitzer, D. Kleinman and D. Walsh, *Phys. Rev.*, 113, 127 (1959).
153. R.S. Katiyar, P. Dawson, M.M. Hargreave, and G.R. Wilkinson, *J. Phys. C*, 4, 2421 (1971).
154. J. Bernasconi, P. Bruesch, D. Kuse, and H.R. Zeller, *J. Phys. Chem. Solids*, 35, 145 (1974).
155. Y. Ogawa, I. Harada, H. Matsuura, T. Shimanouchi, and J. Hiraishi, *Spectrochim. Acta*, 32A, 49 (1976).

156. J. Biellmann and B. Prevot, *Infrared Phys.*, 20, 99 (1980).
157. W.G. Spitzer, R.C. Miller, D.A. Kleinman, and L.E. Howarth, *Phys. Rev.*, 126, 1710 (1962).
158. J.C. Galzerani and R.S. Katiyar, *Solid State Commun.*, 41, 515 (1982).
159. M. Balkanski, P. Moch, and M.K. Teng, *J. Chem. Phys.*, 46, 1621 (1967).
160. B. Khelifa, A. Delahaigue, and P. Jouve, *J. Phys. Chem. Solids*, 36, 457 (1975).
161. Reference 19, p. 265.
162. L.C. Kravitz, J.D. Kingsley, and E.L. Elkin, *J. Chem. Phys.*, 49, 4600 (1968).
163. L.R. Fredrickson and J.C. Decius, *J. Chem. Phys.*, 63, 2727 (1975).
164. R.E. Carlson and J.C. Decius, *J. Chem. Phys.*, 60, 1251 (1974).
165. P. Dawson, M.M. Hargreave, and G.R. Wilkinson, *J. Phys. C*, 4, 240 (1971).
166. P. Dawson, M.M. Hargreave, and G.R. Wilkinson, *Spectrochim. Acta*, 31A, 1055 (1975).
167. L.P. Mosteller and F. Wooten, *J. Opt. Soc. Am.*, 58, 511 (1968).
168. J.C. Decius, R. Frech, and P. Bruesch, *J. Chem. Phys.*, 58, 4056 (1973).
169. M.V. Belousov and V.F. Pavinich, *Opt. Spectrosc. (USSR)*, 45, 771 (1978).
170. J. Kroupa, *Opt. Commun.*, 30, 282 (1979).
171. M. Frindi, M. Peyrard and M. Remoissenet, *J. Phys. C*, 13, 3493 (1980).
172. I. Tajima, H. Takahashi and K. Machida, *Spectrochim. Acta*, 37A, 905 (1981).
173. W.H. Wright, *J. Chem. Phys.*, 46, 2951 (1967).
174. L.B. Clark and M.R. Philpott, *J. Chem. Phys.*, 53, 3790 (1970).

175. E.E. Koch and A. Otto, Chem. Phys., 3, 370 (1974).
176. W.B. Person, G.C. Pimentel and O. Schnepp, J. Chem. Phys., 23, 230 (1955).
177. G.R. Hunt, C.H. Perry and J. Ferguson, Phys. Rev. A, 134, 688 (1964).
178. A.S. Barker, Phys. Rev. A, 136, 1290 (1964).
179. L.R. Painter, T.S. Riedinger, R.D. Birkhoff and J.M. Heller, J. Appl. Phys., 51, 1747 (1980).
180. "Laboratory Manual on Crystal Growth", edited by Dr. I. Tarján and M. Mátrai (Akadémiai Kiadó, Budapest, 1972), pp. 139-146.
181. M.M. Woolfson, "An Introduction to X-Ray Crystallography", (Cambridge University Press, 1970), p. 152.
182. J.E. Bertie, "Apodization and Phase Correction", in Proc. NATO Adv. Study Inst., Florence, Italy, 1980, edited by J.R. Durig and R. Reidel (Dordrecht, 1980).
183. P.R. Griffiths, "Chemical Infrared Fourier Transform Spectroscopy", (John Wiley and Sons, New York, 1975), pp. 23-30.
184. G. Hass, J. Opt. Soc. Am., 72, 27 (1982).
185. J.R. Birch, Infrared Phys., 18, 613 (1978).
186. C. Rocchiccioli, C.R. Acad. Sci., Ser. B, 249, 236 (1959).
187. W.R. Runyan, "Silicon Semiconductor Technology", (McGraw-Hill Book Co., New York, 1965), p. 199.
188. Reference 187, p. 192.
189. B.J. Berenblut, P. Dawson and G.R. Wilkinson, Spectrochim. Acta, 29A, 29 (1973).
190. Reference 19, pp. 273-280.
191. D.B. Chase, Appl. Spectrosc., 36, 240 (1982).
192. "CRC Handbook of Chemistry and Physics", 62nd edition (CRC Press, Cleveland, 1981) p. A-113.

193. H.J. Bowlden and J.K. Wilmshurst, J. Opt. Soc. Am., 53, 1073 (1963).
194. W.G. Fateley, F.R. Dollish, N.T. McDevitt, and F.F. Bentley, "Infrared and Raman Selection Rules for Molecular and Lattice Vibrations: The Correlation Method (John Wiley and Sons, New York, 1972).
195. S. Bhagavantam and T. Venkatarayudu, Proc. Indian Acad. Sci., 9A, 224 (1939).
196. D.F. Hornig, J. Chem. Phys., 16, 1063 (1948).
197. R.S. Halford, J. Chem. Phys., 14, 8 (1946).
198. Reference 108, p. 109.
199. H. Boutin and S. Yip, "Molecular Spectroscopy with Neutrons", (M.I.T. Press, Cambridge, Massachusetts, 1968), p. 146.
200. A. Eriksson and J. Lindgren, J. Mol. Struct., 48, 417 (1978).
201. G.C. Pimentel, A.L. McClellan, W.B. Person and O. Schnepp, J. Chem. Phys., 23, 234 (1955).
202. Reference 108, p. 89.
203. D.J. Gardiner, R.B. Girling, and R.E. Hester, J. Mol. Struct., 13, 105 (1972).
204. H.D. Lutz and H.J. Klüppel, Ber. Bunsenges. Phys. Chem., 79, 98 (1975).
205. R.G. Whitfield and G.E. Leroy, J. Chem. Phys., 68, 2151 (1978).
206. Reference 19, p. 59.
207. Y. Onodera and Y. Toyozawa, J. Phys. Soc. Jpn., 24, 341 (1968).
208. J.B. Bates and H.D. Stidham, J. Phys. Chem. Solids, 37, 183 (1976).
209. E.W. Montroll and R.B. Potts, Phys. Rev., 100, 525 (1955).
210. W. Soheuermann and C.J.H. Schutte, J. Raman Spectrosc., 1, 605 (1973).

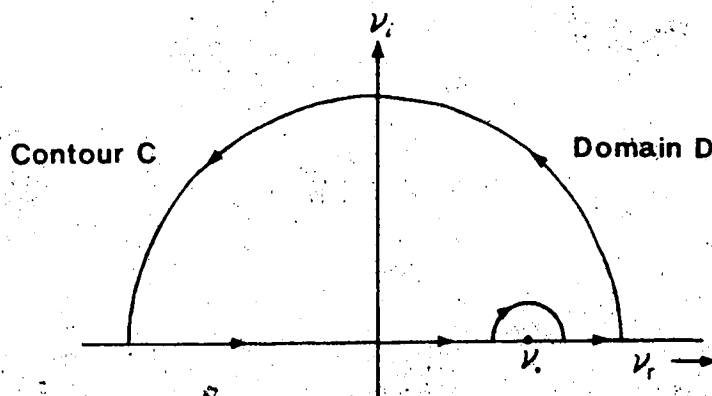
211. Reference 62, p. 401.
212. G. Riley, S. Suzuki, and W.J. Orville-Thomas, in "Vibrational Intensities in Infrared and Raman Spectroscopy", edited by W.B. Person and G. Zerbi (Elsevier Scientific Publishing Co., Amsterdam, 1982), Chapter 8.
213. J.W. Warner and M. Wolfsberg, J. Chem. Phys., 78, 1722 (1983).
214. S. Califano and V. Schettino, Chapter 20 of Reference 212.
215. G. Wilemski, J. Quant. Spectrosc. Radiat. Transfer, 20, 291 (1978).
216. E.B. Wilson, Jr., J.C. Decius and P.C. Cross, "Molecular Vibrations", (McGraw-Hill Book Co. Inc., New York, 1955).
217. D.F. Hornig and D.C. McKean, J. Phys. Chem., 59, 1133 (1955).
218. T. Motojima, S. Ikawa and M. Kimura, J. Quant. Spectrosc. Radiat. Transfer, 25, 29 (1981).
219. S. Ikawa and S. Maeda, Spectrochim. Acta, 24A, 655 (1968).
220. S.R. Polo and M.K. Wilson, J. Chem. Phys., 23, 2376 (1955).
221. J.C. Decius and D. Murhammer, Spectrochim. Acta, 36A, 965 (1980).
222. G.N. Krynauw and C.J.H. Schutte, Z. Physik. Chem. Neue Folge, 55, 121 (1967).
223. I.M. Mills, in "Infrared Spectroscopy and Molecular Structure", edited by M. Davies (Elsevier Publishing Co., Amsterdam, 1963), Chapter 5.
224. J.M. Flaud and C. Camy-Peyret, J. Mol. Spectrosc., 55, 278 (1975).
225. S.A. Clough, Y. Beers, G.P. Klein, and L.S. Rothman, J. Chem. Phys., 59, 2254 (1973).
226. K. Kuchitsu and Y. Morino, Bull. Chem. Soc. Jpn., 38, 815 (1965).

- 227. R. Frech, J. Chem. Phys., 76, 86 (1982).
- 228. G.W. Hart and J.L. Hollenberg, Spectrochim. Acta, 34A, 367 (1978).
- 229. R.W.G. Wyckoff, "Crystal Structures", 2nd ed., Vol. 2 (Interscience Publishers, New York, 1964), p. 380.
- 230. Reference 192, p. B-131.
- 231. Reference 2, p. 176.
- 232. E. Kreyzig, "Advanced Engineering Mathematics", 3rd ed. (John Wiley and Sons, New York, 1972), p. 530.
- 233. Reference 2, p. 247.

# APPENDIX A

## Derivation of Kramers-Kronig Dispersion Relation Between the Real and Imaginary Dielectric Constant

Derivation of the dispersion relation between the real and imaginary components of the complex dielectric function  $\epsilon(\nu)$ , requires an analytic continuation of  $\epsilon(\nu)$  into the upper half of the complex frequency plane.<sup>231</sup> This is represented in Figure A.1 as Domain D, with  $\nu_r$  and  $\nu_i$  denoting the real and imaginary frequency axes, respectively. A contour integration as indicated by pathway C yields the desired dispersion relation. The singularity at  $\nu_0$  along the real frequency axis corresponds to a frequency of resonance absorption, and is enclosed by the contour integral. For a real crystal which possesses several absorption frequencies, this method is easily generalized by summing the partial contributions from each resonance frequency.



# APPENDIX A, continued

In order to apply Cauchy's integral formula,<sup>232'</sup> the contour integral  $C$  must approach zero as the frequency radius becomes infinite. However,  $\lim_{\nu \rightarrow \infty} \hat{\epsilon}(\nu) = 1$  and not 0. The integration must therefore be performed for the modified function  $f(\nu) = \hat{\epsilon}(\nu) - 1$ , which satisfies both this limiting condition and the requirements of causality, boundedness, and linearity. From equation [1.9], it can be seen that  $(\hat{\epsilon}(\nu) - 1)/4\pi$  is the proportionality constant between the electric field  $\underline{E}$  and the induced polarization  $\underline{P}$ . Since polarization cannot be induced in the medium prior to the application of the electric field,  $f(\nu)$  must also be a causal response function.

Cauchy's integral formula then gives that:

$$\oint_C \frac{f(\nu)}{\nu - \nu_0} = P \int_{-\infty}^{\infty} \frac{f(\nu)}{\nu - \nu_0} = i\pi f(\nu_0) \quad [A.1]$$

where  $P$  = Cauchy principal value

and  $f(\nu_0) = \hat{\epsilon}(\nu_0) - 1$ .

Substitution of  $f(\nu) = \hat{\epsilon}(\nu) - 1$  gives:

$$\hat{\epsilon}(\nu_0) - 1 = \frac{1}{\pi i} P \int_{-\infty}^{\infty} \frac{\hat{\epsilon}(\nu) - 1}{\nu - \nu_0} d\nu. \quad [A.2]$$

The  $-1$  term in the integrand may be dropped since:

$$P \int_{-\infty}^{\infty} \frac{1}{\nu - \nu_0} d\nu = 0. \quad [A.3]$$

# APPENDIX A, continued

Thus,

$$\hat{\epsilon}(v_0) - 1 = \frac{1}{\pi i} P \int_{-\infty}^{\infty} \frac{\hat{\epsilon}(v)}{v - v_0} dv. \quad [A.4]$$

Separation of real and imaginary parts gives:

$$\epsilon'(v_0) - 1 = \frac{1}{\pi} P \int_{-\infty}^{\infty} \frac{\epsilon''(v)}{v - v_0} dv \quad [A.5]$$

$$\text{and } \epsilon''(v_0) = \frac{1}{\pi} P \int_{-\infty}^{\infty} \frac{\epsilon'(v)}{v - v_0} dv. \quad [A.6]$$

The fact that  $\hat{\epsilon}(v)$  relates two real field quantities,  $\underline{E}$  and  $\underline{D}$ , imposes the condition that:<sup>233</sup>

$\hat{\epsilon}(-v) = \hat{\epsilon}^*(v)$ , and therefore:

$$\epsilon'(-v) = \epsilon'(v)$$

$$\text{and } \epsilon''(-v) = \epsilon''(v).$$

Equations [A.5] and [A.6] can now be expressed as integrals over positive frequencies:

$$\epsilon'(v_0) - 1 = \frac{2}{\pi} P \int_0^{\infty} \frac{v \epsilon''(v)}{v'^2 - v_0^2} dv \quad [A.7]$$

$$\epsilon''(v_0) = \frac{2v_0}{\pi} P \int_0^{\infty} \frac{\epsilon'(v)}{v'^2 - v_0^2} dv. \quad [A.8]$$

These are the Kramers-Kronig dispersion relations for  $\hat{\epsilon}(v)$  given in equations [1.59] and [1.60]. The corresponding relations between  $n(v)$  and  $k(v)$ , and  $\theta(v)$  and  $\ln R(v)$ , are obtained in an analogous manner.<sup>63</sup>

## APPENDIX B

Reflectance of Polycrystalline  $\text{Ba}(\text{ClO}_3)_2 \cdot \text{H}_2\text{O}$  at 298°K

$\nu$ ( $\text{cm}^{-1}$ )	R	$\nu$ ( $\text{cm}^{-1}$ )	R	$\nu$ ( $\text{cm}^{-1}$ )	R
49.4	.2359	119.5	.2375	350.0	.0961
58.5	.2469	120.1	.2580	375.0	.1062
65.8	.2614	120.7	.2791	408.8	.0953
68.9	.2722	121.3	.2989	413.6	.0840
71.3	.2861	122.0	.3165	419.4	.0736
74.4	.2972	122.6	.3323	427.1	.0636
75.6	.3084	123.2	.3461	469.5	.0756
76.8	.3188	123.8	.3573	472.4	.0861
78.6	.3297	125.0	.3720	475.3	.0970
80.5	.3399	128.1	.3548	478.2	.1100
82.9	.3501	128.7	.3404	497.5	.0979
84.7	.3652	129.3	.3249	501.4	.1155
86.0	.3775	129.9	.3111	502.3	.1282
86.6	.3894	132.9	.3312	503.3	.1399
87.2	.4031	134.8	.3193	506.2	.1195
87.8	.4156	135.4	.2966	507.1	.1049
88.4	.4292	136.0	.2689	509.1	.0899
89.0	.4476	136.6	.2395	510.0	.0797
89.6	.4687	137.2	.2115	511.0	.0612
90.2	.4848	137.8	.1871	512.0	.0384
91.5	.5040	138.4	.1671	512.9	.0213
92.1	.5190	139.0	.1516	529.3	.0315
92.7	.5348	139.6	.1405	542.8	.0415
93.9	.5486	140.9	.1274	562.1	.0518
95.7	.5607	142.7	.1172	582.4	.0622
98.8	.5422	143.9	.1036	594.9	.0724
99.4	.5273	145.1	.0871	601.6	.0836
100.0	.5075	146.4	.0726	605.5	.0957
100.6	.4808	154.3	.0605	608.4	.1079
101.2	.4519	162.2	.0731	619.0	.0949
101.8	.4280	167.7	.0624	620.9	.0790
102.4	.4109	169.5	.0514	621.9	.0660
103.0	.3983	188.9	.0636	622.9	.0518
104.3	.3851	193.8	.0767	623.8	.0397
111.0	.3668	198.6	.0887	625.7	.0284
111.6	.3503	203.4	.1030	635.4	.0394
112.2	.3304	212.1	.0930	647.9	.0495
112.8	.3077	215.9	.0796	673.0	.0596
113.4	.2816	218.8	.0693	712.5	.0697
114.0	.2521	237.2	.0579	761.7	.0799
114.6	.2225	241.0	.0453	804.1	.0899
115.2	.1982	262.2	.0557	828.2	.1003
115.9	.1833	275.7	.0657	846.6	.1109
118.3	.2024	297.9	.0758	859.1	.1216
118.9	.2188	321.0	.0858	868.7	.1320

## APPENDIX B, continued

$\nu$ (cm <sup>-1</sup> )	R	$\nu$ (cm <sup>-1</sup> )	R	$\nu$ (cm <sup>-1</sup> )	R
876.4	.1422	959.4	.4107	1031.7	.0756
882.2	.1525	960.3	.4232	1033.6	.0595
887.1	.1638	961.3	.4354	1035.5	.0447
890.9	.1749	962.3	.4475	1037.5	.0328
893.8	.1854	963.2	.4595	1040.4	.0207
896.7	.1985	964.2	.4712	1045.2	.0101
898.6	.2090	965.2	.4828	1162.8	.0202
900.5	.2217	966.1	.4946	1202.4	.0251
902.5	.2368	967.1	.5062	1222.6	.0272
904.4	.2537	968.0	.5177	1242.9	.0292
906.3	.2708	969.0	.5291	1266.0	.0313
908.3	.2870	970.0	.5402	1294.0	.0333
910.2	.3018	970.9	.5509	1326.7	.0354
912.1	.3154	971.9	.5610	1362.4	.0374
914.0	.3292	973.8	.5773	1427.0	.0394
916.0	.3429	980.6	.5631	1481.0	.0414
917.9	.3557	981.5	.5518	1555.3	.0434
919.8	.3663	982.5	.5385	1586.1	.0456
926.6	.3534	983.5	.5234	1593.8	.0477
928.5	.3413	984.4	.5065	1597.7	.0498
930.4	.3236	985.4	.4880	1600.6	.0525
931.4	.3089	986.4	.4684	1603.5	.0547
932.4	.2885	987.3	.4477	1606.4	.0506
933.3	.2616	988.3	.4265	1607.3	.0470
934.3	.2289	989.3	.4057	1608.3	.0431
935.3	.1936	990.2	.3857	1609.3	.0396
936.2	.1625	991.2	.3672	1610.2	.0369
937.2	.1430	992.2	.3507	1612.2	.0346
941.0	.1618	993.1	.3363	1619.9	.0366
942.0	.1756	994.1	.3240	1626.6	.0388
943.0	.1899	995.0	.3137	1637.2	.0408
943.9	.2044	997.0	.2974	1671.0	.0429
944.9	.2187	998.9	.2847	1706.6	.0449
945.9	.2327	1000.8	.2735	2118.4	.0470
946.8	.2464	1002.8	.2621	2154.1	.0490
947.8	.2597	1004.7	.2497	2202.3	.0511
948.8	.2726	1006.6	.2369	2250.5	.0531
949.7	.2852	1008.5	.2225	2299.7	.0551
950.7	.2977	1010.5	.2055	2631.3	.0571
951.7	.3100	1012.4	.1877	2965.0	.0551
952.6	.3223	1014.3	.1693	3055.6	.0527
953.6	.3345	1016.3	.1533	3444.2	.0547
954.5	.3469	1018.2	.1419	3472.2	.0568
955.5	.3595	1021.1	.1307	3484.7	.0590
956.5	.3723	1024.9	.1174	3493.4	.0612
957.4	.3851	1027.8	.1033	3499.2	.0633
958.4	.3980	1029.8	.0907	3504.0	.0659

## APPENDIX B, continued

$\nu$ ( $\text{cm}^{-1}$ )	R	$\nu$ ( $\text{cm}^{-1}$ )	R	$\nu$ ( $\text{cm}^{-1}$ )	R
3507.8	.0680	3588.8	.0539	5095.0	.0520
3516.5	.0652	3590.8	.0503	5141.2	.0498
3518.4	.0616	3592.7	.0467	5245.4	.0521
3519.4	.0593	3594.6	.0434	5280.1	.0541
3520.4	.0570	3596.5	.0404	5318.7	.0562
3521.3	.0547	3598.5	.0382	5338.0	.0582
3522.3	.0526	3601.4	.0358	5604.1	.0562
3524.2	.0492	3631.3	.0378	5712.1	.0582
3526.2	.0472	3642.8	.0398	5758.4	.0603
3537.7	.0493	3661.2	.0419	6275.2	.0623
3542.5	.0516	3692.0	.0439	6637.7	.0602
3547.4	.0539	3723.8	.0460	6687.9	.0581
3552.2	.0561	3761.4	.0480	6853.7	.0560
3557.0	.0587	3857.9	.0500	6869.2	.0539
3561.8	.0609	4142.3	.0520	7143.0	.0561
3567.6	.0632	4219.4	.0541	7173.9	.0582
3585.0	.0601	4670.7	.0561	7197.0	.0586
3586.9	.0572	5071.8	.0540		

## APPENDIX C

Reflectance of (001) Face of Single Crystal  $\text{Ba}(\text{ClO}_3)_2 \cdot \text{H}_2\text{O}$   
at 298 K;  $\underline{E} \parallel b$  and  $\underline{E} \perp b$

$\underline{E} \parallel b$					
$\nu$ ( $\text{cm}^{-1}$ )	R	$\nu$ ( $\text{cm}^{-1}$ )	R	$\nu$ ( $\text{cm}^{-1}$ )	R
114.7	.3626	168.7	.0622	503.3	.1990
115.7	.2575	169.7	.0388	504.2	.2281
116.6	.2201	170.6	.0266	505.2	.2690
117.6	.2364	172.6	.0151	506.2	.3196
118.6	.2798	183.2	.0257	507.1	.3681
119.5	.3322	190.9	.0378	508.1	.4026
120.5	.3873	197.6	.0496	510.0	.3649
121.4	.4292	203.4	.0617	511.0	.2732
122.4	.4836	208.2	.0748	512.0	.1574
123.4	.5045	214.0	.0887	512.9	.0668
124.3	.4842	220.8	.0999	513.9	.0261
125.3	.4407	222.7	.1105	514.9	.0144
126.3	.3855	225.6	.1229	521.6	.0247
127.2	.3441	228.5	.1376	527.4	.0355
128.2	.2889	235.2	.1231	537.0	.0456
129.2	.2038	236.2	.1123	554.4	.0562
130.1	.1418	237.2	.1007	578.5	.0666
132.1	.1647	238.1	.0869	593.0	.0773
133.0	.2214	239.1	.0722	599.7	.0882
134.0	.2602	240.0	.0566	603.6	.0996
135.9	.2280	241.0	.0424	606.5	.1153
136.9	.1736	242.9	.0291	608.4	.1257
137.8	.1142	245.8	.0179	613.2	.1095
138.8	.0595	264.2	.0281	614.2	.0949
139.8	.0324	278.6	.0385	615.1	.0745
148.4	.0447	304.7	.0490	616.1	.0541
150.4	.0678	339.4	.0599	617.1	.0387
152.3	.0782	412.6	.0700	619.0	.0266
154.2	.0977	458.9	.0811	626.7	.0375
156.2	.1126	471.5	.0927	636.3	.0476
157.1	.1237	476.3	.1078	658.5	.0576
158.1	.1478	482.1	.0873	701.9	.0677
159.1	.1691	489.8	.0995	769.4	.0777
161.0	.1871	493.6	.1097	823.4	.0878
162.9	.1990	496.5	.1225	848.5	.0979
164.8	.1710	498.5	.1363	867.8	.1084
165.8	.1451	500.4	.1482	881.3	.1190
166.8	.1189	501.4	.1600	890.9	.1296
167.7	.0909	502.3	.1767	898.6	.1400

## APPENDIX C, continued

 $E \parallel b$ 

$\nu$ ( $\text{cm}^{-1}$ )	R	$\nu$ ( $\text{cm}^{-1}$ )	R	$\nu$ ( $\text{cm}^{-1}$ )	R
904.4	.1502	996.0	.6367	1586.1	.0547
910.2	.1617	997.0	.6255	1590.0	.0575
915.0	.1728	997.9	.6132	1592.9	.0605
918.9	.1846	998.9	.5989	1594.8	.0632
922.7	.1978	999.9	.5835	1596.7	.0668
926.6	.2096	1000.8	.5674	1597.7	.0689
928.5	.2212	1001.8	.5496	1598.7	.0714
930.4	.2347	1002.8	.5298	1599.6	.0743
934.3	.2211	1003.7	.5091	1600.6	.0776
936.2	.2087	1004.7	.4882	1601.5	.0810
941.0	.2237	1005.7	.4669	1602.5	.0845
943.0	.2410	1006.6	.4449	1603.5	.0873
944.9	.2608	1007.6	.4223	1606.4	.0786
945.9	.2721	1008.5	.3972	1607.3	.0675
946.8	.2836	1009.5	.3686	1608.3	.0544
947.8	.2955	1010.5	.3379	1609.3	.0419
948.8	.3085	1011.4	.3073	1610.2	.0320
949.7	.3223	1012.4	.2766	1611.2	.0257
950.7	.3362	1013.4	.2442	1612.2	.0222
951.7	.3510	1014.3	.2106	1619.9	.0251
952.6	.3676	1015.3	.1781	1622.8	.0277
953.6	.3854	1016.3	.1486	1626.6	.0303
954.5	.4038	1017.2	.1230	1631.4	.0326
955.5	.4241	1018.2	.1018	1637.2	.0348
956.5	.4469	1019.2	.0848	1647.8	.0369
957.4	.4710	1020.1	.0709	1663.3	.0390
958.4	.4949	1021.1	.0594	1698.0	.0410
959.4	.5188	1023.0	.0423	1760.6	.0431
960.3	.5419	1024.9	.0304	1994.0	.0451
961.3	.5625	1027.8	.0190	2304.5	.0471
962.3	.5804	1032.6	.0078	2836.7	.0491
963.2	.5970	1131.0	.0179	3155.9	.0512
964.2	.6124	1198.5	.0272	3381.5	.0532
965.2	.6253	1223.6	.0293	3432.6	.0554
966.1	.6365	1245.7	.0314	3451.9	.0576
967.1	.6472	1276.6	.0334	3465.4	.0597
968.0	.6574	1312.3	.0354	3473.1	.0617
970.0	.6728	1352.8	.0375	3481.8	.0637
971.9	.6870	1402.0	.0395	3486.6	.0660
974.8	.7010	1462.7	.0416	3489.5	.0681
978.7	.7126	1516.7	.0437	3492.4	.0702
987.3	.6995	1546.6	.0458	3495.3	.0729
990.2	.6860	1563.9	.0480	3497.2	.0751
992.2	.6722	1574.5	.0501	3500.1	.0783
994.1	.6574	1581.3	.0523	3502.1	.0808

APPENDIX C, continued.E||b

$\nu$ (cm <sup>-1</sup> )	R	$\nu$ (cm <sup>-1</sup> )	R	$\nu$ (cm <sup>-1</sup> )	R
3504.0	.0838	3520.4	.0479	3542.5	.0301
3505.9	.0862	3521.3	.0416	3546.4	.0323
3507.8	.0888	3522.3	.0361	3550.3	.0346
3513.6	.0863	3523.3	.0312	3556.0	.0367
3514.6	.0831	3524.2	.0271	3565.7	.0387
3515.6	.0789	3525.2	.0242	3577.3	.0411
3516.5	.0739	3527.1	.0208	3600.4	.0432
3517.5	.0681	3533.9	.0230	3649.6	.0453
3518.4	.0616	3536.8	.0254	3780.7	.0474
3519.4	.0547	3539.7	.0279	4399.8	.0486

E⊥b

104.1	.2052	144.6	.3121	219.8	.0615
106.0	.1791	145.6	.2032	221.7	.0494
108.0	.1989	146.5	.1225	225.6	.0375
110.8	.2116	147.5	.0870	254.5	.0480
111.8	.2238	149.4	.1205	271.9	.0585
115.7	.2042	150.4	.1633	295.0	.0689
116.6	.1868	151.3	.1942	319.1	.0792
117.6	.1747	152.3	.1832	341.3	.0893
119.5	.1917	153.3	.1632	365.4	.0994
120.5	.2172	154.2	.1430	381.8	.1094
121.4	.2432	155.2	.1203	398.2	.1199
122.4	.2698	156.2	.0913	407.8	.1086
123.4	.2878	157.1	.0673	412.6	.0957
124.3	.3046	158.1	.0529	415.5	.0847
125.3	.3187	160.0	.0423	419.4	.0715
126.3	.3465	166.8	.0524	422.3	.0613
127.2	.4085	170.6	.0661	427.1	.0491
128.2	.4503	177.4	.0551	465.7	.0596
130.1	.4670	180.3	.0427	469.5	.0705
131.1	.4917	189.9	.0552	474.4	.0821
132.1	.5296	193.8	.0672	478.2	.0929
133.0	.5609	198.6	.0821	482.1	.1047
138.8	.5885	201.5	.0929	485.0	.1159
139.8	.6084	202.4	.1037	487.9	.1284
140.7	.5814	206.3	.1155	491.7	.1395
141.7	.5430	214.0	.1033	495.6	.1280
142.7	.4960	215.9	.0911	497.5	.1128
143.6	.4137	217.9	.0767	499.4	.0978

## APPENDIX C, continued

E1b

$\nu$ (cm <sup>-1</sup> )	R	$\nu$ (cm <sup>-1</sup> )	R	$\nu$ (cm <sup>-1</sup> )	R
501.4	.0807	877.4	.1536	937.2	.1292
503.3	.0648	881.3	.1646	938.2	.0711
505.2	.0436	884.2	.1748	939.1	.0380
506.2	.0308	887.1	.1873	940.1	.0201
508.1	.0160	889.9	.2012	942.0	.0081
520.6	.0263	891.9	.2128	945.9	.0208
533.2	.0363	893.8	.2262	947.8	.0347
552.5	.0464	895.7	.2423	949.7	.0528
572.7	.0570	897.7	.2614	951.7	.0740
586.2	.0675	898.6	.2728	952.6	.0866
593.9	.0785	899.6	.2847	953.6	.1007
598.7	.0885	900.5	.2982	954.5	.1163
602.6	.1019	901.5	.3143	955.5	.1341
605.5	.1161	902.5	.3318	956.5	.1552
607.4	.1299	903.4	.3497	957.4	.1798
609.4	.1442	904.4	.3694	958.4	.2088
611.3	.1599	905.4	.3921	959.4	.2435
612.2	.1700	906.3	.4158	960.3	.2847
613.2	.1838	907.3	.4398	961.3	.3313
614.2	.2022	908.3	.4655	962.3	.3814
615.1	.2236	909.2	.4924	963.2	.4315
616.1	.2455	910.2	.5177	964.2	.4757
617.1	.2643	911.2	.5405	965.2	.5109
618.0	.2747	912.1	.5623	966.1	.5374
620.0	.2563	913.1	.5828	967.1	.5569
620.9	.2247	914.0	.5996	968.0	.5713
621.9	.1796	915.0	.6138	970.0	.5857
622.9	.1291	916.0	.6281	974.8	.5699
623.8	.0819	916.9	.6422	976.7	.5492
624.8	.0457	917.9	.6535	977.7	.5349
625.7	.0247	919.8	.6712	978.7	.5191
626.7	.0145	924.7	.6571	979.6	.5022
642.1	.0256	925.6	.6429	980.6	.4826
653.7	.0359	926.6	.6285	981.5	.4605
676.8	.0462	927.5	.6169	982.5	.4368
712.5	.0565	928.5	.6059	983.5	.4112
757.8	.0671	929.5	.5926	984.4	.3825
797.4	.0771	930.4	.5756	985.4	.3514
819.6	.0872	931.4	.5528	986.4	.3191
836.9	.0979	932.4	.5187	987.3	.2858
849.4	.1086	933.3	.4682	988.3	.2513
858.1	.1186	934.3	.3982	989.3	.2170
865.8	.1301	935.3	.3102	990.2	.1855
872.6	.1421	936.2	.2143	991.2	.1570

APPENDIX C, continued

<u>E1b</u>					
$\nu$ <u>(cm<sup>-1</sup>)</u>	<u>R</u>	$\nu$ <u>(cm<sup>-1</sup>)</u>	<u>R</u>	$\nu$ <u>(cm<sup>-1</sup>)</u>	<u>R</u>
992.2	.1315	3104.8	.0466	3592.7	.0433
993.1	.1096	3359.3	.0486	3593.7	.0401
994.1	.0919	3449.0	.0508	3594.6	.0375
995.0	.0773	3497.2	.0528	3595.6	.0350
996.0	.0650	3512.7	.0549	3596.5	.0325
997.9	.0470	3532.9	.0571	3597.5	.0304
999.9	.0351	3539.7	.0591	3599.4	.0270
1002.8	.0238	3545.4	.0612	3601.4	.0247
1007.6	.0133	3549.3	.0634	3604.3	.0225
1019.2	.0030	3553.2	.0656	3619.7	.0250
1081.8	.0130	3558.0	.0682	3626.4	.0273
1161.9	.0231	3561.8	.0709	3632.2	.0293
1197.5	.0262	3567.6	.0730	3640.9	.0314
1225.5	.0282	3582.1	.0707	3651.5	.0336
1260.2	.0303	3584.0	.0682	3665.0	.0356
1304.6	.0323	3585.9	.0644	3683.3	.0377
1354.7	.0343	3586.9	.0618	3720.9	.0398
1411.6	.0363	3587.9	.0590	3787.5	.0421
1511.9	.0383	3588.8	.0561	4107.6	.0444
1655.5	.0404	3589.8	.0530	4398.8	.0444
1799.2	.0424	3590.8	.0500		
2460.7	.0445	3591.7	.0468		

## APPENDIX D

Kramers-Kronig Derived Values of the Dielectric Function  
for Polycrystalline  $\text{Ba}(\text{ClO}_3)_2 \cdot \text{H}_2\text{O}$

$\nu$ ( $\text{cm}^{-1}$ )	$\epsilon'$	$\epsilon''$	$\nu$ ( $\text{cm}^{-1}$ )	$\epsilon'$	$\epsilon''$
49.4	8.12	1.49	96.4	-4.06	17.04
50.6	8.15	1.74	97.0	-4.65	15.30
52.5	7.92	1.48	97.6	-4.96	13.60
55.5	8.15	1.13	98.2	-4.91	12.02
58.6	8.68	1.34	98.8	-4.60	10.67
62.2	8.84	1.58	99.4	-4.17	9.54
64.0	8.86	1.33	100.0	-3.63	8.59
69.5	10.01	1.53	100.6	-2.97	7.86
72.0	10.99	1.77	101.3	-2.29	7.43
72.6	11.01	2.04	101.9	-1.73	7.21
76.2	12.23	2.50	106.1	-.78	6.92
76.9	12.41	2.83	107.4	-.92	6.64
77.5	12.50	3.07	108.6	-1.18	6.21
78.7	12.91	3.53	109.2	-1.26	5.89
79.3	13.08	3.87	109.8	-1.29	5.53
79.9	13.15	4.16	110.4	-1.26	5.16
80.5	13.29	4.39	111.0	-1.16	4.79
81.1	13.50	4.71	111.6	-.98	4.44
81.7	13.59	5.15	112.2	-.77	4.14
82.3	13.49	5.45	112.8	-.53	3.87
84.2	14.15	5.78	113.5	-.26	3.62
84.8	14.47	6.10	114.1	.06	3.41
85.4	14.81	6.32	115.3	.82	3.18
86.0	15.41	6.55	117.1	1.98	3.45
86.6	16.31	7.11	117.7	2.31	3.70
87.2	17.17	8.10	118.3	2.60	4.03
87.8	17.83	9.27	118.9	2.81	4.46
88.4	18.56	10.61	119.6	2.90	4.96
89.1	19.42	12.68	120.2	2.84	5.53
89.7	19.55	15.79	120.8	2.57	6.07
90.3	18.04	18.82	121.4	2.12	6.51
90.9	15.85	20.66	122.0	1.57	6.77
91.5	14.00	22.13	124.4	-.55	6.27
92.1	11.72	23.96	125.0	-.88	5.90
92.7	8.26	25.19	125.7	-1.12	5.50
93.3	4.63	24.78	126.3	-1.26	5.07
93.9	1.97	23.39	126.9	-1.30	4.66
94.5	.01	21.95	127.5	-1.25	4.29
95.2	-1.70	20.50	128.1	-1.14	3.98
95.8	-3.10	18.83	128.7	-1.00	3.74

## APPENDIX D, continued

$\nu$ ( $\text{cm}^{-1}$ )	$\epsilon'$	$\epsilon''$	$\nu$ ( $\text{cm}^{-1}$ )	$\epsilon'$	$\epsilon''$
129.9	-.69	3.49	509.1	.94	1.54
133.0	-.96	3.17	510.1	.84	1.34
133.6	-1.04	2.88	511.0	.81	1.08
134.2	-.99	2.56	512.0	.88	.82
134.8	-.86	2.28	513.9	1.17	.51
135.4	-.69	2.07	520.7	1.71	.30
136.6	-.32	1.81	522.7	2.64	.10
143.3	.63	1.57	505.5	3.56	.33
145.8	.88	1.36	607.5	3.73	.55
164.1	1.80	1.56	609.4	3.79	.91
167.7	1.58	1.31	611.3	3.66	1.27
170.2	1.67	1.07	613.2	3.41	1.60
179.3	2.00	.84	621.9	1.69	1.36
198.6	3.03	1.11	622.9	1.61	1.13
202.5	3.14	1.31	623.8	1.60	.91
204.4	3.05	1.58	625.8	1.71	.58
208.3	2.72	1.82	628.7	1.93	.35
215.0	2.18	1.58	638.3	2.30	.15
217.9	2.10	1.35	830.2	3.74	-.05
222.7	2.20	1.12	879.4	5.02	-.26
240.1	1.97	.91	892.9	6.15	-.46
243.0	1.99	.69	904.4	9.18	-.09
248.8	2.19	.49	905.4	9.60	.18
346.1	3.45	.71	906.4	10.02	.54
364.5	3.49	.92	907.3	10.42	.98
375.1	3.53	1.14	908.3	10.78	1.49
385.7	3.47	1.36	909.3	11.07	2.09
392.4	3.33	1.57	910.2	11.29	2.74
416.5	2.39	1.37	911.2	11.44	3.43
422.3	2.34	1.15	912.2	11.51	4.16
429.1	2.38	.95	913.1	11.51	4.94
439.7	2.54	.74	914.1	11.41	5.76
467.6	2.89	.54	915.0	11.19	6.61
476.3	3.58	.77	916.0	10.82	7.47
478.2	3.70	1.03	917.0	10.30	8.30
480.2	3.63	1.35	917.9	9.61	9.08
484.0	3.46	1.59	918.9	8.76	9.74
486.0	3.35	1.80	919.9	7.76	10.23
489.8	2.94	2.01	920.8	6.67	10.50
497.5	2.42	1.79	922.8	4.55	10.29
501.4	2.62	2.10	923.7	3.69	9.90
502.4	2.50	2.41	924.7	2.99	9.43
503.3	2.12	2.66	925.7	2.44	8.92
505.2	1.26	2.38	926.6	1.99	8.43
506.2	1.11	2.06	927.6	1.61	7.94
507.2	1.07	1.82	928.5	1.27	7.45

## APPENDIX D, continued

$\nu$ ( $\text{cm}^{-1}$ )	$\epsilon'$	$\epsilon''$	$\nu$ ( $\text{cm}^{-1}$ )	$\epsilon'$	$\epsilon''$
929.5	.97	6.92	978.7	-2.78	2.13
930.5	.74	6.35	980.6	-2.36	1.82
931.4	.61	5.72	982.5	-1.98	1.60
932.4	.60	5.09	986.4	-1.37	1.36
933.4	.71	4.47	1000.9	-.42	1.14
934.3	.94	3.91	1008.6	-.18	.92
935.3	1.28	3.42	1021.1	.15	.71
936.3	1.70	3.01	1029.8	.29	.48
937.2	2.18	2.73	1040.4	.62	.28
939.2	3.17	2.50	1182.1	1.83	.08
942.0	4.56	2.79	1311.3	2.12	.04
943.0	4.97	3.03	1598.7	2.49	.08
944.0	5.34	3.35	1600.6	2.53	.13
944.9	5.67	3.73	1602.5	2.56	.22
945.9	5.93	4.17	1603.5	2.56	.28
946.9	6.13	4.65	1604.5	2.54	.35
947.8	6.26	5.18	1605.4	2.48	.41
948.8	6.32	5.74	1606.4	2.40	.45
949.8	6.29	6.32	1609.3	2.16	.39
950.7	6.18	6.91	1610.3	2.11	.33
951.7	5.98	7.50	1611.2	2.09	.28
952.7	5.69	8.09	1612.2	2.09	.23
953.6	5.32	8.65	1613.2	2.10	.19
954.6	4.85	9.18	1615.1	2.11	.13
955.5	4.29	9.66	1618.0	2.15	.08
956.5	3.64	10.07	1622.8	2.19	.04
957.5	2.90	10.39	1679.7	2.33	.00
959.4	1.28	10.65	1776.1	2.38	.04
961.3	-.35	10.39	1916.9	2.35	.00
962.3	-1.09	10.09	2034.5	2.39	-.04
963.3	-1.77	9.69	2095.3	2.39	-.08
964.2	-2.37	9.22	2130.0	2.42	-.12
965.2	-2.88	8.69	2332.5	2.62	-.08
966.2	-3.31	8.13	2383.6	2.63	-.04
967.1	-3.65	7.53	2460.7	2.64	.00
968.1	-3.90	6.92	2505.1	2.63	.04
969.0	-4.08	6.31	2615.0	2.59	.00
970.0	-4.17	5.72	2652.6	2.66	.04
971.0	-4.19	5.14	2752.9	2.64	.08
971.9	-4.14	4.60	2914.9	2.63	.12
972.9	-4.04	4.09	3381.6	2.55	.08
973.9	-3.88	3.63	3496.3	2.76	.12
974.8	-3.69	3.23	3502.1	2.82	.17
975.8	-3.47	2.88	3505.0	2.86	.21
976.8	-3.24	2.58	3506.9	2.87	.26
977.7	-3.01	2.33	3508.8	2.88	.31

## APPENDIX D, continued

$\nu$ (cm <sup>-1</sup> )	$\epsilon'$	$\epsilon''$	$\nu$ (cm <sup>-1</sup> )	$\epsilon'$	$\epsilon''$
3510.8	2.88	.38	3583.1	2.56	.71
3512.7	2.86	.46	3592.7	2.17	.67
3514.6	2.80	.53	3594.7	2.12	.61
3516.5	2.71	.59	3596.6	2.09	.56
3522.3	2.42	.53	3598.5	2.06	.50
3524.3	2.37	.46	3600.4	2.05	.45
3526.2	2.35	.38	3602.4	2.04	.40
3528.1	2.35	.32	3604.3	2.05	.35
3530.0	2.36	.27	3607.2	2.06	.29
3532.9	2.40	.21	3610.1	2.07	.25
3536.8	2.44	.17	3613.9	2.10	.20
3559.9	2.70	.22	3618.8	2.13	.15
3563.8	2.73	.27	3625.5	2.17	.11
3566.7	2.75	.32	3635.1	2.21	.07
3569.6	2.75	.38	3656.4	2.28	.03
3571.5	2.75	.42	3711.3	2.36	-.01
3573.4	2.74	.46	4095.1	2.48	-.05
3575.4	2.73	.51	4231.0	2.58	-.01
3577.3	2.71	.56	4303.4	2.57	.03
3579.2	2.68	.62	4399.8	2.54	.03
3581.2	2.63	.67			

## APPENDIX E

Kramers-Kronig Derived Values of the Dielectric Function  
for the (001) Crystal Face of  $\text{Ba}(\text{ClO}_3)_2 \cdot \text{H}_2\text{O}$

E||b

$\nu$ ( $\text{cm}^{-1}$ )	$\epsilon'$	$\epsilon''$	$\nu$ ( $\text{cm}^{-1}$ )	$\epsilon'$	$\epsilon''$
114.7	-1.28	3.10	225.6	2.95	2.15
115.7	-.28	2.79	227.5	2.72	2.45
116.6	.36	3.11	229.4	2.23	2.66
117.6	.63	3.79	233.3	1.25	2.41
118.6	.38	4.60	235.2	.94	2.01
119.5	-.42	5.08	236.2	.86	1.80
121.4	-2.11	4.29	238.1	.80	1.41
122.4	-2.56	3.34	240.0	.86	1.06
123.4	-2.31	2.40	242.0	1.03	.83
124.3	-1.82	1.87	244.9	1.20	.62
125.3	-1.38	1.60	251.6	1.52	.39
127.2	-.78	1.35	283.4	2.20	.16
131.1	.40	1.60	389.5	2.80	.34
132.1	.32	1.98	394.3	2.80	.23
134.0	-.45	1.71	476.3	3.86	.45
134.9	-.40	1.29	478.2	3.91	.79
135.9	-.22	1.01	479.2	3.85	1.03
137.8	.22	.70	483.0	3.13	.75
149.4	2.12	.93	485.9	3.33	.54
150.4	2.28	1.18	496.5	4.20	.75
151.3	2.25	1.38	498.5	4.53	.97
154.2	2.39	1.80	501.4	5.16	1.32
155.2	2.33	2.02	502.3	5.59	1.67
157.1	2.31	2.35	503.3	6.10	2.31
158.1	2.15	2.82	504.2	6.56	3.44
159.1	1.62	3.11	505.2	6.55	5.48
161.0	.75	2.90	506.2	4.64	7.95
161.9	.38	2.65	507.1	.86	8.19
162.9	.12	2.28	508.1	-1.55	5.81
163.9	.05	1.89	509.1	-1.76	3.38
164.8	.08	1.55	510.0	-1.11	1.99
165.8	.18	1.29	511.0	-.45	1.29
166.8	.28	1.09	512.0	.06	.93
168.7	.52	.76	512.9	.46	.72
172.6	.97	.50	514.9	1.02	.51
209.2	2.98	.75	523.5	1.95	.30
214.0	3.11	1.01	600.7	3.38	.53
217.9	3.10	1.28	604.5	3.65	.83
221.7	3.19	1.56	606.5	3.76	1.21
223.7	3.14	1.85	607.4	3.74	1.49

## APPENDIX E, continued

E II b

$\nu$ ( $\text{cm}^{-1}$ )	$\epsilon'$	$\epsilon''$	$\nu$ ( $\text{cm}^{-1}$ )	$\epsilon'$	$\epsilon''$
608.4	3.61	1.81	959.4	.84	18.74
609.4	3.34	2.07	960.3	-1.92	18.10
614.2	1.62	1.84	961.3	-4.20	16.71
615.1	1.45	1.50	962.3	-5.80	14.97
616.1	1.42	1.19	963.2	-6.85	13.17
617.1	1.46	.93	964.2	-7.44	11.41
619.0	1.64	.59	965.2	-7.64	9.81
621.9	1.90	.37	966.1	-7.59	8.44
638.3	2.44	.17	967.1	-7.41	7.27
882.2	4.21	.38	968.0	-7.14	6.26
901.5	4.91	.58	969.0	-6.79	5.40
909.2	5.33	.81	970.0	-6.42	4.70
915.0	5.71	1.04	970.9	-6.07	4.10
918.9	6.05	1.30	971.9	-5.70	3.58
921.8	6.31	1.59	972.9	-5.34	3.15
923.7	6.46	1.84	973.8	-5.00	2.79
925.6	6.57	2.05	974.8	-4.68	2.47
927.5	6.81	2.29	975.8	-4.37	2.19
928.5	6.97	2.52	976.7	-4.08	1.97
929.5	7.09	2.86	978.7	-3.56	1.59
930.4	7.06	3.29	980.6	-3.09	1.31
931.4	6.83	3.70	982.5	-2.69	1.10
932.4	6.44	3.92	985.4	-2.18	.87
935.3	5.65	3.53	989.3	-1.63	.66
936.2	5.65	3.30	996.0	-.93	.45
937.2	5.76	3.10	1010.5	-.06	.24
939.1	6.21	2.89	1108.8	1.59	.04
943.0	7.49	3.19	1583.2	2.55	.08
943.9	7.84	3.41	1590.0	2.65	.13
944.9	8.22	3.70	1593.8	2.75	.18
945.9	8.61	4.07	1595.8	2.81	.24
946.8	8.98	4.53	1597.7	2.89	.33
947.8	9.33	5.06	1598.7	2.94	.39
948.8	9.69	5.70	1599.6	2.99	.47
949.7	10.01	6.48	1600.6	3.03	.59
950.7	10.24	7.36	1601.5	3.05	.74
951.7	10.42	8.35	1602.5	3.04	.93
952.6	10.51	9.56	1603.5	2.95	1.15
953.6	10.38	10.95	1604.4	2.76	1.36
954.5	9.99	12.45	1605.4	2.47	1.49
955.5	9.29	14.11	1607.3	1.86	1.36
956.5	8.05	15.90	1608.3	1.68	1.16
957.4	6.13	17.48	1609.3	1.58	.96
958.4	3.64	18.50	1610.2	1.55	.77

## APPENDIX E, continued

E||b

$\nu$ (cm <sup>-1</sup> )	$\epsilon'$	$\epsilon''$	$\nu$ (cm <sup>-1</sup> )	$\epsilon'$	$\epsilon''$
1611.2	1.56	.62	3508.8	3.02	1.16
1612.2	1.60	.50	3509.8	2.95	1.26
1613.1	1.63	.41	3510.7	2.86	1.35
1614.1	1.68	.34	3511.7	2.74	1.43
1615.0	1.72	.28	3512.7	2.61	1.49
1616.0	1.75	.24	3516.5	2.01	1.44
1617.9	1.82	.17	3517.5	1.88	1.36
1619.9	1.88	.13	3518.4	1.78	1.27
1623.7	1.97	.09	3519.4	1.69	1.16
1632.4	2.09	.05	3520.4	1.63	1.05
3453.8	2.67	.09	3521.3	1.60	.95
3472.2	2.75	.14	3522.3	1.57	.85
3481.8	2.80	.18	3523.3	1.56	.75
3488.6	2.88	.22	3524.2	1.56	.66
3492.4	2.94	.27	3525.2	1.58	.58
3495.3	2.99	.33	3526.2	1.59	.51
3497.2	3.03	.39	3527.1	1.61	.44
3499.2	3.06	.46	3528.1	1.63	.38
3500.1	3.08	.50	3529.1	1.67	.33
3501.1	3.09	.55	3530.0	1.70	.28
3502.1	3.11	.59	3531.9	1.76	.21
3503.0	3.13	.65	3533.9	1.83	.16
3504.0	3.13	.72	3536.8	1.89	.12
3504.9	3.13	.80	3540.6	1.98	.07
3505.9	3.12	.88	3549.3	2.10	.03
3506.9	3.10	.96	4399.8	2.45	.05
3507.8	3.07	1.06			

E⊥b

104.1	5.18	3.50	118.6	5.43	2.04
106.0	4.74	2.79	119.5	6.16	1.68
107.0	5.21	2.46	121.4	8.29	1.99
108.0	5.81	2.67	122.4	9.31	2.83
108.9	5.90	3.03	123.4	9.84	3.80
111.8	6.20	3.55	124.3	10.32	4.73
112.8	5.99	4.02	125.3	10.84	5.41
115.7	4.75	3.70	126.3	12.44	6.38
116.6	4.66	3.13	127.2	14.63	11.04
117.6	4.87	2.50	128.2	10.79	16.31

## APPENDIX E, continued

E1b

$\nu$ (cm <sup>-1</sup> )	$\epsilon'$	$\epsilon''$	$\nu$ (cm <sup>-1</sup> )	$\epsilon'$	$\epsilon''$
131.1	1.48	16.62	387.6	3.41	1.60
132.1	-2.26	15.95	394.3	3.26	1.87
133.0	-5.10	13.00	401.1	2.88	2.08
134.0	-5.38	10.01	412.6	1.99	1.85
134.9	-5.11	8.16	416.5	1.85	1.60
135.9	-4.91	6.85	420.4	1.79	1.39
136.9	-4.74	5.60	424.2	1.79	1.18
137.8	-4.31	4.68	429.0	1.84	.94
138.8	-4.11	3.73	436.8	1.97	.72
139.8	-3.58	2.67	446.4	2.13	.51
140.7	-2.76	2.08	462.8	2.53	.31
141.7	-2.13	1.74	475.3	3.22	.52
142.7	-1.59	1.46	479.2	3.42	.79
144.6	-.58	1.19	482.1	3.54	1.05
148.4	1.04	1.62	484.0	3.60	1.32
149.4	1.15	2.10	485.9	3.58	1.62
150.4	.82	2.55	486.9	3.55	1.83
152.3	.15	2.00	488.8	3.29	2.17
153.3	.21	1.74	490.8	2.98	2.49
155.2	.38	1.36	496.5	1.52	2.25
157.1	.72	1.08	498.5	1.32	1.92
171.6	1.97	1.39	500.4	1.17	1.66
177.4	1.66	1.18	502.3	1.10	1.39
180.3	1.72	.92	504.2	1.02	1.13
186.1	2.11	.72	506.2	1.06	.79
198.6	2.97	.93	508.1	1.23	.54
202.4	3.35	1.28	513.9	1.61	.32
203.4	3.35	1.61	566.9	2.56	.11
205.3	3.04	1.85	603.6	3.84	.34
207.3	2.86	2.06	606.5	4.24	.61
209.2	2.60	2.27	608.4	4.54	1.01
214.0	1.74	1.99	609.4	4.64	1.28
215.9	1.56	1.77	610.3	4.72	1.58
217.9	1.46	1.54	611.3	4.79	1.92
219.8	1.46	1.30	612.2	4.85	2.32
222.7	1.53	1.02	613.2	4.88	2.87
226.6	1.64	.77	614.2	4.74	3.64
236.2	1.94	.55	615.1	4.19	4.54
251.6	2.31	.35	616.1	3.07	5.21
330.7	3.23	.55	618.0	.44	4.54
351.9	3.38	.76	619.0	-.17	3.55
366.4	3.49	.96	620.0	-.31	2.65
374.1	3.50	1.17	620.9	-.20	1.96
382.8	3.48	1.38	621.9	.01	1.47

## APPENDIX E, continued

E1b

$\nu$ (cm <sup>-1</sup> )	$\epsilon'$	$\epsilon''$	$\nu$ (cm <sup>-1</sup> )	$\epsilon'$	$\epsilon''$
622.9	.23	1.13	958.4	6.26	2.69
623.8	.43	.88	959.4	6.95	3.93
625.7	.80	.58	960.3	7.33	5.86
629.6	1.28	.34	961.3	6.74	8.42
641.2	1.86	.14	962.3	4.52	10.82
892.8	7.61	.38	963.2	1.00	11.64
895.7	8.60	.63	964.2	-2.11	10.38
897.7	9.49	.93	965.2	-3.76	8.24
898.6	10.05	1.16	966.1	-4.24	6.27
899.6	10.65	1.46	967.1	-4.16	4.79
900.5	11.36	1.84	968.0	-3.84	3.71
901.5	12.24	2.42	969.0	-3.46	2.93
902.5	13.18	3.28	970.0	-3.07	2.38
903.4	14.09	4.42	970.9	-2.72	1.97
904.4	15.02	5.92	971.9	-2.40	1.66
905.4	15.87	8.04	972.9	-2.12	1.43
906.3	16.20	10.81	974.8	-1.65	1.10
907.3	15.68	14.00	976.7	-1.28	.88
908.3	14.09	17.45	979.6	-.85	.68
909.2	10.94	20.62	985.4	-.26	.46
910.2	6.52	22.37	1010.5	.77	.26
912.1	-2.10	20.77	1197.5	1.92	.07
913.1	-5.12	18.25	2718.1	2.36	.03
914.0	-6.87	15.37	3404.7	2.47	.07
915.0	-7.65	12.74	3504.9	2.57	.11
916.0	-7.91	10.45	3526.2	2.62	.16
916.9	-7.78	8.44	3543.5	2.73	.21
917.9	-7.35	6.79	3548.3	2.77	.25
918.9	-6.77	5.49	3552.2	2.81	.30
919.8	-6.17	4.44	3555.1	2.83	.35
920.8	-5.52	3.59	3558.0	2.86	.39
921.8	-4.87	2.95	3559.9	2.88	.45
922.7	-4.27	2.48	3561.8	2.89	.51
923.7	-3.74	2.12	3563.8	2.88	.57
924.7	-3.27	1.85	3565.7	2.87	.63
925.6	-2.86	1.64	3567.6	2.86	.70
927.5	-2.21	1.31	3569.5	2.83	.76
929.5	-1.65	1.01	3571.5	2.79	.81
931.4	-1.14	.77	3573.4	2.77	.88
934.3	-.42	.54	3574.4	2.75	.92
954.5	3.96	.88	3576.3	2.68	1.00
955.5	4.41	1.09	3578.2	2.60	1.05
956.5	4.94	1.41	3580.2	2.52	1.12
957.4	5.56	1.91	3582.1	2.40	1.16

APPENDIX E, continued

<u>E1b</u>					
$\nu$ ( $\text{cm}^{-1}$ )	$\epsilon'$	$\epsilon''$	$\nu$ ( $\text{cm}^{-1}$ )	$\epsilon'$	$\epsilon''$
3588.8	1.94	1.11	3602.3	1.68	.48
3590.8	1.83	1.03	3604.3	1.69	.41
3591.7	1.79	.98	3606.2	1.72	.35
3592.7	1.75	.92	3609.1	1.75	.30
3593.7	1.72	.87	3612.0	1.78	.25
3594.6	1.71	.82	3614.9	1.81	.19
3595.6	1.69	.77	3618.7	1.86	.14
3596.5	1.67	.72	3625.5	1.93	.10
3597.5	1.67	.67	3632.2	2.00	.06
3598.5	1.66	.63	3673.7	2.16	.02
3599.4	1.66	.59	4398.8	2.35	.04
3600.4	1.67	.55			